Combinations of cosmic microwave background and large-scale structure cosmological probes

Cyrille Doux

UNIVERSITÉ SORBONNE PARIS CITÉ

UNIVERSITÉ PARIS DIDEROT
École doctorale des Sciences de la Terre et de l'Environnement et Physique de l'Univers, Paris - ED 560
Laboratoire Astroparticule et Cosmologie (APC)

Combinaisons de sondes cosmologiques

Deux applications avec les données de Planck et de SDSS-III/BOSS

Cyrille Doux

Thèse de doctorat de Physique de l'Univers
dirigée par Ken Ganga et co-dirigée par Éric Aubourg,

présentée et soutenue publiquement le 14 novembre 2017
devant un jury composé de :

Pr. Danièle Steer	(Université Paris-Diderot, APC)	*Présidente du jury*
Dr. Nathalie Palanque-Delabrouille	(CEA, IRFU/SPP)	*Rapporteur*
Pr. Martin Kunz	(Université de Genève)	*Rapporteur*
Pr. Hiranya Peiris	(University College London)	*Examinatrice*
Dr. Dominique Boutigny	(CNRS, LAPP)	*Examinateur*
Pr. David Spergel	(Princeton University)	*Examinateur*
Dr. Ken Ganga	(CNRS, APC)	*Directeur de thèse*
Dr. Éric Aubourg	(CEA, APC)	*Co-directeur de thèse*

Résumé

Cette thèse s'intéresse aux combinaisons d'observables cosmologiques provenant des mesures du fond diffus cosmologique et des relevés de galaxies, et est basée sur l'exploitation des données du satellite Planck et du Baryon Oscillation Spectroscopic Survey (BOSS) du Sloan Digital Sky Survey. On explore l'utilisation de corrélations croisées entre les jeux de données afin de mettre en évidence de nouveaux effets et d'améliorer les contraintes statistiques sur les paramètres cosmologiques. Dans un premier temps, on mesure pour la première fois une corrélation entre le lentillage gravitationnel du fond diffus cosmologique et le spectre de puissance des fluctuations de la forêt Lyman-α des quasars. Cet effet, d'origine purement non-linéaire, est interprété comme la réponse du spectre de puissance à des grandes échelles. Il montre comment les fluctuations dans la densité en hydrogène neutre dans le milieu intergalactique sont influencées par des fluctuations à grande échelle dans la densité de matière noire. Le signal mesuré est compatible avec l'approche théorique et des simulations menées par d'autres groupes. Dans un deuxième temps, on développe un formalisme permettant une analyse conjointe de la densité de galaxies et de quasars de BOSS avec le lentillage gravitationnel du fond diffus cosmologique. La prise en compte des corrélations croisées entre ces sondes permet de diminuer les barres d'erreurs de certains paramètres cosmologiques de 20%, ce qui équivaut à augmenter la surface couverte par les relevés de presque 50%. Cette analyse est complétée par la mesure des anisotropies de température du fond diffus cosmologique afin de contraindre tous les paramètres du modèle standard ΛCDM, ainsi que les biais des galaxies. Puis on étend le modèle afin d'explorer les contraintes sur l'équation d'état de l'énergie noire et la somme des masses des neutrinos.

Mots-clés — Cosmologie - Fond diffus cosmologique - Relevés de galaxies - Lentillage gravitationnel - Forêt Lyman-α- Energie noire - Matière sombre

Abstract

This thesis addresses the combinations of cosmological probes from the measurements of the cosmic microwave background (CMB) and galaxy redshift surveys, and exploits data from the Planck satellite and the Baryon Oscillation Spectroscopic Survey (BOSS) of the Sloan Digital Sky Survey. It explores how cross-correlations between different data sets can be used to detect new signals and improve contraints on cosmological parameters. First, we measure, for the first time, the cross-correlation between gravitational lensing of the CMB and the power spectrum of the Lyman-α forest in the spectra of quasars. This effect, which emerges from purely non-linear evolution, is interpreted as the response of the power spectrum to large-scale modes. It shows how fluctuations in the density of neutral hydrogen in the intergalactic medium are affected by large-scale fluctuations in the density of dark matter. The measured signal is compatible with the theoretical approach and simulations run by another group. In a second time, we develop a formalism enabling the joint analysis of the galaxy/quasar density contrast and CMB lensing. Taking cross-correlations between these probes into account reduces error bars on some cosmological parameters by up to 20%, equivalent to an increase in the size of the survey of about 50%. This analysis is completed by CMB temperature anisotropies information in order to constrain all the parameters of the ΛCDM standard model and galaxy biases at once. Finally, it is extended to obtain contraints on the dark energy equation of state as well as the sum of the masses of neutrinos.

Keywords — Cosmology - Cosmic microwave background - Galaxy redshift survey - Gravitational lensing - Lyman-α forest - Dark energy - Dark matter

A mes grands-parents.

Remerciements

Je souhaite tout d'abord remercier chaleureusement mes deux directeurs de thèse, Ken et Éric, pour m'avoir fait confiance, pour avoir su être présents tout en me donnant une liberté totale (parfois déroutante, mais toujours riche d'enseignements), pour m'avoir permis de voyager et de rencontrer des chercheur(se)s exceptionnel(le)s, pour leur bonne humeur et pour tout ce que j'ai appris auprès d'eux ! J'ai eu cette chance inouïe d'être toujours allé voir mes "boss" avec le sourire, et je les en remercie.

I would like to kindly thank all the jury members for their participation to my thesis defense –I was truly honored. I am particularly grateful to the referees who read and reported this manuscript. I would like to thank David Spergel for the project he launched me on (see Chapter 5), for inviting me to Princeton and giving me the opportunity to present my work there several times, for the enriching discussions we had (that I remember spending a week to decipher the first time) and finally for accepting to be examiner of my defense.

Ensuite, je tiens à exprimer ma profonde gratitude à ma "maman" et mon "papa" de thèse, Mariana Penna-Lima et Sandro Vitenti. J'ai appris énormément auprès d'eux en cosmologie, en programmation, en analyse statistique et en théorie. En plus de collaborateurs brillants, je me suis fait deux amis que j'espère garder longtemps. En un mot : *obrigado* !

Je voudrais aussi remercier Emmanuel Schaan, rencontré à Princeton alors que nous étions tous deux à l'ENS, pour tout ce que j'ai appris avec lui, pour le travail accompli ensemble, pour son humour sophistiqué (si, si) et pour sa vivacité.

Un grand merci à Julien Tréguer, mon ancien co-thésard, avec qui j'ai adoré travailler, mais aussi discuter, des heures durant, science, économie, voyages, nouvelles technologies, cinéma, et j'en passe.

Une pensée pour Robert Cahn qui m'a fait découvrir, avec le sourire, la cosmologie durant un stage à Berkeley, il y a quatre ans, ainsi qu'à Pierre Binétruy, alors enseignant à l'ENS, qui m'avait mis en contact avec Bob. Another thought goes to Judit and Laszlo Sturmann with whom I spent four incredible weeks at Mount Wilson Observatory in 2012, where Hubble carried out his milestone observations in the 1920's.

Je voudrais aussi remercier les nombreux chercheurs de l'APC avec qui j'ai pu échanger durant ces trois années, en particulier Cécile Roucelle, Jean-Christophe Hamilton, Begoña Ascaso, Josquin Errard, Jim Bartlett, Karim Nouï, David Langlois, Jean-Marc Le Goff, Cécile Cavet, Nicolas Busca, Michel Piat et Yannick Giraud-Héraud.

Evidemment, rien n'aurait été pareil sans les thésards de l'APC, notamment les cosmologistes et les théoriciens –*a.k.a.* team QPUC[1]. Un grand merci, donc, à Félix, Frédéric, Amélie, Camille, Pierros, Eleonora, Mikhail, Ranajoy, Leandro, Philippe, Jan, Alessandro, Tuan et Thuong.

Je tiens à remercier Cécile de Hosson et François Gallet, au côté de qui j'ai adoré enseigner. Merci également à mes professeurs de prépa qui m'ont permis d'entrer à l'ENS, et ainsi de mettre un pied dans la recherche. Merci aussi à Stéphane Komilikis, pour les khôlles de physique en hors-piste quantique et les interminables discussions, et à Françoise Bagot, pour des enseignements qui dépassait de loin le programme de français-philo (le *kairos* ! !), ainsi que pour ses entrées et sorties de scène mémorables. Merci aussi à ma professeure de piano, Juliette Linget, dont la patience et la gentillesse ont su faire de chaque cours un bol d'air, même lorsque j'avais plutôt la tête sous l'eau.

Merci aux amis membres du Haut Conseil Suprême Intergalactique de l'International Physicists' Tournament 2016 (puis de la sélection française) pour cette folle aventure, à ceux de la Commission Jeune de la SFP et aux extraordinaires physicien(ne)s rencontré(e)s dans ce cadre, en particulier Yves Bréchet pour ses réflexions scientifiques et politiques.

Merci aux amis rencontrés rue d'Ulm, et en particulier à Raphaël, Mathieu, Maxime, Antoine, Veronica, Nathanaël, Félix, Claire, David, Corentin, Anne, Céline, Danijela, Arnaud. Et merci à ceux rencontrés sur les bancs de l'école maternelle (Vincent), du collège (Kevin) et du lycée (Cyril) : cette "famille" auto-proclamée et l'amitié qui l'unit sont une chance et une force !

Merci à ma famille, en particulier à mes grands-parents, et à ma mère, Patricia, pour ses encouragements et son soutien indéfectible. Cette thèse lui doit bien plus qu'elle ne l'imagine. Merci de m'avoir transmis la curiosité et l'émerveillement face à la nature. Merci pour tout.

Enfin et surtout, merci à Marianne pour son soutien, notamment durant la préparation de cette thèse, et pour son esprit pétillant qui sait tout aussi bien adoucir les aléas de la vie que lui donner ses couleurs, son sel et sa joie.[2]

[1] Le changement de présentateur puis la suppression du jeu en ligne furent des traumatismes dont je ne me remettrai jamais.

[2] En plus, elle a de très beaux yeux gris-vert-bleu !

Contents

Résumé **i**

Abstract **iii**

Remerciements **vii**

Foreword **xiii**

Fiducial cosmological model **xvii**

Index of experiments **xix**

List of publications **xxi**

Introduction **1**

1 The standard model of cosmology **5**
1.1 Gravity and cosmology 8
1.1.1 General relativity 8
1.1.2 The expanding Universe 9
1.2 An overview of particle physics 12
1.3 Thermal history 14
1.3.1 Thermodynamics in an expanding Universe 14
1.3.2 A brief history of the Universe 16
1.4 Cosmological perturbation theory 20
1.4.1 Newtonian perturbation theory 20
1.4.2 Relativistic perturbation theory 22
1.4.3 The matter power spectrum 27
Appendices 33
1.A Notions of quantum field theory 33

2 Cosmological probes **37**
2.1 The cosmic microwave background 38
2.1.1 Anisotropies in the cosmic microwave background 39

2.1.2 Features of the angular power spectrum 40
2.1.3 Secondary anisotropies 42
2.1.4 The polarization of the cosmic microwave background 44
2.1.5 Dependence on cosmological parameters 45
2.1.6 Computation of the power spectrum 47
2.2 Tracers of the large-scale structure 48
2.2.1 Galaxy clustering 48
2.2.2 The Lyman-α forest 53
2.3 Gravitational lensing 57
2.3.1 Physical principle 58
2.3.2 Lensing of the cosmic microwave background 61
2.3.3 Cosmic shear 64
2.4 Comparison of cosmological probes 66

3 Experiments: Planck and SDSS-III/BOSS 69
3.1 The Planck satellite 69
3.1.1 Science goals 69
3.1.2 Satellite and instruments 70
3.1.3 Data processing 73
3.1.4 Main science results 79
3.2 SDSS-III/BOSS 80
3.2.1 The Sloan Digital Sky Survey 80
3.2.2 The instruments 82
3.2.3 Target selection 83
3.2.4 Observing strategy 86
3.2.5 Data reduction 87
3.2.6 Main science results 87

4 Combination of cosmic probes: cross-correlations and joint analyses 91
4.1 Motivations 92
4.1.1 A toy model 92
4.1.2 Why and how to combine cosmological probes? 95
4.2 Measuring correlations 98
4.2.1 Cross-power spectra 98
4.2.2 Projected observables 100
4.2.3 Other techniques 106
4.3 Cross-correlations 109
4.3.1 The first studies: CMB $\times$ LSS 110
4.3.2 Gravitational lensing comes into play 111
4.3.3 Combining tracers of the large-scale structure 114
4.4 Joint analyses 117

4.4.1 Current status . . . 117
4.4.2 Forecasts . . . 118
Appendices . . . 121
4.A Signal-to-noise ratio: auto- *vs* cross-correlation . . . 121

5 Detection of the CMB lensing and Lyman-α forest bispectrum 123
5.1 Introduction . . . 124
5.2 Theoretical approach . . . 125
5.2.1 Power spectrum of the Lyman-α forest transmission . . . 126
5.2.2 Position-dependent power spectrum . . . 130
5.2.3 Application to the correlation of CMB lensing and the Lyman-α forest . . . 131
5.3 Analysis . . . 134
5.3.1 Lyman-α forest power spectrum . . . 134
5.3.2 Results . . . 140
5.3.3 Null tests . . . 143
5.4 Discussion . . . 143
5.5 Perspectives . . . 145

6 Joint analysis of Planck and SDSS-III/BOSS data 149
6.1 Introduction . . . 150
6.2 Theoretical background [reloaded] . . . 151
6.3 Data . . . 154
6.3.1 Planck data . . . 154
6.3.2 SDSS-III/BOSS data . . . 155
6.3.3 CMB lensing–large-scale structure correlations data . . . 158
6.4 Methodology . . . 160
6.4.1 Pseudo spectra . . . 160
6.4.2 Covariance matrix and likelihood . . . 163
6.4.3 Validation . . . 164
6.4.4 Null tests . . . 168
6.5 Analyses and results . . . 172
6.5.1 Cosmological model . . . 172
6.5.2 Statistical analysis . . . 173
6.5.3 Limits and perspectives . . . 188
6.6 Conclusion . . . 191
Appendices . . . 193
6.A X/Y matrices in the covariance . . . 193
6.B MCMC convergence tests . . . 194
6.C Profile likelihood . . . 198

Conclusion 201

A Statistical tools **205**
A.1 Confidence regions: n-σ contours 205
A.2 Bayesian inference 206
A.2.1 Bayes theorem 206
A.2.2 Markov chain Monte Carlo methods 207

B On angular power spectra **211**
B.1 Pseudo power spectra 211
B.1.1 Expectation value 211
B.1.2 Covariance of pseudo spectra 212
B.2 On the distribution of the cross-power spectrum estimator 214

C The `NumCosmo` library **217**
C.1 The `xcor` module 218
C.2 The `halofit` power spectrum 220

D Other numerical tools **223**
D.1 `HEALPix`: spherical pixelization 223
D.2 `CLASS` 225

Bibliography **227**

Foreword

In the popular science book *Endless Universe: beyond the Big Bang*, Paul Steinhardt and Neil Turok wrote

> The history of the Universe can be compared to a play in which the actors – matter and radiation, stars and galaxies – dance across the cosmic stage according to a script set by the laws of physics. The challenge for the cosmologist is to figure the story line after arriving at the show 14 billions years too late, long past the crucial opening scenes.

A century spent gazing at the night sky for the far, ancient Universe taught us one or two things about that play.

First, we know part of the cast. Some of the characters, such as baryons – that is, the Sun, forks, cats and us, *i.e.* ordinary matter – and radiation – a fancy name for *light* –, are even very familiar to us: we have beautiful theories to describe their behaviours to the smallest scales, that we were able to extensively test in laboratories. Some characters are more of a puzzle. We know they're here, but we still miss some information: this is the case of neutrinos, that have unknown masses, amongst other peculiarities. And finally, some characters are just hypothetical. That is, we haven't seen them directly, but some observations betray their presence: they are called *dark matter*, responsible for no less than the large-scale structure of the Universe and the cohesion of galaxies, and *dark energy*, that fuels the accelerated expansion of the Universe. Unless we're missing something...

Then, we also know a couple of things about the physics of the cosmos, the rules behind the script, dictating characters how to move and interact. We know how particles do so up to some energy level: that's particle physics – or special effects executive. And we know how they behave when lots of them are put together, thanks to thermodynamics. We also have a nice theory about gravity, and how space-time bends, stretches, twists and grows along with its content: this is Einstein's theory of general relativity.

General relativity tells us how the evolution of the stage – dubbed *space-time* – depends on the characters, their momentum and pressure. Assuming that we occupy no special position in the theater (Copernican principle) and that it is isotropic – try and visualize it now! –, Einstein's equations have a simple solution discovered

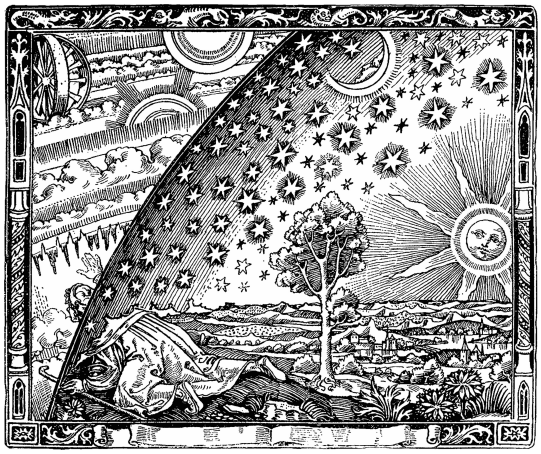

Figure 1 – The Flammarion engraving from Camille Flammarion's 1888 book *L'atmosphère: météorologie populaire.*

by Alexander Friedmann in 1922 and Georges Lemaître in 1927, that describe an expanding Universe and were confirmed by Hubble's 1929 milestone observation that the more distant *extragalactic nebulæ* were, the faster they seemed to flee. Switching gears, this means that long enough ago, everything was closer together, and thus, hotter.

Now, we can start filling the story line. We have some ideas about a couple of events that occurred not long after the beginning of the play, elegantly named the *Big Bang*. At early times, the Universe was dense and hot. Particles formed a soup in which they interacted *via* the four interactions we know: the strong interaction, the weak interaction, electromagnetism and gravity. Soup, as it should, cools down while the Universe expands, allowing particles to form bigger and bigger conglomerates: first, quarks combined to form baryons, including protons and neutrons, which later on combined into nuclei and subsequently captured electrons to form the first atoms. At this point, the Universe becomes neutral, and photons stop interacting with matter, raising the anchor for a long, quiet flight through the Universe: they form the *cosmic microwave background*, the Universe's birth day picture.

Soup has lumps, too. Cosmologists believe that the structures we see today – galaxies, clouds, clusters and filaments – arose from these seeds after they collapsed under gravity. The origin of those lumps remains mysterious, although the predominant inflationary scenario predicts they were quantum fluctuations swelled to cosmic scales by an extraordinary phase of expansion during fractions of a second, right after the Big Bang.

This draws a cartoon picture of our current knowledge of what is, without a doubt, the greatest play of all times. Of course, many aspects remain yet unknown. A wise man once jokingly said to me :

> How come cosmologists pretend to know the whole story down to fractions of the first second ever, and they can't tell which day of the week it was?

In spite of this shrewd observation, we have a fairly good idea of what happened after that first second, but very early times tackle our theories. And so does 95% of the energy content of the Universe today. We also don't know the end of the play yet, or whether it had one, or, possibly, many prequels. At last, we don't even know the name of the director!

Fiducial cosmological model

The fiducial cosmological model assumed throughout this thesis is the flat ΛCDM model with parameters derived from the Planck analysis with external data sets (denoted "TT,TE,EE+lowP+lensing+ext" in Planck Collaboration *et al.* 2016e, Table 4). Details about the implementation are given in section 6.5.1.

Table 1 – Fiducial cosmological parameters.

Parameter	Description [unit]	Value
H_0	Hubble parameter today [$\mathrm{km\,s^{-1}\,Mpc^{-1}}$]	67.74
ω_b	Baryon physical density today[a]	0.02230
ω_c	Cold dark matter physical density today[a]	0.1188
$\ln 10^{10} A_\mathrm{s}$	Amplitude of the primordial power spectrum	3.064
n_s	Tilt of the primordial power spectrum	0.9667
z_re	Mean redshift of reionization	8.8
m_ν	Sum of the masses of neutrinos [eV]	0.06
w	Dark energy equation of state	-1

[a] It is called *physical* because $\omega_\mathrm{b} \equiv \Omega_\mathrm{b} h^2 \propto \rho_\mathrm{b} H_0^2 \big/ \rho_c \propto \rho_\mathrm{b}$ where $H_0 = 100\,h\,\mathrm{km\,s^{-1}\,Mpc^{-1}}$.

Index of experiments

Table 2 – List of experiments, collaborations and cosmological surveys mentioned in this thesis.

Abbreviation	Full name	Reference
ACT	Atacama Cosmology Telescope	Swetz *et al.* 2011
BICEP	Background Imaging of Cosmic Extragalactic Polarization	Ogburn *et al.* 2010
BOSS	Baryon Acoustic Oscillation Survey	Dawson *et al.* 2013
CFHT	Canada-France-Hawaii Telescope with the MegaCam imaging camera	Boulade *et al.* 2002
DES(-SV)	Dark Energy Survey (Science Verification data)	Dark Energy Survey Collaboration *et al.* 2016
DESI	Dark Energy Spectroscopic Instrument	Levi *et al.* 2013
Euclid	ESA's Euclid satellite	Laureijs *et al.* 2011
Fermi-LAT	Fermi Large Area Telescope	Abdo *et al.* 2010
FIRST	Faint Images of the Radio Sky at Twenty Centimeters	Becker *et al.* 1995
Herschel	ESA's Herschel satellite	Pilbratt *et al.* 2010
H-ATLAS	Herschel Astrophysical Terahertz Large Area Survey	Eales *et al.* 2010
H-SPIRE	Herschel Spectral and Photometric Imaging REceiver	Griffin *et al.* 2010
KiDS	Kilo-Degree Survey	Jong *et al.* 2013
LSST	Large Synoptic Survey Telescope	LSST Science Collaborations and LSST Project *et al.* 2009

Continued on next page

Table 2 – *Continued from previous page*

Abbreviation	Full name	Reference
NVSS	NRAO VLA Sky Survey	Condon *et al.* 1998
Planck	ESA's Planck satellite	Planck Collaboration *et al.* 2011
PolarBear	PolarBear CMB experiment	Kermish *et al.* 2012
SDSS	Sloan Digital Sky Survey	Eisenstein *et al.* 2011
Spitzer	Spitzer Deep, Wide-Field Survey	Ashby *et al.* 2009
SPT	South Pole Telescope	Carlstrom *et al.* 2011
WISE	Wide-field Infrared Survey Explorer	Wright *et al.* 2010
WFIRST	Wide Field Infrared Survey Telescope	Spergel *et al.* 2013
WMAP	Wilkinson Microwave Anisotropy Probe	Bennett *et al.* 2003

List of publications

Work presented in this thesis is based on the following first-authored papers:

- C. Doux, E. Schaan, E. Aubourg, K. Ganga, K.-G. Lee, D. N. Spergel and J. Tréguer (2016). First detection of cosmic microwave background lensing and Lyman-α forest bispectrum. *Physical Review D*, 94.1, p. 103506. doi: 10.1103/PhysRevD.94.103506

- C. Doux, M. Penna-Lima, S. D. P. Vitenti, J. Tréguer, E. Aubourg and K. Ganga (2017). Cosmological constraints from a joint analysis of cosmic microwave background and large-scale structure. *arXiv.org*, arXiv:1706.04583. arXiv: 1706.04583 [1706] (submitted).

Another co-authored paper is in preparation:

- S. D. P. Vitenti, M. Penna-Lima and C. Doux (n.d.). NumCosmo: Numerical Cosmology library (in preparation).

Introduction

Where does cosmology stand in the mid 2010s?

I started my PhD in September 2014, that is, about a year and a half after the publications of the Planck 2013 results and its cosmological parameters' contraints, and a few months after the "false alarm" from BICEP 2. By that time, the BOSS survey of the Sloan Digital Sky Survey has been completed and is about to deliver its twelfth data release. It has measured the scale of the imprint of the baryon acoustic oscillations to percent-level precision at high redshift, severely constraining the geometry of the Universe. The last generation of imaging surveys (CFHT, KiDS, HSC and DES) is taking data and preliminary analyses are ongoing.

Cosmology stands on a solid basis. In the previous decade, the cosmic microwave background (CMB) has been measured on the full sky to a ground-breaking precision by WMAP. Combined with other independent probes such as distance measurements from supernovæ, it enabled cosmologists to estimate at the percent-level the amounts of baryon, dark matter and dark energy, entering cosmology in what is sometimes called a "precision era". We have measured the amplitude of fluctuations in the matter density and the tilt of the primordial power spectrum. We have a fairly good measurement of the rate of the expansion and we know that our Universe is extremely close to being spatially flat. All observations are more or less consistent with the standard, flat ΛCDM model. Six parameters to rule them all!

However, parts of the picture are more of a puzzle (yay!). The origin of the structures seen in the Universe remains unknown. Inflation is the most commonly accepted paradigm, though no conclusive evidence exists, yet. To this end, cosmologists are awaiting the measurement of primordial B-modes in the polarization of the CMB at large scale, an observation that will turn more arduous than foreseen because of polarized galactic foregrounds. Moreover, we ignore everything about the fundamental nature of dark energy and dark matter, two pillars of the ΛCDM model.

Therefore, cosmology seems to stand at a pivotal point, too. We have a simple, attractive mathematical model, but it involves unobserved components and processes. This is why we need *more* observations, with a higher statistical power, to rule out models and theories for these baffling, but fascinating, components.

What is the subject of this thesis and how did I contribute?

A promising avenue to do so lies in the measurement and exploitation of cross-correlations. Broadly speaking, the idea is that various observations of the Universe contain mutual information, because they are looking at the *same* Universe. This information can be extracted from the data to reinforce statistical constraints, though methods to do so are still under development and optimization.

The combination of independent measurements has enabled the ΛCDM model to emerge – CMB measured the matter content, BAOs give a standard geometric ruler and supernovæ measured the expansion – but correlated probes of the matter density field have not yet been systematically analyzed together. This is precisely the primary goal of this thesis. I developed a method to measure these correlations and integrate them in a statistical pipeline, and then applied it to Planck and BOSS data. In particular, the cross-correlation between the gravitational lensing of the CMB and tracers of the large-scale structure has been measured for multiple combinations of experiments, but, as of the beginning of my thesis, it had not yet been used in statistical analyses to extract cosmological information. During the first months of my thesis, I produced maps of the projected density of galaxies and quasars seen by the BOSS survey, and then measured the cross-correlation with the Planck lensing map. Then, I built a module in the NumCosmo library to compute the theoretical auto- and cross-power spectra. This module was then optimized (a factor of about 1000 in speed) to be integrated to a statistical analysis pipeline. I was then able to run MCMCs to demonstrate how cross-correlations improved cosmological constraints. Then, I complemented this analysis by CMB temperature data in order to constrain all the parameters of the ΛCDM model as well as galaxy biases, at once. Given the statistical power of the joint analysis, I extended the model to measure the dark energy equation of state and the sum of the masses of neutrinos.

But cross-correlations can do much more. We cannot observe all of matter at once, and various probes are sensitive to different types of matter —dark matter, hot gaz, neutral hydrogen, star-forming clouds, *etc*— at different distance scales and different periods of time. Therefore, combining correlated probes can shed light on the interweaving and motions of those different matter components. A second project of my thesis, which was finished earlier, was to measure the correlation between the Lyman-α forest observed in the spectra of quasars and lensing of the CMB. I correlated the amplitude of fluctuations in the density of hydrogen probed by the Ly-a forest with the large-scale density of dark matter weighed by CMB lensing. This bispectrum signal, detected for the first time, is meant to be used to investigate the relationship between neutral hydrogen in the intergalactic medium (IGM) and dark matter. In particular, it provides an independent test against which hydrodynamical simulations of the IGM can be calibrated.

Finally, cross-correlations offer novel possibilities for tests and cross-calibrations.

They are less prone to systematics than auto-correlations and as such, they provide new unbiased statistics that can be used to verify consistency and to calibrate estimators (for example, shear measurement from galaxy shapes). I have performed very preliminary work on weak lensing estimation and on the related deblending issue, which we only mention here.

How is this manuscript organized?

Chapter 1 shall paint a picture of modern cosmology. We will review the key theoretical ingredients at the core of what has become known as the standard model of cosmology. It is based on Einstein's theory of gravity, general relativity, to describe the evolution of the Universe as a whole and uses our knowledge of thermodynamics and subatomic physics to explain what happened during the hot Big Bang scenario, that is, the primordial hot and dense state of the Universe. Then, perturbation theory, which explains how the large-scale structure of the Universe formed and evolved, will be presented.

In chapter 2, we will review some of the most important physical, observable phenomena that are used to probe the content and geometry of the Universe. In particular, we will discuss the cosmic microwave background, tracers of the large-scale structure and weak gravitational lensing, and compare how they help us scrutinize the Universe.

In chapter 3, we will present two experiments, the Planck satellite and SDSS-III/BOSS, that were used during my PhD work.

In chapter 4, we shall go into more detail about the combination of probes. We will detail various mathematical approaches to measuring correlations amongst observables, focusing in particular on the angular power spectrum formalism. Then, we will do a review of the cross-correlations studies in the literature up to mid 2017 and highlight how they use the aforementioned mutual information hidden in different data sets. This will lead us to presenting the principles of joint analyses and existing studies.

In chapter 5, we will present the cross-correlation of the Ly-a forest from SDSS-III/BOSS data with the CMB lensing map from Planck. We will present the theoretical approach based on the position-dependent power spectrum, the analysis and the results.

In chapter 6, we will elaborate on the joint analysis of Planck and BOSS data. After laying the theoretical background and presenting statistical and numerical tools used in the analysis, we shall present the cosmological contraints that were obtained.

CHAPTER 1

The standard model of cosmology

Contents

1.1 Gravity and cosmology 8
1.1.1 General relativity 8
1.1.2 The expanding Universe 9
1.2 An overview of particle physics 12
1.3 Thermal history 14
1.3.1 Thermodynamics in an expanding Universe 14
1.3.2 A brief history of the Universe 16
1.4 Cosmological perturbation theory 20
1.4.1 Newtonian perturbation theory 20
1.4.2 Relativistic perturbation theory 22
1.4.3 The matter power spectrum 27
Appendices 33
1.A Notions of quantum field theory 33
1.A.1 Fundamental principles 33
1.A.2 Types of fields 34
1.A.3 The machinery: Feynman diagrams and renormalization . . 35

Let us start with a lightning history of modern cosmology.

Cosmology – that is, *physical* cosmology – is a rather young science that was born about a century ago. In 1929, Edwin Hubble, working at Mount Wilson Observatory in California (see figure 1.1), found an approximately linear relationship between the recession velocities of galaxies, measured from their spectral redshifts, and their distances inferred from the observations of Cepheids. The further galaxies

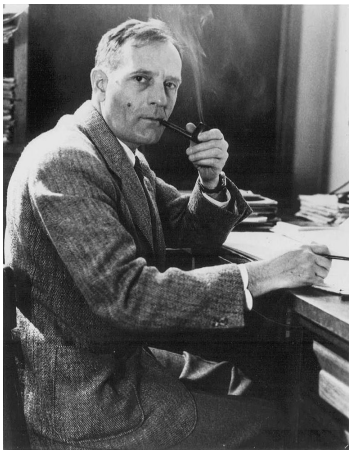
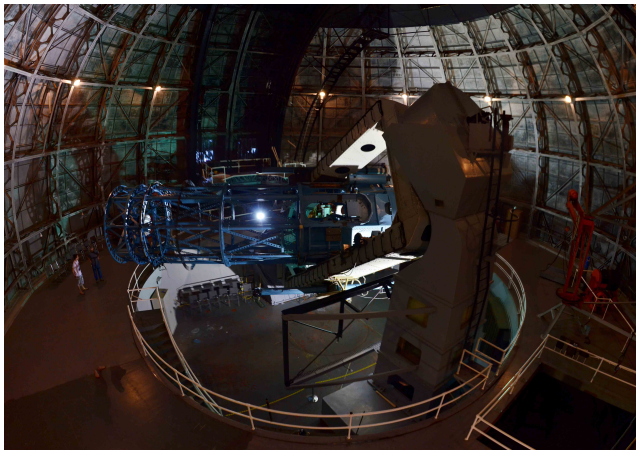

Figure 1.1 – Edwin Hubble (1889-1953) and the Hooker 2.5 m telescope at Mount Wilson Observatory (I took this picture during an intership there in 2012).

are from us, the faster they move away. This phenomenon, known as Hubble's law, was consistent with a cosmological solution of Einstein's general relativity equation found by Lemaître that described an expanding Universe. Though the idea was not immediately accepted, its most striking consequence was that long enough ago, the Universe must have been in a much denser and hotter state, a theory sarcastically named the *Big Bang*[1]. Two key observations ultimately gave support to this theory. The first was the abundance of chemical elements in the Universe, predicted from a primordial nucleosynthesis in the famous $\alpha\beta\gamma$ paper in 1948 (Alpher *et al.* 1948), and the second was the discovery by Penzias and Wilson of the cosmic microwave background (hereafter CMB, Penzias and Wilson 1965), interpreted, in the same issue of the *Astrophysical Journal*, by Dicke, Peebles, Roll and Wilkinson as a relic radiation from the Big Bang with a black-body spectrum (Dicke *et al.* 1965). In the following decades, upper limits on the anisotropies of the CMB and measurements of the rotation curves of galaxies by Vera Rubin (Rubin *et al.* 1978) confirmed earlier evidence that the amount of matter inferred from the observed light was off. This could be solved by speculating the existence of a cold, *dark* form of matter – dark in the sense that it does not interact with light – but this led to inconsistencies with clustering observations and measurements of the Hubble constant, unless a new kind of energy with negative pressure, mathematically similar to a cosmological constant Λ, was hypothesized too. Finally, by the end of the 1990s, two groups led by Perlmutter and Riess gave a decisive indication in favor of the ΛCDM model. Using supernovæ of type IA as standard candles, they established that the expansion of the Universe is accelerated (Perlmutter *et al.* 1999; Riess *et al.* 1998).

Since then, successive space-borne CMB experiments – WMAP and then Planck – and galaxy and supernovæ surveys have set strong constraints on the cosmological

[1]The term was coined by Fred Hoyle on BBC radio's *Third Programme* broadcast on 28 March 1949.

parameters of the ΛCDM model (Hinshaw *et al.* 2003; Planck Collaboration *et al.* 2014a). However, the fundamental nature of dark matter and dark energy[2] eludes us. In fact, while several types of hypothetical particles, such as weakly interacting massive particles, axions or sterile neutrinos, have been proposed as constituents of dark matter, modifications of the laws of gravity – for instance, $f(R)$ gravity, scalar-tensor theories, massive gravity or brane cosmology – could mimic observations as well. But dark energy is even more astounding. Its stress-energy tensor is mathematically similar to the mean stress-energy tensor of vacuum fluctuations $\left\langle 0\middle|\hat{T}_{\mu\nu}\middle|0\right\rangle$ in quantum field theory, though with an energy density about 120 orders of magnitude too small (Weinberg 1989).

In this introduction, we will first review what has become known as the standard model of cosmology. We will present its theoretical foundations, its content and the successive stages of this scenario.

* * *

There are four fundamental interactions, to wit, the strong and weak interactions, electromagnetism, and gravity. Except at very early times – that is during primordial baryogenesis and nucleosynthesis –, the first two do not play a significant role in the evolution of the Universe. The reason is that they act on very small ranges. Confinement, although not analytically proven yet, prevents colored particles such as quarks from being isolated, and the high masses of the W and Z bosons carrying the weak force make it short-range after the electroweak phase transition. Electromagnetic interactions between light and matter are important up to recombination, when the Universe becomes neutral. Consequently, gravity is the fundamental force that drives the large-scale evolution of the Universe after recombination.

In the next sections, we briefly review some of the materials at the core of modern cosmology. We will start by notions of general relativity and its application to cosmology. Then, because primordial cosmology shapes the future of the Universe and determines its content, we will review some rudiments of particle physics before summarizing the thermal history of the Universe. Finally, we will review linear perturbation theory, a fundamental tool to understand the large-scale structure of the Universe.

Well-written, extensive, modern introductions can be found in the literature that do justice to the wonderful history of cosmology. Here, we will rather focus on the scientific material, supposing basic knowledge of general relativity, thermodynamics, particle physics and notions of cosmology. I will try to make this a useful introduction for a master's degree student while insisting on concepts and tools that were useful for my thesis work, and deliberately skipping notions that I did not directly study (for instance, inflation).

[2] As a disclaimer, let's note that the terms *dark matter* and *dark energy* will refer to their contributions in Friedmann's equations, motivated by multiple observations and mathematically consistent with new forms of *matter* and *energy*.

I extensively used a couple of valuable books and lecture notes, in particular:

- P. Peter and J.-P. Uzan (2013). *Primordial Cosmology.* Oxford University Press
- D. Baumann (2015). *Cosmology.* Part III Mathematical Tripos
- E. Gourgoulhon (2013). *Relativité générale.* luth.obspm.fr
- G. F. R. Ellis, R. Maartens and M. A. H. MacCallum (2012). *Relativistic Cosmology.* Cambridge University Press
- J.-B. Zuber (2013). *Invariances en physique et théorie des groupes.* lpthe.jussieu.fr
- S. Dodelson (2003). *Modern Cosmology.* Academic Press
- S. Weinberg (2005). *The Quantum Theory of Fields: Volume 1, Foundations.* Cambridge University Press

1.1 Gravity and cosmology

1.1.1 General relativity

Newton's theory of gravity fails at describing the evolution of the Universe, and thus, modern cosmology relies on Einstein's theory of general relativity. In this geometric theory of gravitation, formulated in 1915 (Einstein 1916), space-time is a flexible, curved continuum, mathematically represented by a pseudo-Riemannian manifold. It is equipped with a metric $g_{\mu\nu}$, that measures space-time intervals as

$$\mathrm{d}s^2 = g_{\mu\nu}\,\mathrm{d}x^\mu\,\mathrm{d}x^\nu\,, \tag{1.1}$$

and with the Levi-Civita connection. The *equivalence principle* of classical mechanics is translated into the axiom that test particles that are only subject to gravity (no other external forces) move along geodesics, according to the equation[3]

$$\frac{\mathrm{d}^2X^\alpha}{\mathrm{d}\tau^2} + \Gamma^\alpha_{\mu\nu}\frac{\mathrm{d}X^\mu}{\mathrm{d}\tau}\frac{\mathrm{d}X^\nu}{\mathrm{d}\tau} = 0, \tag{1.2}$$

where $X^\mu(\tau)$ is the trajectory and $\Gamma^\alpha_{\mu\nu}$ are the Christoffel symbols of the connection. Einstein's field equation relates the geometry of space-time, described by a tensor

[3] An interesting way of deriving the geodesic equation is to write the Euler-Lagrange equation that minimizes the total space-time interval given by

$$S = \int \mathrm{d}s = \int \mathrm{d}\tau \sqrt{g_{\mu\nu}\frac{\mathrm{d}X^\mu}{\mathrm{d}\tau}\frac{\mathrm{d}X^\nu}{\mathrm{d}\tau}}.$$

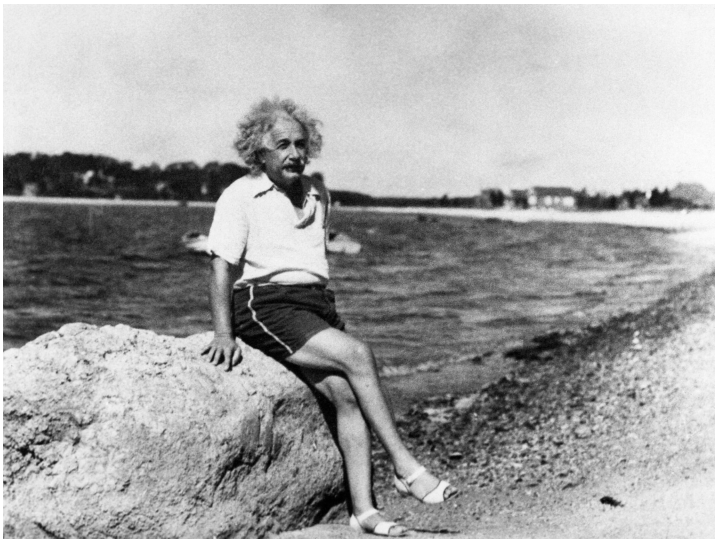

Figure 1.2 – Albert Einstein at Horseshoe Cove in Nassau Point in 1939.

$G_{\mu\nu}\left[g_{\mu\nu}\right]$ involving up-to-second-order derivatives of the metric, to its content, described by the stress-energy tensor $T_{\mu\nu}$, as

$$G_{\mu\nu}\left[g_{\mu\nu}\right] = \kappa T_{\mu\nu}. \tag{1.3}$$

Einstein's tensor is divergenceless, that is $\nabla_\mu G^{\mu\nu} = 0$. This implies that $\nabla_\mu T^{\mu\nu} = 0$, which is the relativistic version of the conservation equation. Written in terms of the Ricci tensor, and adjusting the constant κ to match Newton's theory in the weak-field limit, it reads

$$R_{\mu\nu} - \frac{1}{2} g_{\mu\nu} R + g_{\mu\nu}\Lambda = \frac{8\pi G}{c^4} T_{\mu\nu}, \tag{1.4}$$

where we have now included the cosmological constant term Λ.

1.1.2 The expanding Universe

The *cosmological principle* states that, on large scales, the Universe is spatially homogeneous and spatially isotropic. Translated into mathematical terms, this implies that space-time can be foliated into spatial sections that are maximally symmetric. The metric can thus be written

$$\mathrm{d}s^2 = -c^2\,\mathrm{d}t^2 + a^2(t)\left[\mathrm{d}\chi^2 + f_K^2(\chi)\,\mathrm{d}\Omega^2\right] \tag{1.5}$$

where

$$f_K(\chi) = \begin{cases} \sin\left(\sqrt{K}\chi\right)/\sqrt{K} & K > 0 \\ \chi & K = 0 \\ \sinh\left(\sqrt{-K}\chi\right)/\sqrt{-K} & K < 0 \end{cases}. \tag{1.6}$$

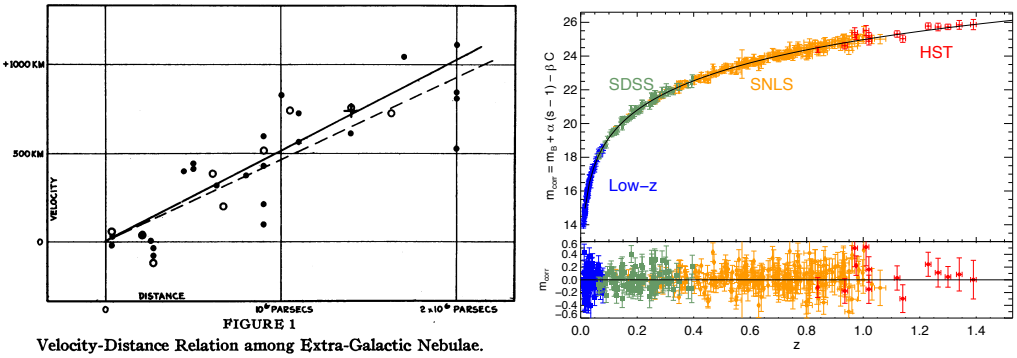

Figure 1.3 – Left: Hubble's original plot of recessional velocity vs. distance, taken from his landmark 1929 paper (Hubble 1929). Right: Hubble diagram (distance *vs* redshift) from (Conley *et al.* 2011) using data from the Sloan Digital Sky Survey, the Supernovæ Legacy Survey and the Hubble Space Telescope.

t represents cosmic time (the foliation index) and the terms in brackets describe spatial *comoving* distances. K is the spatial curvature, related to the spatial Ricci tensor by ${}^{(3)}R = 6K$. It is respectively positive, zero and negative for close, flat and open spatial sections.

$a(t)$ is the *scale factor*, unknown a priori. It describes how spatial sections are expanding (respectively contracting) and distances growing (shrinking) over time, even for static observers – that is, those with constant comoving coordinates. The physical distance between two objects, say two galaxies, is $\boldsymbol{r}(t) = a(t)\boldsymbol{\chi}$ where $\boldsymbol{\chi}$ is the comoving distance that separates them. Differentiating both sides yields

$$\boldsymbol{v} \equiv \dot{\boldsymbol{r}}(t) = H(t)\boldsymbol{r}(t) + a(t)\dot{\boldsymbol{\chi}} \equiv \boldsymbol{v}_{\rm rec} + \boldsymbol{v}_{\rm p}, \tag{1.7}$$

where $H(t) \equiv \dot{a}(t)/a(t)$ is the Hubble expansion rate. The relative velocity has two components: the recession velocity from the Hubble flow, proportional to the distance (see Hubble's original plot on figure 1.3), and peculiar velocities with respect to the cosmological frame.

Now, let's fill the Universe with a perfect, homogeneous and static fluid: the stress-energy tensor becomes diagonal, with $T_{00} = \rho c^2$ and $T_{ii} = p$, where ρ and p are the energy density and pressure of the fluid. A small bit of algebra, and working in units where $c = 1$, leads to Friedmann's equations,

$$H^2 = \left(\frac{\dot{a}}{a}\right)^2 = \frac{8\pi G}{3}\rho + \frac{\Lambda}{3} - \frac{K}{a^2} \tag{1.8}$$

and

$$\frac{\ddot{a}}{a} = -\frac{4\pi G}{3}(\rho + 3p) + \frac{\Lambda}{3}. \tag{1.9}$$

Another equation, not independent, but useful, comes from the matter conservation

equation, $\nabla_\mu T^{\mu\nu} = 0$, that reads

$$\dot{\rho} + 3H(\rho + p) = 0. \tag{1.10}$$

For fluids with an equation of state of the form $p = w\rho$, where w is constant, the solution is

$$\rho(t) \propto a(t)^{-3(1+w)}, \tag{1.11}$$

describing the dilution of energy as the Universe expands. A Universe filled with only such a fluid would have a scale factor evolving as

$$a(t) \propto \begin{cases} t^{\frac{2}{3(1+w)}} & w \neq -1 \\ e^{H_0 t} & w = -1 \end{cases}. \tag{1.12}$$

In our Universe, three distinct phases are particularly important:

Radiation-dominated era. Radiation has $w = \frac{1}{3}$ and therefore the scale factor approximately goes as $a(t) \propto \sqrt{t}$ when radiation dominates the energy budget. Its energy density decreases as $\rho(a) \propto a^{-4}$ because photons are diluted with the expansion and wavelengths are expanded as well.

Matter-dominated era. Cold matter, sometimes referred to as *dust*, has $w = 0$. Therefore, its energy density undergoes a simple volume expansion, $\rho(a) \propto a^{-3}$, and starts dominating about 60 kyr after the Big Bang. During this era, the scale factor increases faster as $a(t) \propto t^{2/3}$.

Dark energy-dominated era. The cosmological constant Λ in the Friedmann equations (1.8) and (1.9) is equivalent to a fluid with equation of state $w = -1$ and constant physical energy density. Therefore, it starts dominating about 9 Gyr after the Big Bang. The Hubble parameter approaches $H_0 \sim \Lambda/3$ and the expansion becomes exponential with $a(t) \propto e^{H_0 t}$.

Defining the critical density $\rho_c = 3H^2 \Big/ 8\pi G$, we can introduce the density parameters[4] for each component X of the fluid ($X = \mathrm{r}, \mathrm{c}, \mathrm{b}, \nu, \mathrm{m}$ for radiation, cold dark matter, baryons, neutrinos and all matter), defined as $\Omega_X = \rho_X/\rho_c$. We additionally define $\Omega_\Lambda = \Lambda \Big/ 3H^2$ and $\Omega_k = -K \Big/ a^2 H^2$, and finally rewrite the first Friedman equation (1.8) in its reduced form

$$\sum_X \Omega_X + \Omega_\Lambda + \Omega_k = 1. \tag{1.13}$$

Changing variables and introducing the cosmological redshift z defined as $a = 1/(1+z)$,

[4] Here, we decided to use this definition, while in the literature, density parameters may be defined as energy fractions, that is $\Omega_{X_0} = \rho_{X_0} / \sum_X \rho_X$. They coincide in the case of flat spatial sections, which will be assumed throughout this manuscript.

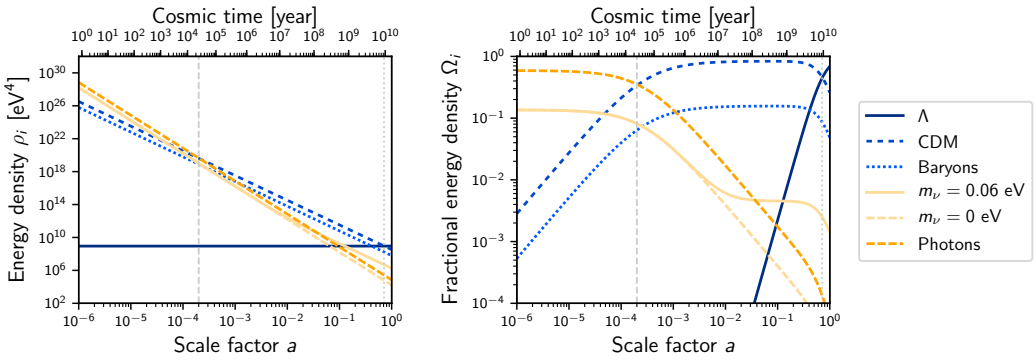

Figure 1.4 – Evolution of the energy densities and energy fractions of the different components of the flat ΛCDM model: dark energy (Λ), cold dark matter (CDM), baryons, massive and massless neutrinos (m_ν) and photons. The dashed and dotted grey vertical lines correspond to the radiation-matter and matter-dark energy equalities.

the Hubble parameter becomes

$$\left(\frac{H(z)}{H_0}\right)^2 = \Omega_{\mathrm{m}}^0(1+z)^3 + \Omega_{\mathrm{r}}^0(1+z)^4 + \Omega_{\mathrm{k}}^0(1+z)^2 + \Omega_\Lambda^0 \tag{1.14}$$

where the superscript ^{0} indicates that we take the values of the density parameters today. The evolution of the energy densities of the components of the ΛCDM is shown in figure 1.4, together with the associated density parameters.

This simple description is however insufficient for several reasons. First, it does not explain why the content of the Universe is what it is. In the primordial, hot Universe, reactions occurred between particles that modified their relative abundances. Second, it does not take into account a key parameter in the evolution of the Universe's content, to wit, temperature. As we shall see, it is the decrease of temperature that freezes the aforementioned reactions, *decoupling* particles from each other. It also does not fully explain why various species (in a broad sense) behave differently, depending on their being *relativistic* or not (an important parameter for neutrinos, as we shall see). We thus need a thermodynamic description that incorporates our knowledge of subatomic physics.

1.2 An overview of particle physics

Let us now review some of the fundamental principles of particle physics. It is based on quantum field theory (QFT, see section 1.A for basic notions), a mathematical framework that unifies quantum mechanics and special relativity. However, QFT does not provide the content of the theory, that is, the list of particles and their interactions. The standard model of particle physics is based on a special type of quantum field

theories called *gauge theories*. In such theories, the Lagrangian is invariant under local transformations of the internal state of particles – spin, isospin, color – generated by the elements of a Lie group. Each generator of the corresponding Lie algebra is associated to a so-called gauge field (a gauge boson), which lives in the adjoint representation of the group, while fermions are placed in smaller representations. The structure of these representations classifies particles by their associated conserved charges. Derivatives in the kinetic terms of the Lagrangian are then replaced by covariant derivatives

$$\partial_\mu \to D_\mu \equiv \partial_\mu - igA_\mu, \tag{1.15}$$

where g is the coupling, to make it *gauge invariant*. In the case of non-abelian gauge theories, the quantization is a bit tricky and may require the introduction of ghost fields and counter terms to cancel anomalies, but they are renormalizable.

The standard model is based on the group $\mathrm{SU}(3)_c \times \mathrm{SU}(2)_L \times \mathrm{U}(1)_Y$. It can be decomposed in two sectors:

Quantum chromodynamics. QCD, which describes the strong interaction, is based on $\mathrm{SU}(3)_c$, and has therefore eight gauge fields – the gluons. Only quarks are coupled to the gluons, and they are placed in the 3-dimensional representation[5], denoted by three *color* indices. Quarks are *confined* by gluons, which means that they cannot be found isolated, and always assemble into colorless composite particles: hadrons contain a quark of each color and mesons a quark and its color-complementary anti-quark.[6] Unlike the electroweak interaction, it is asymptotically free, *i.e.* its coupling decreases with energy (Gross and Wilczek 1973; Politzer 1973).

Electroweak interaction. The weak interaction and electromagnetism are jointly described by a gauge theory based on the group $\mathrm{SU}(2)_L \times \mathrm{U}(1)_Y$. Three massless vector bosons are associated to $\mathrm{SU}(2)_L$ and one to $\mathrm{U}(1)_Y$, all of which combine thanks to the Higgs mechanism into the massive $W^\pm$, Z^0 bosons and the photon. The conserved charges are the weak isospin T_3 and the weak hypercharge Y, related to the electromagnetic Q charge by $Q = Y/2 + T_3$. Electroweak interactions act only on the left-handed fermions (hence the L subscript), combined in weak isospin-$\frac{1}{2}$ doublets of $\mathrm{SU}(2)_L$, such as left-handed electrons and electronic neutrinos, while right-handed fermions are in the trivial representation.

Altogether, and written in a form that hides a bit of dust under the carpet, the Lagrangian of the standard model reads[7]

[5] Other fermions, *i.e.* the leptons, live in the trivial 1-dimensional representation.

[6] Recently, a resonance a five quarks, the *pentaquark* has been observed at LHC.

[7] This extremely shortened expression comes from a coffee mug sold at CERN, and is described in Woithe *et al.* 2017. It is somewhat qualitative, in the sense that it hides many implicit summations over particles, but it suits our purpose well. Note that the first "h.c" is not technically necessary and is interpreted at CERN as "hot coffee"!

$$\mathcal{L} = -\frac{1}{4} F_{\mu\nu} F^{\mu\nu}$$
$$+ i \bar{\psi} \not{D} \psi + h.c$$
$$+ \psi_i y_{ij} \psi_j \phi + h.c$$
$$+ |D_\mu \phi|^2 - V(\phi)$$

The first line is the kinetic term of all gauge fields; the second line contains the kinetic term of all fermions, the covariant derivative $\not{D}$ hiding the coupling to the gauge fields; the third line is the coupling to the Higgs boson of fermions, with the mixing matrices between mass and interaction eigenstates, responsible for the electroweak symmetry breaking that gives their masses to all fermions; the fourth line has the kinetic term of the Higgs boson (again, with the coupling to gauge fields) and the Higgs mexican-hat potential, accounting for the spontaneous symmetry breaking and the Higgs mechanism.

If questions remain unsolved – the Majorana or Dirac nature of neutrinos or the matter-antimatter assymmetry –, the standard model provides a consistent picture of subatomic physics, which was successfully applied to describe primordial cosmology.

1.3 Thermal history

We've arrived to the section on special effects of the play, where fireworks and all kinds of flashy phenomena take place: the theory of the hot Big Bang. We will first briefly introduce the key theoretical concepts and equations, and then we will review the major adventures of the tale of the Universe.

1.3.1 Thermodynamics in an expanding Universe

1.3.1.1 Thermodynamics at equilibrium

The key to understanding the thermal history of the Universe is to compare the rate of reactions, generically denoted as Γ, to the rate of expansion H. When $\Gamma \gg H$, reactions are fast enough to maintain thermodynamic equilibrium[8] and the phase-space distribution of particles is given by

$$f(\boldsymbol{p}, T) = \frac{g}{(2\pi)^3} \frac{1}{e^{(E(\boldsymbol{p})-\mu)/T} \pm 1} \tag{1.16}$$

[8] A distinction can be made here: chemical reactions ensure *chemical* equilibrium while elastic interactions ensure *thermal* equilibrium. Both must occur at a sufficient rate to ensure thermodynamic equilibrium.

with the $-$ sign for Bose-Einstein and $+$ sign for Fermi-Dirac distributions. g is the degeneracy of the species, *i.e.* the number of internal degrees of freedom, $E(\boldsymbol{p}) = \sqrt{p^2 + m^2}$ is the energy of a particle of momentum $\boldsymbol{p}$, which depends only on its norm $p = \|\boldsymbol{p}\|$, μ is the chemical potential and T is the equilibrium temperature. The number density n, energy density ρ and pressure P are defined as

$$n(T) = \int \mathrm{d}^3\boldsymbol{p}\, f(\boldsymbol{p}, T) \tag{1.17}$$

$$\rho(T) = \int \mathrm{d}^3\boldsymbol{p}\, f(\boldsymbol{p}, T) E(\boldsymbol{p}) \tag{1.18}$$

$$P(T) = \int \mathrm{d}^3\boldsymbol{p}\, f(\boldsymbol{p}, T) \frac{p^2}{3E(\boldsymbol{p})}. \tag{1.19}$$

To a good approximation, chemical potential can be neglected at all times, and thus we can set $\mu = 0$. Several limit cases are interesting.

- $T \gg m$: the mass of the particle is negligible with respect to its kinetic energy – or zero for massless particles – and it said to be relativistic and acts as radiation. We obtain, for bosons,

$$n = \frac{\zeta(3)}{\pi^2} g T^3,\ \rho = \frac{\pi^2}{30} g T^4 \text{ and } P = \frac{\rho}{3}, \tag{1.20}$$

  and thus $w = \frac{1}{3}$.[9] The number and energy densities of fermions get multiplicative terms, respectievely $\frac{3}{4}$ and $\frac{7}{8}$.

- $T \ll m$: it this limit, the density of particles, as long as they are in thermal equilibrium, decreases exponentially as

$$n = g \left(\frac{mT}{2\pi}\right)^{\frac{3}{2}} e^{-m/T} \tag{1.21}$$

  and pressure is negligible with respect to the energy density, so that $w \approx 0$.

In the case of neutrinos, they are still relativistic when they decouple, due to their very low masses. However, they do become non-relativistic between recombination and now: their equation of state goes from $1/3$ to 0, explaining the behaviour of their energy density in figure 1.4.

The temperature of the Universe T is defined as that of the bath of particles that are in thermal equilibrium, and therefore corresponds to that of the photons. For an adiabatic evolution, it can be shown that the quantity sa^3, where s is the entropy density and a the scale factor, is constant over time. Therefore, the temperature decreases as $T \propto a^{-1}$, as long as the number of relativistic particles in thermal equilibrium remains the same. When a species becomes non-relativistic, its entropy is transferred to the thermal bath, resulting in a small sudden temperature jump.

[9] The dependence of the energy density $\rho \propto T^4$ is also known as the Stephan-Boltzmann law.

1.3.1.2 Beyond equilibrium

The rate Γ of various reactions depends somehow on temperature. Therefore, as the Universe expands, temperature decreases, and, when $\Gamma \sim H$, the reaction freezes. Thermodynamic equilibrium is not ensured anymore, and the evolution of the phase-space distribution f of various species is given by the Boltzmann equation

$$L\left[f\right] = C\left[f\right] \tag{1.22}$$

where the Liouville operator L is a total derivative with respect to time and C is the collision term that describes interactions between particles (which involves the M-matrix of each possible interaction). If the distribution function depends only on energy, $f(E,t)$, then the Liouville operators reads

$$L\left[f\right] = E\frac{\partial f}{\partial t} - Hp^2\frac{\partial f}{\partial E} \tag{1.23}$$

where $p^2 = \|\boldsymbol{p}\|^2$ (not to be confused with pressure). For species i, we obtain, by integration over momentum $\boldsymbol{p}$, the equation describing the evolution of the number density,

$$\frac{1}{a^3}\frac{\mathrm{d}(n_i a^3)}{\mathrm{d}t} = C_i\left[\{n_j\}\right]. \tag{1.24}$$

For the reaction $1+2 \rightleftharpoons 3+4$, it becomes

$$\frac{1}{a^3}\frac{\mathrm{d}(n_i a^3)}{\mathrm{d}t} = -\left\langle\sigma v\right\rangle\left[n_1 n_2 - \left(\frac{n_1 n_2}{n_3 n_4}\right)_{\mathrm{eq}} n_3 n_4\right] \tag{1.25}$$

where the terms in parenthesis are the equilibrium values and $\langle\sigma v\rangle$ is the thermally averaged cross-section. This is known as the *master equation*. Defining the number of particles per unit comoving volume $N_i \equiv n_i/s$, we obtain

$$\frac{\mathrm{d}\ln N_1}{\mathrm{d}\ln a} = -\frac{\Gamma}{H}\left[1 - \left(\frac{N_1 N_2}{N_3 N_4}\right)_{\mathrm{eq}}\frac{N_3 N_4}{N_1 N_2}\right], \tag{1.26}$$

Noticeably, we find the ratio of the reaction and expansion rates. An important consequence of this equation is that when this ratio becomes small, the number density of particle per unit comoving volume becomes constant: this can result in *decoupling* or *freeze-out*. As we shall see very soon, this explain why there is matter rather nothing!

1.3.2 A brief history of the Universe

In the previous section, we have laid the theoretical tools necessary to understand the thermal history of the Universe. When thermal equilibrium is ensured, we know the distributions of particles. When departing from equilibrium, the Boltzmann equation

tells us how these distributions evolve.

Baryogenesis [$t \sim$?, $z \sim$?, $T \sim$?] Baryogenesis is the hypothetical phase where the baryonic symmetry is broken, so that annihilation reactions produce more matter than antimatter, while creating much more photons.

Electroweak phase transition [$t \sim 20\,\mathrm{ps}$, $z \sim 10^{15}$, $T \sim 125\,\mathrm{GeV}$] When temperature goes below the Higgs mass, it acquires a non-zero vacuum expectation value, thus breaking electroweak symmetry and giving their masses to all other particles. The scale of the weak interaction is considerably reduced from this point.

QCD phase transition [$t \sim 20\,\mu\mathrm{s}$, $z \sim 10^{12}$, $T \sim 150\,\mathrm{MeV}$] Quarks, that are asymptotically free, now become confined by gluons, and form hadrons and mesons.

Neutrino decoupling [$t \sim 1\,\mathrm{s}$, $z \sim 6 \times 10^9$, $T \sim 1\,\mathrm{MeV}$] Weak interactions that were coupling neutrinos to the other fermions, such as

$$\mathrm{e}^- + \overline{\nu}_\mathrm{e} \rightleftharpoons \mathrm{e}^- + \overline{\nu}_\mathrm{e},$$

stop. Decoupled neutrinos form another cosmic background that has not been detected yet.

Electron-positron annihilation [$t \sim 6\,\mathrm{s}$, $z \sim 2 \times 10^9$, $T \sim 0.5\,\mathrm{MeV}$] When temperature goes below the mass of the electron, the annihilation process

$$\mathrm{e}^+ + \mathrm{e}^- \rightleftharpoons \gamma + \gamma$$

stops. The entropy of electrons and positrons is transferred to photons, but not to neutrinos, which are decoupled. Therefore the ratio of their temperature is

$$\frac{T_\nu}{T_\gamma} = \left(\frac{4}{11}\right)^{1/3}. \tag{1.27}$$

The energy density of relativistic neutrinos is related to that of photons by

$$\rho_\nu = N_\mathrm{eff}\frac{7}{8}\left(\frac{4}{11}\right)^{4/3}\rho_\gamma \tag{1.28}$$

where N_eff would be 3 – the number of neutrino flavours – in the case of instantaneous decoupling. However, neutrinos were not completely decoupled when electrons and positrons annihilated and gained some energy, thus raising N_eff to a value of 3.046.[10]

[10] This theoretical value also includes spectral distortions from a Fermi-Dirac distribution arising from the energy dependence of weak interactions (high-energy neutrinos are more strongly coupled).

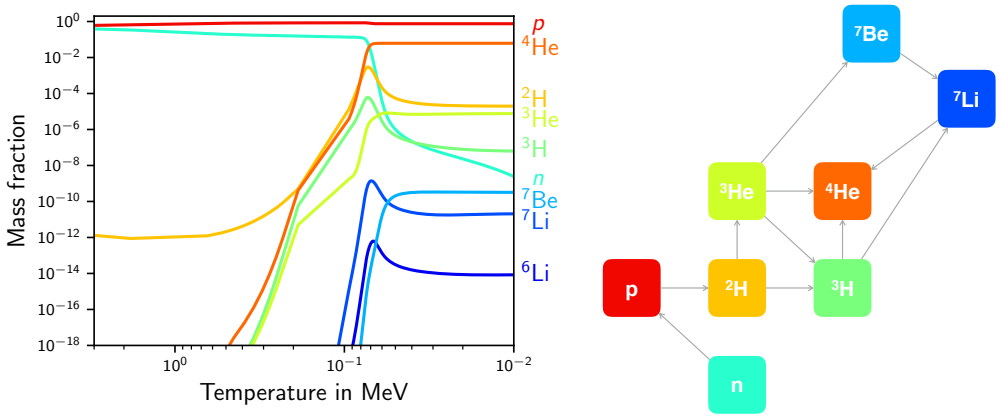

Figure 1.5 – Big Bang nucleosynthesis. The mass fractions of the nucleons and light elements nuclei are plotted against decreasing temperature (therefore increasing time). These curves were obtained by numerical integration using the `PArthENoPE` code (Pisanti *et al.* 2008). The diagram on the right shows the simplified network of nuclear reactions for these light elements.

Big Bang nucleosynthesis [$t \sim 3\,\mathrm{min}$, $z \sim 4 \times 10^8$, $T \sim 100\,\mathrm{keV}$] Three minutes after the Big Bang, the first atomic nuclei start forming. Above 1 MeV, protons and neutrons are at equilibrium, coupled by weak interactions via processes such as

$$\mathrm{n} + \nu_\mathrm{e} \rightleftharpoons \mathrm{p} + \mathrm{e}^- .$$

Because neutrons are slightly more massive ($m_n - m_p = 1.3\,\mathrm{MeV}$), equation (1.21) tells us that they must be less numerous, as can be seen on figure 1.5. But equilibrium is broken and neutrons first freeze out, and then start decaying for temperatures below 0.2 MeV. The production of heavier nuclei by strong interactions then goes through multiple steps, producing sequentially deuterium, tritium, helium, *etc.* These reactions are governed by a set of coupled Boltzmann equations that can be numerically solved, predicting the relative abundance of light elements, in agreement with observations.

Matter-radiation equality [$t \sim 60\,\mathrm{kyr}$, $z \sim 3\,400$, $T \sim 0.75\,\mathrm{eV}$] As mentioned earlier, this is the point where the radiation energy density becomes smaller than that of matter and the expansion rate thus increases.

Recombination [$t \sim 260 - 380\,\mathrm{kyr}$, $z \sim 1\,400 - 1\,100$, $T \sim 0.3\,\mathrm{eV} = 3\,600\,\mathrm{K}$] Until recombination starts, the Universe is ionized because photons are energetic enough to break atoms as they form, and the reaction

$$\mathrm{e}^- + \mathrm{p} \rightleftharpoons H + \gamma$$

is at equilibrium. However, when the temperature reaches $T \sim 0.3\,\mathrm{eV}$, it becomes energetically favourable for nuclei to capture free electrons, forming

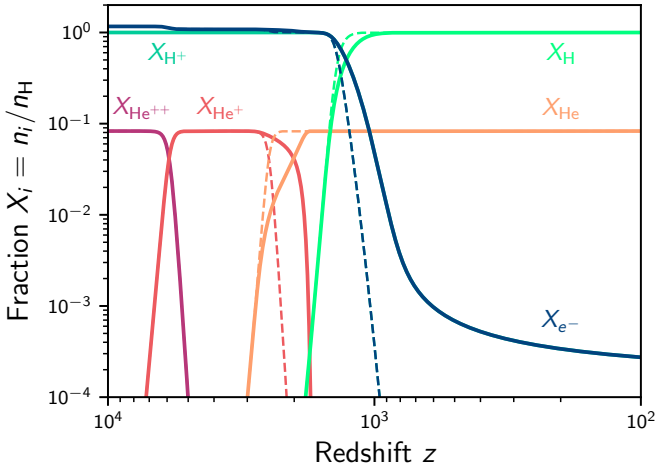

Figure 1.6 – Recombination of hydrogen and helium atoms as described in Seager *et al.* 1999. The fractions of the number density of these elements with respect to the density of hydrogen nuclei is plotted versus redshift. The fraction of free electrons is also shown in blue. The dashed lines are the equilibrium predictions while the solid lines were obtained by numerically solving the Boltzmann equation with the `NumCosmo` library (see appendix C).

hydrogen and helium atoms (see figure 1.6). Importantly, the threshold temperature is much smaller than 13.6 eV – the binding energy of the hydrogen atom – because their are about $\eta \sim 10^9$ photons per proton/electron.

Photon decoupling [$t \sim 380\,\mathrm{kyr}$, $z \sim 1\,090$, $T \sim 0.25\,\mathrm{eV}$] Photons were tightly coupled to electron via Thomson scattering,

$$\mathrm{e}^- + \gamma \rightleftharpoons \mathrm{e}^- + \gamma,$$

whose reaction rate is proportional to the density of electrons. Applying the master equation (1.25) to this reaction, one obtains the evolution of the fraction of free electron, X_e,

$$\frac{\mathrm{d}X_e}{\mathrm{d}x} = -\frac{\lambda}{x^2}\left[X_e^2 - (X_e^{\mathrm{eq}})^2\right], \tag{1.29}$$

where $x = B_\mathrm{H}/T$, with $B_\mathrm{H} = 13.6\,\mathrm{eV}$ denoting the binding energy of hydrogen, and $\lambda \equiv [n_b \langle\sigma v\rangle/H]_{T=B_\mathrm{H}}$. Shortly after recombination starts, the density of free electrons drops and photons decouple: their mean free path grows to cosmological scales and they start propagating freely, forming the *cosmic microwave background*.

Reionization [$t \sim 100 - 400\,\mathrm{Myr}$, $z \sim 10 - 30$, $T \sim 2 - 8\,\mathrm{meV}$] After a few hundred of millions of years, the first stars turn on. Their combined ultraviolet radiation progressively re-ionizes all neutral hydrogen in the intergalactic medium, as

can be observed in the Lyman-α forest of quasars. This process is thus of astrophysical origin rather than cosmological.

Dark energy-matter equality [$t \sim 9\,\mathrm{Gyr}$, $z \sim 0.4$, $T \sim 0.33\,\mathrm{meV}$] At this point, the energy density of the Universe becomes dominated by dark energy. The expansion starts accelerating anew.

Extinction of dinosaurs [$t \sim 13.8\,\mathrm{Gyr}$, $z \sim 0.004$, $T \sim 0.24\,\mathrm{meV}$] 🦕

Birth of Isaac Newton [$t \sim 13.8\,\mathrm{Gyr}$, $z \sim 3 \times 10^{-8}$, $T \sim 0.24\,\mathrm{meV}$] 

Today [$t \sim 13.8\,\mathrm{Gyr}$, $z = 0$, $T \sim 0.24\,\mathrm{meV} = 2.725\,5\,\mathrm{K}$]

1.4 Cosmological perturbation theory

So far, we have described a homogeneous Universe. But it is full of inhomogeneities: there are stars, galaxies, black holes, all over the place! Luckily, on the largest scales, *i.e.* above a few megaparsecs, these inhomogeneities are small. Indeed, anticipating a bit, fluctuations of the temperature of the CMB are of order $\Delta T/T \sim 10^{-5}$. Overdensities may grow under gravitational attraction, but as long as they remain small, we can treat them using a perturbative approach.

1.4.1 Newtonian perturbation theory

Let us start with a brief reminder of classical perturbation theory. In this context, matter density and pressure are supposed to be slightly different from a mean value. They can thus be written

$$\rho = \bar{\rho} + \delta\rho \tag{1.30}$$

$$P = \bar{P} + \delta P \tag{1.31}$$

with $\delta\rho, \delta P \ll \bar{\rho}\bar{P}$. Combining the classical hydrodynamics equations in the Euclidian space-time,

$$\partial_t \rho + \boldsymbol{\nabla} \cdot \rho \boldsymbol{v} = 0 \qquad \text{(Continuity equation)} \tag{1.32}$$

$$\partial_t \boldsymbol{v} + (\boldsymbol{v} \cdot \boldsymbol{\nabla})\boldsymbol{v} = -\frac{1}{\rho}\boldsymbol{\nabla} P - \boldsymbol{\nabla}\Phi \qquad \text{(Euler equation)} \tag{1.33}$$

$$\nabla^2 \Phi = 4\pi G \delta\rho \qquad \text{(Poisson equation)}, \tag{1.34}$$

where Φ is the gravitational potential, leads to the equation evolution for $\delta\rho(\boldsymbol{x}, t)$

$$\left(\partial_t^2 - c_\mathrm{s}^2 \nabla^2\right) \delta\rho = 4\pi G \bar{\rho}\ \delta\rho, \tag{1.35}$$

where $c_\mathrm{s}^2 = (\delta P/\delta\rho)_S$ is the (squared) speed of sound in the fluid. The Jeans length

$$\lambda_\mathrm{J} \equiv c_\mathrm{s}\sqrt{\frac{\pi}{G\bar{\rho}}} \tag{1.36}$$

is the length above which any perturbation starts growing exponentially.

In an expanding space-time, length are rescaled by the scale factor $a(t)$. This has two consequences for us: it modifies the derivatives in the previous equations, and now the mean density and pressure may evolve with time. Switching variables and defining the density contrast δ as

$$\rho(\boldsymbol{x}, t) = \bar{\rho}(t)\left(1 + \delta(\boldsymbol{x}, t)\right), \tag{1.37}$$

we obtain at first order in $\delta \ll 1$

$$\ddot{\delta} + 2H\dot{\delta} = \frac{c_\mathrm{s}^2}{a^2}\nabla^2\delta + 4\pi G\bar{\rho}\delta. \tag{1.38}$$

The speed of sound is now rescaled by a factor a and the Jeans length depends on time through $\bar{\rho}$. Interestingly, a friction term involving the Hubble parameter has appeared on the left-hand side of the equation, accounting for the suppression of structures due to the expansion.

If we neglect pressure, the Laplacian term disappears and equation (1.38) involves only time derivatives. The density contrast's time and space-dependence may be split as

$$\delta(\boldsymbol{x}, t) = D_+(t)\epsilon_+(\boldsymbol{x}) + D_-(t)\epsilon_-(\boldsymbol{x}), \tag{1.39}$$

with a growing mode (subscript $+$) and a decaying mode (subscript $-$). The growth parameter D obeys the equation

$$\ddot{D} + 2H(t)\dot{D} - \frac{3}{2}H^2(t)\Omega_\mathrm{m}(t)D = 0, \tag{1.40}$$

which has two solutions,

$$D_- = H \quad \text{and} \quad D_+(a) = \frac{5}{2}E(a)\Omega_\mathrm{m}^0\int_0^a \frac{\mathrm{d}a'}{\left[a'E(a')\right]^3}, \tag{1.41}$$

where $E(a) \equiv H(a)/H_0$. Noticeably, if the Universe is dominated by matter, then $D_+ \propto a$, but when dark energy becomes dominant, the expansion accelerates and slows the growth of structures down. The dependence of the growth function on background dynamics through $E(a)$ makes it an important quantity to test the ΛCDM model.

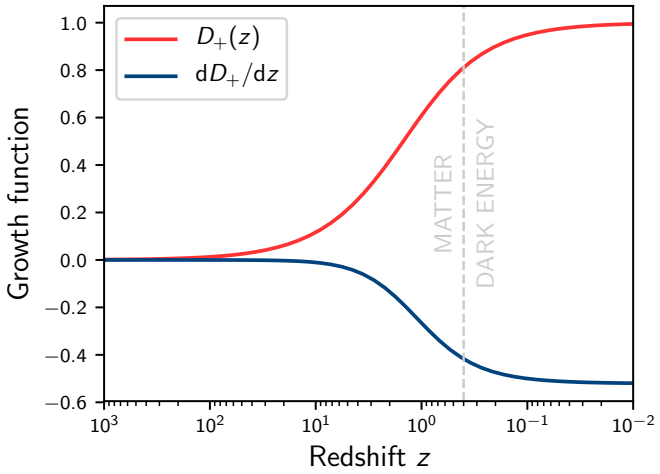

Figure 1.7 – Perturbation growth function versus redshift. The dashed lines marks the transition from the matter-dominated era to the dark energy-dominated era during which the expansion slows the growth of structures.

1.4.2 Relativistic perturbation theory

Let us now turn to the relativistic theory. We will not detail any calculation, but we will underline the main differences with the classical theory.

1.4.2.1 Perturbed Einstein equations

Inhomogeneities may now perturb the geometry of space-time itself. Therefore, the metric will be written as

$$g_{\mu\nu} = \bar{g}_{\mu\nu} + \delta g_{\mu\nu} \tag{1.42}$$

where $\bar{g}_{\mu\nu}$ is the *background* metric – here, the FLRW metric – and $\delta g_{\mu\nu} \ll 1$ is the small perturbation. The same decomposition can be made for the Einstein tensor $G_{\mu\nu}$ and the stress-energy tensor $T_{\mu\nu}$. Einstein's equation will be expanded order-by-order, such that

$$\overline{G}_{\mu\nu} = 8\pi G \overline{T}_{\mu\nu} \quad \text{and} \quad \delta G_{\mu\nu} = 8\pi G \delta T_{\mu\nu}. \tag{1.43}$$

A technical difficulty occurs: we are trying to compare two different manifolds (background and perturbed), but there isn't such a thing as a distance between two different spaces. Therefore, mapping coordinates between them (that is, choosing a *gauge*) is somewhat arbitrary and introduces non-physical degrees of freedom. This can be dealt with by defining gauge-invariant quantities that do not vary under a change of coordinates, or, equivalently, by fixing the gauge to remove these additional degrees of freedom. In the Newtonian gauge, the perturbed metric can be written

as[11]

$$\mathrm{d}s^2 = a^2(\eta)\left[-(1+2\Phi)\,\mathrm{d}\eta^2 + ((1-2\Psi)\delta_{ij} + 2\overline{E}_{ij})\,\mathrm{d}x^i\,\mathrm{d}x^j\right]. \tag{1.44}$$

Here, we use conformal time η defined by $a(\eta)\,\mathrm{d}\eta = \mathrm{d}t$. This metric has two *scalar* degrees of freedom, Φ and Ψ. Ψ is the curvature perturbation of constant time hypersurfaces and will appear in the Poisson equation (and thus corresponds to the Newtonian potential at small scales). Vector modes are chosen to be zero in this gauge. Finally, $\overline{E}_{ij}$, which is traceless and divergenceless, accounts for tensor perturbations, *i.e.* gravitational waves.

Similarly, the stress-energy tensor can be written, in the Newtonian gauge,

$$\delta T_{00} = a^2\rho\,(\delta + 2\Phi) \tag{1.45}$$

$$\delta T_{0i} = -a^2(\rho + P)v_i \tag{1.46}$$

$$\delta T_{ij} = a^2 P\left[2\overline{E}_{ij} + \left(\frac{\delta P}{P} - 2\Psi\right)\delta_{ij} + \pi_{ij}\right]. \tag{1.47}$$

Here, δ is the density contrast defined in equation (1.37). $a\boldsymbol{v}$ is the perturbed velocity of a comoving observer, decomposed into a scalar and divergenceless vector part as $v_i = D_i v + \bar{v}_i$. Finally $\pi_{\mu\nu}$ is the anisotropic stress tensor which will be neglected from now on, which ensures that $\Psi = \Phi$.

Plugging these expressions into Einstein equations and using the conservation of the stress-energy tensor yields the relativistic forms of the equations from the previous section. The continuity equation (1.38) can be rewritten in its relativistic form, and for an adiabatic evolution[12], as

$$\delta' + \left(1 + \frac{\bar{P}}{\bar{\rho}}\right)\left(\nabla^2 v - 3\Phi'\right) + 3\mathcal{H}\left(c_\mathrm{s}^2 - \frac{\bar{P}}{\bar{\rho}}\right)\delta = 0, \tag{1.48}$$

where δ' is the derivative of δ with respect to conformal time η and $\mathcal{H} \equiv a'/a$. Euler and Poisson equations become

$$\boldsymbol{v}' + \mathcal{H}\left(1 - 3c_\mathrm{s}^2\right)\boldsymbol{v} = -\boldsymbol{\nabla}\Phi - \frac{\boldsymbol{\nabla}\delta P}{\bar{\rho} + \bar{P}} \tag{1.49}$$

and

$$\nabla^2\Psi = 4\pi G a^2 \bar{\rho}\Delta, \tag{1.50}$$

where $\bar{\rho}\Delta = \bar{\rho}\delta - 3\mathcal{H}\left(\bar{\rho} + \bar{P}\right)v$ is a gauge invariant quantity. Finally, the evolution of the scalar mode is given by

$$\Psi'' + 3\mathcal{H}\left(1 + c_\mathrm{s}^2\right)\Psi' + \left[2\mathcal{H}' + \mathcal{H}^2\left(1 + 3c_\mathrm{s}^2\right) - c_\mathrm{s}^2\nabla^2\right]\Psi = 0. \tag{1.51}$$

The term between the brackets has very important consequences. If we decompose

[11] For simplicity, we assume that spatial sections are flat.

[12] This means that we suppose that $\delta P/\delta\rho = c_\mathrm{s}$.

the gravitational potential into Fourier modes of comoving vector number k, the laplacian ∇^2 is replaced by $-k^2$, which must be compared to the $\mathcal{H}^2$ term. For adiabatic perturbations, we have $c_\mathrm{s}^2 \approx w$ and using Friedmann equations, we can rewrite it in a more concise way

$$\Psi'' + 3\mathcal{H}\,(1+w)\,\Psi' + wk^2\Psi = 0. \tag{1.52}$$

Therefore, we can get an idea of the behaviour of the gravitational potential for different regimes.

- If $k \ll \mathcal{H}$, that is when the mode's scale is larger than the characteristic expansion length $1/\mathcal{H}$, then Ψ is approximately constant.
- If $k \gg \mathcal{H}$, it depends on the value of w of the dominant component:
  - During the radiation era, $w = 1/3$ and the gravitational potential oscillates.
  - During the matter era, $w = 0$ and the gravitational potential is constant.

This behaviour can be seen on figure 1.8. In particular, the gauge invariant quantity

$$\zeta \equiv \Phi + \frac{2}{3\mathcal{H}}\frac{\Phi' + \mathcal{H}\Phi}{1 + \bar{P}/\bar{\rho}}, \tag{1.53}$$

written here in the Newtonian gauge and known as the *comoving curvature perturbation*, does not evolve for super-Hubble scales $k \ll \mathcal{H}$. For these modes, it can be rewritten

$$\zeta = -\frac{5+3w}{3(1+w)}\Phi, \tag{1.54}$$

where w is the equation of state of the fluid. ζ is constant during the radiation-to-matter transition while w goes from $1/3$ to 0. Therefore, the large-scale gravitational potential must decrease by a factor $9/10$.

1.4.2.2 Multiple fluids

So far, we have considered a single fluid. To go beyond this simplification, the total density, pressure and velocity must be written as the sum of several components with their own densities, pressures and velocities.

In the case of adiabatic fluctuations, it is assumed that all physical quantities in the perturbed space-time can be related to those of the background Universe by a small but common time shift. Therefore, the ratio $\delta\rho/\bar{\rho}' \propto \delta/1+w$ is common to all species, so that matter and radiation perturbations are related by

$$\delta_\mathrm{r} = \frac{4}{3}\delta_\mathrm{m}. \tag{1.55}$$

We can now write the equations for the various components in the fluid approximation.

CDM *Cold* dark matter has no pressure, therefore $P = 0$ and $c_\mathrm{s} = 0$, such that

$$\delta_\mathrm{c}' = k^2 v_\mathrm{c} + 3\Psi', \tag{1.56}$$

$$v_\mathrm{c}' = -\mathcal{H} v_\mathrm{c} - \Phi. \tag{1.57}$$

Baryons Electrons and nuclei are tightly coupled by electromagnetic forces, such that they have the same density contrast δ_b. Baryons are coupled to photons via Thomson scattering, which adds a force in the Euler equation

$$\delta_\mathrm{b}' = k^2 v_\mathrm{b} + 3\Psi', \tag{1.58}$$

$$v_\mathrm{b}' = -\mathcal{H} v_\mathrm{b} - \Phi - c_\mathrm{s}^2 \delta_\mathrm{b} + \frac{4\rho_\gamma}{3\rho_\mathrm{b}} \tau' (T_\gamma - T_\mathrm{b}), \tag{1.59}$$

where $\tau' = a n_e \sigma_\mathrm{T}$ is the differential opacity[13], σ_T denoting the Thomson cross-section, and $T_{\gamma/\mathrm{b}}$ are the temperature of photons and baryons.

Photons Photons obey

$$\delta_\gamma' = \frac{4}{3} k^2 v_\gamma + 4\Psi' \tag{1.60}$$

$$v_\gamma' = -\frac{1}{4}\delta_\gamma - \Phi - \frac{16}{45}\frac{k^2}{\tau'} v_\gamma + \tau' (T_\gamma - T_\mathrm{b}), \tag{1.61}$$

where the velocity term in the second equation comes from the anisotropic pressure.

The numerical integration of these equations is shown in figure 1.8. Several phases must be distinguished.

Before a mode becomes sub-Hubble, it is frozen. Then, after BBN and before recombination, baryons and photons are tightly coupled, such that, to first order in k/τ', their velocities are equal. Combining the previous equations yields

$$\delta_\gamma'' + \frac{R'}{1+R}\delta_\gamma' + k^2 c_\mathrm{s}^2 \delta_\gamma = 4\left[\Psi'' + \frac{R'}{1+R}\Psi' - \frac{1}{3}k^2\Phi\right] \tag{1.62}$$

with

$$R = \frac{3\rho_\mathrm{b}}{4\rho_\gamma} \quad \text{and} \quad c_\mathrm{s}^2 = \frac{1}{3}\frac{1}{1+R}. \tag{1.63}$$

This describes a forced damped oscillator. These density oscillations are due to the opposing effects of the radiation pressure *vs* gravity and are called *baryon acoustic oscillations*. They started when the mode becomes sub-Hubble and froze

[13] It is related to the optical depth τ by $\mathrm{d}\tau/\mathrm{d}\eta = -\tau'$.

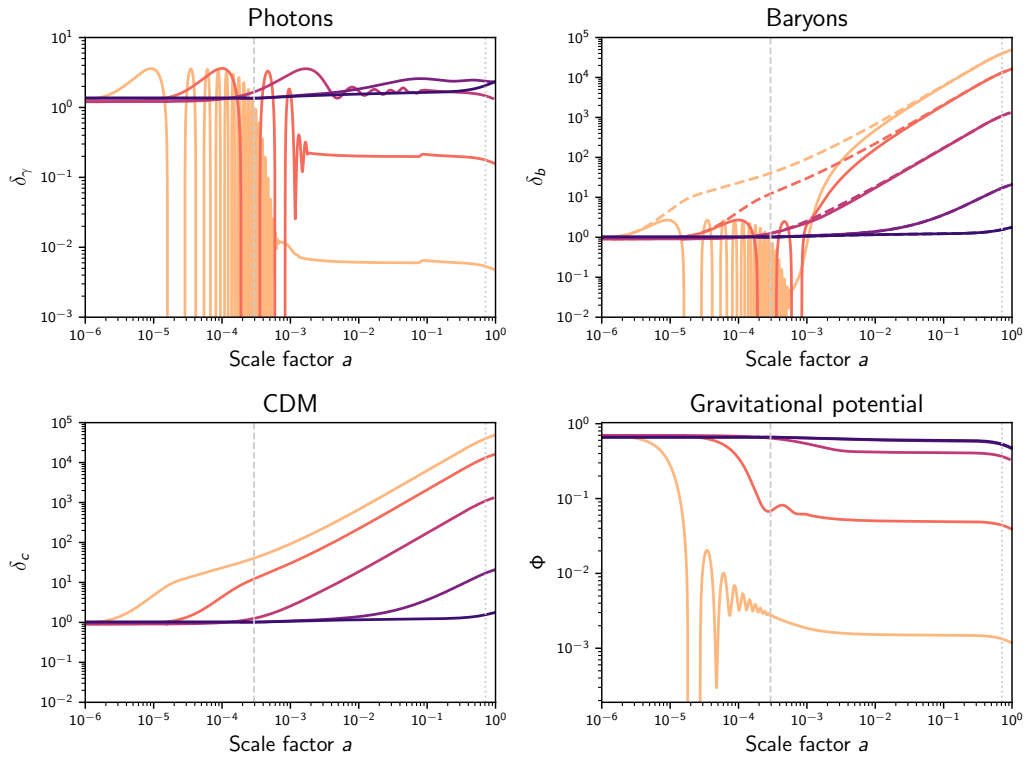

Figure 1.8 – Evolution of the photon, baryon and CDM density contrasts and of the gravitational potential for modes $k = 1 \times 10^{-5}\,\mathrm{Mpc}^{-1}$ (purple) to $1 \times 10^{-1}\,\mathrm{Mpc}^{-1}$ (orange). The vertical grey dashed and dotted lines respectively correspond to the radiation-matter and matter-dark energy equalities. In the top right plot, the evolution of CDM density modes is shown as dashed lines, for comparison with the evolution of baryon density modes.

at recombination, leaving an imprint in the distribution of matter, which has been detected in the anisotropies of the cosmic microwave background and the clustering of galaxies. During that time though, dark matter is not coupled and its perturbations grow logarithmically. After decoupling, baryons only interact gravitationally with dark matter and perturbations grow rapidly to match those of dark matter (shown as dashed lines in the top right panel of figure 1.8).

1.4.2.3 Kinetic approach

The fluid approximation presented so far captures the evolution of perturbations and its key features: the difference between sub- and super- Hubble modes, the baryon acoustic oscillations and the growth of structures. However, it has several caveats and a kinetic approach based on the Boltzmann equation is required, first, to derive the coupling – and *decoupling* – between photons and baryons and then, to describe the propagation of relativistic fluids – photons and neutrinos – that have a large mean free path. Their perturbed distribution in energy evolves over time, the densities being

only one moment of this distribution. Moreover, the presence of massive neutrinos, that behave first as radiation and later as free-streaming matter, breaks some of the assumptions made so far. Finally, the anisotropic stress of photons and neutrinos shall be taken into account, thus making the two gravitational potential slightly different.

In the case of photons, the distribution is Bose-Einstein and depends only on the temperature, written

$$T(\boldsymbol{x}, t) = T_0(t)\,(1 + \Theta(\boldsymbol{x}, t))\,. \tag{1.64}$$

The Boltzmann equation in the perturbed metric, for the temperature contrast $\boldsymbol{k}$-mode at conformal time η propagating in the direction $\hat{\boldsymbol{n}}$, $\Theta(\boldsymbol{k}, \eta, \hat{\boldsymbol{n}})$, can be written

$$\Theta' + ik\mu(\Theta + \Phi) = \Psi' + \tau' \left[\Theta_0 - \Theta + ik\mu v_b + \frac{1}{16} n_i n_j \Pi^{ij}\right] \tag{1.65}$$

where $\mu = \boldsymbol{k} \cdot \boldsymbol{n}/k$, $\tau' = a\sigma_{\mathrm{T}} n_e$, like in the previous section, and Π^{ij} is the anisotropic stress-tensor, related to the quadrupole Θ_2. The right-hand side contains the coupling to baryons via Thomson scattering. Expanding Θ in Legendre multipoles Θ_ℓ, one can write a set of differential equations with a recurrence relation, called the *Boltzmann hierarchy*.

The case of neutrinos is slightly more complicated because of the non-zero mass dependence. Their distribution is assumed to slightly deviate from a homogeneous Fermi-Dirac distribution[14] and must be parametrized differently because of the momentum dependence (see details in Ma and Bertschinger 1995).

These equations are solved by numerical integration in codes such as `CAMB` (Lewis *et al.* 2000) or `CLASS` (Lesgourgues and Tram 2011).

1.4.3 The matter power spectrum

We have written the equations governing the evolution of density perturbations and of the gravitational potential. In order to obtain a well-defined Cauchy problem, we need to know the initial conditions. However, these are unknown. All we can do is to take snapshot of the densities in our past light-cone, which is insufficient to determine all k-modes. Moreover, if structures that we observe today emerged from primordial quantum fluctuations, then it becomes impossible to know these conditions. Therefore, a statistical description – based on the hypothesis of *ergodicity*[15] – is required.

[14] This assumption is an approximation because no Fermi-Dirac distribution can satisfy the Boltzmann equation in the FLRW background metric.

[15] This hypothesis means that, for a single realization of the Universe, different regions explore the whole configuration space, such that, on scales much smaller than the size of the observable Universe, averages over realizations can be approached by averages over statistically independent space patches.

1.4.3.1 The linear matter power spectrum

The density fields $\delta(\boldsymbol{x}, t)$ at early times are assumed to be Gaussian random fields, which means that their statistics is fully captured by their two-point correlation function ξ_δ, defined as

$$\left\langle \delta(\boldsymbol{x}, t)\delta(\boldsymbol{x'}, t)\right\rangle = \xi_\delta\left(\boldsymbol{x}, \boldsymbol{x'}\right). \tag{1.66}$$

All odd-order correlation functions vanish. The cosmological principle implies that it is only a function of the distance between the two points $r = \left\|\boldsymbol{x'} - \boldsymbol{x}\right\|$. Switching to Fourier space, this defines the *power spectrum*, as[16]

$$\left\langle \delta(\boldsymbol{k}, t)\delta^*(\boldsymbol{k'}, t)\right\rangle = \delta^{(3)}\left(\boldsymbol{k} - \boldsymbol{k'}\right) P\left(\boldsymbol{k}, t\right). \tag{1.67}$$

The correlation function and the power spectrum are related by a Hankel transform

$$\xi(r, t) = \int_0^\infty \frac{\mathrm{d}k}{2\pi^2} k^2 P_\delta(k, t) \frac{\sin kr}{kr}. \tag{1.68}$$

Inflation, among other theories, predicts the power spectrum of the fluctuations of the inflaton scalar field, which are transferred to the comoving curvature perturbation ζ. Its dimensionless power spectrum $\mathcal{P}_\zeta$, defined as

$$\mathcal{P}_\zeta(k) = \frac{k^3}{2\pi^2} P_\zeta(k), \tag{1.69}$$

is close to scale invariant, which means that it can be written

$$\mathcal{P}_\zeta(k) = A_\mathrm{s}\left(\frac{k}{k_0}\right)^{n_\mathrm{s}-1}, \tag{1.70}$$

where the spectral index n_s is close to 1. The pivot scale k_0 is generally chosen to be $0.05\,\mathrm{Mpc}^{-1}$. The gravitational potential in the radiation-dominated era, Φ_RD, is related to ζ via equation (1.54), by

$$\zeta = -\frac{3}{2}\Phi_\mathrm{RD} \tag{1.71}$$

and thus

$$\mathcal{P}_{\Phi_\mathrm{RD}}(k) = \frac{4}{9}\mathcal{P}_\zeta(k). \tag{1.72}$$

As seen in figure 1.8, modes that re-enter the Hubble horizon[17] before the radiation-matter equality are suppressed and oscillates before being quasi-frozen in the matter-dominated era. This transition can be encoded by the so-called transfer function $T_\Phi(k)$ defined as

$$\Phi_\mathrm{MD}(k) = \frac{9}{10} T_\Phi(k)\Phi_\mathrm{RD}(k) \tag{1.73}$$

[16] Since δ is real-valued, $\delta^*(\boldsymbol{k}) = \delta(-\boldsymbol{k})$ and therefore $\left\langle \delta(\boldsymbol{k}, t)\delta(\boldsymbol{k'}, t)\right\rangle = \delta^{(3)}\left(\boldsymbol{k} + \boldsymbol{k'}\right) P\left(\boldsymbol{k}, t\right)$.

[17] This is a confusing abuse of language, though shared in the literature.

where the 9/10 factor is the global decrease mentioned at the end of section 1.4.2.1, used here such that the transfer function behaves as

$$T_\Phi(k) \sim \begin{cases} 1 & k \ll k_{\mathrm{eq}} \\ \left(k_{\mathrm{eq}}/k\right)^2 \ln k/k_{\mathrm{eq}} & k \gg k_{\mathrm{eq}} \end{cases}. \tag{1.74}$$

The relativistic Poisson equation can be written $k^2\Phi_{\mathrm{MD}}(k,a) = 4\pi G a^2 \bar{\rho}\Delta(k,a)$ where $\Delta \equiv \delta - 3aHv$ is the gauge-invariant comoving matter density perturbation, or, using the definition of the cosmological parameters

$$\Delta(k,a) = \frac{2ak^2\Phi_{\mathrm{MD}}(k,a)}{3\Omega_{\mathrm{m}}H_0^2}. \tag{1.75}$$

We split the time and space dependencies of Δ and introduce the matter growth function during the matter-dominated era D_+ as in section 1.4.1, defined as

$$\frac{\Delta(k,a_1)}{\Delta(k,a_2)} = \frac{D_+(a_1)}{D_+(a_2)}, \tag{1.76}$$

which implies

$$\frac{\Phi(k,a_1)}{\Phi(k,a_2)} = \frac{a_2}{a_1}\frac{D_+(a_1)}{D_+(a_2)}. \tag{1.77}$$

Choosing the normalization of D_+ such that it is 1 deep in the matter-dominated era, we can relate the late-time matter power spectrum to the primordial curvature power spectrum by

$$\mathcal{P}_{\mathrm{m}}(k,z) = \frac{4}{25}\left(\frac{k^2}{\Omega_{\mathrm{m}}H_0^2}\right)^2 T_\Phi^2(k) D_+^2(z)\mathcal{P}_\zeta(k). \tag{1.78}$$

This approach, though useful, is only an approximation because we have separated the time and space dependencies of the perturbed fields even though they are coupled in the equations[18]. In particular, the presence of neutrinos induces a non vanishing anisotropic stress tensor (so that the gravitational potentials are no longer equal) and a scale dependence of the growth factor. Therefore, the equations derived in the previous section shall be used to compute the evolution of the power spectrum: since they are linear, we can initialize the perturbed quantities at their standard deviation (given by the square root of the primordial power spectrum), integrate them over time and take their squared values to obtain the power spectrum at any time (see figure 1.9). All perturbation quantities can be related to the gravitational potential at early times in the radiation-dominated era when all useful modes are super-Hubble. Therefore, specifying the primordial power spectrum of ζ is sufficient to find the initial conditions of all Boltzmann equations.

[18] Otherwise, there wouldn't be acoustic waves!

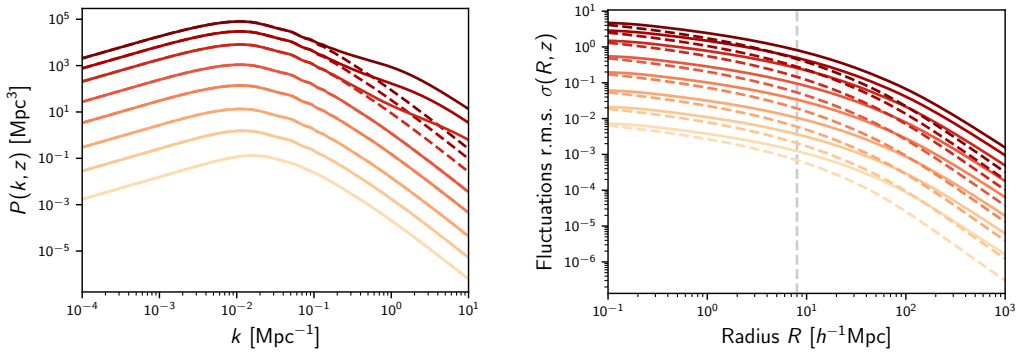

Figure 1.9 – Matter power spectrum (left) and r.m.s. of matter density linear perturbations (right) for redshifts 0, 1, 3, 10, 30, 100, 300 and 1 000 (from dark red to yellow). On the left panel, dashed lines correspond to the linear power spectrum while solid lines represent the non-linear power spectrum. On the right panel, dashed lines correspond to a gaussian window function and solid lines correspond to a top-hat window function. The gray vertical line is $R = 8\,h^{-1}\,\mathrm{Mpc}$. The power spectrum was computed with `NumCosmo` using `CLASS` as the backend and a `halofit` prescription.

1.4.3.2 Towards the non-linear regime

As perturbations grow, the density contrast of small-scale modes might come to be of order unity or even more[19], indicating that the linear perturbation theory described above is breaking. In this regard, let's define the variance of the density contrast with a window function of scale R and at redshift z as

$$\sigma^2(R, z) \equiv \left\langle \left(\int \mathrm{d}^3\boldsymbol{x}\, \delta(\boldsymbol{x}, z) W_R(\boldsymbol{x}) \right)^2 \right\rangle . \tag{1.79}$$

It can be related to the power spectrum as

$$\sigma^2(R, z) = \int \frac{k^2\,\mathrm{d}k}{2\pi^2} P(k, z) \left| \widetilde{W}(k, R) \right|^2 \tag{1.80}$$

where $\widetilde{W}(k, R)$ is the Fourier transform of the window function. In particular, we define σ_8^2 as the variance of fluctuations at $z = 0$ with a top-hat window function of radius $R = 8\,h^{-1}\,\mathrm{Mpc}$, extrapolated from the linear theory. In that case, $\widetilde{W}(k, R) = 3\,j_1(kR)/kR$ where j_1 is the spherical Bessel function. As it turns out, σ_8 is of order unity, which means that scales below $\sim 10\,\mathrm{Mpc}$ have reached the non-linear regime (see figure 1.9).

Several approaches exist for exploring the non-linear regime:

***N*-body simulations** Large cosmological simulations involving many particles (possibly, several species) interacting gravitationally can probe the non-linear regime.

[19] Note that separate k-modes may have a large value, but that doesn't matter: only the real space density is relevant here.

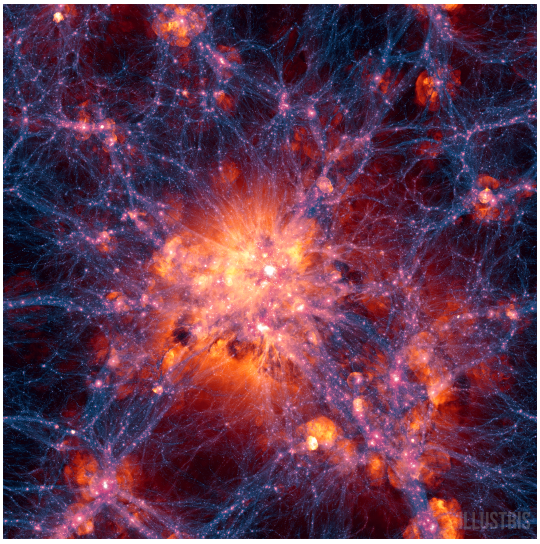

Figure 1.10 – Snapshot of the Illustrisfootnote 20 simulation around a cluster. The dark matter density is in purple and the gas velocity field is overlaid in orange.

They might then be used to calibrate fitting formulae for the non-linear power spectrum as was done for the `halofit` prescription (Bird *et al.* 2012; Smith *et al.* 2003; Takahashi *et al.* 2012) or to create emulators (spline-based interpolators, see *e.g.* Lawrence *et al.* 2017). They can also include non-gravitational astrophysical processes, such as feedback processes from active galaxy nuclei (AGN), supernovæ explosions shockwaves, ionizing radiation from stars, stellar evolution, *etc.* One of the largest simulations to date is the Illustris Project[20] (see figure 1.10 and Vogelsberger *et al.* 2014).

Halo model In the halo model (see Cooray and Sheth 2002, for a review), galaxies are clustered inside large haloes, following a halo occupancy distribution depending on the halo mass. The computation of the power spectrum is then split between an intra- and an inter-halo contribution.

Higher order perturbation theory Another approach is to extend the perturbation theory to second order (or even more). One can derive rules to compute Feynman-like diagrams to go beyond tree-level equations (Bernardeau *et al.* 2002) and even perform renormalization (Crocce and Scoccimarro 2006).

An important consequence of non-linearities is that different k-modes, that were independent in the linear theory, are coupled in the non-linear regime. Therefore, higher-order correlation functions or power spectra – called *bispectra* and *trispectra* for 3- and 4-points functions – become non-zero. The *squeezed* limit is a special configuration of the bispectrum $B(\boldsymbol{k_1}, \boldsymbol{k_2}, \boldsymbol{k_3})$ where one of the modes is close to zero, for instance $k_3 \approx 0$, implying that $\boldsymbol{k_1} \approx -\boldsymbol{k_2}$. That case describes the response of

[20] http://www.illustris-project.org/

the power spectrum at scale k_1 to the large-scale density, *i.e.* the local mean density. This is the approach we will use in chapter 5.

Appendices

1.A Notions of quantum field theory

Modern particle physics relies on the formalism of quantum field theory (QFT), a general framework – in the sense that it provides mathematical tools but not the physics itself – that combines hypotheses from quantum mechanics and special relativity. We will here sketch some of the principles of this theory, based on Peter and Uzan 2013; Weinberg 2005; Zuber 2013 and personal class notes.

1.A.1 Fundamental principles

The fundamental assumptions of quantum field theory are:

- Algebra of operators: the physical state of a system at time t is represented by a vector $|\psi(t)\rangle$ in a Hermitian space $\mathcal{H}$. Physical observables are represented by linear operator acting on these states, such that their expectation values are $\langle A\rangle = \langle\psi(t)|A|\psi(t)\rangle$.

- Unitarity: the evolution of $|\psi(t)\rangle$ is given by a linear, unitary operator $U(T)$ that can be set in a non-projective representation of the group of time transformations.

- Lorentz group: so as to be a relativistic theory, states and operators live in representations of the proper, orthochronous Lorentz (or Poincaré) group $\mathcal{L}_+^\uparrow$ whose universal cover is $\mathrm{SL}(2,\mathbb{C})$ and Lie algebra $\mathrm{su}(2)\oplus\mathrm{su}(2)$. They are indexed by two half-integers that determine the spin of the particle. P and T symmetries allow the definition of a basis of one-particle states labelled by their 4-momenta p^μ and internal states, and obtained from a hypothesized vacuum thanks to creation operators $\left|\psi_{\boldsymbol{p},\sigma}\right\rangle = a^\dagger(\boldsymbol{p},\sigma)\,|0\rangle$.

- Pauli exclusion principle: the bosonic or fermionic nature of particles defines commutation and anticommutation relationships for n-particles states, the ensuing spin-statistics theorem constraining bosons (fermions) to have integer (half-integer) spins.

- In/out states: the Hamiltonian can be decomposed into a free part and an interaction part (the potential) as $H = H_0 + V$. Initial and final states $|\phi\rangle$ of an interaction are eigenstates of the free Hamiltonian H_0 and can be obtained from the Lippmann–Schwinger equation, $\left|\psi^\pm\right\rangle = |\phi\rangle + (E - H_0 \pm i\epsilon)^{-1}\,V\left|\psi^\pm\right\rangle$. They define the Lorentz-invariant S-matrix as

$$S_{\alpha\beta} = \left\langle\psi_\beta^-\middle|\psi_\alpha^+\right\rangle = \langle\phi_\beta|S|\phi_\alpha\rangle\,, \tag{1.81}$$

  which is interpreted as the *transition probability* from state α to state β.

- Evolution equation: Schrödinger's equation, $i\hbar\partial_t |\psi\rangle = \hat{H} |\psi\rangle$, is applied to the time evolution operator U in the interaction representation, *i.e.*

$$i\partial_t U(t) = V_{\text{int}}(t)U(t) \tag{1.82}$$

where

$$V_{\text{int}}(t) = e^{+iH_0 t} V e^{-iH_0 t} = \int \mathrm{d}^3\vec{x}\ \mathcal{H}_{\text{int}}(\vec{x}, t), \tag{1.83}$$

and thus the S-matrix reads

$$S = T\left[\exp -i \int \mathrm{d}^4\mathbf{x}\ \mathcal{H}_{\text{int}}(\mathbf{x})\right] \tag{1.84}$$

where the expansion of the exponential is time ordered. It can be rewritten $S_{\alpha\beta} = \delta_{\alpha\beta} - 2\pi i\delta^{(4)}(\sum_\beta p^\mu_{\text{out}} - \sum_\alpha p^\mu_{\text{in}})M_{\alpha\beta}$, introducing the M-matrix, a central quantity for computing cross-sections.

1.A.2 Types of fields

Particles are represented by operator-valued fields, that transform according to a representation of the Lorentz group. Three of them are of particular interest:

- Scalar fields carry a $(0,0)$ representation of the Lorentz group, are therefore spinless, and can be written (because of micro-causality)

$$\phi(\mathbf{x}) = \int \frac{\mathrm{d}^3\vec{p}}{\left((2\pi)^3 p^0\right)^{1/2}} \left[e^{+ip_\mu x^\mu} a(\vec{p}) + e^{-ip_\mu x^\mu} a^\dagger(\vec{p}).\right] \tag{1.85}$$

Therefore they obey the Klein-Gordon equation[21]

$$\left(\partial_\mu \partial^\mu - m^2\right)\phi = 0. \tag{1.86}$$

The Higgs boson and the hypothetical inflaton are scalars.

- Vector fields belong to the $(1,0) \oplus (0,1)$ representation. Massive vector fields, such as the W and Z bosons, can be decomposed in a spin 0 scalar field and a spin 1 field, while massless vector fields, like photons, have two spin 1 contributions (two directions of polarization).

- Dirac spinors represent all known fermions: electrons, positrons, muons, neutrinos, quarks, *etc.* They transform under the $(\frac{1}{2}, 0) \oplus (0, \frac{1}{2})$ representation and contain two spin $\frac{1}{2}$ fields: the right- and left-handed particles. They obey the Dirac equation

$$\left(\not{\partial} + m\right)\psi = 0. \tag{1.87}$$

[21] We use the $(-+++)$ signature of the metric.

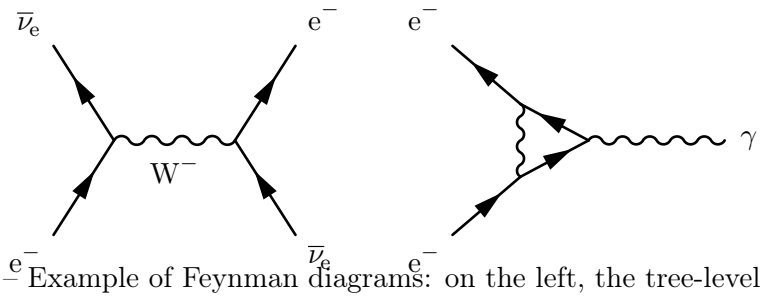

Figure 1.11 – Example of Feynman diagrams: on the left, the tree-level interaction between an electron and a neutrino; on the right, the emission of a photon by an electron, at 1-loop order.

1.A.3 The machinery: Feynman diagrams and renormalization

The Hamiltonian is written as a function of these fields which are themselves integrals of creation and annihilation operators. (Anti)commutators of these operators,

$$\Big[a(\boldsymbol{p},\sigma,n), a^\dagger(\boldsymbol{p}',\sigma',n')\Big]_\pm = \delta^3(\boldsymbol{p}-\boldsymbol{p}')\delta_{\sigma\sigma'}\delta_{nn'} \tag{1.88}$$

then provide rules to compute the perturbative expansion of the exponential in equation (1.84). The terms of this expansion are represented by Feynman's diagrams, that also give a pictorial representation of interactions.

Several issues then arise.

First, the above rules are defined for the Hamiltonian, which is a function of the fields ϕ and their momenta Π_ϕ. However, writing the Lagrangian $\mathcal{L}$ – which is a function of ϕ and $\dot{\phi}$ – of a theory is advantageous because its symmetries are more explicit, which allows to derive conserved currents and charges thanks to Noether's theorem. However, switching from a description to the other is not always straightforward, in particular because the momenta $\Pi_\phi = \delta\mathcal{L}\Big/\delta\dot{\phi}$ may be ill-defined (*e.g.* if the Lagrangian does not imply $\dot{\phi}$). Such issues usually occur when the description is redundant and gauge invariances imply constraints, which can be dealt with thanks to Dirac's method.

Then, graphs including loops (see figure 1.11) may contain divergent integrals that can be tamed with mathematical tricks such as dimensional regularization. However, this requires an ultraviolet cut-off, which will have to be dealt with.

Feynman rules can be extended for the computation of Green functions defined as the vacuum expectation value of the product of n field operators,

$$\langle 0|\phi(x_1)\dots\phi(x_n)|0\rangle = \tag{1.89}$$

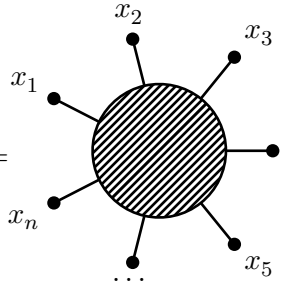

which can be rewritten as path integrals, as proposed by Feynman in his thesis

(Feynman 1942). These are helpful as they can be related to the propagator and vertices.

Now, another difficulty arises when we start coupling fields, abandoning their respective free theories. Consider the propagator of a Dirac spinor: in the complete theory, it should have contributions from internal loops and can be written as a series,

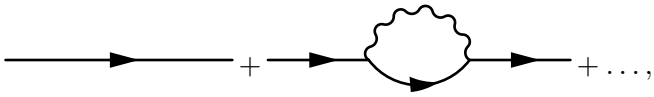

(1.90)

which can be linked to the propagator of a free theory with different masses and coupling constants. That's where *renormalization* kicks in. There is no reason why the fields normalizations and constants – couplings and masses – written in the Lagrangian should be the observable ones. By requiring the proper behaviour of Green functions in the full theory, that is asking that they are finite, one determines how to rescale – or, renormalize – the *bare* constants and fields as a function of energy, thus absorbing all the ultraviolet divergences. A theory is renormalizable if only a finite number of Green functions are divergent, such that a finite number of rescaling operations are needed. While this seems constraining at first sight, non-renormalizable theories are actually physically irrelevant because they make no predictions.

CHAPTER 2

Cosmological probes

Contents

2.1 The cosmic microwave background 38
2.1.1 Anisotropies in the cosmic microwave background 39
2.1.2 Features of the angular power spectrum 40
2.1.3 Secondary anisotropies 42
2.1.4 The polarization of the cosmic microwave background . . . 44
2.1.5 Dependence on cosmological parameters 45
2.1.6 Computation of the power spectrum 47
2.2 Tracers of the large-scale structure 48
2.2.1 Galaxy clustering 48
2.2.2 The Lyman-α forest 53
2.3 Gravitational lensing 57
2.3.1 Physical principle 58
2.3.2 Lensing of the cosmic microwave background 61
2.3.3 Cosmic shear 64
2.4 Comparison of cosmological probes 66

Now that we have the most important theoretical ingredients, let us turn to the observations and describe the various probes of the Universe. Note that we will not describe direct geometric probes such as supernovæ or strong lenses, which provides distance measurements, as they were not the topic of this thesis work. We will, however, describe probes of the large-scale structure. First, we will explore the physics of the anisotropies in the cosmic microwave background. Then, we will describe tracers of the large-structure at later times, focusing on galaxies and the

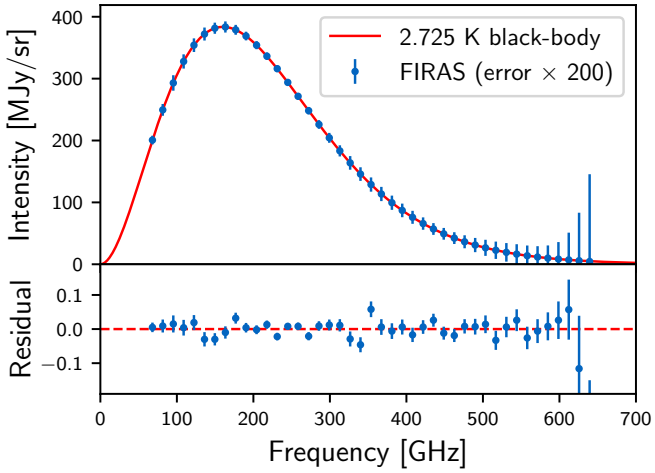

Figure 2.1 – Electromagnetic spectrum of the monopole of the CMB measured by FIRAS (in blue) and the best fit black-body spectrum with a temperature of 2.725 K (in red). The precision is such that error bars have been multiplied by a factor 200 to be visible. Importantly, the bottom plot shows the deviation from the black-body spectrum, constraining possible non-thermal processes such as energy gain from hot electrons. The data is from Fixsen *et al.* 1996, available at `https://lambda.gsfc.nasa.gov/product/cobe/firas_prod_table.cfm`.

Lyman-α forest of quasars. Finally, we will present gravitational lensing by the large-scale structure in the weak regime.

2.1 The cosmic microwave background

The CMB is the thermal photon bath left over after recombination ended. Its spectrum is extremely close to the black-body spectrum found by Max Planck in 1900,

$$B_\nu(T) = \frac{2h\nu^3}{c^2} \frac{1}{e^{\frac{h\nu}{k_\mathrm{B}T}} - 1}, \tag{2.1}$$

as confirmed by the FIRAS instrument on board of the COBE satellite (see figure 2.1). Therefore, photons were very close to thermodynamic equilibrium when they were emitted. Their initial temperature of about 3 000 K has cooled down to $T_0 = 2.725\,\mathrm{K}$ due to the expansion, indicating that the redshift of the last scattering surface is $z_* \sim 1\,090$.

These photons are a rich source of information for cosmology. They were released only 380 000 years after the Big Bang and act as a portrait of the primordial Universe, and in particular of its inhomogeneities. They navigated through matter structures under formation since then and have witnessed several cosmological and astrophysical effects, distorting – spatially or spectroscopically – primary anisotropies or introducing new ones, which will be referred to as *secondary* anisotropies.

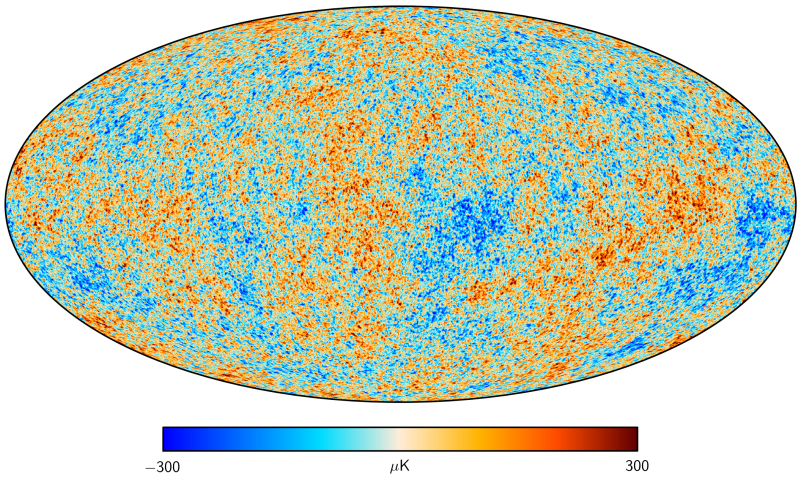

Figure 2.2 – Map of the anisotropies of the CMB measured by Planck (Planck Collaboration *et al.* 2016b).

2.1.1 Anisotropies in the cosmic microwave background

Inhomogeneities in the energy density of photons imply inhomogeneities in the local temperature of photons, related by $\delta_\gamma = 4\,\delta T/T$, by virtue of the Stefan-Boltzmann law. However, the temperature contrast of the photons collected by instruments today, $\Theta \equiv \delta T/T$, is not simply $\delta_\gamma/4$ because photons can be spectroscopically shifted by the gravitational potential and the Doppler effect. Indeed, a photon loses energy when escaping a gravitational potential well. The complete formula in the linear regime, derived by Sachs and Wolfe (Sachs and Wolfe 1967), reads

$$\Theta(\hat{\boldsymbol{n}}) = \underbrace{\left[\frac{1}{4}\delta_\gamma + \Phi\right]_{\mathrm{LSS}}}_{\text{Sachs-Wolfe}} \underbrace{- \hat{\boldsymbol{n}}\cdot\boldsymbol{\nabla} v_\mathrm{b}\Big|_{\mathrm{LSS}}}_{\text{Doppler}} + \underbrace{\int_{\mathrm{LSS}}^{\mathrm{now}} \mathrm{d}\eta \left[\Phi' + \Psi' - n^i n^j \overline{E}'_{ij}\right](\boldsymbol{x}(\eta), \eta)}_{\text{ISW}} \tag{2.2}$$

where $\hat{\boldsymbol{n}}$ is the direction of observation. The Sachs-Wolfe term contains the intrinsic density contrast and the gravitational potential, both evaluated at the last scattering surface (LSS) when the photons were released. The Doppler boost is due to the velocity of baryons in the plasma, v_b. Finally, the Integrated Sachs-Wolfe (ISW) term is due to net energy gain (or loss) of photons crossing successive gravitational wells that are evolving: if a potential well is smoothed between entry and exit of a photon, then it gains energy. Importantly, this term vanishes in a matter-dominated Universe. Therefore, the late-time ISW effect betrays the existence of a dominating dark energy component.

The first interesting figure is the absolute level of the anisotropies, of order $\Delta T/T \sim 10^{-5}$. This means that the Universe was very smooth, as a result of the small level of primordial fluctuations and the strong coupling in the baryons-photons plasma. Nonetheless, small fluctuations have been measured to a resolution of about $5'$ (see the map on figure 2.2). Again, they are random, so their statistics are interesting.

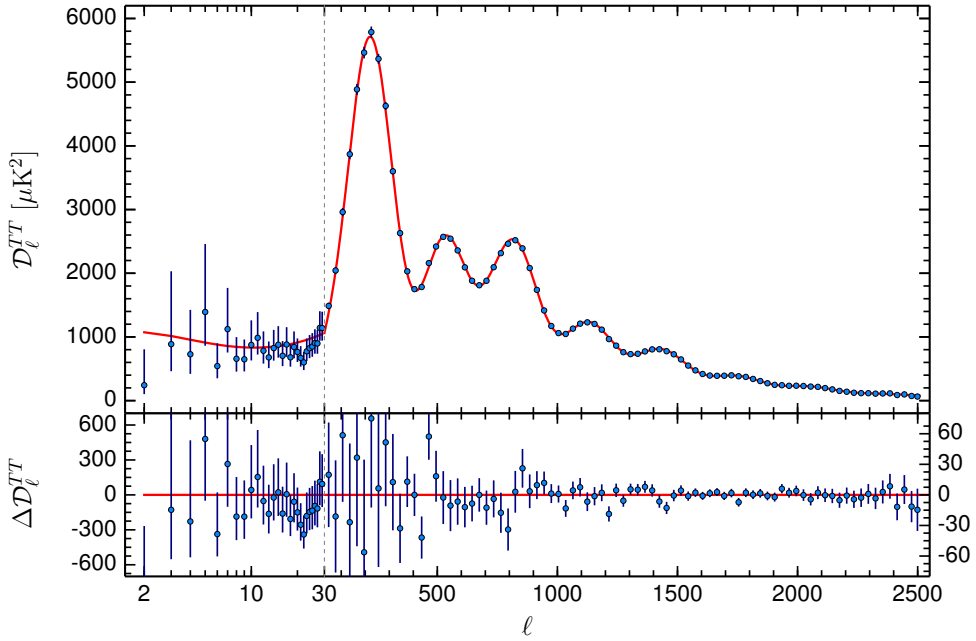

Figure 2.3 – Power spectrum $\mathcal{D}_\ell^{TT} = \ell(\ell+1)C_\ell^{TT}/2\pi$ of the CMB temperature anisotropies measured by Planck (Planck Collaboration *et al.* 2016e).

2.1.2 Features of the angular power spectrum

Under the assumption of isotropy, the correlation function $\langle\Theta(\hat{\boldsymbol{n}})\Theta(\hat{\boldsymbol{n}}')\rangle$ depends only on $\hat{\boldsymbol{n}}\cdot\hat{\boldsymbol{n}}'$ and can be expanded in Legendre polynomials P_ℓ as

$$\langle\Theta(\hat{\boldsymbol{n}})\Theta(\hat{\boldsymbol{n}}')\rangle = \sum_{\ell=0}^{\infty}\frac{2\ell+1}{4\pi}P_\ell(\hat{\boldsymbol{n}}\cdot\hat{\boldsymbol{n}}')C_\ell^{TT}, \tag{2.3}$$

where C_ℓ^{TT} is the temperature angular power spectrum[1], shown in figure 2.3. Let us outline some of its important features.

Large angular scales For super-Hubble modes, the Sachs-Wolfe term dominates. The gravitational potential can be related to overdensities, such that

$$\Theta_{\mathrm{SW}} = \frac{1}{3}\Phi = -\frac{1}{6}\delta_\gamma, \tag{2.4}$$

and as a consequence, cold spots correspond to over-dense regions. At these scales, we have $\ell(\ell+1)C_\ell^{TT} \propto \ell^{n_\mathrm{s}-1}$ such that the power spectrum is almost flat, a feature known as the Sachs-Wolfe plateau.

Intermediate scales The acoustic waves in the baryon-photon plasma described

[1] We will develop the formalism of angular power spectra in more detail in chapter 6.

by equation (1.62) freeze at recombination. Density modes at their maxima (compression) or minima (dilation) at this point create peaks in the power spectrum. The first peak is related to the largest distance travelled by these waves, called the *sound horizon* and given by

$$r_s = \int_0^{\eta_\star} \mathrm{d}\eta\, c_s = \int_0^{\eta_\star} \frac{\mathrm{d}\eta}{\sqrt{3(1+R)}} \approx 145\,\mathrm{Mpc} \tag{2.5}$$

where $R = 3\rho_\mathrm{b}/4\rho_\gamma$. This is equivalent to an angular size

$$\theta_* = r_s/D_A(z_*) = 0.6^\circ \tag{2.6}$$

where $D_A(z_*)$ is the comoving angular diameter distance at redshift z_*. The next peaks correspond to damped harmonic modes. Note that compression peaks are bigger because the gravitational potential shifts the oscillations to higher densities.

Small scales At small scales, the diffusion of photons from hot to cold regions tends to smooth fluctuations, a phenomenon known as *Silk damping*. In the fluid approximation, we can use equations from section 1.4.2.2. Small-scale modes of the gravitational potential have been been greatly reduced before recombination (see figure 1.8) so that we neglect it at small scale. Moreover, the time scale of the oscillations is much smaller than the expansion time scale, such that R can be considered constant here. Expanding the difference of the velocity fields of baryons and photons, $v_\mathrm{b} - v_\gamma$, to first order in $1/\tau'$, we can write the evolution equation of the photon density contrast, similar to equation (1.62), as

$$\delta_\gamma'' + \frac{k^2 c_\mathrm{s}^2}{\tau'}\left(\frac{16}{15} + \frac{R^2}{1+R}\right)\delta_\gamma' + k^2 c_\mathrm{s}^2 \delta_\gamma = 0. \tag{2.7}$$

We can define a damping scale k_D such that

$$k_\mathrm{D}^{-2} = \frac{1}{6}\int_0^{\eta_\star} \frac{\mathrm{d}\eta}{\tau'}\left[\frac{1}{1+R}\left(\frac{16}{15} + \frac{R^2}{1+R}\right)\right] \tag{2.8}$$

of order $k_\mathrm{D} \approx 0.14\,\mathrm{Mpc}^{-1}$.

Another equally important smoothing effect is due to the width of the last scattering surface. The probability that a photon is scattered for the last time at η, called the *visibility function*, is

$$g(\eta) = \tau' e^{-\tau} \tag{2.9}$$

where τ is the *optical depth*, such that $\mathrm{d}\tau/\mathrm{d}\eta = -\tau'$. The temperature contrast which is observed is therefore an average of the contrast along the line of sight

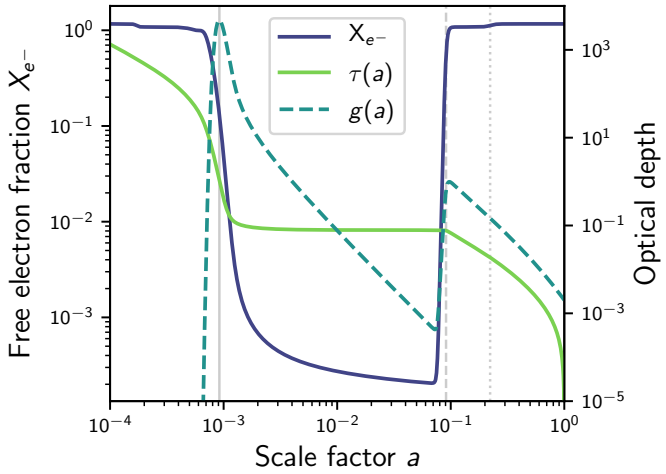

Figure 2.4 – Free electron fraction X_{e^-} and optical depth τ as a function of scale factor a during recombination and reionization. The optical depth and the visibility function, defined here by $g(a) = \mathrm{d}\tau/\mathrm{d}a\, e^{-\tau}$, correspond to the right vertical axis. The solid, dashed and dotted gray lines mark recombination, reionization of hydrogen and reionization of helium, respectively.

weighted by the visibility function. This results in an exponential cut of power at small scales, since in Fourier space, $\hat{g}(k) \propto \exp\left(-\frac{1}{2}k^2\sigma_{\mathrm{LSS}}^2\right)$ where σ_{LSS} is the width of the last-scattering surface.

2.1.3 Secondary anisotropies

In the previous section, we have described the primary anisotropies, that is, those originating at the time where CMB photons are emitted. However, during their course from the last scattering surface to our telescope, they have had various interactions with matter and the structures they crossed.

Reionization – When the first stars are turned on, they emit ultraviolet radiation that can *re*-ionize hydrogen and helium atoms. The fraction of free electrons rises again (see figure 2.4) until all of the intergalactic medium is ionized. CMB photons are scattered by these electrons via Thomson scattering, causing a blurring of the anisotropies on all scales smaller than the horizon at the epoch of reionization. As a consequence, the power spectrum of CMB anisotropies is decreased by $e^{-2\tau_{\mathrm{reion}}}$ on small scales (for $\ell \gtrsim 20$), where τ_{reion} is the optical depth through the reionization era (visible as a plateau in figure 2.4). Its value is dependent on the reionization history, that is, the exact time and space[2] dependence of the free electron fraction, and, in particular, to the typical redshift z_{re} when reionization occurs.

[2]Reionization occurs sooner close to ionizing radiation emitters, a phenomenon known as *patchy* reionization (Becker *et al.* 2015; Smith and Ferraro 2017).

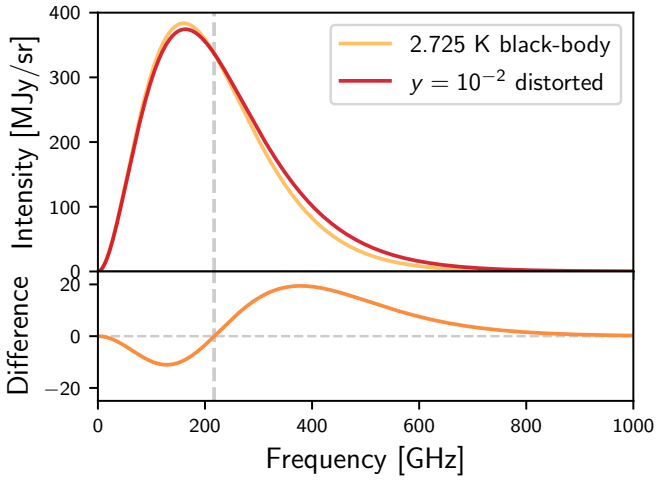

Figure 2.5 – Spectrum of the CMB at temperature $T_{\rm CMB} = 2.725\,\mathrm{K}$ and spectrum distorted by the SZ effect for a (non-realistic) Compton parameter of $y = 1 \times 10^{-2}$. The difference of the spectra is shown in the bottom plot, where the characteristic distortion of the SZ effect is visible: small frequency photons are shifted towards higher frequencies while their number is constant, implying a stable point at $\nu = 217\,\mathrm{GHz}$.

The Sunyaev-Zel'dovich effect – The intra-cluster medium (ICM) contains hot free electrons, visible thanks to their bremsstrahlung emission in the X-ray domain. When cold CMB photons go through clusters, they get a kick in energy via inverse Compton scattering from the bath of hot electrons, inducing a frequency dependent distortion of the spectrum: this is the thermal SZ effect (tSZ). This shift can be parametrized by an equivalent frequency-dependent temperature shift[3], which, in the non-relativistic Kompaneets approximation, is given by (Birkinshaw 1999; Hill and Spergel 2014; Sunyaev and Zeldovich 1970)

$$\frac{\Delta T}{T_{\rm CMB}} = g_\nu(x) y = g_\nu(x) \frac{\sigma_{\rm T}}{m_e c^2} \int \mathrm{d}l\, P_e(l), \tag{2.10}$$

where P_e is the ICM electron pressure integrated over the line of sight, g_ν is the thermal Sunyaev-Zel'dovich spectral function, given by $g_\nu(x) = x\coth(x/2) - 4$ where $x = h\nu/k_{\rm B}T_{\rm CMB}$ is the dimensionless frequency. y is called the Compton parameter and has a typical value of $\sqrt{\langle y^2 \rangle} \sim 10^{-5}$ (estimated from the spread for clusters seen by Planck). The tSZ spectral function is zero for $x \approx 3.83$, that is $\nu \approx 217\,\mathrm{GHz}$ and thus, below (respectively above) this frequency, clusters imprint cold (respectively hot) points in the CMB map.

If a cluster is in motion with respect to the CMB frame, an additional temperature shift $\Delta T/T_{\rm CMB} \approx -\tau\, v_\parallel/c$, where $v_\parallel$ is the velocity along the line of

[3]The distorted spectrum can be computed as $I_\nu = B_\nu(T_{\rm CMB} + \Delta T(\nu))$ where $B_\nu(T)$ is the black-body spectrum at temperature T.

sight, is created by Doppler effect: this is the kinetic SZ effect.

The integrated Sachs-Wolfe effect – As mentioned earlier, if a gravitational potential is changing over time because of the expansion, photons gain more energy when entering it than when escaping it. However, it is a small effect, of order $\Delta T/T \sim 10^{-6}$, at large scales.

Gravitational lensing by large-scale structure – Photon trajectories are bent by matter over-densities, causing a distortion of the observed CMB map by large-scale structures of order $2'$, coherent on $2°$ patches. This decreases the amplitude of the power spectrum at percent level and broadens the peaks. It will be discussed in more details in section 2.3.

Point sources Though technically not secondary anisotropies, intra- and extragalactic point sources may contribute to the microwave signal observed by CMB experiments. See, for instance, Afshordi *et al.* 2004.

2.1.4 The polarization of the cosmic microwave background

CMB photons are slightly polarized – at the 10^{-6} level – because of Thomson scattering interactions with electrons in the primordial plasma. Indeed, if the incident flux of electrons around some point in the plasma has a quadrupolar distribution, the net polarization will be non-zero in the direction perpendicular to the quadrupole plane. This can come from:

Scalar perturbations : electrons falling towards a potential well accelerate when they get closer to the overdensity. There are fewer electrons coming from the radial direction than from the tangential one, forming a quadrupole.

Vector perturbations : they can in principle create vortices in the electron velocity field, but they are usually considered negligible.

Tensor perturbations : gravitational waves distort circular potential wells into elliptical ones, thus forming quadrupolar distributions.

Patterns of polarization are generally decomposed into a divergence mode (E) and a curl mode (B). Scalar perturbations produce only E-modes while tensor perturbations produce both E- and B-modes. Secondary E-modes are also produced by Thomson scattering of CMB photons by free electrons after reionization, creating a large-scale bump in the E-mode power spectrum, which is proportional to the reionization optical depth squared $\tau^2_{\rm reion}$. Finally, distortions caused by gravitational lensing can cause E-modes to leak into B-modes at scales $\ell \gtrsim 100$. Measurements of the polarization of CMB anisotropies are shown in figure 2.6.

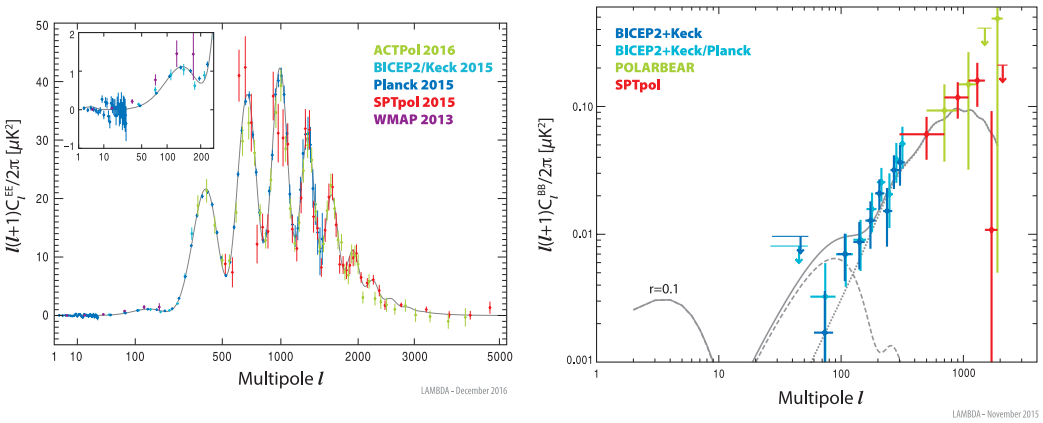

Figure 2.6 – EE and BB power spectra measurements from several ground- and space-based CMB experiments. Figure from https://lambda.gsfc.nasa.gov/.

2.1.5 Dependence on cosmological parameters

Primordial anisotropies of the CMB probes the Universe 380 000 years after the Big Bang and their power spectrum is sensitive to the parameters of the cosmological model that we have mentioned so far (and listed in table 1). In figure 2.7, the theoretical CMB power spectrum is plotted for varying parameters.

Let us comment on the impact of these parameters.

Amplitude The amplitude of the CMB power spectrum is broadly proportional to $A_s e^{-2\tau}$, except for very large scales, $l \lesssim 20$. The later reionization occurs, the smaller the optical depth τ, thus increasing A_s or z_{re} have opposite effects.

Geometry The Hubble parameter, H_0, and the dark energy equation of state, w, determine the late expansion of the Universe and therefore modify angular scales (as non-zero curvature Ω_k would), thus inducing a horizontal shift of the power spectrum.

Matter On the one hand, the higher the density of baryons, the larger BAO waves are. Therefore, an increase in ω_b results in higher compression peaks. On the other hand, CDM is decoupled from the plasma, thus increasing the fraction of CDM tends to tame the amplitude of the waves.

Primordial spectrum Varying n_s, which depends on the outcome of the inflationary phase, tilts the CMB power spectrum, making it *bluer* for higher values of n_s.

Neutrinos The mass of neutrinos has a small effect on the CMB, which is somewhat degenerate with the Hubble parameter. This is due to the fact that they still act as radiation (they are *relativistic*) at recombination.

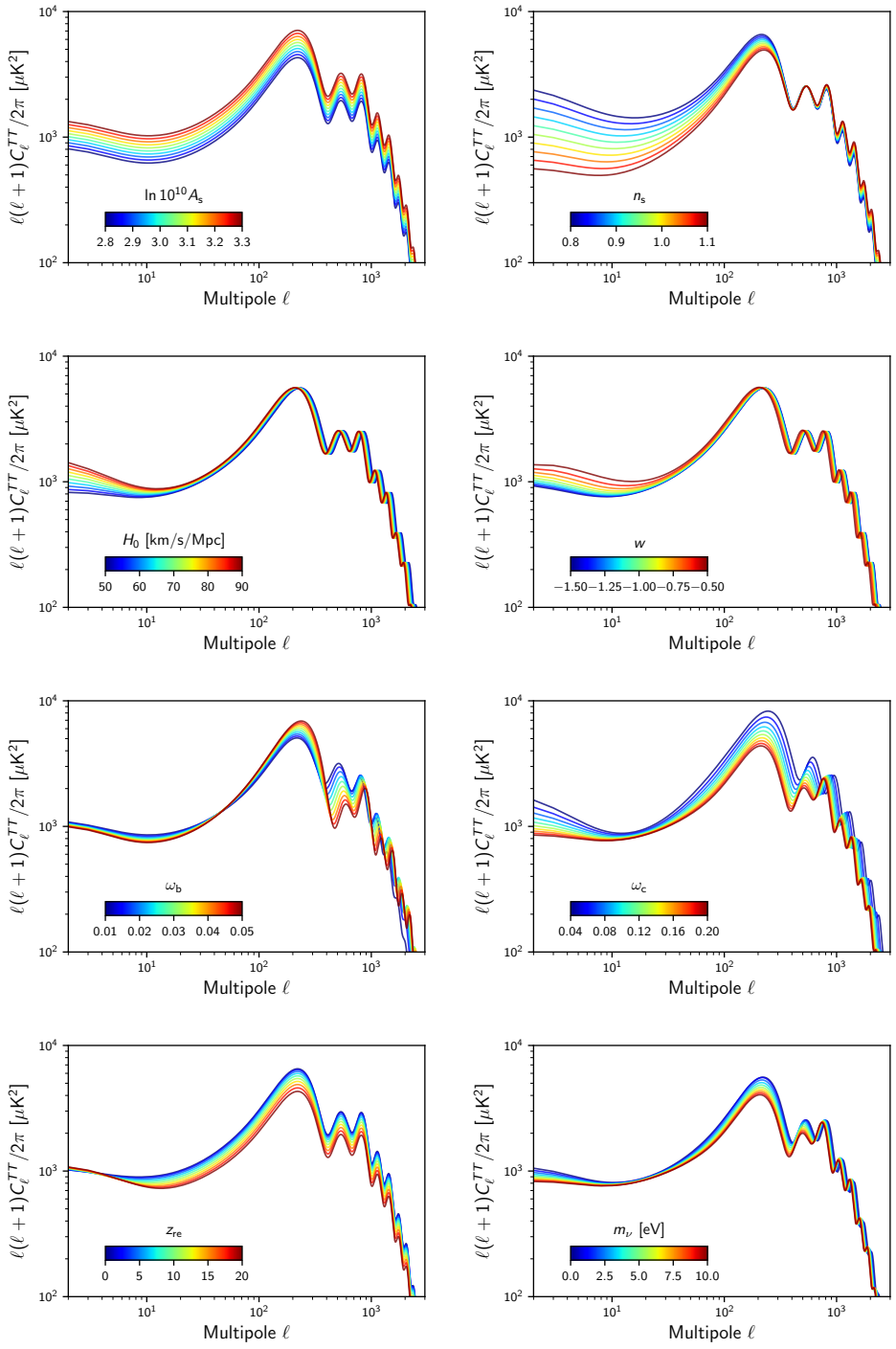

Figure 2.7 – Effects of varying the cosmological parameters on the CMB power spectrum. Here we use a flat ΛCDM model as a reference ($\Omega_\Lambda = 1-\Omega_m-\Omega_r$), varying one parameter at a time. The fiducial values are those from Planck Collaboration *et al.* 2016e using CMB temperature and polarization and CMB lensing data as well as external BAO and H_0 measurements (referred to as "TT,TE,EE+lowP+lensing+ext"). Note that, for illustrative purposes, the ranges in which parameters are varied are much greater than current constraints.

2.1.6 Computation of the power spectrum

The temperature constrast of photons at position $\boldsymbol{x}$, propagating in the direction $\hat{\boldsymbol{n}}$ and at conformal time η, $\Theta(\boldsymbol{x}, \hat{\boldsymbol{n}}, \eta)$, can be decomposed as a sum of contributions from scalar, vector and tensor modes. Each of these can further be expanded in Fourier space as

$$\Theta(\boldsymbol{x}, \hat{\boldsymbol{n}}, \eta) = \int \frac{\mathrm{d}^3\boldsymbol{k}}{(2\pi)^{3/2}} \sum_{\ell m} \Theta_\ell^{(m)}(k, \eta) G_{\ell m}(\boldsymbol{x}, \hat{\boldsymbol{n}}), \tag{2.11}$$

where

$$G_{\ell m}(\boldsymbol{x}, \hat{\boldsymbol{n}}) = (-i)^\ell \sqrt{\frac{4\pi}{2\ell+1}} e^{i\boldsymbol{k}\cdot\boldsymbol{x}} Y_{\ell m}(\hat{\boldsymbol{n}}) \tag{2.12}$$

is a decomposition over plane waves and spherical harmonics $Y_{\ell m}$. The index m is directly related to the scalar-vector-tensor decomposition: $m = 0$ indicates scalar modes, $m = \pm 1$ denotes the two polarizations of vector modes and $m = \pm 2$ those of tensor modes ($+$ and $\times$).

As seen in chapter 1, the evolution of the temperature contrast obeys a Boltzmann equation, that gives the evolution of the Fourrier coefficients $\Theta_\ell^{(m)}(k, \eta)$ at all times. The collision term of the Boltzmann equation encodes all the interactions that can modify the photon temperature:

- Thomson scattering with charged particles up to photon decoupling and during reionization;
- Doppler boost due to baryon velocity;
- gravitational Doppler effect;
- interaction with gravitational waves.

These equations are evolved together with the Boltzmann equations of the other components (dark matter, baryons and neutrinos) from the end of inflation up to now. It can be shown (see chapter 6) that the power spectrum is given by

$$(2\ell+1)^2 C_\ell^{TT} = \frac{2}{\pi} \int k^2 \, \mathrm{d}k \sum_{m=-2}^{m=+2} \left| \Theta_\ell^{(m)}(k, \eta_{\mathrm{now}}) \right|^2. \tag{2.13}$$

In practice, codes such as `CLASS` use some relevant approximations (Blas *et al.* 2011), such as the photon-baryon tight coupling approximation, as well as optimizations, such as the integration of radial modes, to make the computation fast enough for analysis purposes.

2.2 Tracers of the large-scale structure

The matter density field is not directly observable: all we see is light and all we can measure are fluxes, spectra – used to estimate redshifts – and positions on the sky. Therefore, one has to rely on *tracers* that can only be used to *infer* the underlying field. Indeed, their distribution is usually different than that of all matter, the relationship between these distributions being strongly dependent on the type of tracer and often encoded by a *bias* that is time and scale dependent. For instance, galaxies are found only where the density is high enough to form stars while neutral hydrogen is found far enough from ionizing sources.

2.2.1 Galaxy clustering

One illustrative way to think about galaxy clustering is to compare it to glitter play dough: galaxies are like sparkling specks, spread across an invisible dark matter matrix, according to some complex rules set by gravity and astrophysics, that one seeks to weigh.

2.2.1.1 Power spectrum and correlation function

The overdensity of galaxies can be related to that of matter by a generic expression of the form (Gil-Marìn *et al.* 2015a)

$$\delta_g(\boldsymbol{x}, z) = \mathcal{B}\left[\delta(\boldsymbol{x}, z)\right] \tag{2.14}$$

where $\mathcal{B}$ is a *bias* functional of the density field[4]. A possible, simple parametrization is to write it as a Taylor expansion

$$\mathcal{B}\left[\delta(\boldsymbol{x}, z)\right] = \sum_{k=1}^{\infty} \frac{b_k(z)}{k!} \delta^k(\boldsymbol{x}, z), \tag{2.15}$$

but it may also be written as a scale-dependent bias in Fourier space as

$$\delta_g(k, z) = b(k, z)\delta(k, z), \tag{2.16}$$

or explicitly involve the matter velocity field. In the simplest model, valid at large scales and for a homogeneous sample of galaxies, the densities are simply proportional and related by a redshift-dependent bias as $\delta_g(\boldsymbol{x}, z) = b_g(z)\delta(\boldsymbol{x}, z)$. Therefore, the matter power spectrum is related to that of galaxies by $P_g(k, z) = b_g^2(z)P(k, z)$, and similarly for the correlation function. The galaxy correlation function and the power spectrum have been measured at redshifts $z \sim 0 - 1$, providing constraints in the scale range $k \sim 0.01 - 0.2\,h\,\mathrm{Mpc}^{-1}$ (see figure 2.8).

[4] See Desjacques *et al.* 2016 for a review on bias.

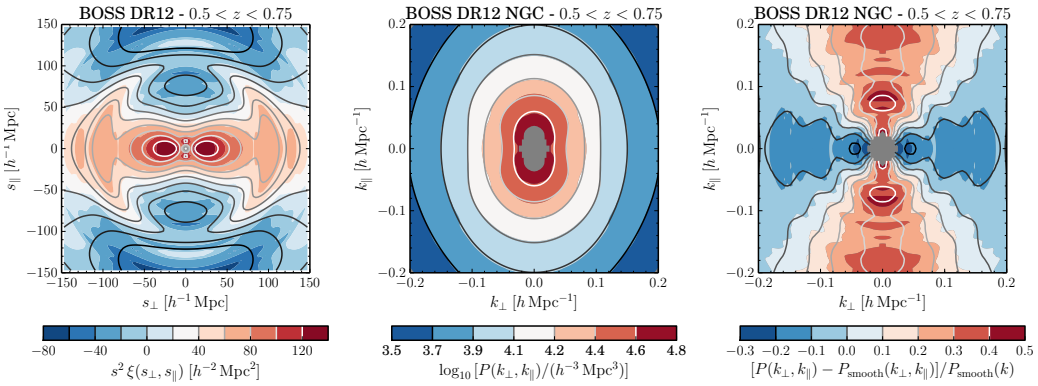

Figure 2.8 – Measured anisotropic galaxy correlation function (left) and power spectrum (middle). The rightmost plot shows the difference between the measured power spectrum and a smooth power spectrum without BAO-related wiggles. The BAO "ring" is clearly visible in the correlation function. Figures from (Alam *et al.* 2017).

The bispectrum of galaxies, defined in section 1.4.3.2, probes the non-gaussianity of the density field. It originates from non-linear gravitational evolution at small scales, or from possible primordial non-gaussianities that affect large-scale clustering.

Note, however, that several complications come from the way we observe these galaxies, which we shall see in section 2.2.1.3.

2.2.1.2 Baryon acoustic oscillations

Before recombination, density waves propagate in the baryon-photon plasma, under the opposite effects of gravity and radiation pressure. Each primordial over-density is thus surrounded by an over-dense growing shell of baryons and photons. After the BAOs froze at recombination, this shell stops at a radius given by the sound horizon r_s, forming a bump in the correlation function of baryons (see figure 2.9). Photons keep streaming, while baryons and dark matter interact through gravity and fall into each other's overdensities. The large-scale distribution of baryons and dark matter then slowly evolves under the action of gravity until they completely match at low redshift. Finally, massive neutrinos become non-relativistic, they start feeling the gravitational pull from large-scale structures.

Tracers of the large-scale structure must also exhibit the BAO peak in their correlation functions. Moreover, it has been shown that this scale is robust to cosmological evolution (Eisenstein *et al.* 2007; Seo and Eisenstein 2007), making it a standard ruler, *i.e.* a well-calibrated distance that can be compared to theoretical predictions for r_s, thus constraining the geometry of the Universe.

So as to observe this characteristic feature, one needs to precisely measure the positions of a large number of galaxies, spanning a large volume. This requires spectroscopic observations, in order to derive precise redshift estimates (as opposed to

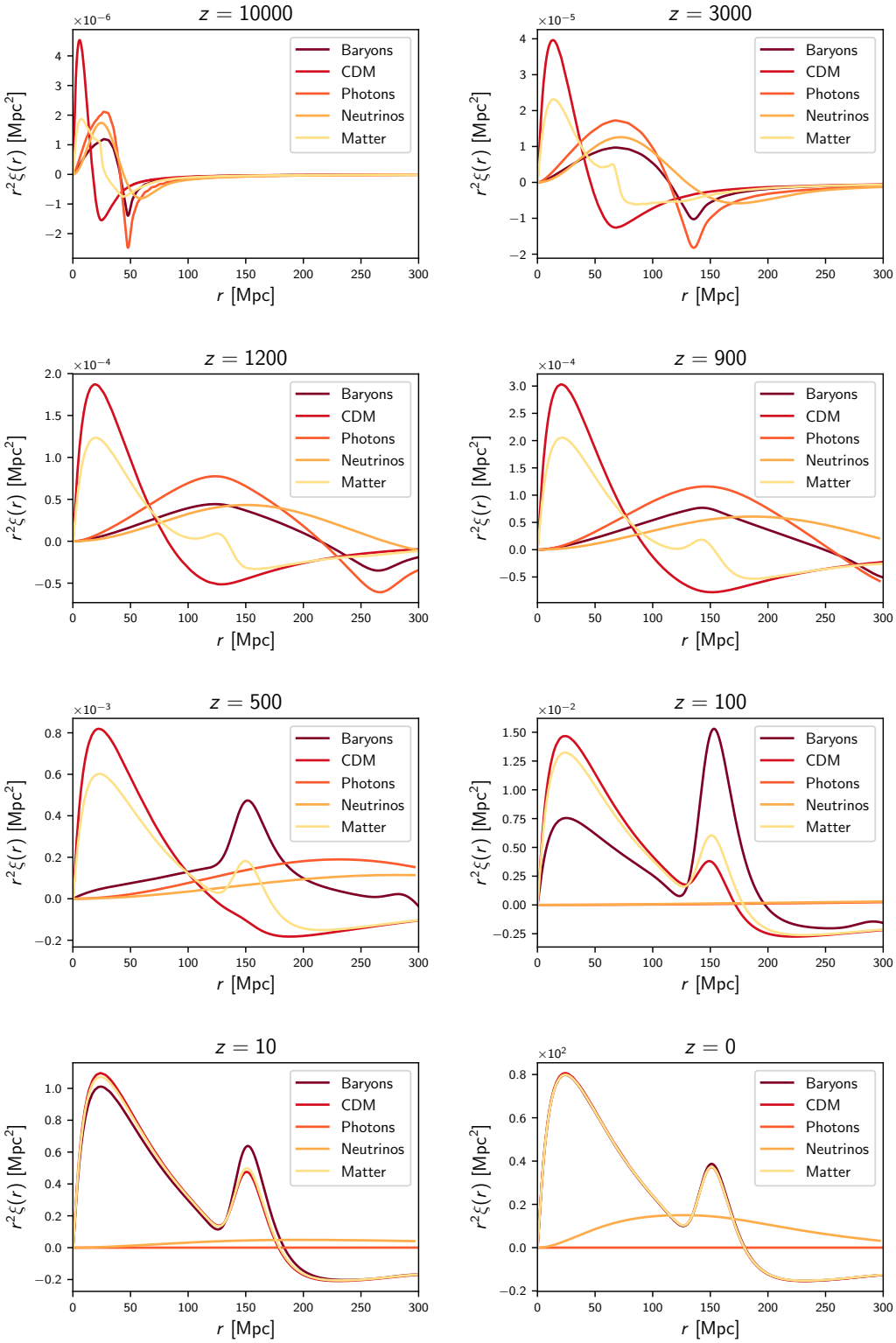

Figure 2.9 – Correlation functions of the different components in the Universe – dark matter, baryons, photons and neutrinos – and of all matter, as a function of redshift, from linear perturbation theory.

photometric redshifts, estimated from band fluxes). Nonetheless, it has been observed and measured up to redshift $z \sim 0.6$ (Anderson *et al.* 2012, 2014; Aubourg *et al.* 2015; Cuesta *et al.* 2016).

Since the BAO pattern is imprinted in the three-dimensional distribution of galaxies, it can be measured along the line of sight or perpendicular to it, yielding two comoving scales, $s_\parallel$ and $s_\perp$. These distances can be related to, respectively, the angular diameter distance, $D_A(z) = f_K(\chi(z))/(1+z)$, and the Hubble parameter $H(z)$, or the Hubble distance $D_H(z)$, by (Bassett and Hlozek 2009)

$$D_A(z) = \frac{s_\perp}{\Delta\theta(1+z)} \quad \text{and} \quad D_H(z) \equiv \frac{c}{H(z)} = \frac{s_\parallel}{\Delta z}. \tag{2.17}$$

In principle, the radial and angular measurements should both match the predicted BAO scale r_s, offering a consistency check of the cosmological model (the so-called Alcock-Paczynski test, Alcock and Paczynski 1979). If the measurement is averaged over all directions, then it contrains the quantity (Percival 2013)

$$D_V(z) \equiv \left((1+z)^2 D_A^2(z) \frac{cz}{H(z)}\right)^{1/3}, \tag{2.18}$$

that combines the angular diameter distance and the Hubble parameter.

2.2.1.3 Relativistic effects

Galaxy surveys can only measure the apparent positions of galaxies and their redshifts. Therefore, the relationship between the galaxy number density fluctuations measured in redshift-space and the total matter density fluctuations is impacted by relativistic effects (Bonvin and Durrer 2011; Challinor and Lewis 2011). The most important are the so-called redshift-space distortions and the effect of cosmic magnification.

2.2.1.3.1 Redshift-space distortions

We cannot measure the distance to a given galaxy with a ruler but rather have to infer it from its estimated redshift. However, the observed redshift is the sum of the cosmological redshift and a contribution due to the peculiar velocity of the galaxy by Doppler effect. This makes the mapping from redshift-space to real-space positions non-trivial since it implies knowing the velocity field as well. This effect is called *redshift-space distortions* and manifests itself differently at large and small scales.

- At large scales, galaxies have coherent infall motions towards the centers of large potential wells such as growing galaxy clusters. Therefore, their distribution seems flattened in the direction of the line of sight. This so-called *Kaiser effect* can be corrected for by modifying the relationship between the power spectra

to (Kaiser 1987)

$$P_g(\boldsymbol{k}, z) = b_g^2 \left(1 + \beta\mu^2\right)^2 P(\boldsymbol{k}, z) \tag{2.19}$$

where $\mu = k_\parallel/k$, with $k = \|\boldsymbol{k}\|$, and

$$\beta \equiv \frac{1}{b_g(a)} \frac{\mathrm{d}\ln D_+}{\mathrm{d}\ln a}. \tag{2.20}$$

Therefore, measuring the power spectrum at different angles μ is a powerful method to study structure formation parametrized in $f \equiv \mathrm{d}\ln D_+/\mathrm{d}\ln a$. Another workaround consists in *reconstructing* the true positions of galaxies before measuring their clustering properties (White 2015). This requires to infer the velocity field from the density field via the continuity equation, which can easily be inverted in the linear regime, and then applying small displacements to galaxies.

- On small scales, galaxies have random motions within virialized, bound objects such as clusters. Clustering is smeared out by the large velocity dispersion, sometimes modelled as an exponential cut, $\exp\left(-k^2\Sigma_{\mathrm{NL}}\right)$, and the redshift-space distribution of galaxies is instead elongated along the line of sight, forming what is called the *Finger of God*.

Redshift-space distortions have been measured in the galaxies of the SDSS-III/BOSS survey (Gil-Marìn *et al.* 2016, 2017; Reid *et al.* 2012), constraining the growth of structure at redshift $z \sim 0.3 - 0.6$.

2.2.1.3.2 Magnification

Photons emitted by galaxies are deflected by the large-scale structure through gravitational lensing (addressed in the next section). For a galaxy survey with a magnitude cut, this has two opposite effects. First, lensed galaxies may be magnified, appear brighter than they actually are and pass the threshold luminosity, even though their intrinsic luminosity is too low (and vice-versa). Then, lensing modifies the apparent volume, thus diluting the galaxy density in the case of positive convergence. These effects can be parametrized by including a lensing term in the relationship between the galaxy and the matter densities, such that

$$\delta_g(\boldsymbol{x}, z) = b_g(z)\delta(\boldsymbol{x}, z) - (5s - 2)\kappa(\boldsymbol{x}, z), \tag{2.21}$$

where κ is the convergence at the position of the galaxy and s is the slope of the galaxy number count at the high magnitude limit,

$$s = \left.\frac{\mathrm{d}\log N(< m)}{\mathrm{d}m}\right|_{m=m_{\max}}. \tag{2.22}$$

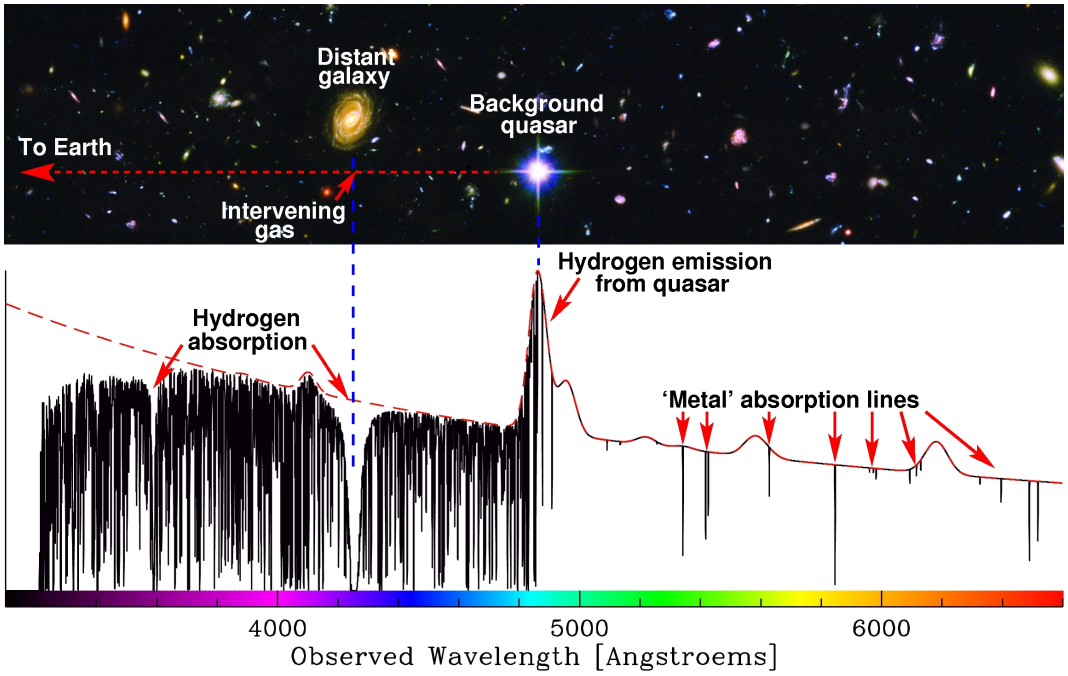

Figure 2.10 – Sketch of the Lyman-α forest in the spectrum of a quasar. Credit: Joe Liske/ESO.

This effect is important at large redshift (Zıour and Hui 2008), where the convergence κ becomes non-negligible, and has been measured in quasar samples (Scranton *et al.* 2005).

2.2.2 The Lyman-α forest

For a historical review, see Rauch 2001 *and* Rauch 1998.

The Lyman-α forest is an absorption phenomenon observed in the spectra of high redshift quasars (quasi-stellar objects or QSOs, see Osmer 2001, for an overview) blueward of their Lyman-α ultraviolet emission line[5]. It reveals the presence of intervening neutral hydrogen between the observer and the quasar, that carves the redshifted spectrum with many absorption lines.

2.2.2.1 Quasars and the intergalactic medium

Quasars are bright sources in the radio, visible and ultraviolet parts of the electromagnetic spectrum. Originally thought to be variable stars, they are now considered as the most energetic objects in the class of active galactic nuclei. Their luminosity is believed to be powered by accretion of large amounts of matter on the central massive black hole of distant galaxies, emitting a continuous, non-thermal spectrum.

[5]The Lyman series are the transition of neutral hydrogen from an excited state to the electron ground state. The transition from $n = 2$ to $n = 1$ is the Lyman-α transition, at rest-frame wavelength $\lambda_\alpha = 1\,216$ Å.

The intergalactic medium (IGM, see McQuinn 2016, for a review) is composed of diffuse matter surrounding galaxies and clusters, and could harbour as much as 90% of baryons in the Universe. Its physical properties – composition, temperature, density – are intimately related to the formation and radiative activity of galaxies. When the light of a quasar crosses the IGM, the neutral hydrogen (HI) it contains absorbs photons at wavelengths corresponding to its rest-frame energy transitions, most notably in the Lyman series. Successive such crossings leave a collection of absorption lines that are continually redshifted along with the whole spectrum. The measured wavelength of these lines can be directly translated into cosmological distances, thus making the whole process similar to a geological core sample of neutral hydrogen (see figure 2.10).

The depth and width of the absorption lines depend on the number density of neutral hydrogen in the IGM. If $X_{\mathrm{HI}}(z)$ denotes the number fraction of hydrogen atoms that are neutral at redshift z and Y the mass fraction of helium, then the mean density at redshift z is

$$n_{\mathrm{HI}}(z) = X_{\mathrm{HI}}(z)(1-Y)\frac{\rho_{\mathrm{b}}(z)}{m_p c^2} = 1.9\times10^{-7}\,\mathrm{cm}^{-3}\times X_{\mathrm{HI}}(z)(1+z)^3. \tag{2.23}$$

At thermal equilibrium, the absorption cross-section integrated over the resonance of the Lyman-α transition is given by (see section 23 of Peebles 1993)

$$\sigma(\nu) = \frac{3}{8\pi}\Lambda_{2p\to1s}\lambda_\alpha^2\phi_\alpha(\nu) \tag{2.24}$$

where $\phi_\alpha(\nu)$ is the absorption line profile and

$$\Lambda_{2p\to1s} = \frac{\omega_\alpha^3 e^2}{3\pi\varepsilon_0\hbar c^3}\sum_m \left|\left\langle\psi_{2p}\middle|\boldsymbol{x}\middle|\psi_{1s}\right\rangle\right|^2 = 6.25\times10^8\,\mathrm{s}^{-1} \tag{2.25}$$

is the spontaneous radiative decay rate from the $2p$ to the $1s$ state of hydrogen (the lifetime of the $2p$ state is thus $\tau_{2p} = 1/\Lambda_{2p\to1s} = 1.6\,\mathrm{ns}$). The line profile $\phi_\alpha(\nu)$ is the convolution of two line broadening effects. First, due to Heisenberg's incertitude principle, the transition has a Lorentzian profile with a natural width of order $\Delta E/E \sim \lambda_\alpha/c\tau_{2p} \sim 10^{-8}$. Then, thermal broadening due to the Doppler effect induced by peculiar velocities of atoms in the gaz is modelled by a Maxwell-Boltzmann distribution law. Now, the fraction of absorbed flux at observed frequency ν is given by $e^{-\tau(\nu)}$ where

$$\tau(\nu) = \int_0^{z_{\mathrm{QSO}}} n_{\mathrm{HI}}(z)\sigma(\nu(1+z))\frac{c\,\mathrm{d}z}{(1+z)H(z)} \tag{2.26}$$

is the optical depth. Here, the cross-section is evaluated at the frequency of the photon at redshift z and the fraction term is simply the infinitesimal proper distance

$\mathrm{d}l$. For a Dirac profile at $\nu = \nu_\alpha$, we obtain

$$\tau(\nu) = \frac{3 n_{\mathrm{HI}}(z_\alpha) \Lambda_{2p\to 1s} \lambda_\alpha^3}{8\pi(1+z_\alpha) H(z_\alpha)} \tag{2.27}$$

where $z_\alpha = \nu_\alpha/\nu - 1$. Plugging in the values for the ΛCDM model, the optical depth is

$$\tau(\nu) \sim 10^4 \times X_{\mathrm{HI}}(z_\alpha) \left(\frac{100\,\mathrm{km\,s^{-1}\,Mpc^{-1}}}{H(z_\alpha)} \right) (1+z_\alpha)^2 \tag{2.28}$$

Therefore, a very small fraction of neutral hydrogen ($X_{\mathrm{HI}} \sim 10^{-5}$) is sufficient to absorb a significant flux ($\tau \sim 1$). At redshift $z \sim 6$, reionization is well over (Becker *et al.* 2007), but the small remaining fraction of neutral hydrogen is sufficient to absorb the almost entire flux of quasars, leaving a discontinuity in the spectra of quasars known as the Gunn-Peterson trough (Gunn and Peterson 1965). At lower redshift, hydrogen is in photoionization equilibrium, *i.e.* the rate of recombination equals that of ionization by absorption of UV photons with energy higher than the Lyman limit of 912 Å. This equilibrium is determined by the physical parameters of the IGM and the ionizing UV flux, and it directly impacts the distribution of HI versus that of UV emitters (mostly stars) and, therefore, that of dark matter[6].

Now, consider a HI "cloud" of small extent[7] and its column density $N_{\mathrm{HI}} = \int n_{\mathrm{HI}}\,\mathrm{d}l$ expressed in cm^{-2}. The observed equivalent width of a line at redshift z_0 and frequency ν_0 is given by

$$W = \frac{1+z_0}{F(\nu_0)} \int F(\nu) \left(1 - e^{-\tau(\nu)}\right) \mathrm{d}\nu \tag{2.29}$$

where $F(\nu)$ is the observed emission spectrum of the quasar. At low density, τ is small and the width can be approximated by

$$W \sim \int \tau(\nu)\,\mathrm{d}\nu = N_{\mathrm{HI}} \int \sigma(\nu)\,\mathrm{d}\nu \sim 0.5(1+z) \left(\frac{N_{\mathrm{HI}}}{10^{14}\mathrm{cm}^{-2}} \right) \text{Å}, \tag{2.30}$$

while for high densities, we obtain, using a Lorentzian profile of width $\Lambda_{2p\to 1s}$,

$$W \sim 7 \left(\frac{N_{\mathrm{HI}}}{10^{20}\mathrm{cm}^{-2}} \right)^{1/2} \text{Å}. \tag{2.31}$$

Therefore, HI systems are classified as a function of their column density:

[6] The rate of recombination is given by $\alpha(T) n_p n_e$ and that of ionization by $\Gamma_{\mathrm{HI}} n_{\mathrm{HI}}$. Since $n_{\mathrm{HI}} \ll n_e = n_p$, we have, at equilibrium, $n_{\mathrm{HI}} = (\alpha(T)/\Gamma_{\mathrm{HI}})\, n_p^2$. Neutral hydrogen is thus more clustered than baryons.

[7] The term of "cloud" is a bit of a historic misnomer because simulations in the 1990s (Miralda-Escudé *et al.* 1996) and subsequent observations revealed that the IGM density is largely determined by the distribution of dark matter, and is thus more accurately described as a diffuse web structure. HI clouds would require an important external force to sustain the gaz pressure and are therefore rare. In the following, we will rather use the generic term of "HI systems".

$N_{\mathrm{HI}} \sim 10^{13} - 10^{16}\,\mathrm{cm}^{-2}$ These systems are the most abundant at $z \sim 3$ and produce narrow lines that can be distinguished from one another, thus tracing baryons in the IGM on a wide range of scales ($0.1 - 100\,\mathrm{Mpc}$).

$N_{\mathrm{HI}} \sim 10^{17}\,\mathrm{cm}^{-2}$ Lyman-limit systems are dense enough for their core to be protected from ionizing UV radiation and to contain enough neutral hydrogen to fully absorb radiation at the Lyman-α resonance.

$N_{\mathrm{HI}} \gtrsim 10^{20}\,\mathrm{cm}^{-2}$ Damped Lyman-α systems (DLAs, Noterdaeme *et al.* 2012) produce wide absorption lines where the damping tails of the Lorentzian profile are perceptible.

2.2.2.2 Clustering in the Lyman-α forest

The ratio between the observed spectrum $f(\lambda)$ and the emission spectrum of the quasar $C(\lambda)$ – also called the *continuum* – at observed wavelength λ,

$$F(\lambda) \equiv \frac{f(\lambda)}{C(\lambda)} = e^{-\tau(\lambda)}, \tag{2.32}$$

is also referred to as the *transmission*. Its mean value $\bar{F}(z)$ depends on cosmology and the mean density of neutral hydrogen, as stated in the previous section. Fluctuations in the density of HI result in transmission fluctuations, defined as

$$\delta_F(z) = \frac{F(z)}{\bar{F}(z)} - 1. \tag{2.33}$$

These fluctuations are, in turn, related to the matter density field δ, though in a non-linear way. A more detailed discussion of this aspect will be provided in chapter 5.

Be that as it may, clustering measurements from the Lyman-α forest probe the matter power spectrum on a wide range of scales.

Line-of-sight power spectrum The one-dimensional power spectrum probes matter on the smallest scales (Croft *et al.* 1998; McDonald *et al.* 2000, 2006; Zaldarriaga *et al.* 2001), thus constraining the mass of neutrinos (the more massive they are, the more they suppress small-scale fluctations, see Palanque-Delabrouille *et al.* 2013, 2015b), but also exotic models of dark matter, such as warm dark matter (Viel *et al.* 2013), sterile neutrinos dark matter (Seljak *et al.* 2006) and primordial black hole dark matter (Afshordi *et al.* 2003).

3D power spectrum Combining different lines of sight enables to probe the matter power spectrum on larger scales (McQuinn and White 2011; Slosar *et al.* 2011).

BAO On the largest scales, the three-dimensional correlation function of the Lyman-α forest exhibits a bump at the scale of baryon acoustic oscillations. It has been

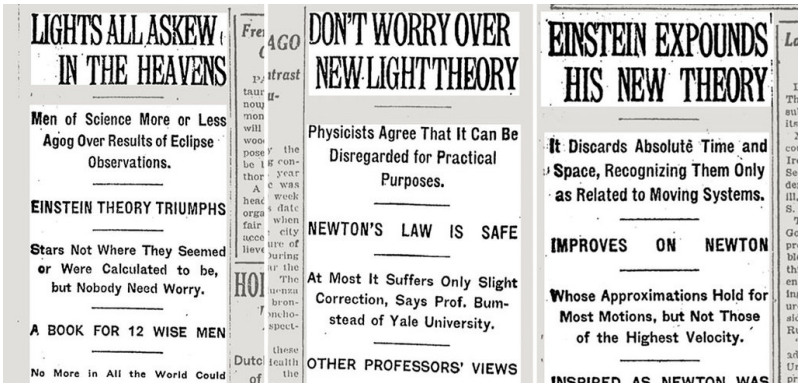

Figure 2.11 – Article headlines on covers of the New York Times from Nov. 10, 1919, left; Nov. 16, 1919, center; and Dec. 3, 1919 (from a review in Roston 2015).

measured by the SDSS-III/BOSS survey (Bautista *et al.* 2017; Busca *et al.* 2013; Delubac *et al.* 2015; Slosar *et al.* 2013), providing an accurate distance measurement at large redshift, thus constraining the geometry of the Universe.

QSO-Lyman-α cross-correlation Correlating the transmission in the Lyman-α forest with the position of quasars enables another strong measurement of the BAO scale, imprinted as a through in the cross-correlation function (Font-Ribera *et al.* 2013, 2014).

Tomographic mapping With a high density of forests, it becomes possible to make a three-dimensional map of neutral hydrogen in the IGM (Bautista *et al.* 2017; Lee *et al.* 2014a,b, 2016).

2.3 Gravitational lensing

Observation by Arthur Eddington of the deflection of light from nearby stars by the Sun during the 1919 solar eclipse brought Einstein's theory to fame by offering one of its first observational confirmation (see covers of the NY Times on figure 2.11). General relativity predicts that matter bends space-time, thus warping geodesics followed by photons. In other words, sufficiently large clumps of matter can focus diverging rays of light just like an optical lens.

Gravitational lensing has become a major tool in astronomy and cosmology. A mass passing in front of another background source temporarily increases its luminosity. This effect, called microlensing, can be used to trace small objects in our galaxy, like exoplanets, or dark matter subhalo structures (for statistical microlensing, see, for instance, Cyr-Racine *et al.* 2016). But it can also be used on much greater scales: clusters of galaxies strongly distort the images of more distant galaxies forming arcs and multiple images, that can be used to reconstruct the distribution of matter and eventually the mass of the cluster (see figure 2.12). When a variable source such as a quasar aligns with a galaxy or a cluster or galaxies, the light curves of multiple

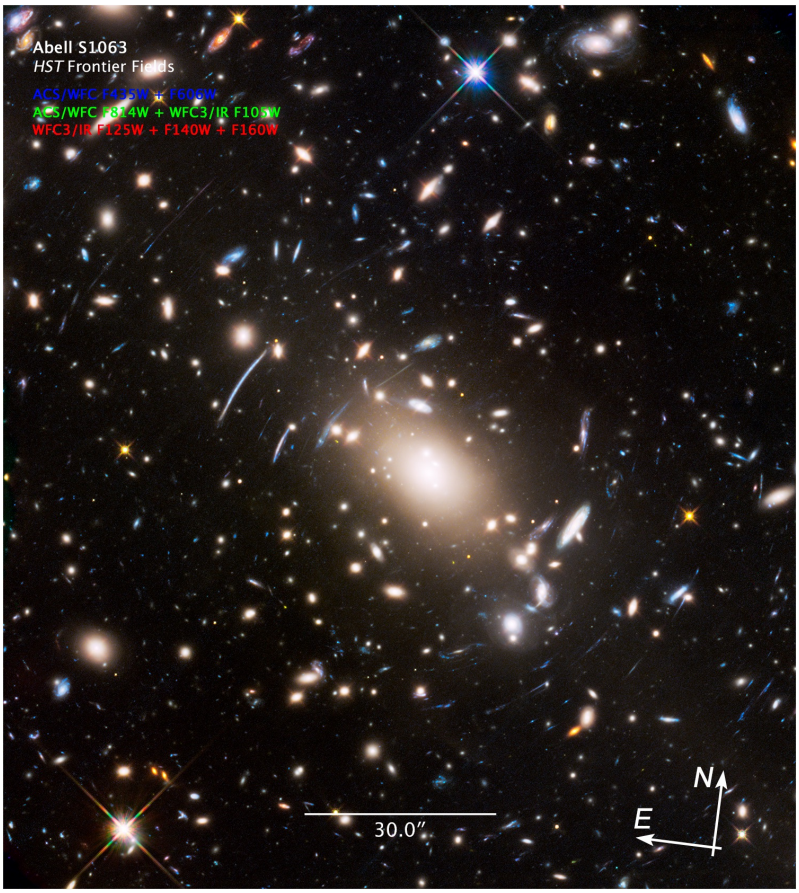

Figure 2.12 – Abell S1063, a galaxy cluster at redshift $z = 0.348$, distorts the images of background galaxies into arcs and enhances them by acting like a magnifying glass. Credit: NASA, ESA, and J. Lotz (STScI)

images will be delayed due to the extra distance to be covered. This effect can be used to constrain the geometry of the Universe and measure the Hubble constant H_0 (for a recent study, see, for instance, Bonvin *et al.* 2017). On the largest scales, the whole distribution of matter acts a distorting lens, twisting and enhancing background galaxies and distorting the trajectories of CMB photons.

2.3.1 Physical principle

This section is based on Bartelmann and Schneider 2001; Hoekstra and Jain 2008; Schneider *et al.* 2006.

2.3.1.1 Single lens

A point-like object of mass M deflects a light-ray by an angle given by

$$\alpha = \frac{4GM}{bc^2} \tag{2.34}$$

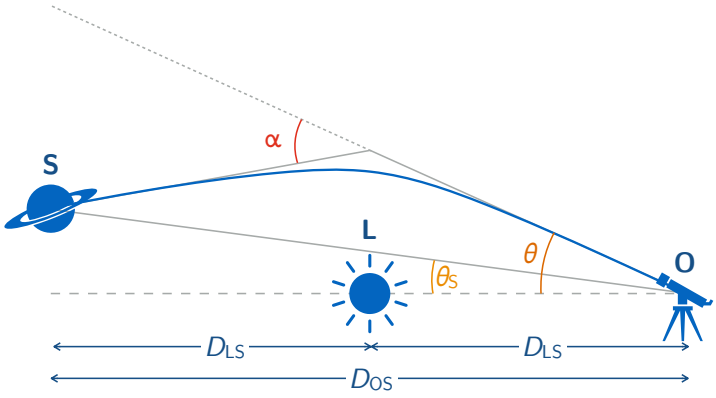

Figure 2.13 – Deflection of a light-ray emitted by a source (S) at angle θ_S by a point-like mass (the lens L) towards the observer (O). The source appears to be at angle θ.

where b is the impact factor[8]. In the limit of small angles, the source, at real angular position θ_S with respect to an arbitrary pole, appears at angle θ given by the *lens equation*,

$$\theta = \theta_S + \frac{D_{LS}}{D_{OS}}\alpha(\theta), \tag{2.35}$$

where D_{LS} and D_{OS} are the distances between the source **S** and, respectively, the lens **L** and the observer **O** (see figure 2.13).

For a lens that is extended in the plane perpendicular to the line of sight but thin along the line of sight, the deflection angle reads

$$\boldsymbol{\alpha}(\boldsymbol{\theta}) = \frac{4G}{c^2}\int \mathrm{d}^2\boldsymbol{\theta}'\,\Sigma(\boldsymbol{\theta}')\frac{\boldsymbol{\theta}-\boldsymbol{\theta}'}{\left|\boldsymbol{\theta}-\boldsymbol{\theta}'\right|^2}, \tag{2.36}$$

where $\Sigma(\boldsymbol{\theta})$ is the *surface mass density*, that is, the density of the lens projected along the line of sight, which reads

$$\Sigma(\boldsymbol{\theta}) = \int \mathrm{d}\chi\,\rho(\chi\boldsymbol{\theta}). \tag{2.37}$$

Finally, the apparent image of the background source, I, is given by a remapping of its intrinsic surface brightness, I_S, according to

$$I(\boldsymbol{\theta}) = I_S(\boldsymbol{\theta}_S[\boldsymbol{\theta}]). \tag{2.38}$$

2.3.1.2 Lensing by the large-scale structure

This section follows the derivation from Schneider *et al.* 1992 *and* Schneider *et al.* 2006.

[8] This can be shown by solving the geodesic equation in the Schwarzschild metric induced by the point-like mass.

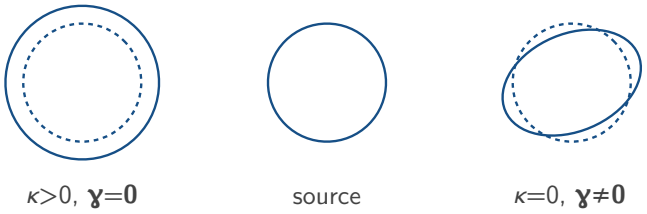

Figure 2.14 – Effects of lensing convergence and shear.

We consider two light rays separated by an angle $\hat{\boldsymbol{\theta}}$ at the observer and their comoving separation vector $\boldsymbol{x}(\hat{\boldsymbol{\theta}}, \chi)$ at comoving distance χ. The geodesic equation (1.2) implies that

$$\frac{\mathrm{d}^2\boldsymbol{x}}{\mathrm{d}\chi^2} + K\boldsymbol{x} = -\frac{2}{c^2}\boldsymbol{\nabla}_\perp \Phi\left(\boldsymbol{x}(\hat{\boldsymbol{\theta}}, \chi), \chi\right) \tag{2.39}$$

where the gravitational potential is evaluated at position $\boldsymbol{x}(\hat{\boldsymbol{\theta}}, \chi)$ and the corresponding lookback time. $\boldsymbol{\nabla}_\perp$ denotes the two-dimensional gradient perpendicular to the line of sight. Denoting the angular separation at comoving distance χ

$$\hat{\boldsymbol{\beta}}(\chi) \equiv \frac{\boldsymbol{x}(\hat{\boldsymbol{\theta}}, \chi)}{f_K(\chi)} \tag{2.40}$$

and the distortion matrix (*i.e.* the jacobian matrix)

$$\mathcal{A}(\hat{\boldsymbol{\theta}}, \chi) \equiv \boldsymbol{\nabla}_{\hat{\boldsymbol{\theta}}}\hat{\boldsymbol{\beta}}, \tag{2.41}$$

then

$$\mathcal{A}(\hat{\boldsymbol{\theta}}, \chi) = \mathbb{1} - \frac{2}{c^2}\int_0^\chi \mathrm{d}\chi' \, \frac{f_K(\chi - \chi')f_K(\chi')}{f_K(\chi)} \boldsymbol{\nabla}_\perp^2 \Phi\left(\boldsymbol{x}(\hat{\boldsymbol{\theta}}, \chi'), \chi'\right) \mathcal{A}(\hat{\boldsymbol{\theta}}, \chi'), \tag{2.42}$$

where the right-hand side involves the two-dimensional hessian matrix of the gravitational potential. In the regime of *weak lensing*, we can evaluate the derivatives of the gravitational potential along the unperturbed ray for which $\boldsymbol{x}(\hat{\boldsymbol{\theta}}, \chi) = f_K(\chi)\hat{\boldsymbol{\theta}}$. This is known as the *Born approximation*. The distortion matrix becomes

$$\mathcal{A}(\hat{\boldsymbol{\theta}}, \chi) = \mathbb{1} - \boldsymbol{\nabla}_{\hat{\boldsymbol{\theta}}}\phi \tag{2.43}$$

where we have introduced the *lensing potential* given by

$$\phi(\hat{\boldsymbol{\theta}}, \chi) = \frac{2}{c^2}\int_0^\chi \mathrm{d}\chi' \, \frac{f_K(\chi - \chi')}{f_K(\chi')f_K(\chi)} \Phi\left(f_K(\chi')\hat{\boldsymbol{\theta}}, \chi'\right). \tag{2.44}$$

We further decompose this matrix into

$$\mathcal{A}(\hat{\boldsymbol{\theta}}, \chi) = \begin{pmatrix} 1 - \kappa - \gamma_1 & -\gamma_2 \\ -\gamma_2 & 1 - \kappa + \gamma_1 \end{pmatrix}, \tag{2.45}$$

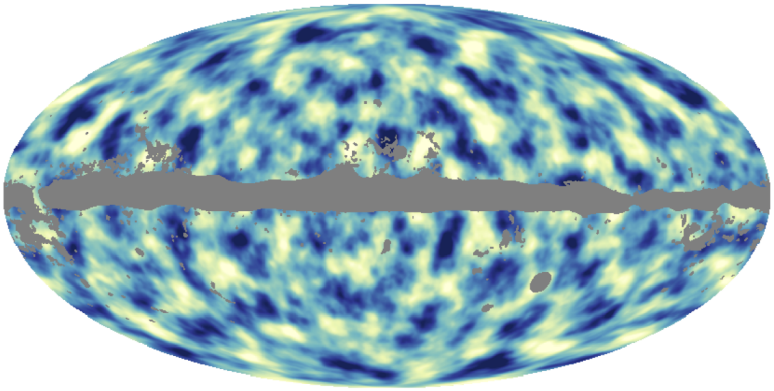

Figure 2.15 – Map of the CMB lensing potential measured by Planck in galactic coordinates (Planck Collaboration *et al.* 2014b).

defining the lensing convergence κ, a scalar field, and the complex shear $\boldsymbol{\gamma} = \gamma_1 + i\gamma_2$, a spin-2 field (see figure 2.14). Making use of the Poisson equation, the convergence can be written as a projection of the matter (over)density field as

$$\kappa(\hat{\boldsymbol{\theta}}, \chi) = \frac{\nabla^2 \phi}{2} = \frac{3}{2}\left(\frac{H_0}{c}\right)^2 \Omega_{\mathrm{m}}^0 \int_0^{\chi} \mathrm{d}\chi' \, \frac{f_K(\chi - \chi') f_K(\chi')}{f_K(\chi)} \frac{\delta(f_K(\chi')\hat{\boldsymbol{\theta}}, \chi')}{a(\chi')}. \quad (2.46)$$

Finally, the apparent surface brightness of a source is related to the intrinsic one by

$$I = \mu I_S \quad \text{with} \quad \mu = \frac{1}{|\mathcal{A}|} = \frac{1}{(1-\kappa)^2 - |\boldsymbol{\gamma}|^2} \approx 1 - 2\kappa \quad (2.47)$$

where the approximation is that of the weak lensing regime.

2.3.2 Lensing of the cosmic microwave background

Photons of the cosmic microwave background are deflected by large-scale structures on their way to our telescopes. As a consequence, the anisotropies of CMB temperature are blurred, as if seen through a glass brick of inhomogeneous width. While a small source of complications for CMB temperature studies, this deflection can be mathematically recovered. The output is a measure of the projected mass of all matter that stands between the last scattering surface and us.

2.3.2.1 Effects of CMB lensing

Typical structures at large redshift induce a deflection of CMB photons of order $\beta = 4GM \Big/ bc^2 \approx 0.3'$. They undergo of order 50 such deflections, resulting in an r.m.s. deflection of order $\sqrt{50} \times \beta \approx 2'$. The observed temperature is thus remapped according to

$$T_{\mathrm{obs}}(\hat{\boldsymbol{n}}) = T(\hat{\boldsymbol{n}} + \boldsymbol{\nabla}\phi(\hat{\boldsymbol{n}})), \quad (2.48)$$

inducing coherent displacement on patches of scale $\sim 2°$.

On the one hand, this induces a smearing of the peaks of the temperature power spectrum and a correlation of spherical harmonics coefficients that are otherwise uncorrelated. On the other hand, this correlation is used to reconstruct the lensing potential (see Okamoto and Hu 2003 and section 2.3.2.2), which is an extraordinary probe of all matter between the last scattering surface and us. The lensing potential, shown in figure 2.15, has been measured on the full sky (except in the galactic plane) by the Planck collaboration (Planck Collaboration *et al.* 2014b) and on smaller patches, but with higher resolution, by ground-based experiments.

Both temperature and polarization are affected by lensing. In polarization, lensing of E-modes produce B-mode patterns that dominate the signal over potential primordial B-modes at multipoles higher than $\ell \gtrsim 100$ (see the right plot in figure 2.6). While we shall see how the lensing signal is estimated with temperature anisotropies, the formalism is quite similar for polarization.

2.3.2.2 Estimation of the lensing potential

Gravitational lensing of the CMB induces a departure of temperature from a purely gaussian statistics, such that temperature contrast multipole coefficients $a_{\ell m}$ become correlated. Decomposing the temperature in spherical harmonics,

$$T(\hat{\boldsymbol{n}}) = \sum_{\ell=0}^{\infty} \sum_{m=-\ell}^{\ell} T_{\ell m} Y_{\ell m}(\hat{\boldsymbol{n}}), \tag{2.49}$$

the covariance of temperature spherical harmonic coefficient, where the average is over CMB realizations for a fixed lensing field, is (Hanson *et al.* 2011; Okamoto and Hu 2003; Planck Collaboration *et al.* 2014b)

$$\left\langle T_{\ell m} T_{\ell' m'} \right\rangle = \underbrace{C_\ell^{TT} \delta_{\ell\ell'} \delta_{mm'}}_{\text{Gaussian part}} + \underbrace{\sum_{LM} (-1)^M \begin{pmatrix} \ell & \ell' & L \\ m & m' & M \end{pmatrix} W^{\phi}_{\ell\ell' L} \phi_{LM}}_{\text{lensing distortion}}, \tag{2.50}$$

where the term in parenthesis is the Wigner-3j symbol and $W^{\phi}_{\ell\ell' L}$ is a weight function that involves linear combinations of the lensed CMB temperature power spectrum multipoles. Here, we assume that the lensing field is gaussian distributed as well, such that lensed temperature spherical harmonics coefficients are gaussian too. An estimator of the lensing potential spherical harmonic coefficients is given by

$$\hat{\phi}_{LM} = A_L \sum_{\ell_1 m 1} \sum_{\ell_2 m_2} (-1)^M \begin{pmatrix} \ell_1 & \ell_2 & L \\ m_1 & m_2 & -M \end{pmatrix} g_{\ell_1 \ell_2}(L) T_{\ell_1 m_1} T_{\ell_2 m_2}, \tag{2.51}$$

where A_L is a normalization and $g_{\ell_1 \ell_2}(L)$ are weights. They are determined by imposing that the estimator is unbiased, *i.e.* $\left\langle \hat{\phi}_{LM} \right\rangle = \phi_{LM}$ and by minimizing the

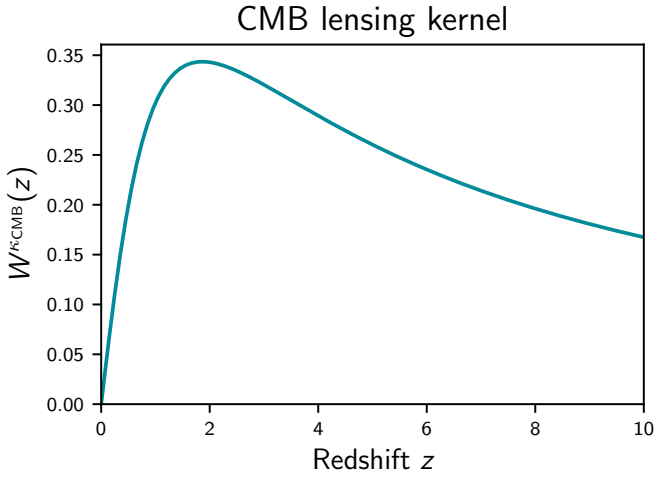

Figure 2.16 – Kernel function of CMB lensing.

variance of the estimator with respect to the weights $g_{\ell_1\ell_2}(L)$ (see Okamoto and Hu 2003, for the detailed calculations).

2.3.2.3 CMB lensing power spectrum

CMB photons are deflected by all matter between the last-scattering surface and the observer. Therefore, the convergence of CMB photons is simply

$$\kappa_{\rm CMB}(\hat{\boldsymbol{\theta}}) = \kappa(\hat{\boldsymbol{\theta}}, \chi_*) \tag{2.52}$$

where $\chi_* = \chi(z_* \approx 1\,090)$ is the comoving distance to the last scattering surface. For flat spatial sections, we can write

$$\kappa_{\rm CMB}(\hat{\boldsymbol{\theta}}) = \int_0^{z_*} W^{\kappa_{\rm CMB}}(z)\delta(\chi(z)\hat{\boldsymbol{\theta}}, z) \tag{2.53}$$

where

$$W^{\kappa_{\rm CMB}}(z) = \frac{3}{2}\frac{\Omega_{\rm m}^0 H_0^2}{c}\frac{(1+z)}{H(z)}\chi(z)\left(1 - \frac{\chi(z)}{\chi(z_*)}\right). \tag{2.54}$$

This broad kernel peaks at $z \sim 2$ (see figure 2.16).

The power spectrum of its anisotropies, shown in figure 2.17, has rapidly gained interest as a complementary source of information for cosmological constraints, since it is very sensitive to the matter density parameter $\Omega_{\rm m}$ and the amplitude of the matter power spectrum $A_{\rm s}$ or σ_8. At very large multipoles, the Born approximation fails and the lensing power spectrum is affected by the non-linearities of the matter density field (Calabrese *et al.* 2015; Fabbian *et al.* 2017). Ray tracing through N-body simulations can be used to improve predictions at small scale or for strong lenses (Hilbert *et al.* 2009).

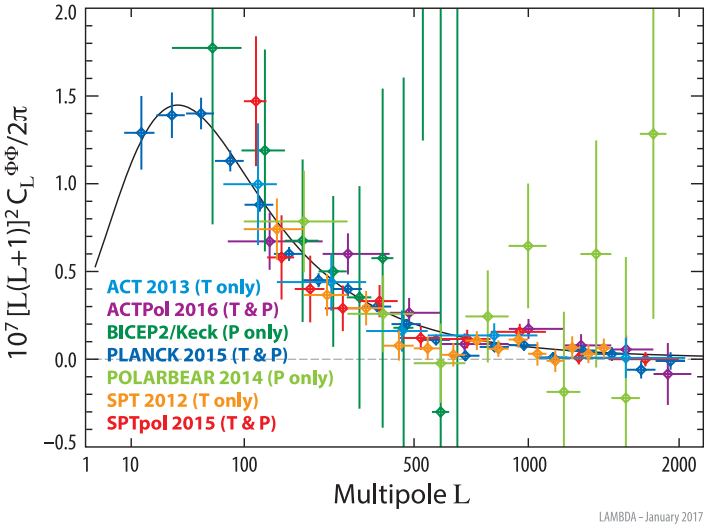

Figure 2.17 – Power spectrum of the CMB lensing potential measured by contemporary experiments, from temperature (T) and/or polarization (P). Figure from https://lambda.gsfc.nasa.gov/.

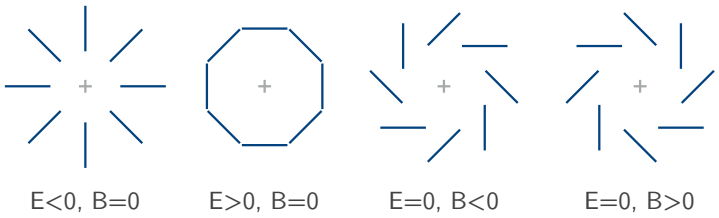

Figure 2.18 – Decomposition of polarization or cosmic shear into E- and B-modes.

2.3.3 Cosmic shear

In this section, we shall briefly review weak gravitational lensing of galaxy images. Though not used in the work presented in this thesis, this probe is gaining momentum as a way to map mass in the Universe and studying dark energy. Ongoing lensing surveys, such as DES (Dark Energy Survey, Dark Energy Survey Collaboration *et al.* 2016), KiDS (Kilo-Degree Survey, Jong *et al.* 2013) and CFHT (Canada-France-Hawaii Telescope, Boulade *et al.* 2002), are delivering very encouraging results for the next generation of very large surveys such as LSST(Large Synoptic Survey Telescope, LSST Science Collaborations and LSST Project *et al.* 2009), Euclid (Refregier *et al.* 2010) and WFIRST (Wide Field Infrared Survey, Spergel *et al.* 2013). In particular, galaxy weak lensing is successfully being used in ongoing joint analyses, as we shall see in chapter 4.

Imagine the circle in figure 2.14 is the contour of a galaxy[9]. Lensing by foreground matter, *i.e.* between the galaxy and us, implies a distorsion and a magnification of its

[9]Note that this very notion is absolutely non-trivial: a galaxy is an extended object with a profile, the limits of which cannot be unambiguously and universally defined, *i.e.* an arbitrary (but motivated) choice has to be made.

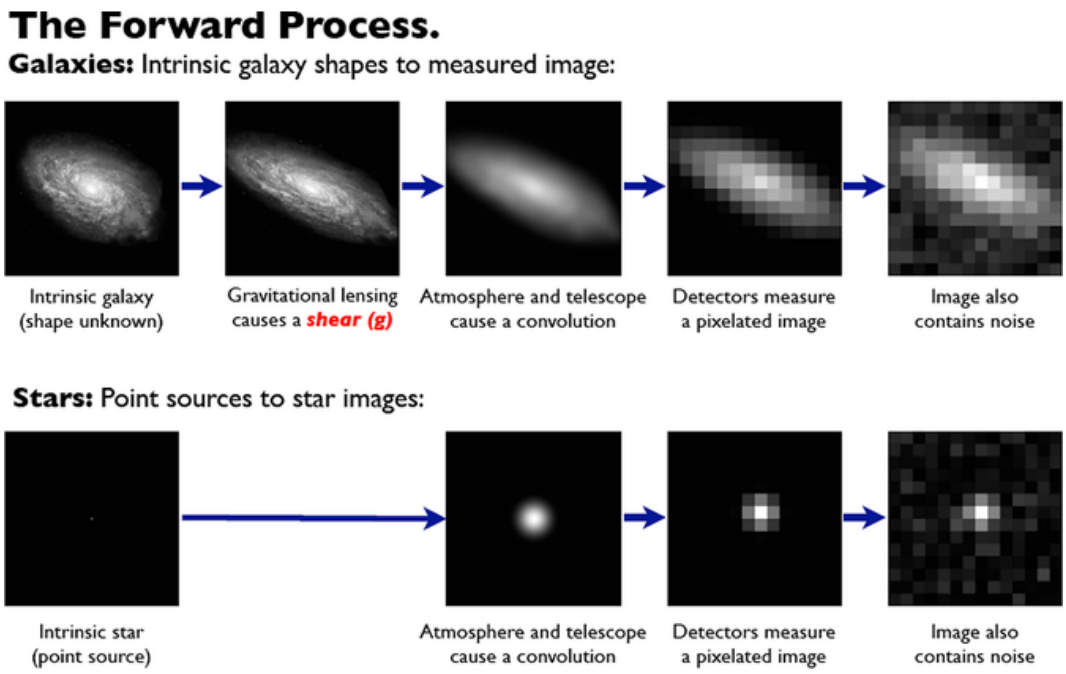

Figure 2.19 – The sheared image of a resolved galaxy is first blurred by the atmosphere and then pixelized by the detector. Faint galaxies may be difficult to separate from the detector noise, which includes photon noise, but also other, more complicated, sources of noise. Figure from Bridle *et al.* 2009.

apparent shape and size, due to, respectively, shear and convergence of the integrated (foreground) matter density field. Galaxies are not perfect spheres, but are more or less elliptical, making it possible to define an orientation for each galaxy (that of the major axis, for instance). On average, is a given patch of the sky, there should be no preferred direction; however, coherent lensing by foreground matter can result in a locally favoured orientation, producing patterns similar to that of CMB polarization (since shear is a spin-2 field, see figure 2.18). In particular, positive (respectively negative) E-modes surround overdensities (respectively underdensities), while B-modes are not produced by gravitational lensing and may therefore be measured to test for systematics.

Once the sky has been imaged in multiple bands, the process schematically goes as follows (Hoekstra and Jain 2008):

1. A catalog of sufficiently bright galaxies and stars is built. The fluxes of galaxies in different bands is used to infer photometric redshifts, potentially using a machine learning-based algorithm calibrated on external spectroscopic data.

2. Stars are used to measure the anisotropic, time- and color-dependent point spread function (PSF) of the telescope and the atmosphere.

3. Shapes or ellipticities of galaxies are measured and somehow deconvolved from the PSF (see figure 2.19).

4. Local averages are used to produce tomographic shear maps. Their power spectrum can be measured and compared to theoretical expectations.

While apparently simple, each of these steps requires dealing with various kinds of systematic effects that can propagate in subsequent steps, down to the estimation of cosmological parameter.

2.4 Comparison of cosmological probes

The leitmotiv of this thesis is that advances in cosmology can be made with combinations of various cosmological probes, taking advantage of their different dependences on the matter density field. Therefore, it seems useful, at this point, to sketch a comparison of the probes mentioned in this chapter, in terms of redshift and scale ranges, nature and location of what is observed, and constraining power on cosmological models.

Let us briefly mention two other probes of anisotropies in the Universe, as they are of interest for cross-correlation studies.

The cosmic infrared background The CIB is a relic radiation composed of the combined thermal emission of dust within early, star-forming galaxies at redshift $z \sim 1-2$ (Planck Collaboration *et al.* 2014f). It is visible at frequencies of order 1 THz (see the bump in figure 4.6), superimposed over the high frequency tail of the CMB, but separating it from other components is a challenging task. The redshift dependence of the CIB contain valuable information about the history of star formation, while its anisotropies can inform us on galaxy formation.

21 cm intensity mapping In the near future, arrays of radio telescopes will map the intensity of the redshifted 21 cm emission line of neutral atomic hydrogen (HI) over a large volume. HI clouds harboured by galaxies are the progenitors for star forming regions. Only the brightest galaxies will be individually detected, however, the total emission of hundreds of clouds can be mapped over the sky within thin redshift bins, a technique called *intensity mapping*. This technique can be applied up to very high redshifts (up to $z \sim 200$, according to Furlanetto *et al.* 2006) and is therefore expected to provide new insight on epoch of reionization.

In table 2.1, we enumerate some key comparable characteristics for each of the aforementioned cosmological probes. Of course, such an exercise requires some approximations, but the goal is to try and demonstrate that these observables offer of variety of filters to look at the Universe, and to capture their main differences and complementarities.

Table 2.1 – Comparison of a selection of cosmological probes. For each probe, we estimate the redshift and scale ranges probed, and we precise the measured quantity, the physical nature and location of its source, and finally the cosmological parameters it constrains the most remarkably.

Probe	Redshift	Scale (k in $h\,\mathrm{Mpc}^{-1}$)	Observable	Source	Location	Cosmological phenomena	Associated parameters
CMB temperature	1 090	10^{-3}-10^{-1}	Temperature anisotropies	Density of photon-baryon plasma	Everywhere	Primordial power spectrum, BAO, reionization	A_s, n_s, ω_c, ω_b, τ, H_0
CMB polarization	1 090 (+ reionization bump)	10^{-3}-10^{-1}	Polarization anisotropies	Velocity of photon-baryon plasma	Everywhere	Primordial power spectrum, BAO, reionization, tensor modes	τ, r[a]
CMB lensing	0-1 090 with a peak at $z \sim 2$	$\sim 10^{-2} - 10^{-1}$, depends on resolution	Lensing convergence	All matter	Mostly DM haloes	Integrated mass distribution	Ω_m
Optical galaxy/QSO clustering (including BAO & RSD)	0-5	10^{-2}-0.5	Positions in 3D	Stellar light	Mostly DM haloes	Mass distribution, geometry, growth of structures	Ω_k (or $\Omega_\Lambda/\Omega_\mathrm{m}$), f, σ_8, w, m_ν
SZ effect	0-2	Depends on resolution	Compton-y parameter	Free electrons	Clusters	Abundance of baryons, cluster number counts (growth of structures)	Ω_b, f_e[b]
Lyman-α forest (including BAO)	2-5	0.1-10	Absorption of QSO spectra	Neutral hydrogen	IGM	Reionization, IGM physics, geometry	Ω_k (or $\Omega_\Lambda/\Omega_\mathrm{m}$), m_ν
Galaxy lensing	0-3	10^{-2}-1	Galaxy shapes	All matter	Mostly DM haloes	Tomographic mass distribution	Ω_m, w (and w_a[c])
CIB	1-4 with a peak at $z \sim 2$	0.04-0.3 for Planck	Thermal dust emission	Dust	Star-forming galaxies	Star formation history, early structure formation	ρ_SFR[d]
21 cm intensity	0-50	Depend on redshift, up to ultra-large scales	Intensity of HI emission	Neutral hydrogen	IGM and primordial galaxies	BAO, reionization and cosmic dawn	τ

[a] r is the ratio of the amplitudes of the scalar and tensor primordial power spectra.
[b] f_e is the free electron fraction.
[c] w_a is used here to signify any parametrization of the time dependence of the dark energy equation of state.
[d] ρ_SFR is the star formation rate density.

CHAPTER 3

Experiments: Planck and SDSS-III/BOSS

Contents

3.1 The Planck satellite 69
3.1.1 Science goals 69
3.1.2 Satellite and instruments 70
3.1.3 Data processing 73
3.1.4 Main science results 79
3.2 SDSS-III/BOSS 80
3.2.1 The Sloan Digital Sky Survey 80
3.2.2 The instruments 82
3.2.3 Target selection 83
3.2.4 Observing strategy 86
3.2.5 Data reduction 87
3.2.6 Main science results 87

3.1 The Planck satellite

3.1.1 Science goals

The Planck mission's[1] objectives include (Planck Collaboration 2006):

[1] This section is based on publications of the Planck Collaboration, as well as the official ESA website at http://sci.esa.int/planck/ and web-based explanatory supplements at https://wiki.cosmos.esa.int/planckpla2015. All images shown here come from one of these websites, unless stated otherwise.

1. Mapping anisotropies in the CMB temperature down to the cosmic variance limit for scales greater than 10 arcminutes.

2. Testing inflation models via a precise measurement of the spectral index, $n_{\rm s}$, of the primordial power spectrum and potential primordial B-modes in anisotropies of the CMB polarization.

3. Looking for evidence of an early phase transition, that could produce topological defects such as cosmic strings.

4. Measuring the TT, TE and EE power spectra to greatly improved precision to derive constraints on cosmological, astrophysical and physical parameters. In particular, σ_8 and $\Omega_{\rm m}$ constraints shall be compared to those derived from galaxy photometric and spectroscopic surveys.

5. Cataloguing thousands of clusters detected by their tSZ effect and comparing the signals to X-ray and weak lensing cluster observations.

3.1.2 Satellite and instruments

3.1.2.1 Spacecraft

The spacecraft is 4.2 m high and 4.2 m large and weighs about 2 000 kg. It is made up of two major modules (Tauber *et al.* 2010b):

The service module comprises the power generator (solar panels), orbit and position controls, the on-board computer (to store and manage raw data, receive and execute commands) and the radio antenna for communications with the ground station.

The payload module comprises the telescope, the focal plane with the two instruments (detailed below) and the cooling and cryogenic systems.

3.1.2.2 Instruments

3.1.2.2.1 The telescope

The telescope (Tauber *et al.* 2010a) is an offset Gregorian combination with a parabolic, 1.5 m primary and an ellipsoidal, 1 m secondary reflector. The central line-of-sight makes an angle of 85° with the spacecraft's rotational axis. A baffle around the mirrors protects the optical system from ghost lights.

3.1.2.2.2 The cooling unit

The cryogenic architecture of Planck is defined by the different temperature needs of the different parts of the spacecraft. The service module contains the warm electronics, that work at 300 K, and is heated by the Sun. However, the elements

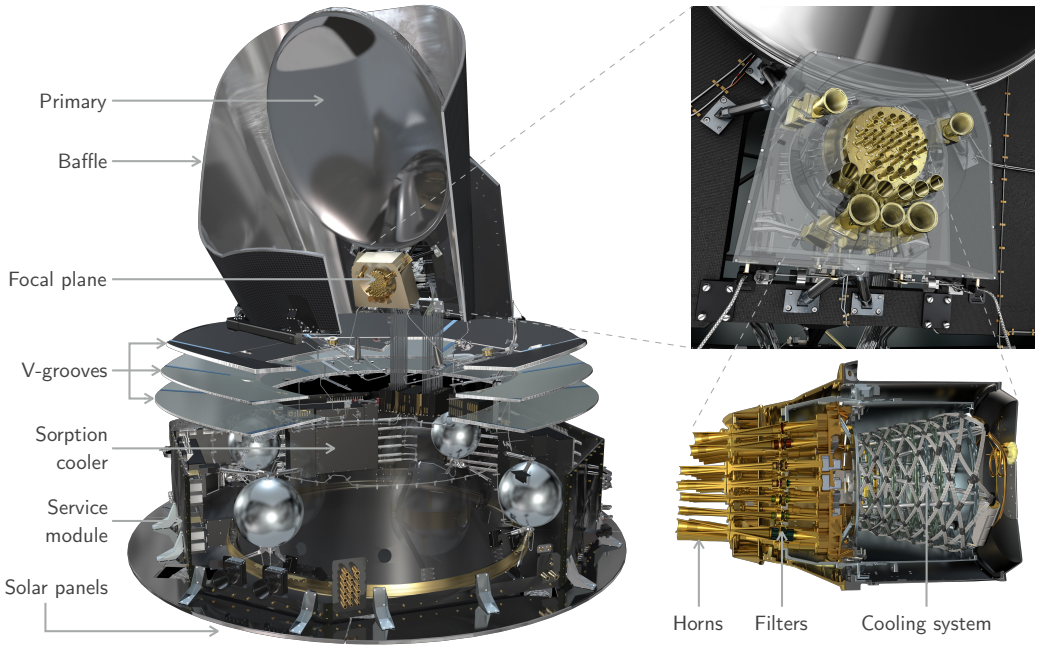

Figure 3.1 – 3D rendering of the Planck satellite (left), focal plane (top right) and HFI instrument (bottom right).

of the payload module, and in particular the detectors, require lower temperatures. Three conical "V-grooves", highly coupled to the cold external environment, are placed between the two modules and isolate them thermally and radiatively, bringing the payload module down to a temperature of about 40 K.

But the coldest part of the Planck satellite are the sensors which are located at the focal plane and operate at about 100 mK for HFI and 20 K for LFI (the two instruments, presented in the next section). This is necessary to look for 10^{-6}-level anisotropies in a 2.72 K background with a detector noise (detailed in section 3.1.3.2) comparable to the photon shot noise. To reach this temperature, several active cooling units are needed: (i) six compressors (the "sorption cooler") perform Joule-Thomson expansion of liquid hydrogen at 20 K, (ii) a mechanical pump performs Joule-Thomson expansion of liquid helium at 4 K, and (iii) an open ^{3}He/^{4}He dilution refrigerator decreases temperature of HFI's bolometers down to 100 mK.

3.1.2.2.3 Detectors

Reflectors guide and focus light towards the focal plane where the detectors are placed. Both instruments (LFI and HFI, see below) consist in a set of detectors composed of aluminium, gold-plated and corrugated horns that shape and focus light towards the sensors per se. HFI detectors are made of three back-to-back such horns while LFI has only one horn per detector. Filters that select spectral bandwidths are placed after the first horn and the diameters of the horns are adjusted to the wavelengths of the filters so as to physically select electromagnetic modes. The exact

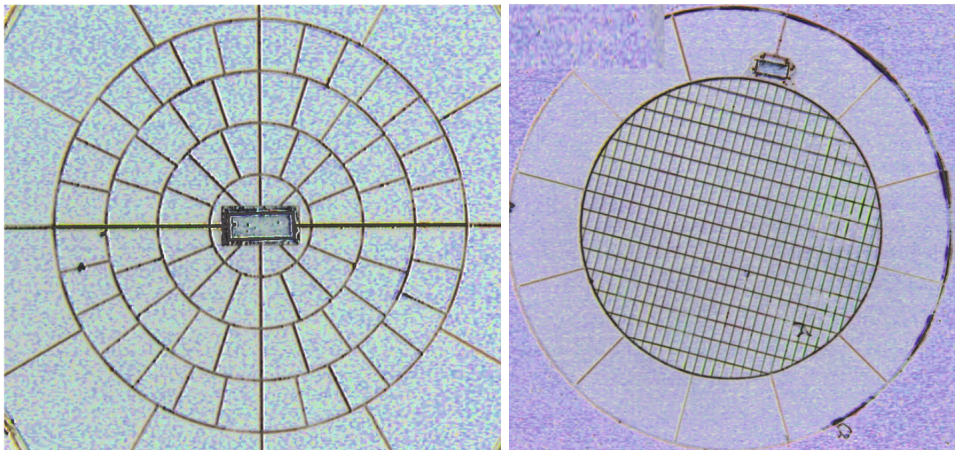

Figure 3.2 – Spider Web Bolometer (left) at 143 GHz and Polarisation Sensitive Bolometer (right) at 217 GHz. The semi-conducting thermometers are visible at the center of SWBs and at the top of the PSBs.

shape of the horns is optimized numerically by electromagnetic simulations.

LFI The Low Frequency Instrument (Bersanelli *et al.* 2010) is made of 22 radiometers that observe the CMB temperature and polarization at 30, 44 and 70 GHz.

HFI The High Frequency Instrument (Lamarre *et al.* 2010) is made of 32 Polarisation Sensitive Bolometers (PSBs) and 20 Spider Web Bolometers (SWBs) that observe the CMB at 100, 143, 217, 353, 545 and 857 GHz (pictures of the bolometers are shown in figure 3.2).

HFI horns and bolometers are placed at the center of the focal plane, surrounded by LFI detectors, as can be see on figures 3.1 and 3.3.

Bolometers are sensors that measure the power P of incident electromagnetic radiation. They consist of an absorber of heat capacity C, connected to a thermal reservoir with a thermal conductance G, and thermally coupled to a resistive thermometer. The temperature of the absorber and the thermometer vary as $\Delta T = P/G$ when radiation is absorbed. This shifts the resistivity of the thermometer, measured by the modification of the electric current that goes through it. The time constant $\tau \equiv C/G$ gives the sensitivity of the detector. In Planck, the absorber is a thin metallic grid (to decrease absorption of cosmic rays) that is designed to match the vacuum impedance and maximize absorption. The PSBs of HFI consist of two perpendicular metallic grids that absorb orthogonal components of the electromagnetic radiation while SWB have a spider-web grid that absorbs all directions of polarization.

Planck bolometers receive incoming radiation that correspond to spectral windows of the CMB black-body radiation. Its average spectral radiance, *i.e.* the power per unit solid angle and per unit of area normal to the propagation, denoted $B_\nu(T)$, is given by equation (2.1). The incident power on the bolometers is obtained by

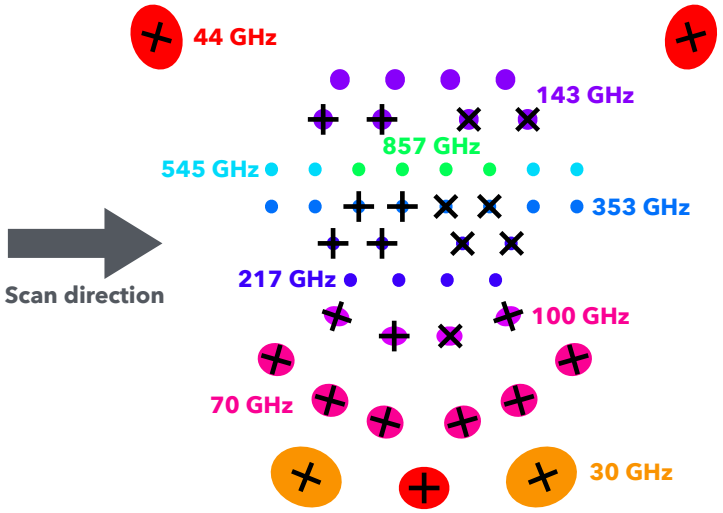

Figure 3.3 – Arrangement of LFI and HFI detectors on the focal plane. Black crosses indicate the orientation of polarization-sensitive detectors. The arrow indicates the direction of scanning as seen from behind the detectors.

successively integrating this spectral radiance over the lobe of the detector (solid angle), area of the primary mirror and spectral bandwidth of the filters. Local thermal fluctuations induce a shift in the spectral radiance, given, to first order, by

$$\Delta B_\nu \approx \frac{\partial B_\nu(T)}{\partial T} \Delta T. \tag{3.1}$$

A shift in temperature thus results in a variation of the incident power absorbed by the bolometers, which can be measured. Converting this power (in watts) into an absolute temperature (in kelvins) requires proper calibration (see section 3.1.3.3).

3.1.2.3 Launch and orbit

Planck was launched on an Ariane 5 rocket, together with the Herschel satellite (Pilbratt *et al.* 2010), on 14 May 2009, at 13:12:02 UTC. It was placed at the Lagrange point (L2) of the Sun-Earth system, about 1.5 million kilometers from Earth. The Planck satellite revolved around its axis, which is always directed towards the Sun (with a small cycloid precession), once per minute (this stabilizes its motion by gyroscopic effect), scanning the sky in rings that cross at the ecliptic poles. Within two-and-a-half years of operation, it performed five full-sky scans.

3.1.3 Data processing

3.1.3.1 TOI processing

The signal coming out of the detectors is first highly amplified by a factor 10^3, before being sampled at high frequency (7 200 Hz) and digitized. This produces time-ordered

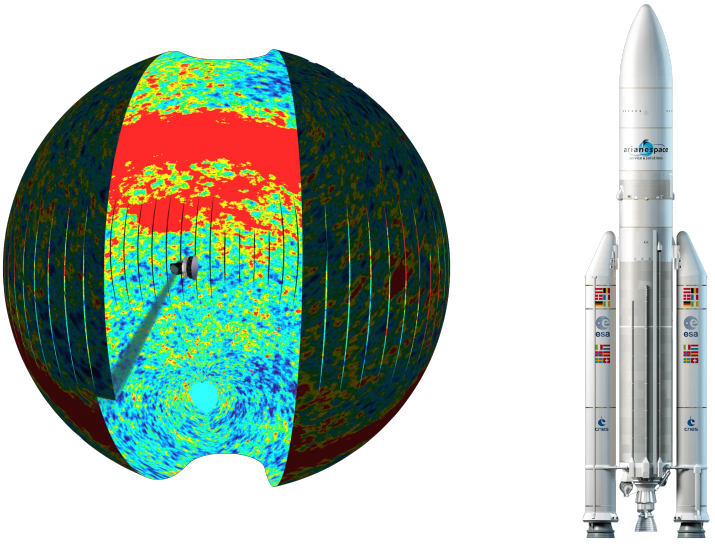

Figure 3.4 – Planck spun around its Sun-pointing axis, such that it observes rings that slowly shift. Within six months, the full sky is covered. Also, an artistic rendering of an Ariane 5 rocket.

information (TOI) data that is transferred along with position data (from the star tracker) to a ground station where data processing begins. We summarize the different steps here:

1. Demodulation of the bolometer power supply frequency;
2. Removal of glitches produced by cosmic rays and flagging of polluted data segments;
3. Correction of the non-linear gain of detectors;
4. Decorrelation of slow thermal variations of the focal plane;
5. Removal of spectral lines created by the 4 K cooler;
6. Deconvolution of the temporal response of bolometers;
7. Bad sample flagging (unstable pointing, cosmic ray glitches, Solar system objects).

3.1.3.2 Noise

Experimental noise has several origins:

- Photon shot noise, due to the intrinsic randomness in the number of photons captured by the detector (modelled by a Poisson law);
- Phonon noise, due to the thermal agitation of the detectors' components;
- Johnson noise, due to the thermal agitation of charge carriers in the electronics;
- Electronic noise, due to fluctuations in the voltage applied to the thermometers;
- Residuals of the 4 K cooler lines;
- Residuals of cosmic ray deglitching;
- Residuals of slow temperature variations of the 100 mK bath.

While photon and phonon noises are white, the last one has a frequency dependence

that goes as $1/f$. For this reason, the current applied to bolometers is alternative, in order to shift the signal to higher frequencies. $1/f$ noise can then be filtered out by a low-pass filter.

3.1.3.3 Optical beam and calibration

The part of the sky observed by a single detector at a given time is characterized by a window function, or *beam*, that depends on the optical system (reflectors) and the transfer function of the detector. Its shape is estimated by observing bright, known sources such as planets: observations of Mars are used to estimate single beams, and observations of Jupiter are used to reconstruct the focal plane. Non-optical contributions are evaluated and deconvolved iteratively from the TOI. Single beams are known to be asymmetric and display non-gaussian tails (side lobes).

Absolute calibration of the TOI is performed by adjusting the data to the known dipole due to the motion of the Sun with respect to the rest frame of the CMB and the time-dependent dipole due to the peculiar motion of the satellite around the Sun. The comparison of the two enables correction of slow variations of the detectors' gains. The two highest frequencies, where CMB is subdominant, use flux measurements of Uranus and Neptune with models of their atmospheres.

3.1.3.4 Map making and component separation

TOI data is then projected to build frequency maps. First, pixel rings are constructed from TOI and pointing information. Then, these rings are combined, which requires adjusting an offset between adjacent rings to correct for the slow temperature drift due to $1/f$ noise, a process called *destriping*. Nine frequency maps in temperature and polarization, shown in figure 3.5, are built independently.

The next step of the analysis is a crucial one. The CMB radiation must be separated from Galactic and extragalactic, astrophysical foreground emissions. These include, for Galactic components, thermal and spinning dust emissions, synchrotron emission, free-free emission and carbon monoxide line emission (which pollutes the 100 GHz map). First, noise is estimated in frequency maps by a series of jackknives, separating data in half-rings (for a fixed pointing, each ring is observed twice), in surveys (6 months full-sky observation) and finally between detectors. Then, masks are built to exclude bright point sources and the Galactic disk.

Then, two routes are possible. They consist of (i) producing cleaned maps of the CMB and measuring their power spectra, or (ii) performing the separation at the power-spectrum level.

Several algorithms were developed for the first approach, all of which exploit the fact that different components have different electromagnetic spectra (see figure 3.7).

NILC The Needlet Internal Linear Combination algorithm performs a minimum-variance linear combination of frequency maps in needlet space (highly localized

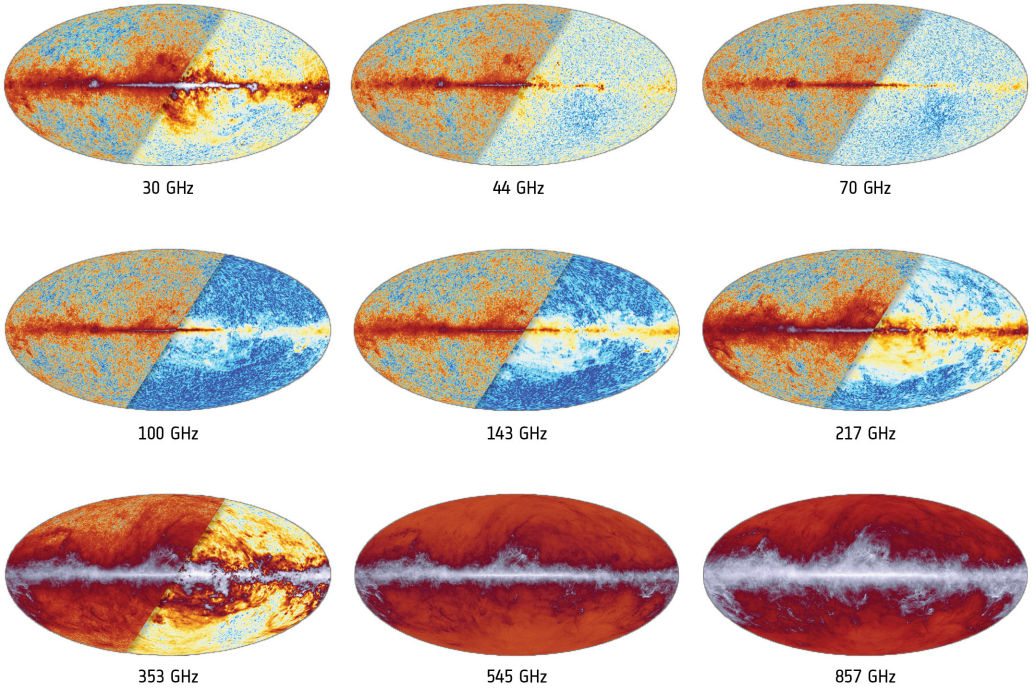

Figure 3.5 – Frequency maps from Planck 2015 data in Galactic coordinates (Planck Collaboration *et al.* 2016b) with temperature on the left and polarization (Stokes parameter I) on the right. Galactic dust emission dominates the signal in the two highest frequencies maps.

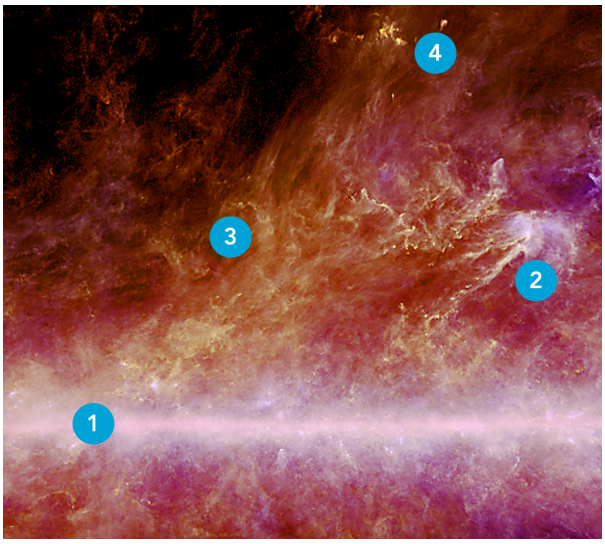

Figure 3.6 – Zoom on the dust emission near the Galactic plane. Several structures are visible: (i) the Galactic plane contains numerous stars, (ii) the warm, filamentary, rho-Ophiuchi complex, a star-forming region, (iii) the Aquila Rift and (iv) a dense and cold molecular cloud. These complex structures must be properly removed from the CMB prior to any cosmological interpretation of the observations.

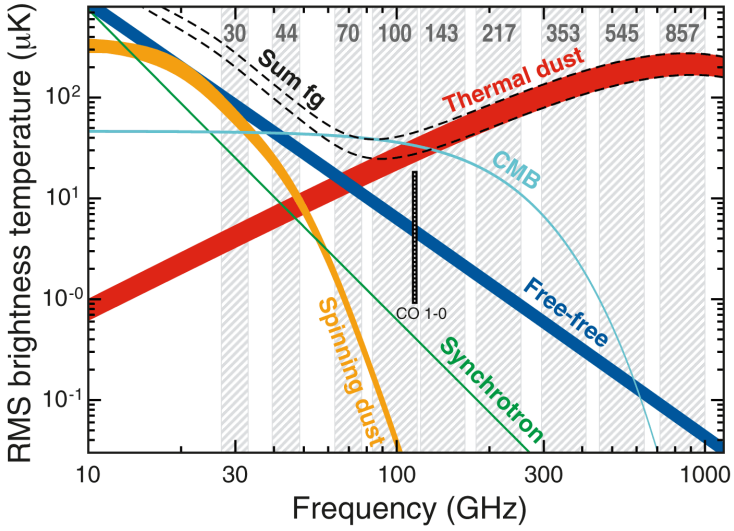

Figure 3.7 – Spectral dependence of anisotropies in the CMB compared to that of the main astrophysical foregrounds. Figure from Planck Collaboration *et al.* 2016c.

radial polynomials on the sphere) to project out the CMB component, knowing its spectral dependence.

SEVEM The Spectral Estimation Via Expectation Maximization algorithm performs differences of neighbor frequency maps and removes a linear combination of those to individual frequency maps. In practice, the output CMB map uses only the 143 and 217 GHz frequencies.

SMICA The Spectral Matching Independent Component Analysis algorithm performs a linear combination of frequency maps in harmonics space, using multipole-dependent weights to separate all components (supposing they are uncorrelated).

Commander-Ruler `Commander` is a Bayesian algorithm that operates in pixel space at low resolution ($N_{\rm side} = 256$) and performs Gibbs sampling of a parametric foreground models to evaluate the CMB power spectrum and component maps. Then `Ruler` can be used to evaluate the amplitude of the CMB component with least-squares methods.

The second approach, used to build likelihoods and derive cosmological constraints, removes contributions to the power spectrum from astrophysical foregrounds in order to fully exploit the small-scale signal and control the propagation of errors (Planck Collaboration *et al.* 2016d).

Low ℓ The low-ℓ ($\ell < 30$) approach is based on cleaned CMB maps from `Commander` described in Planck Collaboration *et al.* 2016c. It assumes that the pixel-space signal is Gaussian distributed, with a correlation function determined from the CMB power spectrum $C_\ell^{TT,TE,EE}$ as in equation (2.3), to which astrophysical foregrounds and instrumental noise has been added.

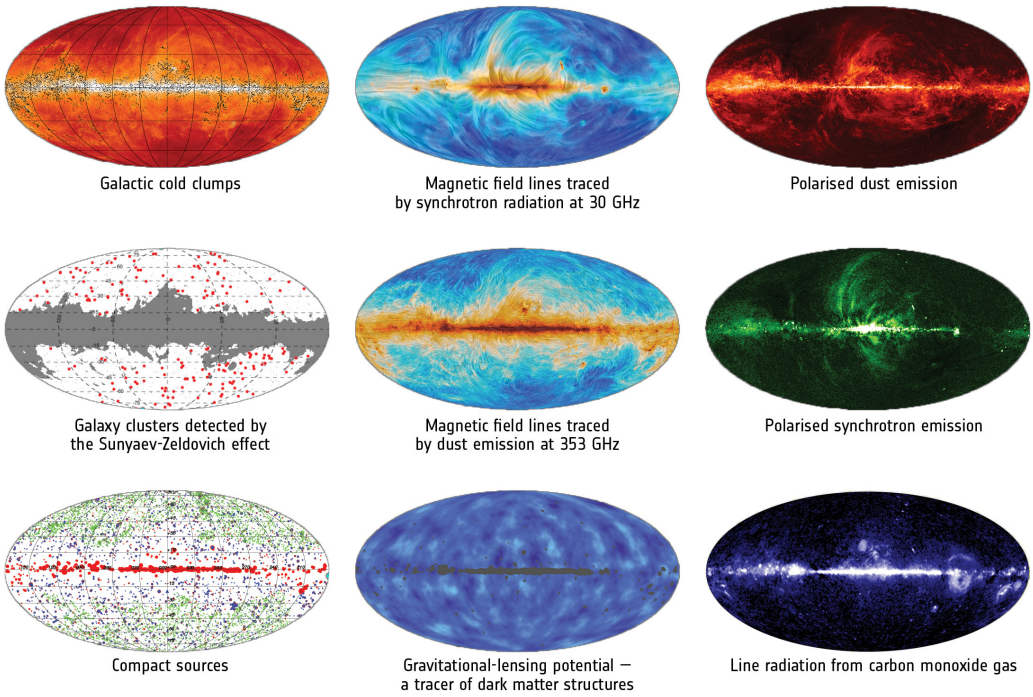

Figure 3.8 – Foreground component maps. The left column shows Galactic and extragalactic point sources, the central column shows the Galactic magnetic field (which polarizes the dust emission) and lensing map, the right column shows diffuse Galactic emissions.

High ℓ The high-ℓ likelihood code `Plik` proceeds uses minimum-variance combinations of the 100, 143 and 217 GHz maps (auto- and cross-spectra) to estimate the TT, TE, EE power spectra, including all non-CMB contributions. The mixing induced by the mask is taken into account in mixing matrices (as in chapter 6) and the effective beam window functions are measured beforehand. Contributions from astrophysical foregrounds are included following a forward-modelling approach, assuming their non-gaussianity (see the structures in figure 3.6) isn't an issue at large multipoles and away from the Galactic plane. Templates for Galactic dust, CIB, tSZ and kSZ contributions are measured from the full range of frequency maps. In particular, the dust template is measured from the 545 and 353 GHz dust-dominated maps (for temperature and polarization respectively). These C_ℓ templates are multiplied by amplitudes, one for each combination of the frequency maps, to be marginalized over. Instrumental uncertainties are also considered. Overall photometric calibration errors are mitigated by an overall amplitude (found to be extremely close to 1); beam uncertainties are taken into account in the mixing and covariance matrices; instrumental noise is estimated from the pixel-space empirical covariance, modulated by small debiasing corrections (related to pixelization and masks). Finally, the covariance matrix of the data vector is obtained from analytical approxima-

tions, quite similar to that used in chapter 6 and detailed in appendix B.1.2, though fully analytical. A battery of (null) tests were performed to ensure the robustness of the derived cosmological constraints.

3.1.4 Main science results

Planck has produced a wealth of scientific results, ranging from Galactic dust and magnetic field to constraints on the physics of the early Universe. Here, we shall focus on some of the most remarkable cosmology-related results.

CMB power spectrum The Planck collaboration measured the power spectra (TT, shown in figure 2.3, but also TE and EE) of the anisotropies of the CMB up to $\ell \leq 2\,500$, down to the cosmic variance limit for $\ell \lesssim 1\,600$.

Cosmological parameters Cosmological constraints on the parameters of the ΛCDM model are obtained by means of MCMC methods (Planck Collaboration *et al.* 2016e), marginalizing over nuisance parameters related to detectors and foregrounds. When complemented by BAO data, supernovæ data, CMB lensing data and very high ℓ CMB data from ground-based experiments (ACT and SPT), they yield the best constraints to date. Aside from constraints on the base ΛCDM model, constraints where obtained on extensions that include massive neutrinos (and other neutrino-related extensions), spatial curvature, running primordial spectral index, quintessence[2] and other dark energy models, non-standard primordial nucleosynthesis and dark matter annihilation models.

Inflation Planck constrained models of inflation by tightening constraints on A_s and n_s, and putting an upper bound on the tensor-to-scalar ratio r.

CMB lensing Planck reconstructed the CMB lensing potential on the whole sky (shown in figure 2.15), measured its amplitude and angular power spectrum, and used it as a complementary source of information to derive cosmological constraints.

SZ clusters Planck made a catalog of clusters detected by their thermal Sunyaev-Zel'dovich effect, a full-sky map of the Compton-y parameter (and measured its power spectrum) and showed evidence of the kinetic SZ effect.

Dust B-modes Thermal emission from dust within the Galaxy is polarized because asymmetric dust grains align with the Galactic magnetic field. This astrophysical foreground is larger than CMB B-modes at large scales where the primordial signal from tensor modes is expected.

[2] Quitessence is a model of dark energy with a special parametrization of a varying equation of state.

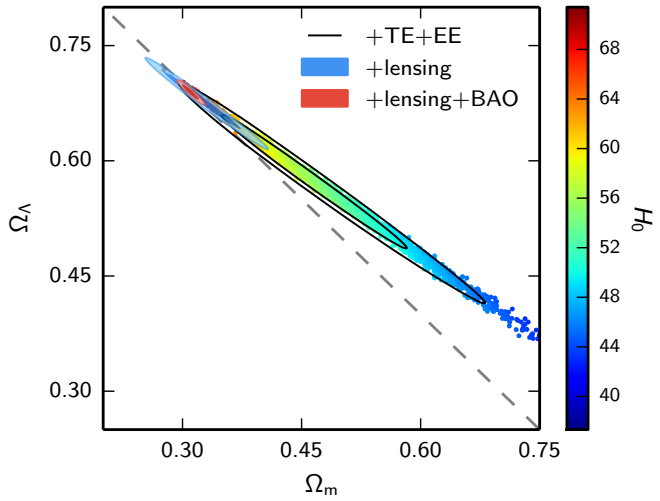

Figure 3.9 – Constraints on Ω_Λ and Ω_m for the curved ΛCDM model. It compares the constraints derived from Planck CMB temperature alone with those derived when adding CMB polarization, CMB lensing and BAO data. Figure from Planck Collaboration *et al.* 2016e.

3.2 SDSS-III/BOSS

3.2.1 The Sloan Digital Sky Survey

The Sloan Digitial Sky Survey[3] (SDSS, Gunn and Knapp 1993) is a major astronomical survey operating a dedicated telescope at the Apache Point Observatory in New Mexico, United States, since 1998. It consists of both an imaging survey, that ended in 2009 and mapped over 14 000 deg^2, and several spectroscopic surveys, that targeted different types of celestial objects, from Milky Way stars to the furthest quasars, with different science goals.

From 2000 to 2008, SDSS-I/II carried out the multi-band imaging of half the northern hemisphere, mapping over a million galaxies. It was completed by a spectroscopic survey of luminous red galaxies (hereafter, LRGs) that enabled the first measurement of the BAO scale (Eisenstein *et al.* 2005), a supernova survey in the so-called Stripe 82 and the Sloan Extension for Galactic Understanding and Exploration (SEGUE), which obtained the spectra of more than a quarter million Milky Way stars to map their motion and composition (including their metallicity).

Work presented in this thesis used data from the third generation (SDSS-III hereafter, Eisenstein *et al.* 2011), comprising the surveys presented below.

APOGEE The Apache Point Observatory Galactic Evolution Experiment obtained high-resolution ($R \equiv \lambda/\Delta\lambda \sim 22\,500$), high signal-to-noise ratio (S/N > 100) infrared spectra of more than 100 000 red giant stars in all parts of the Milky

[3] http://www.sdss.org/

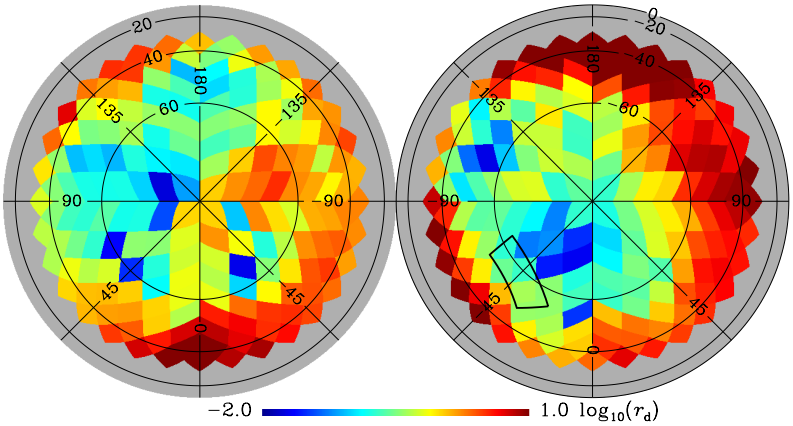

Figure 3.10 – Map in orthographic view of dust contamination in the BB power spectrum from Planck Collaboration *et al.* 2016k. More precisely, in each patch, the dust BB power spectrum at $\ell = 80$ is shown, expressed in units of tensor-to-scalar ratio that would produce the same power. Planck gave an improved estimation of this contamination, demonstrating that dust foregrounds contaminate even high Galactic latitude regions.

Way (bulge, bar, disk and halo), measuring chemical abundances and velocities throughout our galaxy.

BOSS The Baryon Oscillation Spectroscopic Survey (Dawson *et al.* 2013) used a 1 000-fiber spectrograph to precisely measure the redshifts of about 1.5 million luminous red galaxies up to $z < 0.7$, and 200 000 quasars in the range $2.2 < z < 4$, obtaining, in addition, the Lyman-α forest in the spectra of quasars. Its main science goal is a percent-level estimation of the BAO scale (via $D_A(z)$ and $H(z)$) within the redshift ranges covered by galaxies and Lyman-α forests.

MARVELS The Multi-Object APO Radial Velocity Exoplanet Large-area Survey monitored the radial velocities of 11 000 nearby stars with a 60-fiber, interferometric spectrograph, over a period of 18 months, in the search for Jupiter-like exoplanets.

SEGUE-2 In the continuity of the SEGUE survey of SDSS-I/II, SEGUE-2 measured the optical spectra of about 118 000 stars in order to study the kinematic and chemical structure of the Galactic halo and disk.

The fourth generation (SDSS-IV, Blanton *et al.* 2017), which we shall not describe here, is currently taking data.

In the next sections, we will describe the instruments, operations and science results related to the BOSS survey.

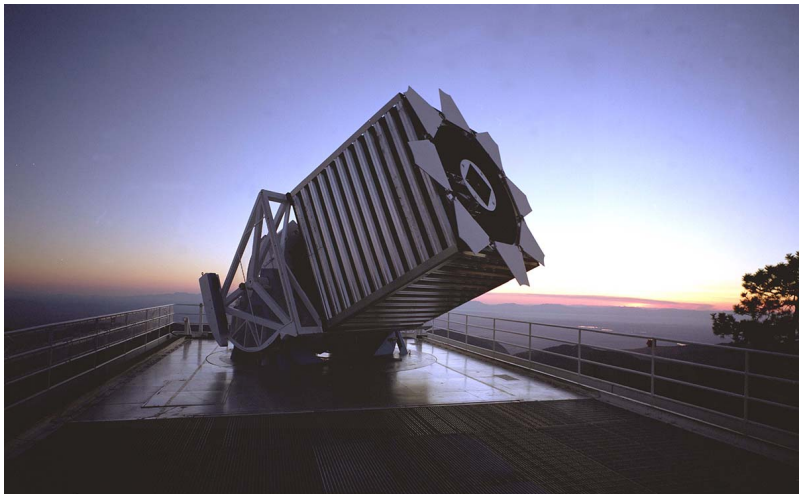

Figure 3.11 – The SDSS telescope at Apache Point Observatory, New Mexico, United States. Photo by Reidar Hahn, Fermilab, taken from Blaustein 0015 on symmetrymagazine.org.

3.2.2 The instruments

3.2.2.1 The telescope

The SDSS telescope (Gunn *et al.* 2006) has a Ritchey-Chrétien design[4] with aperture $f/5$, comprising a 2.5 m primary mirror, a 1.08 m secondary mirror, a Gascoigne astigmatism corrector and two interchangeable aspherical color correctors (one for imaging, the other for spectroscopy). The focal plane has a 3° diameter with small geometric and color distorsions, where either the imaging CCD camera (during SDSS-I/II) or a fiber-fed spectrographs can be placed.

3.2.2.2 The camera

The imaging camera (Gunn *et al.* 1998) consists of 30 CCDs of $2\,048 \times 2\,048$ pixels each, arranged in five rows of six, one for each photometric band covering the optical spectrum (and ordered as r, i, u, z, and g). The camera operates in *drift* mode: the telescope moves along great circles and the CCDs are slowly read, such that images of celestial objects move along columns of the CCD sensors at the same pace these are read (as illustrated in figure 3.12). 24 smaller CCDs are placed around the main CCDs for astrometry.

3.2.2.3 The spectrographs

The spectrograph used during SDSS-I/II underwent a major update for the BOSS survey. Optical fibers of diameter $2''$ are mounted on interchangeable aluminium plates, pointing towards stars, galaxies, quasars or empty spots (to measure the sky

[4] A modified version of the Cassegrain telescope, with hyperbolic primary and secondary mirrors to remove off-axis optical (coma) aberration, important for an imaging survey.

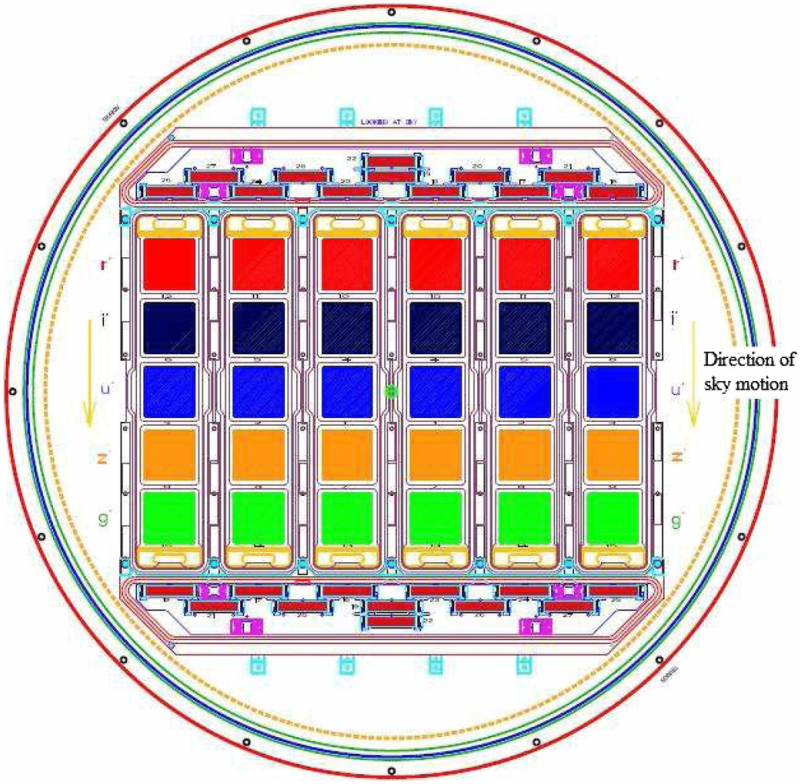

Figure 3.12 – SDSS focal plane array, from Taylor *et al.* 2013.

background) selected after imaging observations. The two identical BOSS spectrographs (Smee *et al.* 2013) placed under the telescope can collect, diffract and analyze light from 1 000 fibers simultaneously. To do so, fibers are stacked and a dichroic splits light at about 6 000 Å, which is then guided towards optimized CCD sensors for the blue and red ends of the spectrum. One axis of the images on the CCDs corresponds to different wavelengths and the other axis corresponds to spectra from different sources. The spectroscopic resolution varies within the range 1560-2270 in the blue channel, 1850-2650 in the red channel.

3.2.3 Target selection

A *photometric* survey is necessary, prior to the *spectroscopic* survey, to image the sky in the five photometric bands and determine targets. A catalog of objects detected by the imaging survey, that contains their angular positions and basic properties derived from their band fluxes, is used to select subsamples that correspond to various kinds of objects (red galaxies, quasars or stars).

3.2.3.1 Imaging

The imaging survey covered about 11 600 $\deg^2$ in the northern Galactic hemisphere and 3 100 $\deg^2$ in the southern hemisphere. The final image covers a total of 14 055 $\deg^2$ of the sky (about a third) in the five photometric bands (*ugriz*). Half a billion

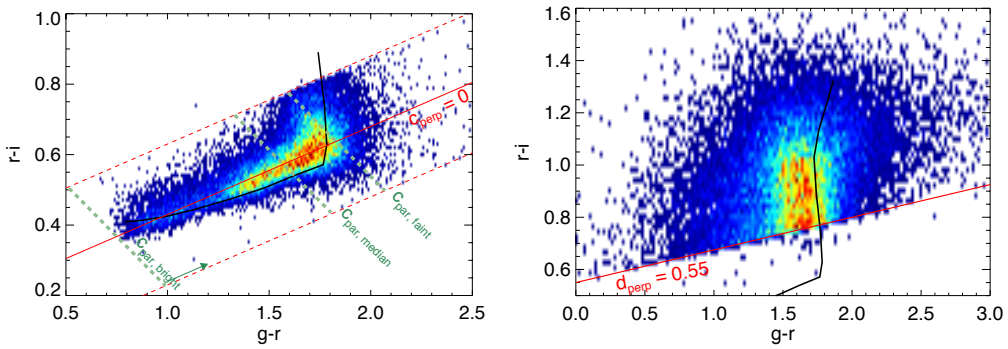

Figure 3.13 – Density plots of LOWZ (left) and CMASS (right) galaxies in the $(g-r, r-i)$ color plane (density increases linearly from blue to red). Cuts in $c_\perp$ and $d_\perp$ are indicated by the red lines. The passive evolution model, on which the cuts are based, is represented by the solid black line. The knee is due to the transition of the 4 000 Å from g- to r-band. Figures from Reid *et al.* 2016.

unique objects were detected and classified from their estimated fluxes with Galactic extinction-corrected magnitude up to $r = 22.5$. Note that there isn't such a thing as an unambiguous, universal flux measurement for all objects. Several estimates are thus computed: the total PSF flux, adapted to point-like objects, the total fiber flux, and model-fitted fluxes (with de Vaucouleurs, exponential or composite models).

3.2.3.2 Galaxy target selection

Galaxy target selection (explained in detail in Reid *et al.* 2016) is based on the color combinations

$$c_\parallel = 0.7(g-r) + 1.2(r-i-0.18), \tag{3.2}$$

$$c_\perp = (r-i) - (g-r)/4 - 0.18, \tag{3.3}$$

$$d_\perp = (r-i) - (g-r)/8. \tag{3.4}$$

These combinations are designed to lie parallel or perpendicular to the color locus of a passively evolving population of galaxies. The 4 000 Å break in the spectra of galaxies transitions from the g-band to the r-band at redshift $z \sim 0.4$. Two catalogs are thus defined: LOWZ, at redshift $z \lesssim 0.4$, based on cuts in $c_\parallel$ and $c_\perp$, and CMASS, at redshift $z \gtrsim 0.4$, based on cuts in $c_\parallel$ and $d_\perp$.

LOWZ LOWZ extends the SDSS-I/II catalog of so-called luminous red galaxies (hereafter LRGs). It selects low-redshift galaxies around the color locus by imposing that

$$|c_\perp| < 0.2, \tag{3.5}$$

and keeps the reddest and brightest galaxies by imposing a redshift-dependent

magnitude cut given by

$$r < 13.5 + c_{\parallel}/0.3. \tag{3.6}$$

This last cut aims at producing a constant number density over the redshift range $[0.2, 0.4]$, making it a *volume-limited* sample. Additionally, a luminosity cut (to avoid blue galaxies passing the threshold) and a star-separation cut are applied

$$16 < r < 19.6, \tag{3.7}$$

$$r_{\rm psf} - r > 0.3, \tag{3.8}$$

where $r_{\rm psf}$ is the total PSF flux, while other magnitudes mentioned here are from the composite model. Intuitively, this difference in r-magnitudes measures the extendedness of objects, distinguishing stars from galaxies. It was shown that these galaxies lie in massive haloes with mean halo mass $5.2 \times 10^{13}\, h^{-1}\, \mathrm{M}_{\odot}$.

CMASS The CMASS sample targets galaxies of constant stellar mass over the redshift range $[0.4, 0.7]$, making it a *mass-limited* sample. The main color cuts are

$$d_{\perp} > 0.55 \tag{3.9}$$

$$i < 19.86 + 1.6(d_{\perp} - 0.8). \tag{3.10}$$

The first one effectively discards low-redshift galaxies while the second one is a redshift-dependent cut that imposes an approximate constant stellar mass. Further cuts,

$$17.5 < i < 19.9, \tag{3.11}$$

$$i_{\rm fiber} < 21.5, \tag{3.12}$$

are imposed to insure a high redshift success rate even in the faint end, and star-seperation cuts similar to that imposed on LOWZ are applied on the i- and z-bands. CMASS galaxies are massive, with masses over $10^{11}\, \mathrm{M}_{\odot}$, but occupy haloes slightly less massive than LOWZ galaxies as a consequence of their higher redshifts. Maraston *et al.* 2013 used spectral energy distribution templates to estimate stellar masses of CMASS galaxies and show that the distribution of stellar masses is narrow and centered around $\log M/\mathrm{M}_{\odot} \sim 11.3$.

3.2.3.3 Quasar target selection

Target selection of quasars (Ross *et al.* 2012) is complicated by several reasons. The first is their similarity to stars in color space (they are said to have close *loci*). The second is that quasars targets were derived from external surveys. The `XDQSO` algorithm (Bovy *et al.* 2011), that was preferred in the data release of SDSS-III, is a

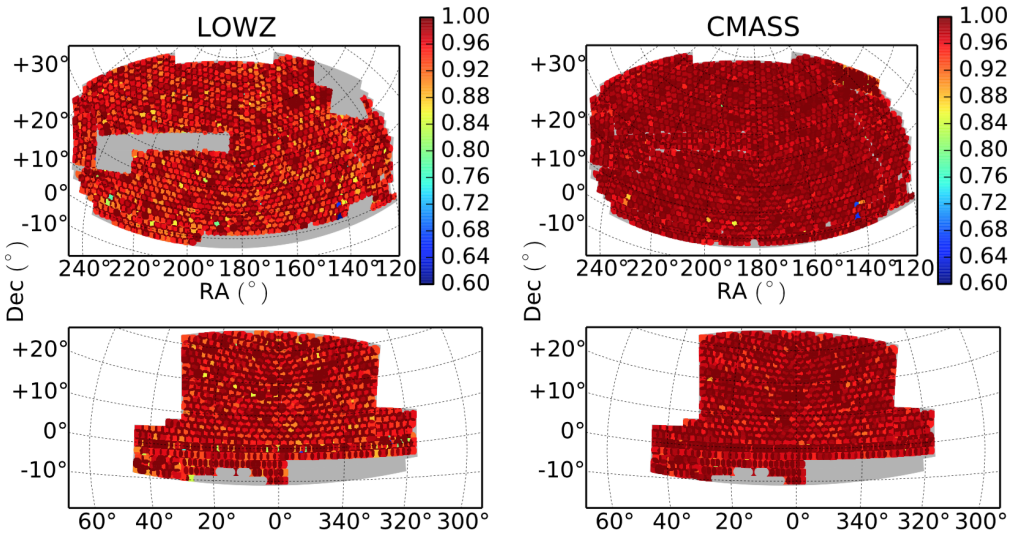

Figure 3.14 – Completeness of LOWZ and CMASS galaxies in the twelfth data release of SDSS-III/BOSS. The projection of observation plates over the sky defines non-overlapping sectors in which in the completeness is computed. Top plots represent the northern Galactic hemisphere, bottom plots the southern hemisphere. Figure from Reid *et al.* 2016.

probabilistic approach that estimate the distributions of quasars and stars in color space (with kernel density estimation technique), properly incorporating photometric errors, to attribute to each SDSS point object the probability of it being a quasar. Objects with a probability greater than 0.424 are flagged as quasars.

Another quasar-specific feature is that the selection need not be uniform for Lyman-α studies. In particular, the key science goal that drives science requirements is the measurement of the BAO scale in the Lyman-α forest. Its signal-to-noise ratio scales linearly with the number of quasars, which requires a mean angular density of quasars of about $15\,\mathrm{deg}^{-2}$, but not necessarily a uniform selection function. The CORE subsample is defined by using single-epoch photometry from SDSS imaging survey with a controlled, uniform selection function, and some magnitude cuts. This sample can be used for quasar clustering measurements.

The quasar catalog of the twelfth data release is described in Pâris *et al.* 2017 and contains about 100 000 quasars in the CORE sample. After classification, about half of targets are confirmed quasars. Their clustering properties and completeness were explored in Eftekharzadeh *et al.* 2015.

3.2.4 Observing strategy

Once targets have been selected, one must decide of an optimized way to assign to each of them an observation plate and fiber, a problem known as the *tiling* strategy (Blanton *et al.* 2003). The goal is to observe as many targets as possible (completeness) and to do so in a way that is as uniform as possible, in order not

to bias clustering measurements, while also minimizing the number of required plates (efficiency) and leaving the smallest possible unobserved area within the BOSS footprint. The constraints are that (i) fibers cannot be closer than $62''$, and (ii) they cannot be within $92''$ of the plate center (for mechanical reasons). A perfectly uniform distribution of plates over the sky (*i.e.* a honeycomb mesh) is suboptimal, as was shown in (Blanton *et al.* 2003). Completeness and efficiency were greatly improved by small departures from uniformity and small overlaps between plates, as explained in Blanton *et al.* 2003.

The positions on the focal plane of the targets at a given observation date are computed, taking into account atmospheric differential refraction. Holes are drilled in aluminium plates and fibers are positioned at a height that maximizes the throughput at 5 400 Å for galaxies and 4 000 Å for quasars. On a given plate, about two hundreds fibers target quasars, six hundreds galaxies, up to one hundred are used for ancillary targets and the remainder, of order one hundred, for calibration and photometric purposes (estimation of atmospheric extinction, seeing, airmass, *etc*).

After a flat-field calibration, the telescope is positioned and tracks the motion of targets during 15 minutes exposures. A simplified version of the data processing pipeline is run to assess whether science requirements were met; otherwise, a rerun is scheduled.

3.2.5 Data reduction

Raw data is transferred to the Lawrence Berkeley National Laboratory, California, United States. There, the automated pipeline, described in Bolton *et al.* 2012, extracts single spectra from the spectrographs' CCD images, performs noise estimation and removal, classification (for remaining stars) and redshift estimation, and flags problematic spectra (usually faint galaxies).

3.2.6 Main science results

There are over 200 publications from the SDSS-III Collaborations, 76 of which are related to BOSS, and over 5 000 publications that used publicly released SDSS data overall, making it a difficult exercise to exhaustively summarize science results. However, important results in cosmology from BOSS alone include (some have already been cited in section 2.2):

BAO Measurements of the BAO scale in the samples of galaxies and in the Lyman-α forest (see figure 3.15), in real and in Fourier space, providing contraints of order 2% or less on $D_A(z)$ and $H(z)$ at $z = 0.32, 0.57$ and 2.34 for, respectively, LOWZ, CMASS and the Lyman-α forest (see Alam *et al.* 2017, and references therein).

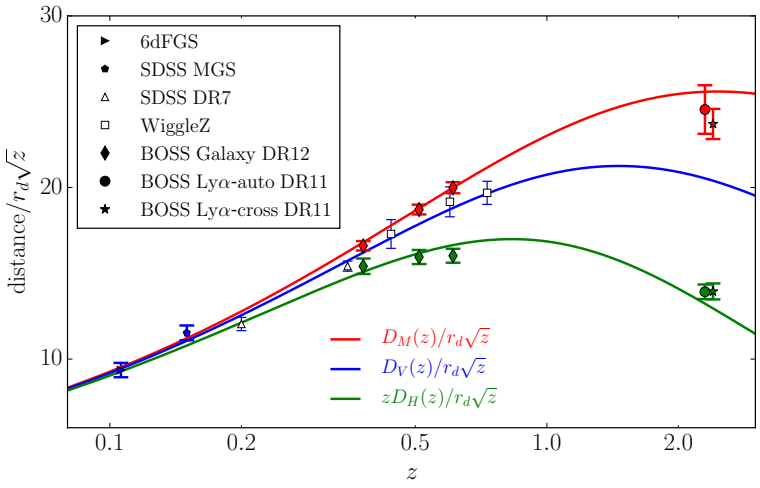

Figure 3.15 – Distance measurements from the BAO scale in galaxy and Lyman-α forest clustering from SDSS-III/BOSS and earlier surveys. Figure from Alam *et al.* 2017.

RSD Measurements of the growth of structures from anisotropic redshift-space clustering, constraining the product $f\sigma_8$ (see figure 3.16).

Power spectrum Measurements of the full-shape galaxy power spectrum and correlation function (see figure 3.17).

Higher-order statistics Measurements of the position-dependent power-spectrum and of the bispectrum of galaxies in various configurations (Beutler *et al.* 2017; Gil-Marìn *et al.* 2015a,b).

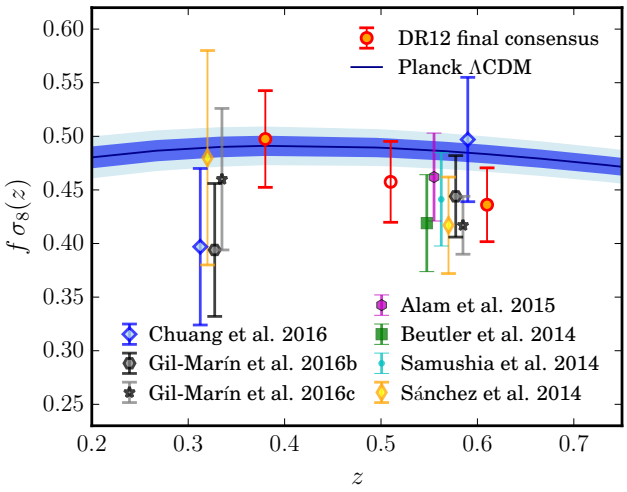

Figure 3.16 – Comparison of $f\sigma_8(z)$ measurements from the data releases 11 and 12. The apparent tension with Planck ΛCDM cosmology is lessened when measurements are performed assuming this same cosmology. Figure from Alam *et al.* 2017.

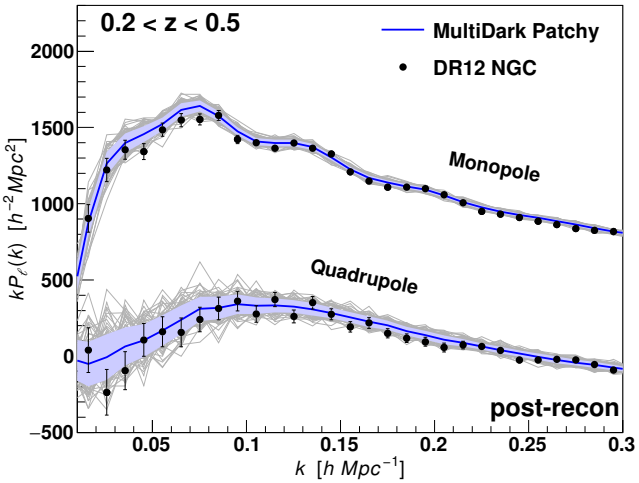

Figure 3.17 – Matter power spectrum measured from the galaxies of the SDSS-III/BOSS survey after reconstruction (Beutler *et al.* 2017). Anisotropic clustering in redshift-space, parametrized by the dependence on μ, can be expanded over Legendre polynomials indexed by multipoles. The monopole and quadrupole are shown here.

CHAPTER 4

Combination of cosmic probes: cross-correlations and joint analyses

Contents

4.1 Motivations 92
4.1.1 A toy model 92
4.1.2 Why and how to combine cosmological probes? 95
4.2 Measuring correlations 98
4.2.1 Cross-power spectra 98
4.2.2 Projected observables 100
4.2.3 Other techniques 106
4.3 Cross-correlations 109
4.3.1 The first studies: CMB × LSS 110
4.3.2 Gravitational lensing comes into play 111
4.3.3 Combining tracers of the large-scale structure 114
4.4 Joint analyses 117
4.4.1 Current status 117
4.4.2 Forecasts 118
Appendices 121
4.A Signal-to-noise ratio: auto- *vs* cross-correlation 121

In *Metaphysics*, Book VIII, Aristotle wrote

πάντων γὰρ ὅσα πλείω μέρη ἔχει καὶ μὴ ἔστιν οἷον σωρὸς τὸ πᾶν.

which loosely translated is,

> The whole is greater than the sum of its parts.

Now that the reader is undoubtedly convinced, let us see how this applies to cosmology. This chapter aims at introducing and motivating the idea of *combining cosmological probes*, by which we mean the effort to extract information from the analysis of statistical correlations between two or more cosmological observations. After a statement of the incentives for this effort, we shall present the principal mathematical tools to measure such correlations. Finally, we will do a review of the literature and explore some of the many avenues leading to new science offered by the combination of cosmological probes.

4.1 Motivations

4.1.1 A toy model

Let us begin with a toy model. Consider a gaussian-distributed, two-dimensional vector, $\boldsymbol{X} = \binom{x}{y} \sim \mathcal{N}(\boldsymbol{\mu}, \boldsymbol{\Sigma})$, with mean $\boldsymbol{\mu}$ and covariance $\boldsymbol{\Sigma}$, where the mean depends on two parameters a and b, for instance as

$$\boldsymbol{\mu} = \begin{pmatrix} \mu_x \\ \mu_y \end{pmatrix} = \begin{pmatrix} a - b \\ a \times b \end{pmatrix}. \tag{4.1}$$

Then, let us denote the variance of the two components σ_x^2 and σ_y^2 and their correlation coefficient ρ, such that their covariance matrix is

$$\boldsymbol{\Sigma} = \begin{pmatrix} \sigma_x^2 & \rho\sigma_x\sigma_y \\ \rho\sigma_x\sigma_y & \sigma_y^2 \end{pmatrix}, \tag{4.2}$$

with determinant $|\boldsymbol{\Sigma}| = \sigma_x^2\sigma_y^2\left(1 - \rho^2\right)$. Finally, consider a sample of n independent realizations of $\boldsymbol{X}$, denoted $\boldsymbol{X}_i = \binom{x_i}{y_i}$. We can compute, thanks to Bayes' theorem, the likelihood of parameters a and b, given these observations and flat priors, as

$$\mathcal{L}(a, b \mid \mathbf{X}_i) \propto \prod_{i=1}^{n} \frac{1}{2\pi\sqrt{|\boldsymbol{\Sigma}|}} \exp\left(-\frac{1}{2}\chi_i^2\right) \quad \text{where} \quad \chi_i^2 = (\boldsymbol{X}_i - \boldsymbol{\mu})^\intercal \boldsymbol{\Sigma}^{-1} (\boldsymbol{X}_i - \boldsymbol{\mu}). \tag{4.3}$$

Now, let us compare four cases:

1. We observe only the first component.
2. We observe only the second component.
3. We observe both components but consider them as independent.
4. We observe both components and consider their correlation.

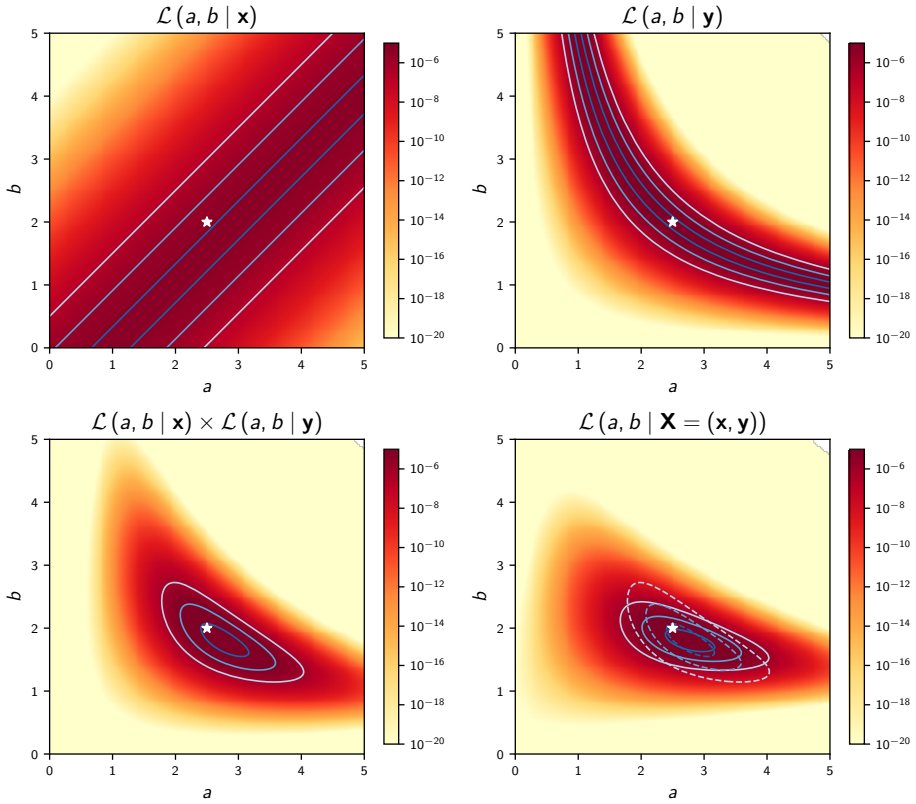

Figure 4.1 – Likelihood of parameters a and b of our toy model in the four cases mentioned in the text, for $a = 2.5$, $b = 2$, $\sigma_x = 6$, $\sigma_y = 5$, $\rho = 0.5$ and $n = 100$. The 1, 2 and 3σ contours are overlaid. The joint analysis uses all of the information available, including the correlation between observables. It yields the *correct* contraints, which are not necessarily tighter. This depends on the exact dependence of the observables on the parameters.

Single components are gaussian distributed as $x \sim \mathcal{N}\left(\mu_x, \sigma_x^2\right)$ (similarly for y). In the third case, we chose ignore the fact that components *are* correlated, which amounts to considering that $\rho = 0$ and simply multiplying the likelihoods of the single components. The fourth case, closer to reality, uses the *joint* distribution of the two components. As seen on figures 4.1 and 4.2, the joint likelihood yields significantly tighter constraints on b in that case (see appendix A.1 of appendix A for a definition n-σ contours).

Let us highlight two facts.

First, the joint likelihood uses *more information* because it takes correlations between components into account. This can be given a mathematical meaning, using the Shannon entropy of a probability distribution with density p, defined as

$$S = \langle -\ln p \rangle = -\int p(x) \ln p(x) \, \mathrm{d}x \,. \tag{4.4}$$

The entropy of a multivariate gaussian is $\ln \sqrt{2\pi e |\mathbf{\Sigma}|}$, such that the difference of

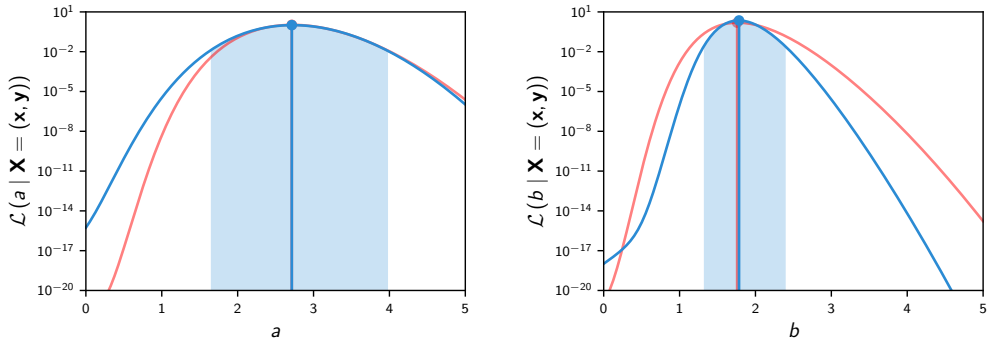

Figure 4.2 – Marginal likelihood of the parameters of our toy model for the same parameters as in figure 4.1. The blue curve shows the joint likelihood while the red curve corresponds to the hypothesis that components are independent. The blue-shaded area gives the 1σ bounds for the joint likelihood, and the maximum likelihood estimator is highlighted by the vertical line.

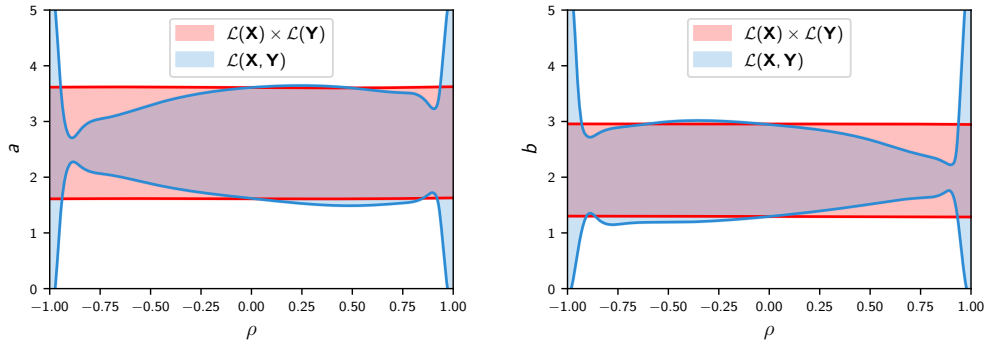

Figure 4.3 – 1σ contraints on the parameters a and b, from the joint likelihood (in blue) and the product likelihood (in red), as a function of the correlation coefficient ρ. These contraints are averaged over 100 realizations containing $n = 100$ data points each.

entropy between the correlated and independent distributions is

$$\Delta S = S_\rho - S_{\rho=0} = \ln \sqrt{1 - \rho^2} \leq 0. \tag{4.5}$$

Therefore, the joint likelihood always has a smaller entropy than the product of independent likelihoods (in the gaussian case).

Then, the joint analysis always yield the *true* contraints because they are based on the correct likelihood, even though they may not be tighter. To see this, we repeat draw samples from our toy model, but this time varying ρ, and measure the error bars on a and b given by the joint likelihood and the product of independent likelihoods. As can be seen on figure 4.3, ignoring the correlation coefficient is generally too conservative. However, it may also be highly optimistic and lead to catastrophic underestimation: here, when $|\rho| \to 1$, the parameters are completely degenerate and

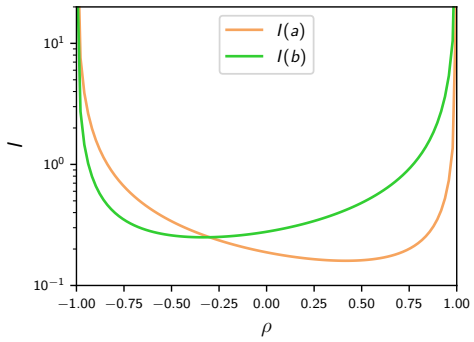

Figure 4.4 – Fisher information for the parameters a and b as a function of the correlation coefficient ρ.

the *true* error bars explode while those from the combined independent analyses hardly vary. The reason is that in the later case, we are using the *same* information twice, which is of course wrong.

The Fisher information(Zegers 2015) gives a bound on how well a parameter can be determined[1], but there is no universal rule regarding how it varies with ρ. It depends on the exact relationship between the observables (or a summary statistics) and the parameters. For our gaussian toy model, the Fisher information is given by

$$\boldsymbol{I} = \frac{\mathrm{d}\boldsymbol{\mu}}{\mathrm{d}\boldsymbol{\theta}}^{\intercal} \Sigma^{-1} \frac{\mathrm{d}\boldsymbol{\mu}}{\mathrm{d}\boldsymbol{\theta}}, \tag{4.6}$$

$$= \frac{1}{\sigma_x^2\sigma_y^2\left(1-\rho^2\right)} \begin{pmatrix} b^2\sigma_x^2 + \sigma_y^2 - 2b\rho\sigma_x\sigma_y & ab\sigma_x^2 - \sigma_y^2 + (b-a)\rho\sigma_x\sigma_y \\ ab\sigma_x^2 - \sigma_y^2 + (b-a)\rho\sigma_x\sigma_y & a^2\sigma_x^2 + \sigma_y^2 + 2a\rho\sigma_x\sigma_y \end{pmatrix} \tag{4.7}$$

where $\boldsymbol{\theta} = \binom{a}{b}$. $I(a)$ reaches extrema when $\rho = \sigma_y/b\sigma_x$ and $\rho = b\sigma_x/\sigma_y$. Therefore, there always exist an extremum in the interval $[-1, 1]$, as can be seen on figure 4.4.

4.1.2 Why and how to combine cosmological probes?

In the field of cosmology, various observables probe the components of the matter density field – stellar light, diffuse hydrogen, dark matter haloes – at different time periods and scales (see figure 4.5). Instead of only measuring the auto-correlation function of each probe independently, one might also measure the cross-correlation

[1] The Cramér-Rao bound states that for any estimator $\hat{\theta}$ of a parameter θ,

$$\mathrm{Var}\left(\hat{\theta}\right) \geq \frac{1}{I(\theta)}$$

where the Fisher information is defined as

$$I(\theta) = \left\langle \frac{\partial}{\partial\theta} \ln p\left(x \mid \theta\right) \right\rangle .$$

In other words, it provides a lower bound on the statistical error that can be achieved on a given parameter. However, finding an estimator that saturates this bound may be difficult.

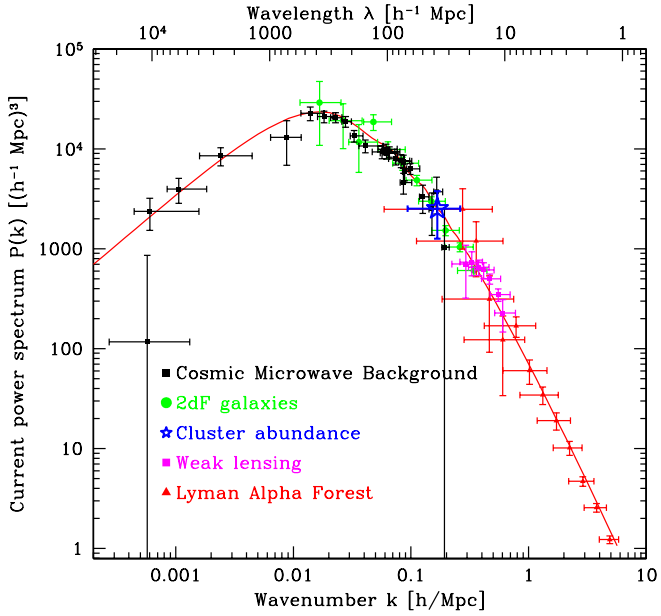

Figure 4.5 – Various cosmological observations probe the matter power spectrum at different scales and must be combined to reach the best constraints on cosmological models (from Tegmark and Zaldarriaga 2002).

functions, which contain complementary information. They can be particularly interesting for several reasons.

1. The cross-correlation of two probes can spot yet unobserved physical phenomena or highlight the spatial connection between components (see chapter 5).

2. Cross-correlation measurements can be included in a joint analysis of several probes to obtain better[2] constraints on cosmological parameters (see chapter 6).

3. Since different experiments are less prone to have the same systematic errors, they offer new avenues of cross-calibration and null tests (Jain *et al.* 2015).

The first point will be explored at length in section 4.3 where we will do a review of cross-correlation studies. In chapter 5, we report the detection of a cross-correlations between the Lyman-α forest of quasars and CMB lensing (see chapter 2 for an introduction to those probes), together with an original approach based on the position-dependent power spectrum.

The second point was illustrated by the toy model in the previous section and will be the subject of section 4.4, where we review the brief literature of this emerging topic in cosmology. In chapter 6, we develop a methodology and numerical tools

[2] If confidence regions on parameters are not smaller, they are, at least, more correct.

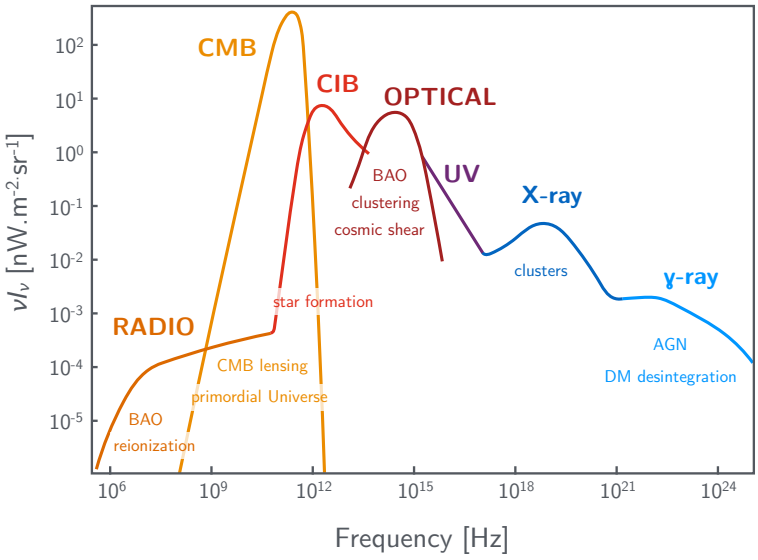

Figure 4.6 – Electromagnetic spectrum of the diffuse extragalactic background radiation over more than 18 orders of magnitude in frequency. Figure inspired from one by Andrew Jaffe at http://www.andrewjaffe.net/blog/2011/09/passion-for-lig.html.

to perform the joint analysis of Planck CMB data and spectroscopic tracers of the large-scale structure observed by SDSS-III/BOSS.

Now, let us comment on the last point. Imagine that an experiment measures a signal S with a multiplicative bias b and has a noise N, such that the data vector can be written $D = bS + N$. Let us consider two such experiments, denoted X and Y. The noise of each experiment is supposed to have a null expectation value but non-zero variance, and the noises are assumed to be uncorrelated amongst data sets. Therefore,

$$\langle D_X D_Y \rangle = b_X b_Y \langle S_X S_Y \rangle + b_X \cancel{\langle S_X N_Y \rangle} + b_Y \cancel{\langle S_Y N_X \rangle} + \cancel{\langle N_X N_Y \rangle}. \tag{4.8}$$

The three last terms are crossed out because noise terms vanish on average. Therefore the cross-correlation of X and Y does not suffer from an additive bias. However, it might have a multiplicative bias if the two observables are not correctly calibrated: the cross-correlation signal can thus be used to detect such biases and improve calibration, a technique that was suggested, in particular, to pin down multiplicative biases in galaxy weak lensing (see Vallinotto 2012, and section 4.3).

Various experiments scan the Universe at different wavelengths (see figure 4.6), spatial resolutions and luminosity depths, providing disparate but complementary data sets. Therefore, data from multiple telescopes can be combined in many different ways to enhance systematics control, and, as a consequence, to improve constraints on cosmological parameters (Jain *et al.* 2015; Rhodes *et al.* 2015).

4.2 Measuring correlations

In order to measure the cross-correlations of various probes, it is useful to develop a common mathematical language. For instance, say we are to measure the cross-correlation between a galaxy sample and CMB lensing. The galaxy sample usually comes as a catalog. Therefore, it is first necessary to build a projected overdensity map of the galaxies which can be compared to the map of CMB lensing convergence by measuring the cross-power spectrum. However, this is not the only way of measuring correlations. Other techniques exist that we shall review afterwards.

4.2.1 Cross-power spectra

Consider two observables on the sphere $A(\hat{\boldsymbol{n}})$ and $B(\hat{\boldsymbol{n}})$, where $\hat{\boldsymbol{n}}$ is the unit vector giving the angular position. Under the assumption of statistical isotropy, the cross-correlation function $\langle A(\hat{\boldsymbol{n}})B^*(\hat{\boldsymbol{n}}')\rangle$ depends only on $\hat{\boldsymbol{n}}\cdot\hat{\boldsymbol{n}}'$ which lives in the interval $[-1,+1]$. Legendre polynomials form an orthogonal basis with respect to the L_2 norm on $[-1,+1]$. Therefore, the correlation function can be decomposed on this basis as

$$\langle A(\hat{\boldsymbol{n}})B^*(\hat{\boldsymbol{n}}')\rangle = \sum_{\ell=0}^{\infty}\frac{(2\ell+1)}{4\pi}P_\ell(\hat{\boldsymbol{n}}\cdot\hat{\boldsymbol{n}}')C_\ell^{AB}, \tag{4.9}$$

where P_ℓ is the Legendre polynomial of rank ℓ. This defines the angular cross-power spectrum C_ℓ^{AB} as a function of multipole ℓ, corresponding to scale $\theta\sim\pi/\ell$.

The two observables can be expanded in spherical harmonics (represented in figure 4.7),

$$A(\hat{\boldsymbol{n}}) = \sum_{\ell=0}^{\infty}\sum_{m=-\ell}^{+\ell}a_{\ell m}Y_{\ell m}(\hat{\boldsymbol{n}}), \tag{4.10}$$

which can be inverted as

$$a_{\ell m} = \int A(\hat{\boldsymbol{n}})Y^*_{\ell m}(\hat{\boldsymbol{n}})\,\mathrm{d}^2\hat{\boldsymbol{n}}\,. \tag{4.11}$$

Using the orthogonality relation

$$\int \mathrm{d}^2\hat{\boldsymbol{n}}\,Y^*_{\ell m}(\hat{\boldsymbol{n}})Y_{\ell' m'}(\hat{\boldsymbol{n}}) = \delta_{\ell\ell'}\delta_{mm'} \tag{4.12}$$

and the addition property

$$\sum_{m=-\ell}^{+\ell}Y_{\ell m}(\hat{\boldsymbol{n}})Y^*_{\ell m}(\hat{\boldsymbol{n}}') = \frac{(2\ell+1)}{4\pi}P_\ell(\hat{\boldsymbol{n}}\cdot\hat{\boldsymbol{n}}'), \tag{4.13}$$

we thus obtain that

$$\langle a_{\ell m}b^*_{\ell' m'}\rangle = C_\ell^{AB}\delta_{\ell\ell'}\delta_{mm'}. \tag{4.14}$$

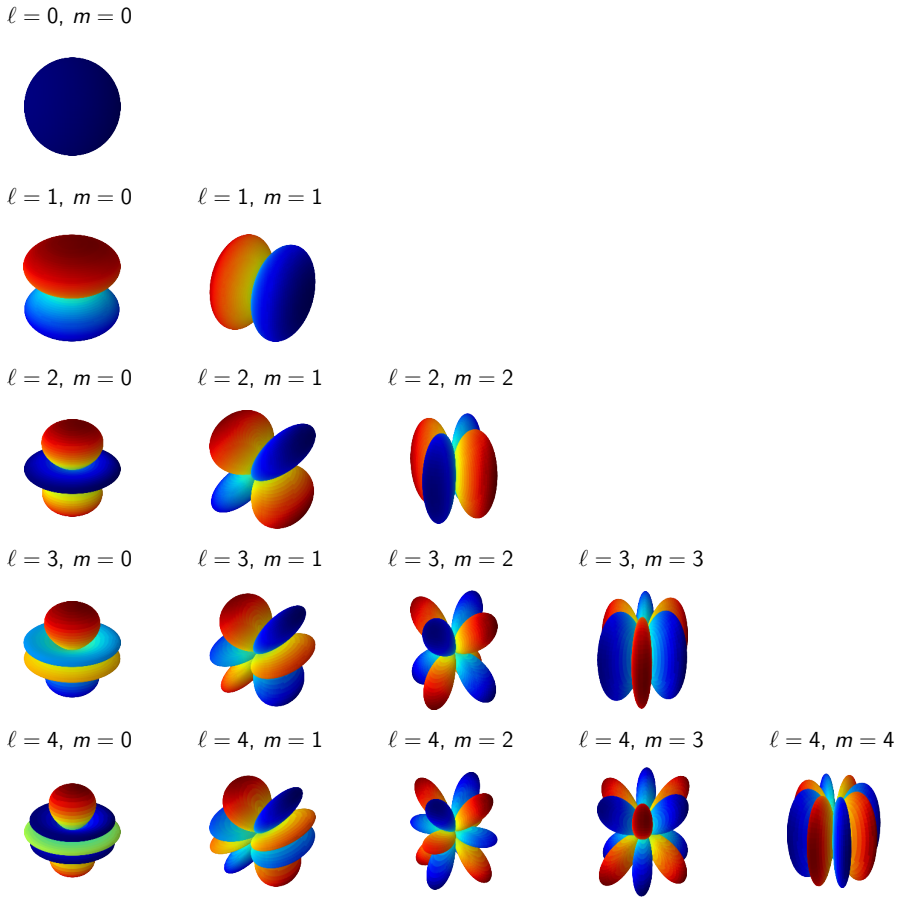

Figure 4.7 – Representation of the few first spherical harmonics. The real part is shown here, blue meaning negative and red positive.

This provides an unbiased estimator for the cross-power spectrum

$$\hat{C}_\ell^{AB} = \frac{1}{2\ell+1} \sum_{m=-\ell}^{\ell} a_{\ell m} b_{\ell m}^*. \tag{4.15}$$

We show in appendix B.1 that the variance of this estimator is

$$\mathrm{Var}\left(\hat{C}_\ell^{AB}\right) = \frac{\left(C_\ell^{AB}\right)^2 + C_\ell^{AA} C_\ell^{BB}}{2\ell+1}, \tag{4.16}$$

implying that $C_\ell^{AB} \Big/ \sigma_{C_\ell^{AB}} \propto \sqrt{\ell + 1/2}$ increases at large scale (or small ℓ). This is known as *cosmic variance* and is due to the limited number of observable modes. The full probability density function is developped in appendix B.2.

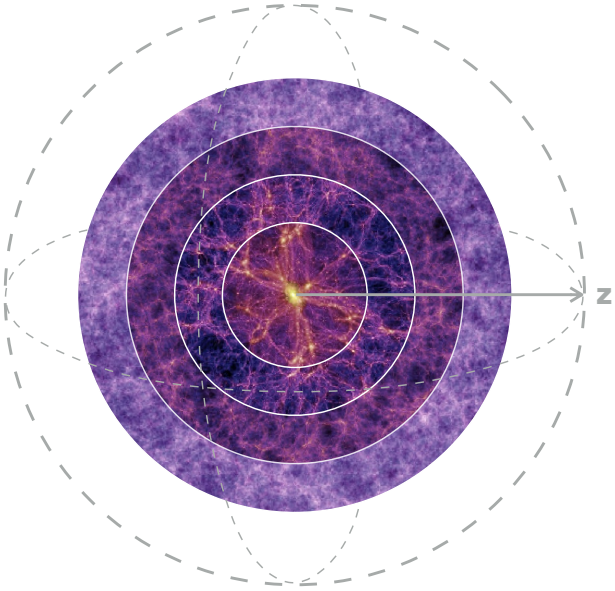

Figure 4.8 – Schematic of projected observables: snapshots of radial slices of the density field at corresponding lookback time are projected on the sky (represented by the outer sphere) with a redshift-dependent weight.

4.2.2 Projected observables

It is common in cosmology to observe quantities that are projections on the sky of the three-dimensional matter density field with some distance-dependent weight: this is the case for CMB lensing, cosmic shear or galaxy number counts. They can be generically written

$$A(\hat{\boldsymbol{n}}) = \int \mathrm{d}z\, W^A(z)\delta\left(\chi(z)\hat{\boldsymbol{n}}, z\right) \tag{4.17}$$

where $\delta\left(\chi(z)\hat{\boldsymbol{n}}, z\right)$ is the matter overdensity at comoving distance $\chi(z)$ in the direction $\hat{\boldsymbol{n}}$ and at redshift z. The weight $W^A(z)$ is called the *kernel* function of the observable A and is characteristic of it.

Let us recall some of these kernels.

Galaxy density For the projected density of galaxies, if we do not take into account relativistic effects (to be discussed in chapter 6), we have

$$W^g(z) = b(z)\frac{\mathrm{d}n}{\mathrm{d}z} \tag{4.18}$$

where $b(z)$ is the galaxy bias and $\mathrm{d}n/\mathrm{d}z$ is the normalized redshift distribution.

CMB lensing The lensing efficiency at redshift z, for a source at redshift z_S, is

$$W_\kappa(z, z_\mathrm{S}) = \frac{3}{2}\left(\frac{H_0}{c}\right)^2 \Omega_\mathrm{m}^0 \frac{(1+z)}{H(z)}\chi(z)\left(1 - \frac{\chi(z)}{\chi(z_\mathrm{S})}\right) \tag{4.19}$$

where $\chi(z)$ is the comoving distance at redshift z. Therefore, the kernel for CMB lensing is given by

$$W_{\kappa_{\rm CMB}} = W_\kappa(z, z_*) \tag{4.20}$$

where $z_* \approx 1\,090$ is the redshift of the last scattering surface.

Galaxy lensing The lensing efficiency must be integrated over the redshift distribution of source galaxies, such that

$$W^{\kappa_{\rm gal}}(z) = \int \mathrm{d}z_{\rm S} \frac{\mathrm{d}n}{\mathrm{d}z_{\rm S}} W_\kappa(z, z_{\rm S}). \tag{4.21}$$

4.2.2.1 Two-points statistics of projected observables

In order to obtain an expression of the cross-power spectrum, we replace $\delta\left(\chi(z)\hat{\boldsymbol{n}}, z\right)$ by its inverse Fourier transform,

$$\delta\left(\chi(z)\hat{\boldsymbol{n}}, z\right) = \int \frac{\mathrm{d}^3\boldsymbol{k}}{(2\pi)^{3/2}} \delta(\boldsymbol{k}, z) e^{i\boldsymbol{k}\cdot\chi(z)\hat{\boldsymbol{n}}}, \tag{4.22}$$

in the previous equation and then plug this expression into equation (4.11). Plane waves can then be decomposed into spherical harmonics,

$$e^{i\boldsymbol{k}\cdot\chi(z)\hat{\boldsymbol{n}}} = 4\pi \sum_{\ell=0}^{\infty} \sum_{m=-\ell}^{+\ell} i^\ell j_\ell(k\chi(z)) Y^*_{\ell m}(\hat{\boldsymbol{k}}) Y_{\ell m}(\hat{\boldsymbol{n}}) \tag{4.23}$$

where j_ℓ is the Bessel spherical function of rank ℓ, $k = \|\boldsymbol{k}\|$ and $\hat{\boldsymbol{k}} = \boldsymbol{k}/k$. Using, again, the orthogonality of spherical harmonics, yields

$$a_{\ell m} = 4\pi i^\ell \int \mathrm{d}z\, W^A(z) \int \frac{\mathrm{d}^3\boldsymbol{k}}{(2\pi)^{3/2}} \delta(\boldsymbol{k}, z) j_\ell(k\chi(z)) Y^*_{\ell m}(\hat{\boldsymbol{k}}). \tag{4.24}$$

Finally, inserting this expression into equation (4.14) and using the definition of the matter power spectrum[3], the assumption of isotropy, and, one last time, the orthogonality of spherical harmonics, we obtain

$$C_\ell^{AB} = \frac{2}{\pi} \int \mathrm{d}z\, W^A(z) \int \mathrm{d}z'\, W^B(z') \int k^2\, \mathrm{d}k\, P(k, z, z') j_\ell(k\chi(z)) j_\ell(k\chi(z')). \tag{4.25}$$

[3] Here, we extend the definition in equation (1.67) to the power spectrum of fluctuations considered at different times, defined as

$$\left\langle \delta(\boldsymbol{k}, z) \delta^*(\boldsymbol{k}', z') \right\rangle = \delta^{(3)}\left(\boldsymbol{k} - \boldsymbol{k'}\right) P(k, z, z').$$

It is sometimes expressed in the literature as $P(k, z, z') = \sqrt{P(k, z) P(k, z')}$, an approximation discussed in Kitching and Heavens 2017.

Equivalently, we have, in real-space, the angular correlation function, $\omega(\theta)$, is related to the three-dimensional correlation function, $\xi(R, z, z')$, by

$$\omega(\theta) = \left\langle A(\hat{\boldsymbol{n}})B^*(\hat{\boldsymbol{n}}')\right\rangle = \int \mathrm{d}z\, W^A(z) \int \mathrm{d}z'\, W^B(z')\xi(R, z, z') \tag{4.26}$$

where $R = \left\|\chi(z')\hat{\boldsymbol{n}}' - \chi(z)\hat{\boldsymbol{n}}\right\|$ denotes the separation and $\hat{\boldsymbol{n}} \cdot \hat{\boldsymbol{n}}' = \cos\theta$.

4.2.2.2 On the Limber approximation

The approximation introduced by Limber (Limber 1953, 1954) simplifies equations (4.25) and (4.26), which are computationally expensive. If the kernel functions have a width Δz and peak at some redshift $\overline{z}$, then it is assumes that:

- the kernel functions vary smoothly over the coherence scale of density fluctuations;
- we consider scales smaller than the fractional width of the kernel functions, $\theta \ll \Delta z/\overline{z}$.

Importantly, in projected observables, the matter density field is integrated over redshift slices that are both radial distance slices (δ is evaluated at position $\chi(z)\hat{\boldsymbol{n}}$) and time slices ($\delta$ is evaluated at lookback time $t_L(z)$). Therefore, the kernel functions might equally be considered as functions over redshift, distance or time. Bearing that in mind, the first assumption means that we assume that the correlation between fluctuations separated by a sufficiently large distance/time is negligible (consistent with the fact that the power spectrum goes to 0 at large scale), and that this distance scale is itself much smaller that the characteristic scale over which the kernel function varies.

In its original form, the approximation was applied to real-space functions (see Simon 2007, for details). Within the separation scale on which the correlation function $\xi(R, \chi, \chi')$ is non-vanishing, the kernels can be evaluated at a middle distance $\overline{\chi} = \left(\chi + \chi'\right)/2$ and the correlation function can be evaluated at the corresponding redshift $\overline{z}$, yielding Limber's equation[4]

$$\omega(\theta) = \int \mathrm{d}\overline{\chi}\, W^A(\overline{\chi})W^B(\overline{\chi}) \int \mathrm{d}\Delta\chi\, \xi(R, \overline{z}) \tag{4.27}$$

where $R = \sqrt{\overline{\chi}^2\theta^2 + \Delta\chi^2}$.

Kaiser derived the Fourier analogue of Limber's equation (Kaiser 1992, Appendix A), which, as we will see, is even more useful because the result is simpler.

[4]The kernel functions expressed as a function of redshift and comoving distance are related by

$$W(z)\,\mathrm{d}z = W(\chi)\,\mathrm{d}\chi\,.$$

The two assumptions made above can be translated into the condition that there exists a distance scale $\delta\chi$ such that:

1. we can slice space into spherical shells of width $\delta\chi$, over which kernel functions can be considered constant;

2. these shells are statistically uncorrelated;

3. the small-scale assumption is that $\theta \ll \delta\chi/\overline{\chi}$, such that we can work under the flat-sky approximation.

The power from different shells can simply be summed to obtain the total power spectrum. Bartelmann and Schneider 2001 (see section 2.4.2) provide an equivalent derivation, which we outline here. The angular correlation function can be expressed, as in equation (4.27), as

$$\omega(\theta) = \int \mathrm{d}\chi\, W^A(\chi) \int \mathrm{d}\chi'\, W^B(\chi') \left\langle \delta(\chi\hat{\boldsymbol{n}}, z)\delta(\chi'\hat{\boldsymbol{n}}'), z' \right\rangle . \tag{4.28}$$

Expanding δ by its Fourier transform, and applying the same approximation for the kernels and the correlation function, we obtain

$$\begin{aligned}\omega(\hat{\boldsymbol{n}}\cdot\hat{\boldsymbol{n}}') = &\int \mathrm{d}\overline{\chi}\, W^A(\overline{\chi}) W^B(\overline{\chi}) \\ &\times \int \frac{\mathrm{d}^3\boldsymbol{k}}{(2\pi)^{3/2}} \int \frac{\mathrm{d}^3\boldsymbol{k}'}{(2\pi)^{3/2}} \underbrace{\left\langle \delta(\boldsymbol{k}, \overline{z})\delta(\boldsymbol{k}', \overline{z}) \right\rangle}_{\delta^{(3)}(\boldsymbol{k}-\boldsymbol{k}')P(k,\overline{z})} \int \mathrm{d}\chi'\, e^{i(\boldsymbol{k}\cdot\chi\hat{\boldsymbol{n}} - \boldsymbol{k}'\cdot\chi'\hat{\boldsymbol{n}}')}.\end{aligned} \tag{4.29}$$

The power spectrum is non-vanishing only if k-modes are equal, such that the integral over $\boldsymbol{k}'$ is removed. In the flat-sky limit, the unit vectors $\hat{\boldsymbol{n}}$ and $\hat{\boldsymbol{n}}'$ can be replaced by two-dimensional vectors $\boldsymbol{\theta}$ and $\boldsymbol{\theta}'$ living on the plane perpendicular to the line of sight and the Fourier modes can be decomposed as a radial mode $k_\parallel$ and a two-dimensional perpendicular mode $\boldsymbol{k}_\perp$. Therefore, the oscillating exponential can be replaced by

$$e^{ik_\parallel(\chi-\chi')} e^{i\boldsymbol{k}_\perp\cdot\chi(\boldsymbol{\theta}-\boldsymbol{\theta}')}. \tag{4.30}$$

The integral over χ' yields a Dirac distribution for $k_\parallel$, which means that only modes perpendicular to the line of sight contribute to the power spectrum. One can then perform the trivial integration over $k_\parallel$ and we obtain[5]

$$\omega(\theta) = \int \mathrm{d}\overline{\chi}\, W^A(\overline{\chi}) W^B(\overline{\chi}) \int \frac{\mathrm{d}^2\boldsymbol{k}_\perp}{(2\pi)^2} P\left(\|\boldsymbol{k}_\perp\|, \overline{z}\right) e^{i\boldsymbol{k}_\perp\cdot\chi\boldsymbol{\theta}}. \tag{4.31}$$

The last step consists of writing the power spectrum in the flat-sky approximation,

[5] We have replaced $\boldsymbol{\theta} - \boldsymbol{\theta}'$ by simply $\boldsymbol{\theta}$ because in the flat-sky approximation, we can set $\hat{\boldsymbol{n}}'$ to be the direction of the line of sight, such that $\boldsymbol{\theta}' = \boldsymbol{0}$.

which is related to the correlation function by

$$C^{AB}(\boldsymbol{l}) = \int \mathrm{d}^2\boldsymbol{\theta}\, \omega(\theta) e^{i\boldsymbol{l}\cdot\boldsymbol{\theta}}. \tag{4.32}$$

The integral over $\boldsymbol{\theta}$ yields a Dirac, imposing that $\boldsymbol{l} = \chi \boldsymbol{k}_\perp$, and we get

$$C^{AB}(\boldsymbol{l}) = \int \frac{\mathrm{d}\overline{\chi}}{\overline{\chi}^2} W^A(\overline{\chi}) W^B(\overline{\chi}) P\left(k = \frac{l}{\chi}, \overline{z}\right). \tag{4.33}$$

Finally, changing the integration variable to redshift, and going back the spherical harmonics spectrum, we get[6]

$$\boxed{C_\ell^{AB} = \int \mathrm{d}z\, \frac{H(z)}{c\chi(z)^2} W^A(z) W^B(z) P\left(k = \frac{\ell + 1/2}{\chi(z)}, z\right) + \mathcal{O}\left(\frac{1}{\ell^2}\right)} \tag{4.34}$$

where we have used that $k = (\ell + 1/2)/\chi(z)$ as shown in LoVerde and Afshordi 2008[7].

A few remarks are in order:

First, regarding the derivation of the Limber equation, it can be noted that the final result can be formally obtained using mathematical "tricks", the validity of which is harder to justify *a priori*. The spherical Bessel functions may be approximated by Dirac distribution around their maxima

$$j_\ell(x) \approx \sqrt{\frac{\pi}{2\ell + 1}} \delta\left(x - (\ell + 1/2)\right), \tag{4.35}$$

as noted in Campagne *et al.* 2017. One can also use the normalization of Bessel functions, given by

$$\int_0^\infty k^2\, \mathrm{d}k\, j_\ell(kr) j_\ell(kr') = \frac{\pi}{2r^2} \delta(r - r') \tag{4.36}$$

to approximate the integral over k in equation (4.25): if the power spectrum varies slowly in comparison to the Bessel functions, it can be taken out of the integral, evaluated at the peak of the integrand $(\ell + 1/2)/\chi(z)$, and the integral yields a Dirac imposing the equality of z and z' (Jeong 2010, Appendix M).

Then, it is important to note that the validity of the approximation is *a posteriori* justified by numerical comparison, which is done within the references cited above and on figure 4.9. The conclusion that all these studies have reached, in various cases, is that the Limber approximation is valid at small scale if the kernel functions are wide enough. It breaks down for small multipoles, generally for ℓ smaller than a few

[6] Though we have implicitly assumed flat spatial sections, it is worth noting that the Limber approximation can be also applied for curved space universe, as in Lesgourgues and Tram 2014, for instance.

[7] In this paper, the Limber approximation is extended to get an error of order $1/\ell^4$ at the price of computing derivatives of the power spectrum and of the kernels.

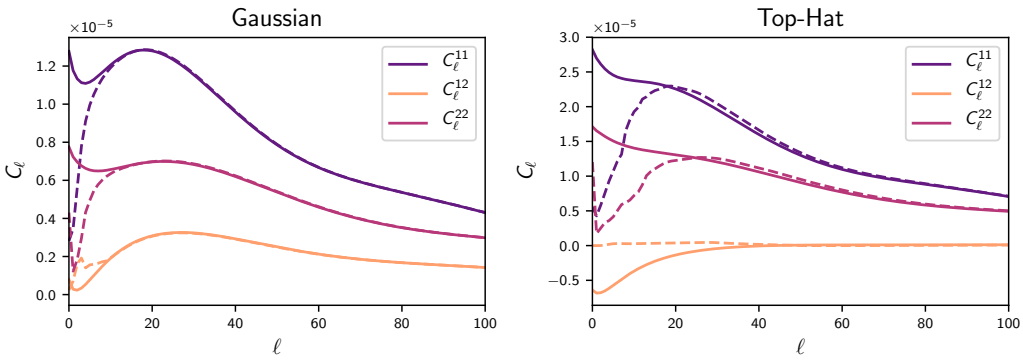

Figure 4.9 – Auto- and cross-spectra for two kernels centered on $\overline{z}_1 = 0.5$ and $\overline{z}_2 = 0.7$ with a half-width of 0.1, with a gaussian (left) and top-hat (right) shape. Solid lines show the spectra computed with the full formula (4.25) and dashed lines show the spectra computed with the Limber equation (4.34). All spectra were computed with the software `CLASSgal` (Di Dio *et al.* 2013).

tens, or for very narrow kernels, such as can be the case for thin redshift bins in the context of galaxy clustering[8] or galaxy lensing. When cross-correlating different or even non-overlapping redshift bins, anti-correlations may appear, due to interferences of the Bessel functions that cannot be captured by the Limber formula, since we sum only positive terms (see the cross-spectrum on the right panel of figure 4.9). Finally, the accuracy of the Limber approximation to evaluate the weak lensing power spectrum is still a matter of concern for future surveys such as LSST and Euclid (Kitching *et al.* 2017; Lemos *et al.* 2017).

4.2.2.3 Another expression

Some observables may not be written as projections of the matter density field like in equation (4.17). For instance, the temperature anisotropies imprinted by the integrated Sachs-Wolfe effect are given by (see, *e.g.* Takeuchi *et al.* 2012)

$$\Theta_{\rm ISW}(\hat{\boldsymbol{n}}) = -\frac{2}{T_{\rm CMB}} \int_0^{\chi_*} \dot{\Phi}(\chi\hat{\boldsymbol{n}}, \chi)\, \mathrm{d}\chi\,, \tag{4.37}$$

where $\dot{\Phi}$ is the time derivative of the gravitational potential. As seen at the end of chapter 1, the initial conditions of all cosmological fields are specified by the primordial gravitational potential $\Phi(k)$, therefore, they can always be written, in Fourier space, as this primordial gravitational potential times a transfer function. Thus, all projected variables may be written

$$A(\hat{\boldsymbol{n}}) = \int \mathrm{d}z \int \frac{\mathrm{d}^3\boldsymbol{k}}{(2\pi)^{3/2}} T^A(k,z)\Phi(k) e^{i\boldsymbol{k}\cdot\chi\hat{\boldsymbol{n}}}, \tag{4.38}$$

[8] Noticeably, in the case of very narrow redshift bins, redshift-space distortions can have non-negligible effects at both large and small angular scales, as shown in Saito 2016.

where $T^A(k,z)$ is a transfer function, specific to observable A. Then, the same computation as in section 4.2.2.1 leads to

$$\boxed{C_\ell^{AB} = \frac{2}{\pi}\int k^2\,\mathrm{d}k\,\Delta^A(k)\Delta^B(k)P_\Phi(k)}, \tag{4.39}$$

where $P_\Phi(k)$ is the power spectrum of the primordial gravitational potential and

$$\Delta^A(k) = \int \mathrm{d}z\,T^A(k,z)j_\ell(k\chi(z)). \tag{4.40}$$

This can be related to the kernels in the previous section by

$$T^A(k,z) = W^A(z)T_\mathrm{m}(k)D(z), \tag{4.41}$$

where $T_\mathrm{m}(k)$ is the matter density fluctuations transfer function[9] and $D(z)$ is the growth factor, such that $\delta(\boldsymbol{k},z) = T_\mathrm{m}(k)D(z)\Phi(k)$. This expression, though exact, is computationally expensive because of the Bessel integrals.

4.2.3 Other techniques

4.2.3.1 Stacking

Stacking techniques consists in summing "stamp" samples of a map, cut around specific positions and potentially rotated (possibly randomly). This technique can be used for cross-correlation studies as visual confirmation, if one observable is suspected to have a specific pattern or signature around locations determined by another variable.

It has been used, for instance, by the Planck Collaboration in the cross-correlation of the gravitational lensing map with the cosmic infrared background (CIB) in Planck Collaboration *et al.* 2014c. The CIB is composed of the redshifted thermal radiation of stellar dust heated by the ultraviolet radiation of young stars. It has thus been emitted by dusty, star-forming galaxies that are found at redshift $z \sim 1-2$. Therefore, the kernels of lensing and CIB have a large overlap, which means that the galaxies sourcing the CIB have an significant contribution to the lensing of the CMB, explaining the intensity of the signal (see the stacked images on figure 4.10).

It has also been used by the Planck Collaboration in Planck Collaboration *et al.* 2016i to highlight the cross-correlation of the CIB with the Sunyaev-Zel'dovich effect, by stacking CIB maps at different frequencies at the position of clusters detected by their SZ signal (see figure 4.11).

[9] Not to be confused with the transfer function $T_\Phi(k)$ of the gravitational potential defined in equation (1.73), though they play a similar role.

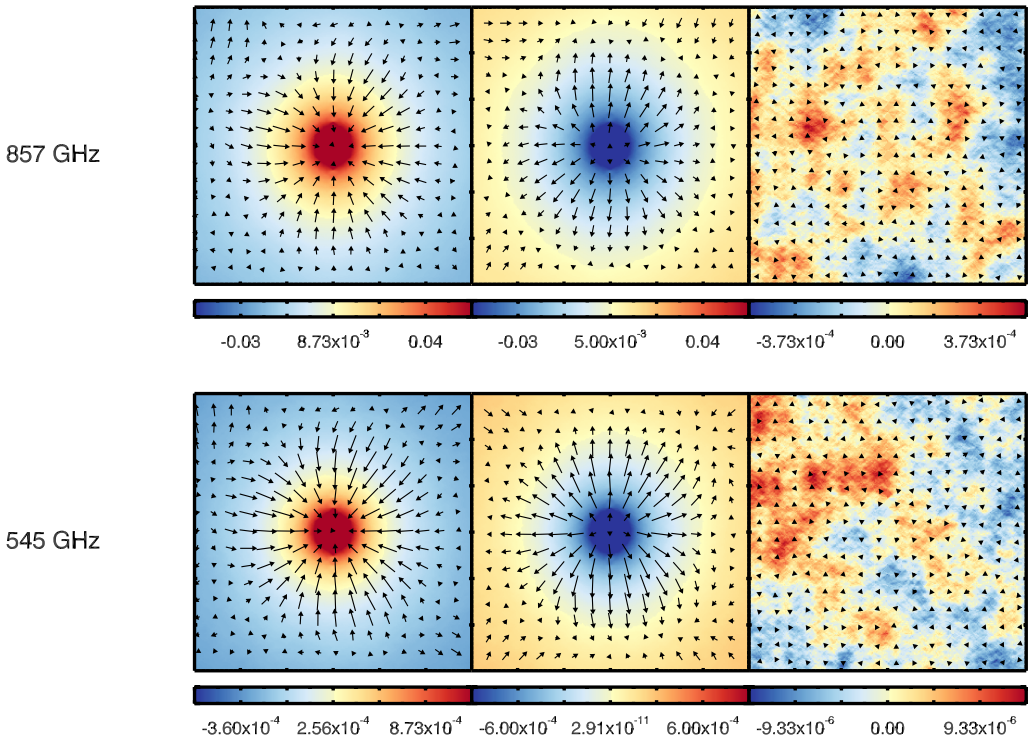

Figure 4.10 – Planck temperature maps at 545 and 857 GHz stacked at peaks (left), troughs (middle) and random locations (right) of the CIB, surperimposed with the lensing deflection angle represented by arrows (from Planck Collaboration *et al.* 2014c).

4.2.3.2 Non-monotonic correlation

Consider a random variable X, uniformly distributed over the interval $]-\pi, \pi]$ and the random variable $Y = \cos X$. Y is deterministically determined by X, however, their covariance is $\langle XY \rangle = 0$ (both have null expectation value). Therefore, the covariance only captures the linear correlation between variables. Other similar examples are shown in the third row of figure 4.12.

In order to quantify the correlation between variables, one can measure the reduction of uncertainty in Y after observing X. Probability distributions can be compared by a distance called the Kullback-Leibler divergence (Kullback and Leibler 1951). For two probability distributions, *i.e.* two finite measures on a probability space Ω, P and Q, the Kullback-Leibler divergence from Q to P is formally defined as

$$D_{\mathrm{KL}}(P \parallel Q) = \left\langle \ln \frac{\mathrm{d}P}{\mathrm{d}Q} \right\rangle_P = \int_\Omega \ln \frac{\mathrm{d}P}{\mathrm{d}Q} \, \mathrm{d}P \,, \tag{4.42}$$

where $\frac{\mathrm{d}P}{\mathrm{d}Q}$ is the Radon-Nikodym derivative of P with respect to Q (Le Gall 2006). For continuous distributions over $\mathbb{R}^k$ (*i.e.* if P and Q are absolutely continuous with

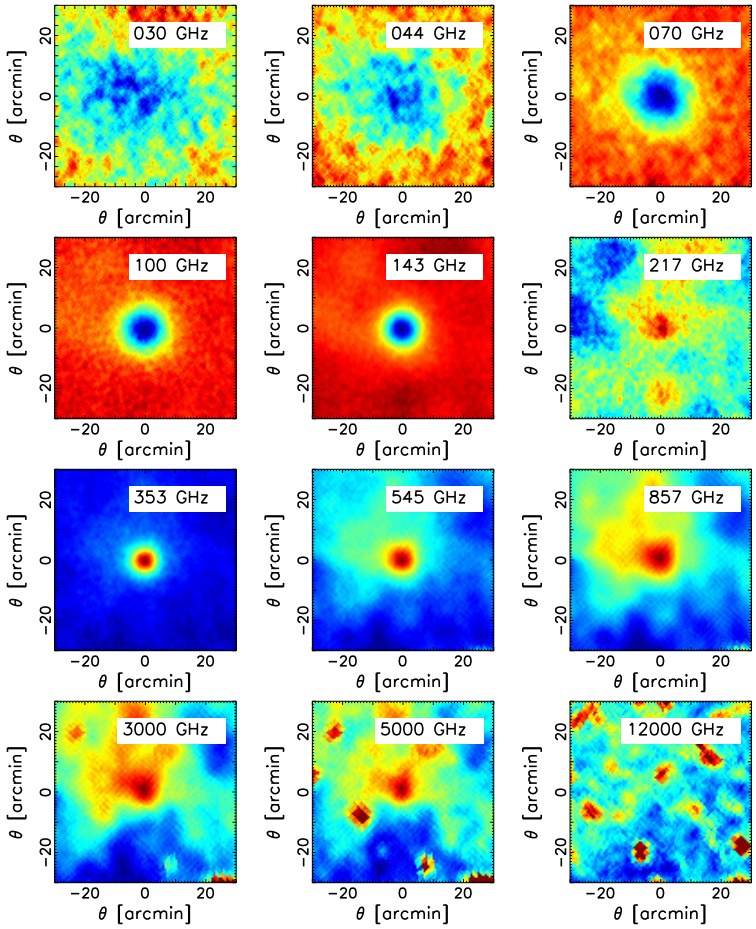

Figure 4.11 – Planck CIB maps stacked at the position of SZ-detected clusters (from Planck Collaboration *et al.* 2016i).

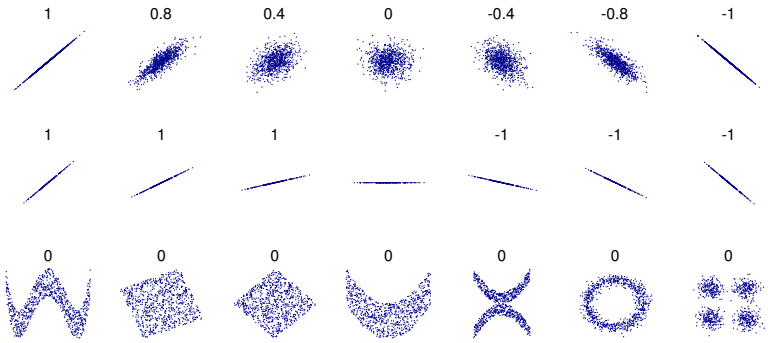

Figure 4.12 – Examples of scatter plots of two random variables with their linear correlation coefficients. In the third row, variables are clearly correlated, in the sense that knowing the value of one gives information on the other, but their linear correlation coefficient is zero. Figure from https://en.wikipedia.org/wiki/Correlation_and_dependence published under licence CC0 1.0.

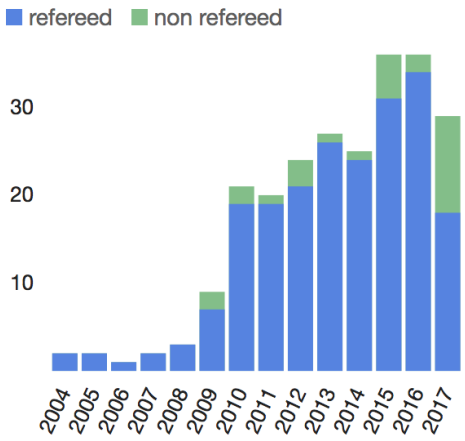

Figure 4.13 – Number of papers in the arXiv `astro-ph.CO` stream with a title containing "cross-correlation" or "joint analysis" since 2004.

respect to the Lebesgue measure), it is given by

$$D_{\mathrm{KL}}(P \parallel Q) = \int_{\mathbb{R}^k} p(x) \ln \frac{p(x)}{q(x)} \, \mathrm{d}^k x \,. \tag{4.43}$$

For instance, for two multivariate gaussian distributions, $P, Q \sim \mathcal{N}\left(\mu_{P,Q}, \Sigma_{P,Q}\right)$, we have

$$D_{\mathrm{KL}}(P \parallel Q) = \frac{1}{2}\left[\mathrm{Tr}\left(\Sigma_Q^{-1}\Sigma_P - \mathbb{1}\right) + \left(\mu_Q - \mu_P\right)^\intercal \Sigma_Q^{-1}\left(\mu_Q - \mu_P\right) + \ln\left(\frac{|\Sigma_Q|}{|\Sigma_P|}\right)\right]. \tag{4.44}$$

Then, one defines the *mutual information* of two random variables X and Y as the Kullback-Leibler divergence from the product of marginal distributions to the joint probability distribution

$$I(X;Y) \equiv D_{\mathrm{KL}}(P(X,Y) \parallel P(X)P(Y)), \tag{4.45}$$

which is exactly the difference of entropies that we computed in equation (4.5). Finally, it can be related to the *cross-entropy*, widely used in statistical learning (Hastie *et al.* 2013), as

$$S(P;Q) = \langle -\ln Q \rangle_P = S(P) + D_{\mathrm{KL}}(P \parallel Q). \tag{4.46}$$

4.3 Cross-correlations

The first cross-correlation studies in cosmology emerged in the early 2000s, and, with increasing amounts of cosmological data, their number kept growing (see figure 4.13). The goal of this section is to review the literature while demonstrating the numerous possibilities to not only detect predicted signal, but also advance our understanding of the Universe and its content.

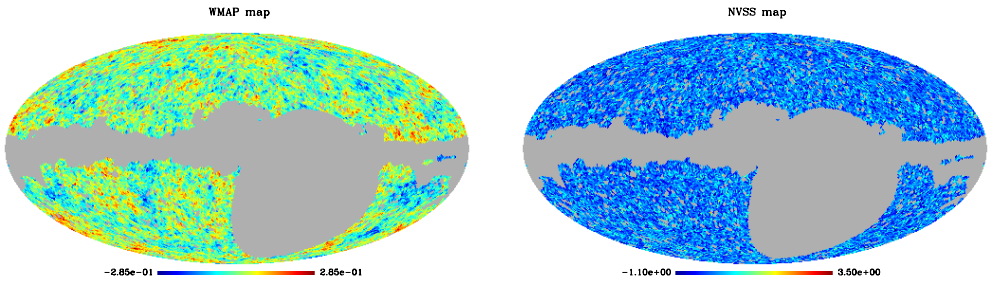

Figure 4.14 – WMAP and NVSS maps at low resolution cross-correlated in Vielva *et al.* 2006.

4.3.1 The first studies: CMB × LSS

The first studies that tried to measure cross-correlations between the CMB and tracers of the large-scale structure were published in the early 2000's. They were cross-correlating temperature fluctuations in the CMB with various tracers with two main purposes (Peiris and Spergel 2000; Wang *et al.* 1999):

- to detect the integrated Sachs-Wolfe effect (also referred to as the Rees-Sciama effect in the non-linear regime, see Crittenden and Turok 1996), which is visible at large scale in the CMB ($\ell \lesssim 10$) and is a direct measurement of the decay of gravitational potential wells due to the cosmic expansion fueled by dark energy;
- to detect the Sunyaev-Zel'dovich effect, which is the spectral imprint left by CMB photons scattered by free electrons, tracing hot gas in galaxy clusters visible in the X-ray domain.

Indeed, these secondary anisotropies are small effects, difficult to disentangle from primary anisotropies or systematics in the map of the CMB alone. However, they are produced by interactions – gravitational or electromagnetic – of CMB photons with the large-scale structure of the Universe. Hence, they have a small, but non-zero, correlation with any tracer of the large-scale structure. Comparing maps thus helps localize these effects on the CMB map.

To this end, the map of CMB temperature anisotropies measured by the COBE (Smoot *et al.* 1990) and WMAP (Bennett *et al.* 2003) satellites were successively correlated with the overdensity maps of radio sources from the NRAO VLA Sky Survey (NVSS, Condon *et al.* 1998) in Boughn and Crittenden 2001, with near-infrared 2MASS galaxies (Jarrett *et al.* 2000) in Afshordi *et al.* 2004, with visible luminous red galaxies and Lyman-α forest in quasars' spectra from the Sloan Digital Sky Survey (SDSS York *et al.* 2000) in Cabré *et al.* 2006; Fosalba *et al.* 2003 and Croft *et al.* 2006 and with X-ray sources from ROSAT (Snowden *et al.*

1997) in Diego *et al.* 2003. These papers, among others, detected the SZ or the ISW effects at different statistical significance levels and placed, at least, upper bounds on dark energy or the density of hot gas in the Universe.

4.3.2 Gravitational lensing comes into play

4.3.2.1 CMB lensing

Gravitational lensing of the CMB (see section 2.3.2) is an extremely powerful probe of the large-scale structure that weighs all matter – dark matter *and* baryons – between us and the last scattering surface. Detecting CMB lensing only with a CMB map requires the measurement of a 4-point correlation function of temperature. Therefore, it is not surprising that CMB lensing was first detected using cross-correlation of a reconstructed CMB lensing map (2-point function only) with tracers. After a missed attempt by Hirata *et al.* 2004 using SDSS galaxies (the signal-to-noise ratio was too low at the time), it was detected for the first time using the NVSS sample and the WMAP CMB data by Smith *et al.* 2007. See section 4.A for a comparison of the signal-to-noise ratio of auto- and cross-power spectra.

The galaxy density-CMB lensing cross-correlation compares the distributions of dark matter and that of galaxies. The amplitude of its cross-power spectrum is an unbiased estimate of the clustering bias of galaxies at large scale, that can be compared to other measurements as a consistency check. It has been measured for many combinations of CMB data and galaxy samples (see table 4.1) and has become a widely used probe.

The South Pole Telescope (Carlstrom *et al.* 2011) and the PolarBear (Kermish *et al.* 2012) collaborations detected, the same way as Smith *et al.* 2007, the lensing of CMB's polarization by cross-correlating their lensing map, reconstructed from polarization maps, with the CIB map of the Herschel satellite (Pilbratt *et al.* 2010) in Hanson *et al.* 2013 and Ade *et al.* 2014.

4.3.2.2 Galaxy lensing

Galaxy lensing has recently been used in cross-correlation analyses in various ways. The shear measured in a source redshift bin can be correlated with itself, a measurement called *cosmic shear*, but it can also be correlated with the density of galaxies in foreground redshift bins causing the lensing of sources, often referred to as *galaxy-galaxy lensing*, and with CMB lensing.

The first detections of the cross-correlation between galaxy lensing and CMB lensing used CFHT[10] data with ACT lensing map in Hand *et al.* 2015, and then with Planck lensing map in Liu and Hill 2015. The DES Collaboration reported a measurement of the cross-correlation between their lensing map and the CMB lensing

[10] Canada-France-Hawaii Telescope with the MegaCam imaging camera, Boulade *et al.* 2002.

Table 4.1 – List of references measuring the cross-correlation between CMB lensing and various galaxy samples observed in different parts of the electromagnetic spectrum.

CMB experiment	Galaxy sample	Wavelength	Reference
WMAP[a]	NVSS[b]	Micro-waves	Smith *et al.* 2007
SPT[c]	WISE[d] & Spitzer/IRAC[e]	Near-IR	Bleem *et al.* 2012
ACT[f]	SDSS[g] XDQSO quasars[h]	Visible	Sherwin *et al.* 2012
SPT[c]	WISE[d]	Near-IR	Geach *et al.* 2013
SPT[c]	Herschel[i]/SPIRE[j]	sub-mm	Holder *et al.* 2013
Planck[k]	Planck CIB map	Far-IR	Planck Collaboration *et al.* 2014c
Planck[k]	SDSS[g] & WISE[d]	Visible & near-IR	DiPompeo *et al.* 2015
Planck[k]	Herschel[i] ATLAS[l]	Far-IR & sub-mm	Bianchini *et al.* 2015, 2016
Planck[k]	Fermi-LAT[m]	Gamma-ray	Fornengo *et al.* 2015
ACT[f]	FIRST[n]	Radio	Allison *et al.* 2015
SPT[c] & Planck[k]	DES-SV[o]	Visible	Giannantonio *et al.* 2016

[a] Wilkinson Microwave Anisotropy Probe, Bennett *et al.* 2003.
[b] NRAO VLA Sky Survey, Condon *et al.* 1998.
[c] South Pole Telescope, Carlstrom *et al.* 2011.
[d] Wide-field Infrared Survey Explorer, Wright *et al.* 2010.
[e] Spitzer Deep, Wide-Field Survey, Ashby *et al.* 2009.
[f] Atacama Cosmology Telescope, Swetz *et al.* 2011.
[g] Sloan Digital Sky Survey, Eisenstein *et al.* 2011.
[h] See Bovy *et al.* 2011.
[i] ESA's Herschel satellite, Pilbratt *et al.* 2010.
[j] Spectral and Photometric Imaging REceiver, Griffin *et al.* 2010.
[k] ESA's Planck satellite, Planck Collaboration *et al.* 2011.
[l] Herschel Astrophysical Terahertz Large Area Survey, Eales *et al.* 2010.
[m] Fermi Large Area Telescope, Abdo *et al.* 2010.
[n] Faint Images of the Radio Sky at Twenty Centimeters, Becker *et al.* 1995.
[o] Dark Energy Survey Science Verification data, Dark Energy Survey Collaboration *et al.* 2016.

maps from Planck and SPT (Kirk *et al.* 2016). Another study, Harnois-Déraps *et al.* 2016, reported detection of the galaxy lensing-CMB lensing cross-correlation using CFHT data (both the CFHT Lensing Survey and the RCS[11] Survey) with Planck's lensing map, both in real-space and in configuration space. This specific cross-correlation is still in its infancy, but is believed to become a powerful tool for shear calibration. The reason is that galaxy lensing requires the measurement of galaxy shapes and orientations from noisy images that are blurred by an varying point-spread function (the image of a point source produced by the telescope). Estimators of the shear $\boldsymbol{\gamma}$ might thus be affected by a multiplicative bias m such that

$$\langle\hat{\boldsymbol{\gamma}}\rangle = (1+m)\boldsymbol{\gamma}_{\rm true}, \tag{4.47}$$

which is difficult to detect with shear measurements alone. However, it appears in the galaxy lensing-CMB lensing cross-correlation as a simple multiplicative factor and can then be easily calibrated (Liu *et al.* 2016b; Schaan *et al.* 2017; Vallinotto 2012). The question whether this will be enough to meet weak lensing science requirements of future surveys, of order $|m| \lesssim 10^{-3}$, is still open.

Galaxy-galaxy lensing measurements were reported by the DES Collaboration

[11] Red Cluster Sequence, Gilbank *et al.* 2011.

(Chang *et al.* 2016) and used to measure the bias of the lens galaxies. Importantly, though cross-correlation are generally less prone to experimental systematics, they can be contaminated by physical effects. In the case of galaxy-galaxy lensing, the intrinsic alignments of galaxies produced by tidal torquing and filaments correlates with the density of galaxies, thus contaminating the cross-correlation measurement (Hall and Taylor 2014; Joachimi and Bridle 2010; Larsen and Challinor 2016; Troxel and Ishak 2014). However, it also contains cosmological information about the formation of structures that might be exploited (Chisari and Dvorkin 2013).

Interestingly, the comparison of the cross-correlations of galaxy positions with CMB lensing and with galaxy lensing, $C_\ell^{\kappa_{\rm gal}g} \Big/ C_\ell^{\kappa_{\rm CMB}g}$ yields a ratio of distances that is independent of galaxy bias or lensing bias, provided that the redshift bin is thin enough Miyatake *et al.* 2017; Singh *et al.* 2017. This offers a new cosmographic measurement at intermediate redshifts and a new consistency test.

Finally, Demetroullas and Brown 2016 reported a detection of cosmic shear by cross-correlating lensing maps from SDSS and FIRST, even though both surveys' auto-correlation measurements are independently systematics-dominated. This opens a new route that may be useful for future surveys with very different systematics (especially when combining ground- and space-based experiments, see section 4.4.2).

4.3.2.3 Clusters and the Sunyaev-Zel'dovich effect

The thermal Sunyaev-Zel'dovich (tSZ) effect has been measured by the Planck Collaboration, which produced an all-sky map of the Compton-y parameter (Planck Collaboration *et al.* 2014e) and extracted cosmological information from SZ-detected clusters (Planck Collaboration *et al.* 2014d). It has been correlated with the map of CMB lensing by Hill and Spergel 2014, demonstrating that baryons trace dark matter down to scales of order 1 Mpc.

The kinetic Sunyaev-Zel'dovich (kSZ) effect is produced by the bulk velocity of free electrons in hot gas and is an order of magnitude smaller than the tSZ effect. Moreover, its electromagnetic spectrum does *not* differ from that of the CMB, unlike the tSZ effect (see section 2.1.3), making it impossible to detect without external information. It was first detected by Hand *et al.* 2012 with the pair-wise velocity technique (relying on the fact that, on average, two nearby galaxies are likely falling towards each other) and then with the full reconstructed velocity field by Planck Collaboration *et al.* 2016l and Schaan *et al.* 2016. These studies have shown clear evidence that a non-negligible fraction of baryons is located in diffuse, warm-hot plasmas around haloes, resulting a electron pressure profile larger than the halo size. This cross-correlation signal can be used to constrain feedback mechanisms from, *e.g.*, active galactic nuclei. While these studies relied on spectroscopic observations to infer the velocity of the clusters, a novel method has recently been suggested (and

successfully applied) to measure the kSZ effect with projected density fields, hence opening the possibility of using any kind of tracer (Ferraro *et al.* 2016; Hill *et al.* 2016).

Finally, the tSZ effect can be used to obtain a proxy of the mass of individual clusters, which can be compared to the mass inferred from the X-ray luminosity. However, it has been shown that it is also possible to infer an unbiased estimate of the mass of a cluster from its contribution to CMB lensing and use it to calibrate the mass-luminosity relationship (Melin and Bartlett 2015; Penna-Lima *et al.* 2017).

4.3.3 Combining tracers of the large-scale structure

4.3.3.1 Combining photometric and spectroscopic surveys

Several avenues exist to take advantage of overlapping photometric and spectroscopic surveys. Cai and Bernstein 2012 and Gaztañaga *et al.* 2012 advocate that galaxy-galaxy lensing cross-correlations – where the density is that mapped by the spectroscopic survey – can constrain galaxy clustering biases and hence break the degeneracy with the redshift-space distortion parameter f, thus enabling better constraints on structure formation. Moreover, matching galaxies seen in both surveys makes it possible to use many narrow redshift bins for weak lensing measurements, and thus to follow the onset of dark energy at a much better resolution. The development of estimators that can extract the radial information from multi-resolution surveys, *e.g.* based on spherical Fourier-Bessel decomposition, is ongoing (Passaglia *et al.* 2017).

Methods to optimally combine multiple tracers are being developed (Abramo *et al.* 2016) that extend the FKP optimal power spectrum estimator for a single type of tracer (Feldman *et al.* 1994). The so-called ultra-large scales are of particular interest for measuring deviations from general relativity and from gaussianity, and they will greatly benefit from the combination of multiple tracers with very different biases (Alonso and Ferreira 2015; Seljak 2009).

4.3.3.2 Studying the epoch of reionization with 21 cm intensity mapping

Combining 21 cm intensity mapping with other spectroscopic and photometric tracers can potentially greatly improve the mapping of the large-scale structure (Jelic *et al.* 2015) and the measurement of the BAO scale (Cohn *et al.* 2016). Moreover, it provides new powerful a tool to compare the distribution of neutral hydrogen with that of galaxies during the epoch of reionization (EoR). In particular, it may be used to study the morphology of reionization (for instance by combining 21 cm intensity mapping and Lyman-α emitters, see Sobacchi *et al.* 2016; Vrbanec *et al.* 2016).

Finally, 21 cm intensity mapping should put stringent constraints on the Universe's reionization history, thus providing a strong handle on the optical depth τ (Liu *et al.*

2016a). This information might then be used as a prior – or better, in a joint analysis with CMB data – to break degeneracies amongst parameters (in particular with the primordial spectrum amplitude A_s).

4.3.3.3 The extragalactic γ-ray background and dark matter

The extragalactic γ-ray background (EGB) is the combined emission of unresolved objects (Ajello *et al.* 2015) such as blazars (quasars with jets in the direction of observation), star-forming galaxies and radio galaxies. Their distance is poorly constrained by γ-ray observations alone. However, by cross-correlating the EGB with spectroscopic tracers in a tomographic fashion, it is possible to constrain the redshift distribution of γ-ray emitters (Cuoco *et al.* 2015; Xia *et al.* 2015). The EGB might also contain a truly diffuse component. Indeed, various models of dark matter predict that the desintegration of WIMPs produces γ-rays. Comparing fluctuations in the EGB with the CMB lensing map (which essentially traces dark matter) can constrain the annihilation rate and mass of dark matter particles (Tröster *et al.* 2017).

4.3.3.4 Testing general relativity

Modified theories of general relativity can be parametrized by two scale- and redshift-dependent arbitrary functions $\mu(k,z)$ and $\gamma(k,z)$ modifying the Poisson equation (1.50) and the relationship between gravitational potentials as

$$k^2\Psi = 4\pi G a^2 \bar{\rho}\mu(k,z)\delta(k,z) \tag{4.48}$$

$$\Phi = \gamma(k,z)\Psi. \tag{4.49}$$

Lensing is sensitive to $\nabla^2(\Psi+\Phi)$ while the velocity field is sensitive to Φ only equation (1.49) . Bearing that in mind, one defines a statistic

$$E_G(k,z) = -\frac{k^2(\Psi+\Phi)}{3H_0^2(1+z)\theta(k,z)}, \tag{4.50}$$

where $\theta(k,z) \equiv \boldsymbol{\nabla}\cdot(a\boldsymbol{v})/aH$ is the divergence of the peculiar velocity field (defined in section 1.4.2.1), which, in the linear regime, is $\theta(k,z) = f(z)\delta(k)$[12]. Thus, we have

$$E_G(k,z) = \frac{\Omega_\mathrm{m}^0\mu(k,z)[\gamma(k,z)+1]}{2f(z)}, \tag{4.51}$$

which simplifies to $E_G(k,z) = \Omega_\mathrm{m}^0 \Big/ f(z)$ within general relativity. In practice, it can be measured by comparing the CMB lensing-galaxy cross-correlation to the

[12] To prove this, we use the the continuity equation, which implies that $\theta = -\dot{\delta}/H$. Since $\delta(t) \propto D(t)$ where D is the growth factor defined in section 1.4.1, we have $\dot{\delta} = H(z)f(z)\delta$, where $f(z) \equiv \mathrm{d}\ln D/\mathrm{d}\ln a$, which leads to the result.

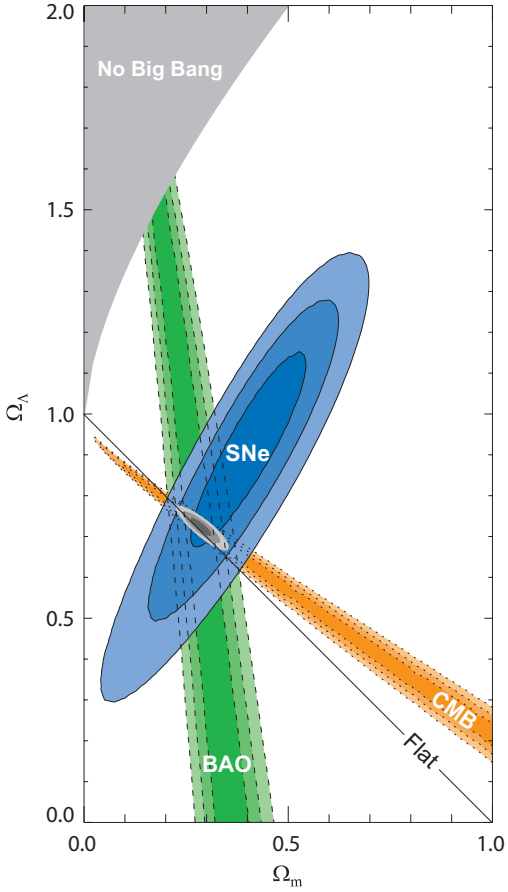

Figure 4.15 – The combination of independent probes – here, CMB, distances from type IA supernovæ and the BAO in galaxies – was used to contrain the parameters of the ΛCDM model by multiplying the likelihoods of each individual probe (figure from Kowalski *et al.* 2008).

auto-correlation of galaxies as (Blake *et al.* 2016; Pullen *et al.* 2016)

$$E_G(\ell, z) = \Gamma \frac{C_\ell^{\kappa g}}{\beta C_\ell^{gg}} \tag{4.52}$$

where $\beta(z) = f(z)/b(z)$, such that the galaxy bias should cancel if the redshift bins are narrow enough (small lensing correction are derived in Moradinezhad Dizgah and Durrer 2016). Pullen *et al.* 2016 found a small tension with the prediction from general relativity, using the CMASS sample from SDSS-III/BOSS at scales greater than $80\,h^{-1}$ Mpc.

4.4 Joint analyses

4.4.1 Current status

The combination of constraints obtained from independent probes led to the current picture of the ΛCDM model (see figure 4.15). However, galaxy surveys – photometric and spectroscopic – and CMB mapping experiments are probing the same underlying matter density field *via* different related physical fields. Early "combined" analyses of CMB and large-scale structure did not include cross-correlations: they treated various probes as independent and multiplied the likelihood to obtain constraints on cosmological parameters (Tegmark and Zaldarriaga 2002; Tegmark *et al.* 2001). As shown in the previous section, these probes *are* correlated, which means that there is additional, complementary information in their combination that should be treated in statistical pipelines.

Joint analyses are still at an early stage, the main reason being that cross-correlation signals needed to be detected at a significant signal-to-noise ratio before they can be used in a statistical analysis. Now, cross-correlations are becoming standard statistical tools in the field of cosmology and joint analyses are blooming.

Joachimi and Bridle 2010 forecasted that the joint analysis of galaxy weak lensing and galaxy density, including cosmic shear, galaxy clustering and the galaxy-galaxy lensing cross-correlation, could, at once, self-calibrate intrinsic alignments and constrain parameters of the cosmological model (see Krause *et al.* 2016 as well). Several analyses were recently published that make use of the correlation between galaxy lensing and either galaxy density or CMB lensing: Baxter *et al.* 2016 used SPT and DES-SV lensing data together with tracers of the large-scale structure and took advantage of the low systematic level of these correlations to infer cosmological constraints, Kwan *et al.* 2017 used the galaxy clustering and galaxy-galaxy lensing signals of the DES-SV data with similar goals and Singh *et al.* 2017 combined the lensing and clustering of SDSS galaxies with CMB lensing from Planck. Very recent studies combined these three correlation function in a single analysis: Uitert *et al.* 2017 with KiDS[13] and GAMA[14] galaxies, Joudaki *et al.* 2017 with KiDS and BOSS galaxies (using the quadrupole of the power spectrum as well), DES Collaboration *et al.* 2017 with the first year of DES data (forecasts were obtained in Park *et al.* 2016 and the pipeline was tested on simulated images in Krause *et al.* 2017), and Miyatake *et al.* 2015; More *et al.* 2015 used the overlapping area between CFHT and BOSS galaxies.

Takada and Spergel 2014 showed that if cluster counts are analyzed together with weak lensing, the first could be used to infer the super-sample variance[15] term

[13] The Kilo-Degree Survey, Jong *et al.* 2013.

[14] Galaxies And Mass Assembly (Driver *et al.* 2009), a database of low-redshift surveys spanning the electromagnetic spectrum from radio waves to the ultraviolet domain.

[15] The super-sample variance is related to density modes larger than the size of the survey that

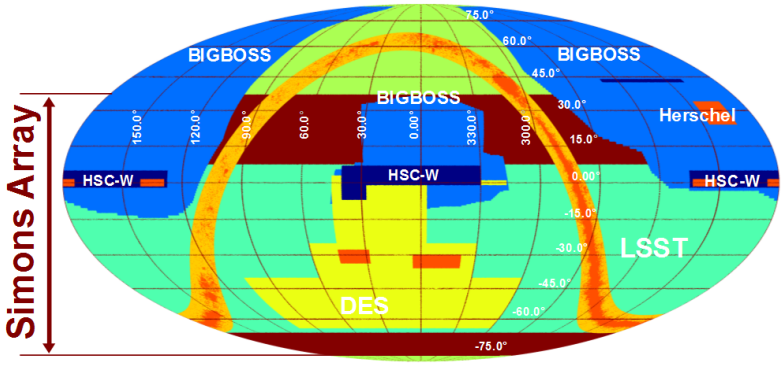

Figure 4.16 – Sky areas mapped by ongoing and future surveys (from Arnold *et al.* 2014)

.

in the weak lensing power spectrum and thus improve the cosmological constraints as if multiplying the survey size by a factor $\sim 2-4$ (another similar study can be found in Yoo and Seljak 2012). Soergel *et al.* 2015 and Giannantonio and Percival 2014 used CMB temperature data and the temperature-galaxy density and CMB lensing-galaxy density cross-correlations to place limits on, respectively, perturbations of the dark sector (*i.e.* assuming that dark energy is a fluctuating field) and primordial non-gaussianity.

Finally, a further step was taken by Nicola *et al.* 2016, 2017 which uses CMB temperature, CMB lensing, galaxy positions, galaxy lensing and distances (from supernovæ and direct H_0 measurements) in a fully joint analysis.

4.4.2 Forecasts

Upcoming large photometric and spectroscopic galaxy surveys – the Large Synoptic Survey Telescope (LSST, LSST Science Collaborations and LSST Project *et al.* 2009), Euclid (Laureijs *et al.* 2011), the Wide Field Infrared Survey Telescope (WFIRST, Spergel *et al.* 2013) and the Dark Energy Spectroscopic Instrument (DESI, Levi *et al.* 2013; Schlegel *et al.* 2009) – and CMB experiments – the Simons Observatory (Suzuki *et al.* 2016) and a Stage-IV CMB experiment (CMB-S4, Abazajian *et al.* 2016) – will map overlapping, wide areas to unprecedented sensitivity (see figure 4.16).

Forecasts and science requirement studies estimate the improvement on cosmological parameters constraints from each individual experiment. However, several works have shown that the combination of these experiments should yield, by far, the most substantial gain for shear calibration (Schaan *et al.* 2017), intrinsic alignements mitigation (Krause *et al.* 2016), the mass of neutrinos (Pearson and Zahn 2014), primordial non-gaussianity (Takeuchi *et al.* 2012), modified gravity (Casas *et al.*

contribute to the observed power. See chapter 6 and Schaan *et al.* 2014 for more detail.

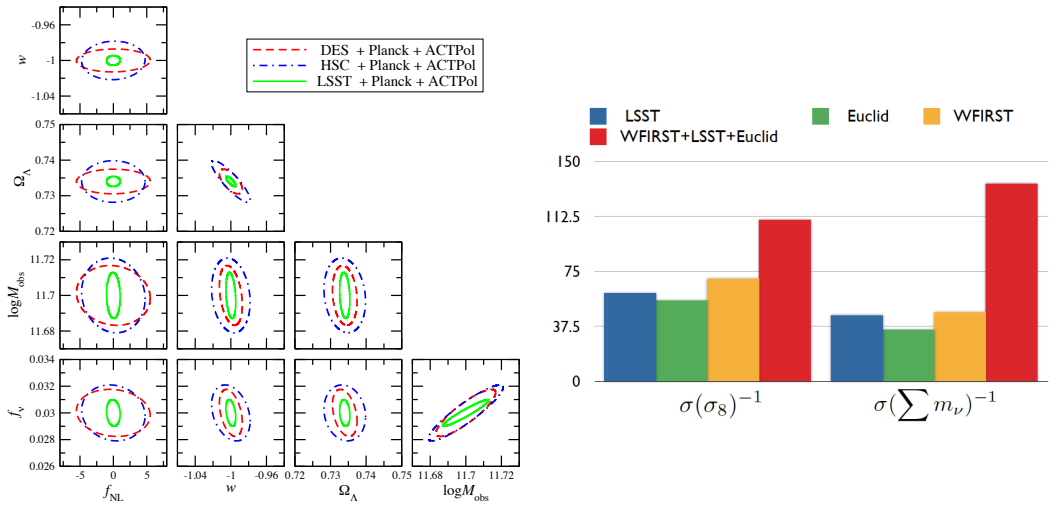

Figure 4.17 – Forecast cosmological constraints on non-gaussianity parameters (left, from Takeuchi *et al.* 2012) and large-scale structure (right, from Jain *et al.* 2015). In both cases, the combination of surveys with complementary observations or instrumental design dramatically improves the constraints.

2017) and cosmology in general (see Rhodes *et al.* 2015, for a review).

In an effort to improve the joint scientific impact of LSST, Euclid and WFIRST, Jain *et al.* 2015 pointed out strategies to take advantage of complementary instrumental characteristics. These include:

Photometric redshifts Errors on photometric redshifts from LSST could be greatly reduced by integrating infrared band observations from Euclid and WFIRST. Moreover, galaxies observed by the spectroscopic instruments of Euclid and WFIRST can be used to calibrate algorithms (for instance as a training set for machine learning algorithms).

Weak lensing Euclid will have much better resolution than LSST as it is not affected by the atmosphere, thus providing a useful input for deblending[16] algorithms. However, its wide infrared band makes it sensitive to all kinds of chromatic effects due to the diffraction-limited, wavelength-dependent PSF. In particular, Euclid should be more sensitive to the bulge of galaxies; LSST, with its greater depth, will see their outskirts; WFIRST will be somewhere in between. Comparing shear estimates from ground- and space-based experiments can improve shear calibration and the cross-correlations of independently estimated shear maps should remove systematics and/or reveal unforeseen ones.

Large-scale structure Spectroscopic observations by Euclid and WFIRST will be used to measure the scale of the baryon acoustic oscillations and the growth of structure. Photometric observations by LSST will probe clustering through

[16] It is expected that of order half of images of galaxies observed by LSST will overlap. Separating these images is called *deblending*.

projected galaxy number density maps and the measurement of tomographic angular power spectra. The combination of these different approaches should provide much tighter constraints on, *e.g.*, σ_8 and the sum of neutrino masses, as shown on figure 4.17.

Carrying a joint analysis is a technical challenge with needs of joint simulations and common pipelines and data access facilities, but the benefits will be great for science.

Appendices

4.A Signal-to-noise ratio: auto- *vs* cross-correlation

As shown in appendix B.1.2, the variance of the angular power spectrum is given by

$$\left(\Delta C_\ell^{AB}\right)^2 = \frac{D_\ell^{AA} D_\ell^{BB} + D_\ell^{AB\,2}}{2\ell + 1} \tag{4.53}$$

where

$$D_\ell^{AB} = \begin{cases} C_\ell^{AA} + N_\ell^A & \text{if } A = B \\ C_\ell^{AB} & \text{otherwise,} \end{cases} \tag{4.54}$$

where N_ℓ^A is the noise power spectrum. As stated earlier, the noises from two different observables do not correlate, and, in principle, cross terms involving noise not contribute to the variance. Therefore, the ratio of signal-to-noise ratios for the cross-power spectrum of A and B and the auto-power spectrum of A is

$$\frac{\left(C_\ell^{AB} \Big/ \Delta C_\ell^{AB}\right)^2}{\left(C_\ell^{AA} \Big/ \Delta C_\ell^{AA}\right)^2} = \frac{2\left(1 + \frac{1}{(S/N)_\ell^A}\right)^2}{\frac{1}{\lambda^2}\left(1 + \frac{1}{(S/N)_\ell^A}\right)\left(1 + \frac{1}{(S/N)_\ell^B}\right) + 1}, \tag{4.55}$$

where

$$(S/N)_\ell^A \equiv \frac{C_\ell^{AA}}{N_\ell^A} \tag{4.56}$$

is the signal-to-noise ratio of the auto-correlation of observable A and

$$\lambda^2 \equiv \frac{C_\ell^{AB\,2}}{(C_\ell^{AA} C_\ell^{BB})} \tag{4.57}$$

is the correlation coefficient squared ($\lambda^2 \leq 1$ by virtue of the Cauchy–Schwarz inequality). This ratio is monotonically decreasing with $(S/N)_\ell^A$ but increasing with $(S/N)_\ell^B$ and λ. Therefore, if observable A, say CMB lensing, is noise-dominated, but its correlation with another signal-dominated is high enough, then the cross-power spectrum has a higher signal-to-noise ratio.

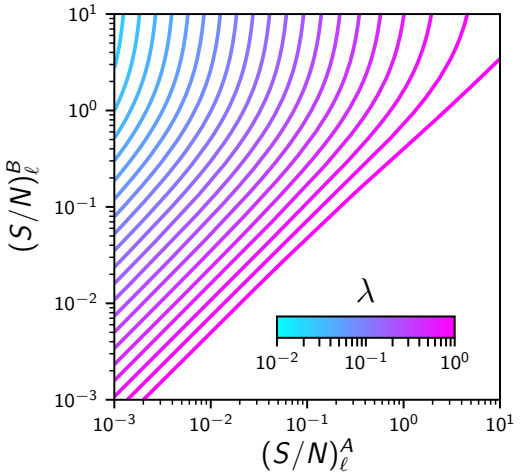

Figure 4.18 – Colored lines correspond to equal signal-to-noise ratio for the cross-power spectrum C_ℓ^{AB} and the auto-power spectrum C_ℓ^{AA} as a function of the signal-to-noise ratios for observables A and B and the correlation coefficient λ. Above the line, the cross-correlation is easier to detect.

CHAPTER 5

Detection of the CMB lensing and Lyman-α forest bispectrum

Contents

5.1 Introduction 124

5.2 Theoretical approach 125

5.2.1 Power spectrum of the Lyman-α forest transmission 126

5.2.2 Position-dependent power spectrum 130

5.2.3 Application to the correlation of CMB lensing and the Lyman-α forest 131

5.3 Analysis 134

5.3.1 Lyman-α forest power spectrum 134

5.3.2 Results 140

5.3.3 Null tests 143

5.4 Discussion 143

5.5 Perspectives 145

In this chapter, I present work that was performed during the first two years of my thesis, in parallel to the larger project presented in the next chapter. This lead to the first detection of the cross-correlation between lensing of the cosmic microwave background and the Lyman-α forest, and a publication in *Physical Review D* (Doux *et al.* 2016) accompanied by a synopsis in APS's *Physics* entitled "Seeing Dark Matter Through the Clouds" (Rini 2016).

5.1 Introduction

The Lyman-α forest as a tracer of matter

As seen in chapter 2, the Lyman-α forest is a powerful tracer of neutral hydrogen on a wide range of scales. On the largest scales, the imprint of the baryon acoustic oscillations in the Lyman-α forest furnishes a precise distance measurement at high redshift, thus constraining the geometry of the Universe, while the smallest scales are used to constrain the mass of neutrinos and properties of dark matter.

The interpretation of these results rely on the Lyman-α transmission tracing the underlying matter density field. If the hydrogen is in photoionization equilibrium with a uniform UV background, and there is no other source of entropy, then the relationship is described analytically through variations of the fluctuating Gunn-Peterson approximation (Croft *et al.* 1998) and is evaluated numerically using hydrodynamical simulations (Borde *et al.* 2014; Rossi *et al.* 2014). However, the connection between Lyman-α transmission and the underlying matter density is complex (Pontzen 2014) and non-linear. It is affected by the proximity effect on the largest scales (Pontzen 2014), by thermal broadening, Jeans smoothing and non-linear gravitational evolution on the smallest scales (Arinyo-i-Prats *et al.* 2015) and by the gas equation of state throughout. For these reasons, and in light of the tension between BAO measurements from the Lyman-α forest and galaxies (see Aubourg *et al.* 2015, and figure 3.15), consistency checks for the link between Lyman-α transmission and matter density are valuable.

Correlation of CMB lensing and the Lyman-α forest

Since most hydrogen is ionized, the Lyman-α forest also traces much greater amounts of ionized hydrogen, and thus, of free electrons. Croft *et al.* 2006 suggested cross-correlating CMB temperature anisotropies with the Lyman-α forest in order to observe the Sunyaev-Zel'dovich effect sourced by the aforementioned free electrons. However, this paper also predicted that this signal would be small and difficult to detect with available data.

In order to test the relationship between neutral hydrogen and dark matter, (Vallinotto *et al.* 2009, 2011) proposed cross-correlating CMB lensing – instead of temperature – with moments of the Lyman-α forest transmission. Indeed, since both the CMB lensing convergence and the Lyman-α transmission probe the density on a given line of sight, it is natural to compute their cross-spectrum. However, the mean Lyman-α transmission is strongly affected by continuum fitting in the quasar spectrum, making this a challenging observable.

Conversely, the small-scale line-of-sight Lyman-α power spectrum is less affected by errors in continuum fitting and is correlated to the local mean matter density because on non-linear evolution, as we shall see in the next section. The convergence

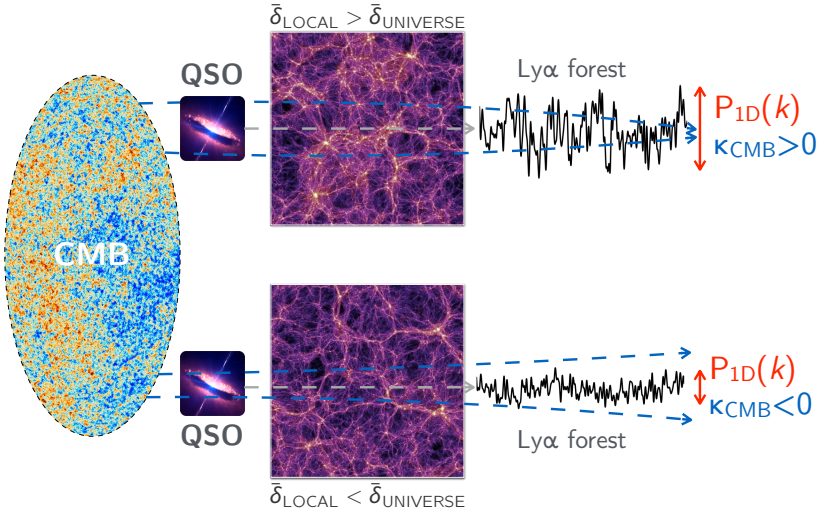

Figure 5.1 – Schematic of the situation. We consider two line of sights towards two quasars, crossing, respectively, an overdense and an underdense region. The line of sight crossing the overdense region has positive CMB lensing convergence (the geodesics followed by CMB photons, in blue, converge) and the Lyman-α forest of a quasar will have large fluctuations because of enhanced small-scale structures. On the contrary, a line of sight crossing an underdense region will have negative convergence (CMB photons move apart) and fluctuations in the Lyman-α forest will be small.

of CMB lensing on the same line of sight can be used as a proxy to evaluate the mean matter density. Thus, we expect a correlation of the one-dimensional power spectrum with the value of CMB lensing convergence along the same line of sight. This signal corresponds to a position-dependent power spectrum (Chiang *et al.* 2014; Schaan *et al.* 2014), or a squeezed bispectrum of the matter density. Simply put, a positive CMB convergence corresponds to an overdense line of sight; on this line of sight, the matter power spectrum is enhanced on all scales, due to non-linear evolution under gravity (Chiang *et al.* 2014; Li *et al.* 2014; Schaan *et al.* 2014) (see figure 5.1 for a schematic of this idea). This bispectrum would therefore vanish at linear order in the perturbation theory of the density field, where short and long modes are independent. Instead, for a non-linear density field, this signal probes the response of the Lyman-α power spectrum to a mean overdensity, as in Zaldarriaga *et al.* 2001.

5.2 Theoretical approach

In this section, we expose the theoretical approach to the Lyman-α- CMB lensing bispectrum. First, we focus on the power spectrum of the Lyman-α forest; then, we present the so-called position-dependent power spectrum formalism; finally, we apply it to the cross-correlation.

5.2.1 Power spectrum of the Lyman-α forest transmission

Fluctuations in the transmission δ_F can be used to trace fluctuations in the matter density field. For small perturbations, the fluctuating Gunn-Peterson approximation (Croft *et al.* 1998) relates the optical depth to the density field as

$$\tau \propto (1+\delta)^{\alpha} \tag{5.1}$$

where $\alpha \approx 2 - 0.7(\gamma - 1)$ and $\gamma \approx 1.6$ is the polytropic exponent of the gas (assuming adiabatic expansion), such that $P = \rho^{\gamma}$ or $T = \rho^{\gamma-1}$ (Pontzen 2014). Therefore, the relationship between δ_F and δ is non-linear, though the linear term is the leading term of a Taylor expansion and defines the large scale bias of transmission (Cieplak and Slosar 2016) as

$$b_\delta = \frac{\mathrm{d}\ln F}{\mathrm{d}\delta}. \tag{5.2}$$

Moreover, transmission is measured in redshift space and is thus affected by coherent gas motions. At first order, this is parametrized by a velocity bias,

$$b_\eta = \frac{\mathrm{d}\ln F}{\mathrm{d}\eta}, \tag{5.3}$$

where $\eta = -H^{-1}\frac{\mathrm{d}v_\parallel}{\mathrm{d}r_\parallel}$ is the velocity field gradient along the line of sight. Unlike the velocity bias of baryons, it is significantly different from unity for the Lyman-α transmission (Arinyo-i-Prats *et al.* 2015 and Blomqvist *et al.* 2015 found $b_\eta \sim -0.2$ on, respectively, simulations and SDSS-III/BOSS data). Note that both biases are negative, because transmission decreases when density increases, and that they differ from the HI biases.

Overall, the three-dimensional power spectrum of transmission can be written, as in Arinyo-i-Prats *et al.* 2015,

$$P_F(k,\mu) = \underbrace{b_\delta(z)^2}_{①}\underbrace{\left(1+\beta\mu^2\right)^2}_{②}\underbrace{P_{\mathrm{lin}}(k)}_{③}\underbrace{D(k,\mu)}_{④}, \tag{5.4}$$

where $k = \|\boldsymbol{k}\|$ and $\mu = \|\boldsymbol{k}_\perp\|/k$. Let us dissect the four terms in this formula.

① is the redshift-dependent linear bias.

② accounts for linear redshift-space distortions as described in chapter 2. Here, $\beta(z) = f(z)\, b_\eta(z)/b_\delta(z)$, which takes the transmission velocity bias into account.

③ is the linear (isotropic) matter power spectrum.

④ encapsulates gravitational non-linearities and IGM physics.

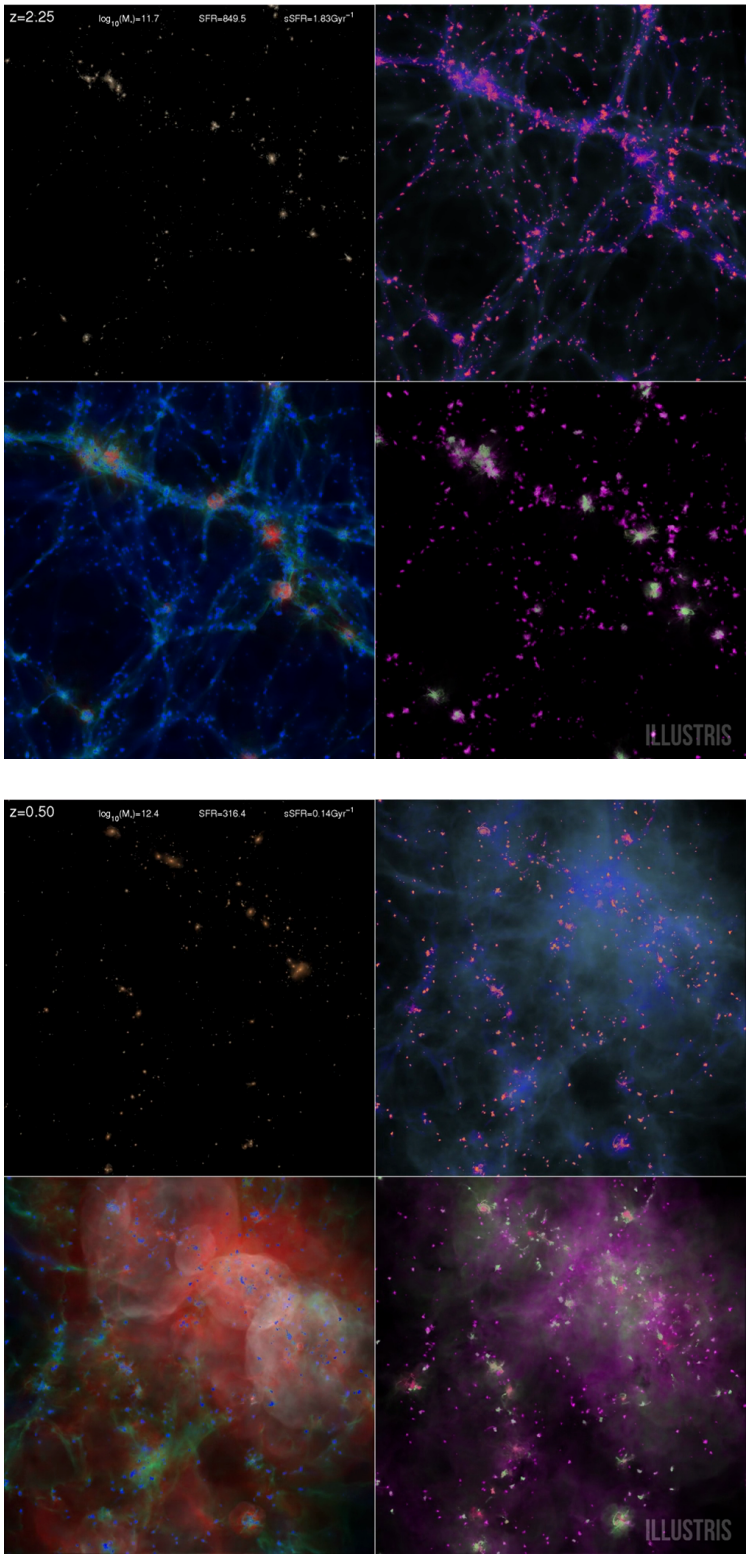

Figure 5.2 – Snapshots from the Illustris simulation showing stellar light (top left), gas density (top right), gas temperature (bottom left) and gas metallicity (bottom right) of a 10 Mpc-wide box at redshift $z = 2.25$ (top panel) and $z = 0.5$ (bottom panel). Astrophysical processes heat the gas and increase its metallicity.

The last term, $D(k,\mu)$, encodes the Lyman-α-specific physics. In principle, it involves many cosmological and astrophysical processes (see McQuinn 2016 for a thorough review, and an illustration in figure 5.2). These include:

Galactic feedback Supernovæ explosions and AGN activity heat the surrounding IGM, increase its metallicity (the fraction of heavy elements) and produce galactic winds and shockwaves known to blow baryons out of galaxies. However, there are indications that these processes may be limited to small volumes around galaxies, such that they do not affect low density regions probed by the Lyman-α forest.

Photoionization The ionizing UV background, emitted by stars and quasars, and the ionization rate, related to the IGM temperature (itself affected by the aforementioned effects), are a priori non-uniform. However, the mean free path of UV photons greatly exceeds the mean distance between emitters, such that their distribution should homogenize rapidly. Most simulations to date thus make the approximation that photoionization is insured by a uniform UV background.

IGM equation of state The equation of state of the IGM, often parametrized as $T \propto \rho^{\gamma-1}$, can be modified by inhomogeneous ("patchy") reionization processes. However, cosmic expansion and cooling via Compton scattering off CMB photons tighten the distribution around a power law. Temperature is an important parameter since it controls line broadening and the gaz pressure, and thus, smoothing of small scale fluctuations.

Here, we employ the fitting formula of Arinyo-i-Prats *et al.* 2015, given by

$$D(k,\mu) = \exp\Bigg(\underbrace{\left[q_1\Delta^2(k) + q_2\Delta^4(k)\right]}_{\text{A}} \underbrace{\left[1 - \left(\frac{k}{k_v}\right)^{a_v}\mu^{b_v}\right]}_{\text{B}} - \underbrace{\left(\frac{k}{k_p}\right)^2}_{\text{C}} \Bigg). \tag{5.5}$$

Various terms account for:

(A) non-linear gravitational enhancement, parametrized by the dimensionless matter power spectrum $\Delta^2(k) = k^3 P_{\rm m}(k) \big/ 2\pi^2$;

(B) absorption line broadening due to non-linear and thermal velocities, causing a smoothing along the line of sight (justifying the μ-dependence);

(C) smoothing of smale scale fluctuations below the Jeans scale, $k_p \approx 10\,h\,\mathrm{Mpc}^{-1}$, due to the gaz pressure.

$D(k,\mu)$ goes to 1 at large scales and is exponentially cut off at small scales with an angle-dependent enhancement at intermediate scales (see figure 5.3). All parameters

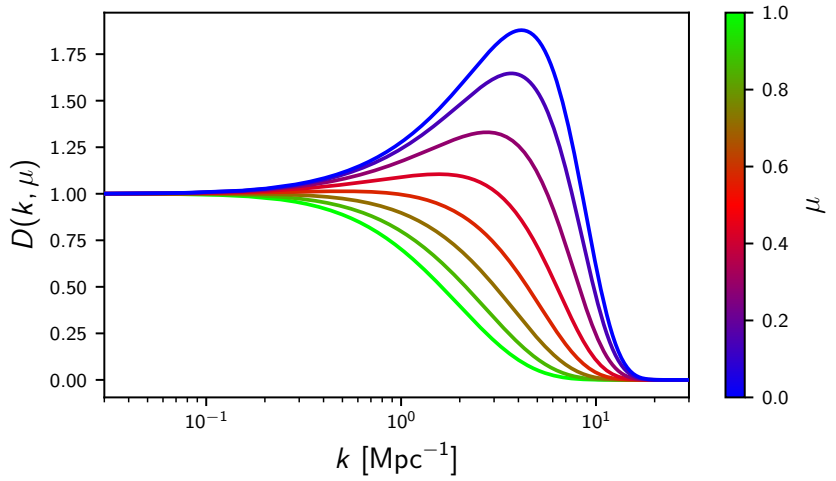

(a) Non-linear term $D(k, \mu)$ of the Lyman-α transmission power spectrum from Arinyo-i-Prats *et al.* 2015.

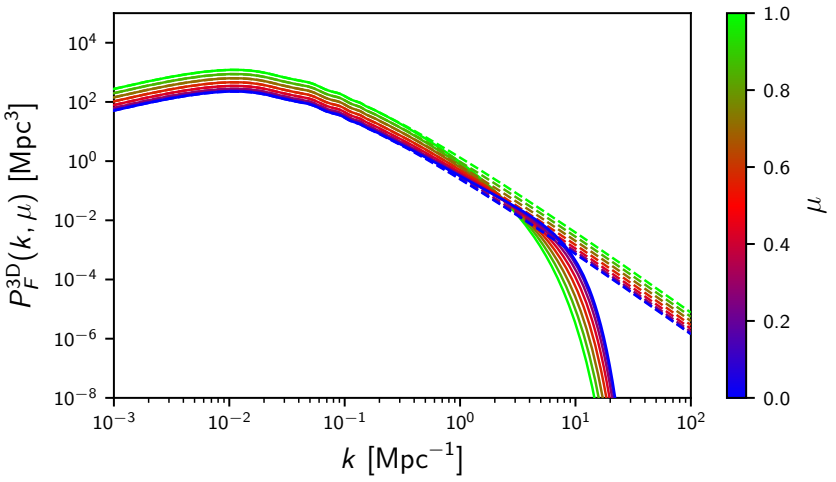

(b) Three-dimensional power spectrum of the Lyman-α transmission $P_F(k, \mu)$ with (solid lines) and without (dashed lines) the non-linear term $D(k, \mu)$.

Figure 5.3 – Non-linear term $D(k, \mu)$ and three-dimensional power spectrum of the Lyman-α transmission $P_F(k, \mu)$ as functions of scale and angle with respect to the line of sight (green for modes along the l.o.s. and blue for modes perpendicular to the l.o.s.). Both are shown for redshift $z = 2.4$.

are redshift-dependent, were fitted on hydrodynamical simulations in five redshift bins between $z = 2$ and $z = 3$ and are interpolated using a spline adjusted to match the best fits.

Finally, the one-dimensional power spectrum of transmission along the line of sight is obtained by integrating over perpendicular modes

$$P_F^{1D}(k_\parallel) = \int \frac{\mathrm{d}^2 \boldsymbol{k}_\perp}{(2\pi)^2} P_F(k, \mu = k_\parallel / k). \tag{5.6}$$

5.2.2 Position-dependent power spectrum

Non-linear gravitational evolution induces a correlation between $\boldsymbol{k}$-modes probed by the matter density bispectrum B. It is defined by

$$\langle\delta(\boldsymbol{k}_1)\delta(\boldsymbol{k}_2)\delta(\boldsymbol{k}_3)\rangle = (2\pi)^3 B(\boldsymbol{k}_1,\boldsymbol{k}_2,\boldsymbol{k}_3)\delta^{(3)}(\boldsymbol{k}_1+\boldsymbol{k}_2+\boldsymbol{k}_3) \tag{5.7}$$

and is non-vanishing if and only if $\boldsymbol{k}_1+\boldsymbol{k}_2+\boldsymbol{k}_3=\boldsymbol{0}$ (the modes form a triangle). Standard perturbation theory can be used to show that (Chiang *et al.* 2014)

$$B(\boldsymbol{k}_1,\boldsymbol{k}_2,\boldsymbol{k}_3) = 2\left[P_{\rm lin}(k_1)P_{\rm lin}(k_2)F_2(\boldsymbol{k}_1,\boldsymbol{k}_2) + 2 \text{ permutations}\right] \tag{5.8}$$

where

$$F_2(\boldsymbol{k}_1,\boldsymbol{k}_2) = \frac{5}{7} + \frac{1}{2}\frac{\boldsymbol{k}_1\cdot\boldsymbol{k}_2}{k_1k_2} + \frac{2}{7}\left(\frac{\boldsymbol{k}_1\cdot\boldsymbol{k}_2}{k_1k_2}\right)^2. \tag{5.9}$$

Now, imagine measuring the matter density field within a given volume, centered at position $\boldsymbol{r}_0$ and specified by a normalized window function $W_{\boldsymbol{r}_0}(\boldsymbol{r})$. We define, as in Chiang *et al.* 2014, the local Fourier transform as

$$\delta(\boldsymbol{k},\boldsymbol{r}_0) \equiv \int \mathrm{d}^3\boldsymbol{r}\,\delta(\boldsymbol{r})W_{\boldsymbol{r}_0}(\boldsymbol{r})e^{i\boldsymbol{k}\cdot\boldsymbol{r}}, \tag{5.10}$$

the local mean density as

$$\bar{\delta}(\boldsymbol{r}_0) \equiv \int \mathrm{d}^3\boldsymbol{r}\,\delta(\boldsymbol{r})W_{\boldsymbol{r}_0}(\boldsymbol{r}) = \delta(\boldsymbol{k}=0,\boldsymbol{r}_0), \tag{5.11}$$

and the position-dependent power spectrum as

$$P(\boldsymbol{k},\boldsymbol{r}_0) = |\delta(\boldsymbol{k},\boldsymbol{r}_0)|^2. \tag{5.12}$$

Expanding around the mean density of the Universe, we have

$$P(\boldsymbol{k},\boldsymbol{r}_0) = P(\boldsymbol{k})\Big|_{\bar{\delta}=0} + \frac{\mathrm{d}P(\boldsymbol{k})}{\mathrm{d}\bar{\delta}}\Big|_{\bar{\delta}=0}\bar{\delta}(\boldsymbol{r}_0) + \mathcal{O}\left(\bar{\delta}^2\right). \tag{5.13}$$

Here, $\mathrm{d}P(\boldsymbol{k})/\mathrm{d}\bar{\delta}$ is related to the bispectrum, integrated over the volume considered and in a special configuration – called "squeezed" – where one of the modes vanishes, such that the two others are opposite. Chiang *et al.* 2014 shows that

$$\frac{\mathrm{d}\ln P_{\rm lin}(\boldsymbol{k})}{\mathrm{d}\bar{\delta}} = \frac{68}{21} - \frac{1}{3}\frac{\mathrm{d}\ln k^3 P_{\rm lin}(\boldsymbol{k})}{\mathrm{d}\ln k}, \tag{5.14}$$

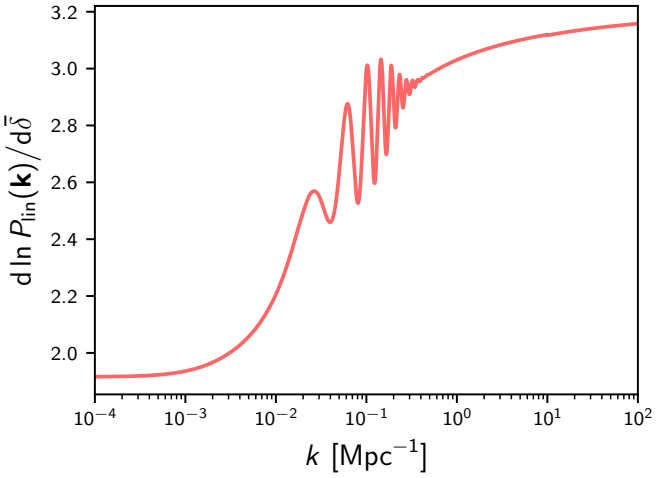

Figure 5.4 – Dependence of the linear matter power spectrum on the local mean density (see equation (5.14)).

and therefore[1]

$$\left\langle P(\boldsymbol{k},\boldsymbol{r}_0)\bar{\delta}(\boldsymbol{r}_0)\right\rangle = \sigma_{\bar{\delta}}^2 \left.\frac{\mathrm{d}P(\boldsymbol{k})}{\mathrm{d}\bar{\delta}}\right|_{\bar{\delta}=0} P(k), \tag{5.15}$$

where $\sigma_{\bar{\delta}}^2$ is the variance of the mean density, given by

$$\sigma_{\bar{\delta}}^2 \equiv \int \frac{\mathrm{d}^3\boldsymbol{k}}{(2\pi)^3}\left|\widetilde{W}_{\boldsymbol{r}_0}(\boldsymbol{k})\right|^2 P(\boldsymbol{k}). \tag{5.16}$$

The position-dependent correlation function (similarly defined) of SDSS-III/BOSS galaxies was measured in Chiang *et al.* 2015 at the 7.4σ level.

5.2.3 Application to the correlation of CMB lensing and the Lyman-α forest

We aim at evaluating the covariance between the one-dimensional power spectrum $P_F(k_\parallel)$ of the Lyman-α forest transmission on one line of sight and the CMB convergence κ on the same line of sight.

The estimate $\hat{\kappa}$ of the convergence from CMB lensing reconstruction Hu and Okamoto 2002; Okamoto and Hu 2003 is first Wiener-filtered. It is obtained by applying a linear transformation in Fourier space (equivalent to a convolution in real

[1] This is just an application of the formula

$$\langle f(X)g(X)\rangle = f(\langle X\rangle)g(\langle X\rangle) + f'(\langle X\rangle)g'(\langle X\rangle)\left\langle (X-\langle X\rangle)^2\right\rangle + \mathcal{O}\left(\left\langle (X-\langle X\rangle)^3\right\rangle\right)$$

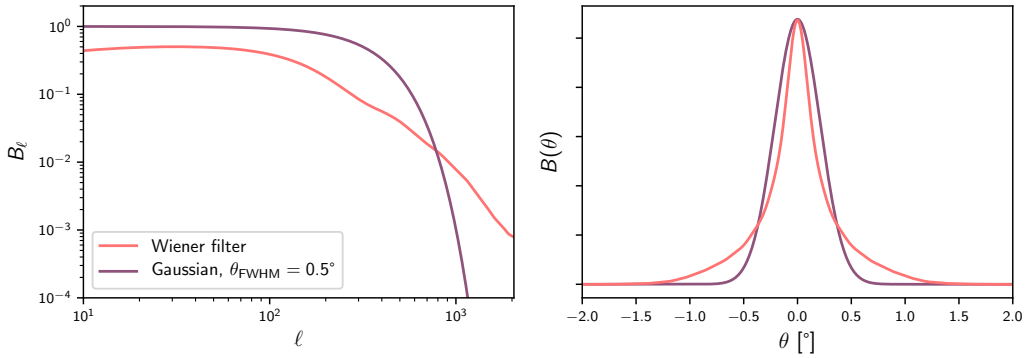

Figure 5.5 – Wiener filter for the Planck lensing map (Planck Collaboration *et al.* 2016f) compared to a gaussian beam of full-width-at-half-maximum $\theta_{\mathrm{FWHM}} = 0.5°$, in multipole space (left panel) and real space (right panel). In multipole space, the Wiener-filter is given by equation (5.17) and the gaussian beam has a spectrum given by $B_\ell = \exp\left(-\ell(\ell+1)\sigma^2/2\right)$ where $\sigma = \theta_{\mathrm{FWHM}}/\sqrt{8\ln 2}$. In real space, the Wiener filter is $\Lambda_\kappa(\theta) = \sum_\ell \frac{2\ell+1}{4\pi}\Lambda_{\kappa,\ell}P_\ell(\cos\theta)$ and has a equivalent width $\Delta\theta = 0.86°$. Both filters are normalized in the real-space plot.

space) to the reconstructed convergence multipoles $\hat{\kappa}_{\ell m}$, such that

$$\hat{\kappa}^{\mathrm{WF}}_{\ell m} = \underbrace{\frac{C_\ell^{\kappa\kappa}}{C_\ell^{\kappa\kappa} + N_\ell^{\kappa}}}_{\Lambda_{\kappa,\ell}} \hat{\kappa}_{\ell m} \tag{5.17}$$

where $C_\ell^{\kappa\kappa}$ and N_ℓ^{κ} are the convergence signal and noise power spectra. The Wiener-filter Λ_κ maximizes the signal-to-noise ratio of the convergence in real space and defines a "cone", whose line of sight dimension is determined by the lensing kernel W_κ, and whose angular size is determined by the Wiener filter. More formally, we define a window function for perpendicular modes $k_\perp$, such that at comoving distance $\chi(z)$,

$$\Lambda_\kappa(k_\perp) = \left.\frac{C_\ell^{\kappa\kappa}}{C_\ell^{\kappa\kappa} + N_\ell^{\kappa}}\right|_{\ell=\chi(z)k_\perp} . \tag{5.18}$$

We split this cone into thin slices of thickness $\mathrm{d}\chi$ and width given by the Wiener filter. This defines a small volume in which we can evaluate the mean density, as in the previous section. The variance of the density field $\bar{\delta}(\chi)$ averaged over this thin slice is given by (see Schaan *et al.* 2014)

$$\mathrm{Var}\big(\bar{\delta}(\chi)\big) = \sigma_{\bar{\delta}}^2(\chi)/\,\mathrm{d}\chi \tag{5.19}$$

with

$$\sigma_{\bar{\delta}}^2(\chi) = \int \frac{\mathrm{d}^2\boldsymbol{k}_\perp}{(2\pi)^2} \left|\Lambda_\kappa(\ell = \chi k_\perp)\right|^2 P_{\mathrm{lin}}(k_\perp, \chi) \tag{5.20}$$

where $P_{\mathrm{lin}}(k_\perp, \chi)$ is the linear matter power spectrum at comoving distance χ. The

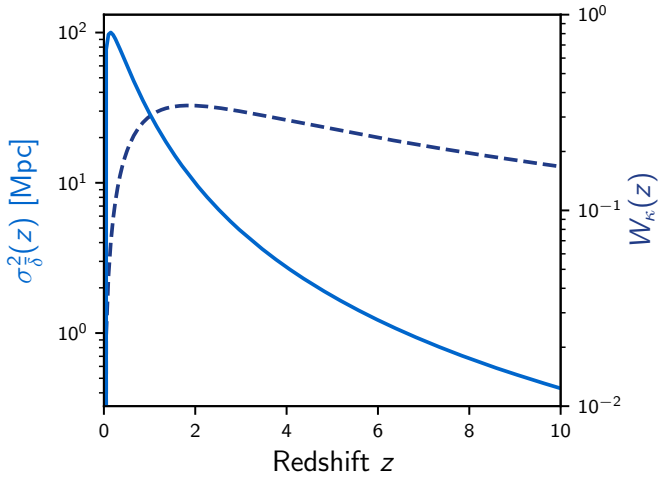

Figure 5.6 – Variance of the local mean density per unit of comoving distance for the Wiener filter. The CMB lensing kernel is shown for comparison (on a different scale).

covariance of $\bar{\delta}(\chi)$ with the 1D power spectrum measured on the same slice is (Schaan *et al.* 2014)

$$\mathrm{Cov}\left[\bar{\delta}(\chi), P_F^{\mathrm{1D}}(k_\parallel, \chi)\right] = \mathrm{Var}\big(\bar{\delta}(\chi)\big)\frac{\partial P_F^{\mathrm{1D}}}{\partial \bar{\delta}}(k_\parallel, \chi) + \mathcal{O}\Big(\sigma_{\bar{\delta}}^4\Big). \tag{5.21}$$

In other words, the response of the Lyman-α power spectrum to the mean matter overdensity produces a non-zero covariance. For a given Lyman-α forest, measured between χ_{min} and χ_{max}, we define an average power spectrum

$$P_F^{\mathrm{1D}}(k_\parallel) = \frac{1}{\Delta\chi}\int_{\chi_{\mathrm{min}}}^{\chi_{\mathrm{max}}} \mathrm{d}\chi\, P_F^{\mathrm{1D}}(k_\parallel, \chi), \tag{5.22}$$

where $\Delta\chi = \chi_{\mathrm{max}} - \chi_{\mathrm{min}}$. Since the CMB convergence is a weighted average of the matter density field, we perform the same average on equation (5.21) to get an integrated bispectrum between the CMB lensing convergence and fluctuations in the Lyman-α forest

$$\begin{aligned} B_{\kappa,\mathrm{Ly}\alpha}(k_\parallel) &\equiv \mathrm{Cov}\left[\kappa, P_F^{\mathrm{1D}}(k_\parallel)\right] \\ &= \frac{1}{\Delta\chi}\int_{\chi_{\mathrm{min}}}^{\chi_{\mathrm{max}}} \mathrm{d}\chi\, W_\kappa(\chi)\frac{\partial P_F^{\mathrm{1D}}}{\partial \bar{\delta}}(k_\parallel, \chi)\sigma^2_{\bar{\delta}}(\chi). \end{aligned} \tag{5.23}$$

We have assumed that various redshift/distance slices are uncorrelated, as in the Limber approximation (see section 4.2.2.2 of chapter 4), because the lensing window function $W_\kappa(\chi)$ varies slowly over the integral width. This width, in turn, is much larger than the scales where the correlation is expected, of order $0.1 - 1\,h\,\mathrm{Mpc}^{-1}$.

To go further, we need to evaluate the response of the Lyman-α power spectrum

to the mean overdensity $\partial P_F^{\mathrm{1D}} \big/ \partial\bar{\delta}$. In the previous section, we have seen how the linear matter power spectrum responds to the local mean density. The linear bias term b_δ, the Kaiser term β and the baryonic non-linearities encapsulated in $D(k,\mu)$ may also respond to a mean overdensity. We characterize the response of these terms by an effective non-linear bias

$$b_2^{\mathrm{eff}}(k,\mu) = \frac{\partial}{\partial\bar{\delta}}\left[\ln\left(b_\delta^2\left(1+\beta\mu^2\right)^2 D(k,\mu)\right)\right]. \tag{5.24}$$

This quantity combines non-linear bias[2] and the response of redshift-space distortions and non-linear clustering of gas. It will be measured from the bispectrum, and can, in principle, be measured from simulations. The response of the Lyman-α forest power spectrum is thus

$$\frac{\partial P_F^{\mathrm{1D}}}{\partial\bar{\delta}}(k_\parallel,\chi) = \int \frac{\mathrm{d}^2\boldsymbol{k}_\perp}{(2\pi)^2} P_F(\boldsymbol{k})\left(\frac{\partial \ln P_{\mathrm{lin}}}{\partial\bar{\delta}} + b_2^{\mathrm{eff}}(k,\mu)\right). \tag{5.25}$$

Combining section 5.2.3 and equation (5.25), the CMB lensing - Lyman-α bispectrum becomes the sum of two terms: one representing the response of the linear matter power spectrum, and one for the non-linear and baryonic terms.

5.3 Analysis

5.3.1 Lyman-α forest power spectrum

5.3.1.1 Data

We use quasar spectra from the twelfth data release of SDSS-III/BOSS (Dawson *et al.* 2013; Lee *et al.* 2012; Pâris *et al.* 2017). The continuum fitting is performed using a mean-flux-regulated principal component analysis[3] method described in Lee *et al.* 2012 that was applied to the DR9 in Lee *et al.* 2013. The domain of the Lyman-α forest of a given quasar spectrum is defined by limits on the rest frame wavelength

$$1\,041\,\text{Å} \leq \lambda_{\mathrm{rf}} \leq 1\,185\,\text{Å}, \tag{5.26}$$

where $\lambda_{\mathrm{rf}} = \lambda/(1+z_{\mathrm{QSO}})$ for a quasar at redshift z_{QSO}.

Spectra displaying damped Lyman-α absorption systems (DLAs, identified using the technique described in Noterdaeme *et al.* 2012) or broad absorption lines

[2] Note that the first-order non-linear bias b_2 is generally defined through the response of the linear bias to an overdensity via $\partial b_1/\partial\bar{\delta} = b_2 - b_1^2$, *e.g.* in Baldauf *et al.* 2016a; Chiang *et al.* 2014. Therefore, if we neglect the Kaiser term and the baryonic term, the quantity b_2^{eff} defined here is related to the non-linear bias b_2 as $b_2^{\mathrm{eff}} = 2(b_2 - b_1^2)/b_1$.

[3] The idea of MF-PCA is to use quasar spectrum templates derived from PCA of high resolution spectra with an overall power law dependence to account for the diversity of SDSS quasars, and to make a global adjustment of fitted continua to correctly reproduce the pre-measured mean transmission fraction.

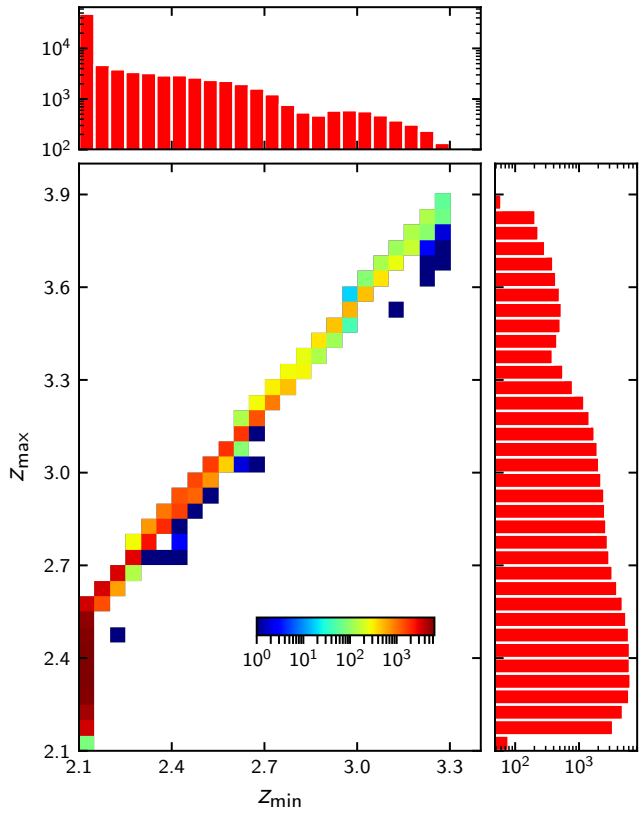

Figure 5.7 – Two dimensional histogram of maximum *vs* minimum redshifts of the sample of Lyman-α forests used for the analysis. One-dimensional, projected histograms are shown with the same scale. There is an accumulation of forests that were cut at the minimum redshift of 2.1.

(BALs, identified by visual inspection in Pâris *et al.* 2017) were discarded. We select quasars with a signal-to-noise ratio in the Lyman-α forest, measured by the BOSS pipeline, greater than 1 and a redshift between 2.15 and 4.0. The noise estimation gives poor results close to the spectrograph blue-end, so we additionally cut parts of the forests below $z = 2.1$ as in Palanque-Delabrouille *et al.* 2013. Finally, we discard quasars lying outside of the Planck lensing mask. These cuts select 87 085 quasars out of the 155 002 in the DR12 catalog. The distribution of forest minimum and maximum redshifts is shown in figure 5.7

The flux transmission fraction in the Lyman-α forest at redshift $z = \lambda/\lambda_{\mathrm{Ly}\alpha}$ is

$$F(z) = \frac{f(z)}{C(z)}, \tag{5.27}$$

where $f(z)$ is the measured flux and $C(z)$ is the estimated continuum. We then

estimate the normalized transmitted flux fraction as a function of redshift as

$$\delta_i(z) = \frac{F_i(z)}{\langle F(z) \rangle} - 1 \tag{5.28}$$

where $\langle F(z) \rangle$ is the mean flux transmission fraction obtained by averaging over quasars and i stands for the forest index (see figure 5.8a). The mean and r.m.s of the transmission fluctuations per redshift pixel are shown in figure 5.8b. The variance $\sigma_{\text{total}}(z)$ is the sum of two contributions, to wit, intrinsic scatter of large-scale structures $\sigma_{\text{LSS}}(z)$ and instrumental noise $\sigma_{\text{noise}}(z)$. The latter is evaluated for each line by measuring the spread for different observations, and then averaged over lines. The total variance is given by the spread of the transmission fluctuations in each redshift pixel. Finally, the cosmological variance is obtained by subtraction

$$\sigma^2_{\text{LSS}}(z) = \sigma^2_{\text{total}}(z) - \sigma^2_{\text{noise}}(z). \tag{5.29}$$

The normalized flux fraction is converted from a function of redshift to a function of radial comoving distance $\chi(z)$, which is evaluated using cosmological parameters from Planck 2015 (TT,TE,EE+lowP+lensing+ext, Planck Collaboration *et al.* 2016e). Because the spacing between pixels of the BOSS spectrograph is logarithmic in wavelength, with $\Delta(\log_{10} \lambda) = 10^{-4}$, and because sky emission lines are masked (on average 1.2% of pixels), the spacing in distance space is slightly irregular, albeit monotonically growing. Therefore the Fourier transform $\tilde{\delta}(k)$ of the normalized transmitted flux fraction $\delta(\chi)$ is computed using the Non-equispaced Fast Fourier Transform library[4] (NFFT, Keiner *et al.* 2009). We checked that it gave correct and precise results for functions with known Fourier transforms but sampled in a similar fashion to Lyman-α forests.

For a forest of length $\Delta\chi$ and mean pixel spacing $\overline{\delta\chi}$, the smallest mode is $k_{\text{min}} = 2\pi/\Delta\chi$ while the largest mode is $k_{\text{max}} = 2\pi/\overline{\delta\chi}$. Forests have a length of $280-420\,h^{-1}\,\text{Mpc}$ with a spacing of order $0.58-0.68\,h^{-1}\,\text{Mpc}$ for forests in the redshift range $2.1 - 3.6$, giving $k_{\text{max}} \approx 6\,h\,\text{Mpc}^{-1}$. These scales are highly affected by non-linear clustering and baryonic effects. Moreover, the power spectrum becomes noisier because of the resolution of the spectrograph (see the spectrograph window function in equation (5.32)), so we restrict our analysis to $k_{\text{max}} = 1.5\,h\,\text{Mpc}^{-1}$, corresponding to scales of order $4\,h^{-1}\,\text{Mpc}$, consistent with Palanque-Delabrouille *et al.* 2013. We note that the large-scale modes over $60\,h^{-1}\,\text{Mpc}$, *i.e.* $k \lesssim 0.1\,h\,\text{Mpc}^{-1}$ may be slightly affected by continuum fitting, though in a way uncorrelated with CMB lensing (this will be discussed in section 5.5).

[4] http://www-user.tu-chemnitz.de/~potts/nfft/

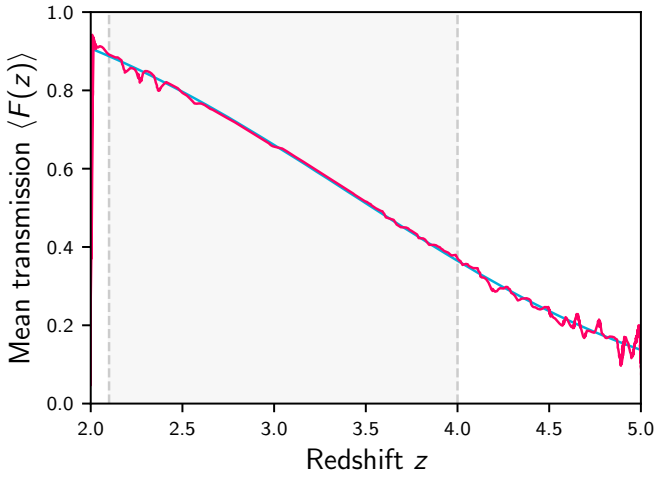

(a) Mean transmission $\langle F(z) \rangle$. The measurement is drawn in red and the fitting function $\langle F(z) \rangle = \exp\left(-0.001845(1+z)^{3.924}\right)$ from Lee *et al.* 2012 in blue.

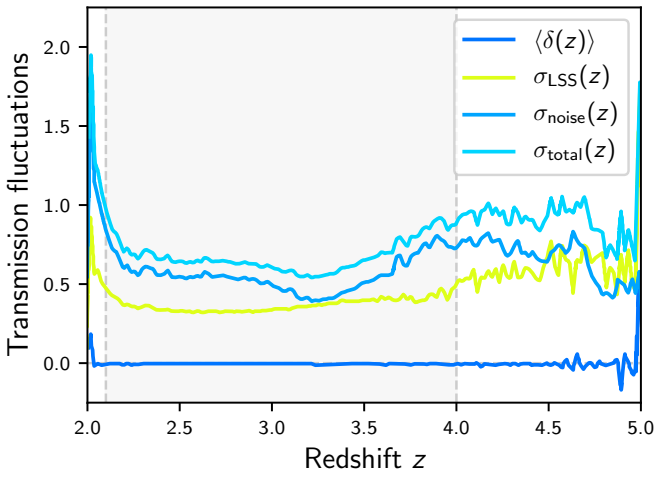

(b) Transmission fluctuations: mean of fluctuations $\langle \delta(z) \rangle$, intrinsic large-scale structure r.m.s. $\sigma_{\mathrm{LSS}}(z)$, mean instrument noise $\sigma_{\mathrm{noise}}(z)$ and total r.m.s. $\sigma_{\mathrm{total}}(z) = \sqrt{\sigma^2_{\mathrm{LSS}}(z) + \sigma^2_{\mathrm{noise}}(z)}$.

Figure 5.8 – Mean transmission fraction and transmission fluctuations statistics for the sample used in the analysis. The vertical dashed lines indicate the redshift interval considered $z \in [2.1, 4.0]$.

5.3.1.2 Estimator

The raw power spectrum is obtained by

$$\hat{P}_i^{\mathrm{raw}}(k) = \frac{\left|\tilde{\delta}_i(k)\right|^2}{\Delta\chi_i}, \tag{5.30}$$

where $\Delta\chi_i$ is the comoving length of the i-th. forest.

Multiple observations of the same quasars allow for an estimation of the noise level $\sigma^2_{\mathrm{noise}}(\chi)$ for each pixel in the forest. We assume the noise to have a white spectrum, which agrees well with McQuinn and White 2011; Palanque-Delabrouille *et al.* 2013, and estimate its power spectrum by averaging over pixels, such that

$$P_i^{\mathrm{noise}} = \overline{\sigma^2_{\mathrm{noise},i}}\frac{\pi}{\Delta k}, \tag{5.31}$$

where $\Delta k = k_{\mathrm{max}} - k_{\mathrm{min}}$.

The resolution of the spectrograph is of order $1\,h^{-1}\,\mathrm{Mpc}$ and varies slowly with wavelength (by about 10% over one forest). Therefore the spectrograph window function is

$$W_{\mathrm{spectro}}(k, R_i) = \exp\left(-\frac{k^2 R_i^2}{2}\right) \times \mathrm{sinc}\left(\frac{k\overline{\delta\chi_i}}{2}\right), \tag{5.32}$$

where R_i is the resolution of the spectrograph averaged over the i-th forest,

$$R_i = \overline{\frac{c(1+z)}{H(z)}\delta_{\mathrm{disp}}\Delta\log\lambda}, \tag{5.33}$$

with δ_{disp} being the measured dispersion in units of $\Delta\log_{10}\lambda$. The second term in equation (5.32), in which $\mathrm{sinc}(x) = \sin(x)/x$, accounts for the pixelization. Finally, the estimator of the one-dimensional power spectrum of the Lyman-α forest is given by

$$\hat{P}_F^{\mathrm{1D}}(k, z) = \left\langle \frac{\hat{P}_i^{\mathrm{raw}}(k) - P_i^{\mathrm{noise}}}{W^2_{\mathrm{spectro}}(k, R_i)} \right\rangle_{i\in z}, \tag{5.34}$$

where the average is over forests falling in the redshift range.

This straightforward measurement of the one-dimensional power spectrum does not correct for subtle instrumental systematics or contamination of the forest by metal lines (such as SiIII) dealt with in Palanque-Delabrouille *et al.* 2013. However, these effects are less important in a cross-correlation measurement, and a precise estimation of the power spectrum is beyond the scope of this work.

5.3.1.3 Measured power spectrum

The first step is to measure the one-dimensional power spectrum in order to obtain the linear bias $b_\delta(z)$ as a function of redshift. The theoretical curves are computed

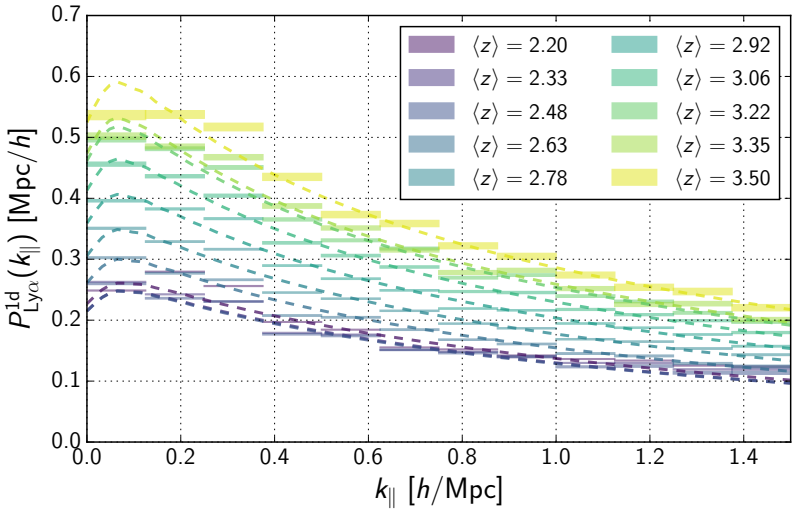

Figure 5.9 – One-dimensional power spectrum of the Lyman-α forest P_F^{1D} in ten redshift bins. The redshifts indicate the mean value of the middle redshifts of the forests. Error bars are computed from the weighted empirical covariance of the power spectra of different forests. Colored boxes represent the measured spectra averaged over these redshifts bins with their uncertainties and k-bins width. Dashed lines are theoretical curves with fitted bias $b_\delta(z)$.

using parameters, except for the linear bias that we aim at fitting, measured from simulations in Arinyo-i-Prats *et al.* 2015. We divide our forest sample into 10 linearly-spaced redshift bins using the central redshift of each forest. Each power spectrum is given a scale-dependent minimum-variance weight

$$w_i(k) \propto n_i^{\rm pix} \left(P^{\rm 1D}_{F,\rm fid}(k, z_i) + \frac{P_i^{\rm noise}}{W^2_{\rm spectro}(k, R_i)} \right)^{-2}, \tag{5.35}$$

where $n_i^{\rm pix}$ is the number of pixels of the i-th forest. The fiducial power spectrum $P_F^{\rm 1D}(k, z)$ is computed using the linear bias measured from simulations in Arinyo-i-Prats *et al.* 2015, which will only be used in the weights.

In order to take into account possible wavelength-dependent bias in the noise estimation, we allow for a common rescaling of the estimated noise power spectrum in each redshift bin. Precisely, we introduce a coefficient α_z in front of $P_i^{\rm noise}$ in equation (5.34), common to all spectra in each redshift bin and fit this parameter jointly with the linear bias $b_\delta(z)$ in each redshift bin. The estimated one-dimensional power spectrum is shown in figure 5.9 together with theoretical curves with best fit biases. The best fit of the linear bias $b_\delta(z)$ is shown in figure 5.10 with error bars including the marginalization over α_z. We fit this result with a power law in $(1 + z)$ of the form $b_\delta(z) = a(1 + z)^b$ and find $a = -0.00507$ and $b = 2.79$. It is represented by the solid blue curve in figure 5.10 and is in fairly good agreement with the bias measured in hydrodynamic simulations in Arinyo-i-Prats *et al.* 2015 (which we

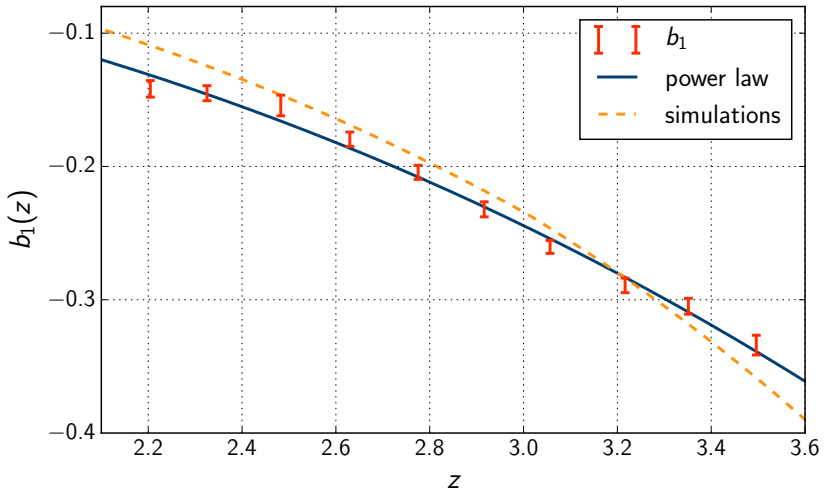

Figure 5.10 – Lyman-α flux transmission linear bias $b_\delta(z)$ as a function of redshift. The data points are depicted with error bars and the power law in $(1+z)$ (see text) is represented by the blue solid curve. The dashed orange curve represents the linear bias measured from hydrodynamical simulations in Arinyo-i-Prats *et al.* 2015. Remark that the transmission is anti-correlated with the amount of hydrogen, hence the negative sign.

only used in the weights).

5.3.2 Results

5.3.2.1 Measurement of the bispectrum

The next step is to compute the weighted, unbiased covariance of the lensing convergence and the one-dimensional power spectrum. Quasars have a significant contribution to the lensing of the CMB because the lensing efficiency W_κ peaks at $z \sim 2$. Therefore, we expect the mean convergence in the directions of quasars to be positive, and indeed find $10^4 \times \langle \kappa_i^{\rm WF} \rangle = 1.35 \pm 0.52$. This value is consistent with the expected amplitude $\kappa = (\Lambda_\kappa * \Sigma)/\bar{\rho} \sim 1.5 \times 10^{-4}$, where Σ is the projected density of the haloes hosting the quasars (computed for a NFW profile (Navarro *et al.* 1996) with a halo mass $M_{\rm h} \sim 2 \times 10^{12} M_\odot/h$ and redshift 2.5 (White *et al.* 2012)) convolved with the Wiener filter and $\bar{\rho}$ is the mean matter density. With the aim of measuring the correlation between our two probes, we subtract the mean value $\left\langle \kappa_i^{\rm WF} \right\rangle$ in the computation of the covariance. So as to decrease the effects of noise in this measurement, we also subtract the mean value of the power spectrum in each k-bin (which does not impact the expectation value of the estimator). The estimator for the correlation of CMB lensing and fluctuations in the Lyman-α forest, *i.e.* the CMB lensing – Lyα integrated bispectrum, is defined as

$$\hat{B}_{\kappa,{\rm Ly}\alpha}(k_\parallel) \equiv {\rm Cov}_{w(k_\parallel)} \left[\kappa^{\rm WF}, P_F^{\rm 1D}(k_\parallel) \right], \tag{5.36}$$

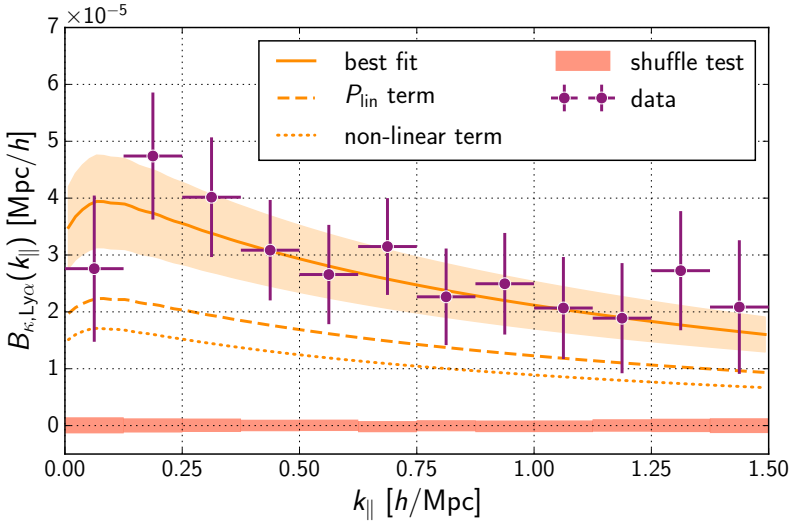

Figure 5.11 – Integrated bispectrum of CMB lensing and fluctuations in the Lyman-α forest. The Wiener-filtered CMB lensing is measured in the direction of quasars for which we measure the Lyman-α forest one-dimensional power spectrum in the range $k_\parallel \sim 0.1 - 1.5\,h\,\mathrm{Mpc}^{-1}$. Data points (in purple) show a signal measured at 5σ. The theoretical curve (solid orange) is the sum of two terms: the response of the linear matter power spectrum (dashed), and the response of the non-linear terms in the Lyman-α power spectrum (non-linear bias b_2, Kaiser term and baryonic non-linear term D) (dotted). While the first involves no free parameters, the latter has an amplitude characterized by the effective non-linear bias $b_2^{\rm eff} = 1.16 \pm 0.53$, see equation (5.24). The orange area represents the 1σ uncertainty on this non-linearity amplitude. We test that our estimator is coherent with zero in the case of no correlation by a shuffling method (thin red boxes, expanded 10 times for visibility).

where

$$\mathrm{Cov}_w\left[x, y\right] = \mathcal{N} \times \sum_i w_i \left(x_i - \langle x \rangle\right) \left(y_i - \langle y \rangle\right) \tag{5.37}$$

with the normalization $\mathcal{N} = \sum_i w_i / \left(\left(\sum_i w_i\right)^2 - \sum_i w_i^2 \right)$. The mean values $\left\langle \kappa^{\rm WF} \right\rangle$ and $\left\langle P_F^{\rm 1D}(k_\parallel) \right\rangle$ are computed using the same weights as well. The measured values in each k-bin are shown in purple in figure 5.11.

We use two methods to compute the covariance matrix for the various k-bins. For the first method, we proceed by computing the signal repeatedly with shuffled indices in $\kappa_i^{\rm WF}$. More precisely, for a given random permutation σ of the quasar indices, we compute $\mathrm{Cov}\left[\kappa_{\sigma(i)}^{\rm WF}, P_{F,i}^{\rm 1D}(k_\parallel)\right]$ and repeat $N = 10,000$ times. We then estimate the mean value (thin red boxes on figure 5.11) and the empirical covariance. For the second method, we use 100 simulations of CMB lensing convergence reconstruction made publicly available by the Planck collaboration on the Planck Legacy Archive[5]. The corresponding matrices of correlation coefficients are shown in figure 5.12. Both methods yields similar results in terms of detection, but the limited number of

[5] http://www.cosmos.esa.int/web/planck/pla

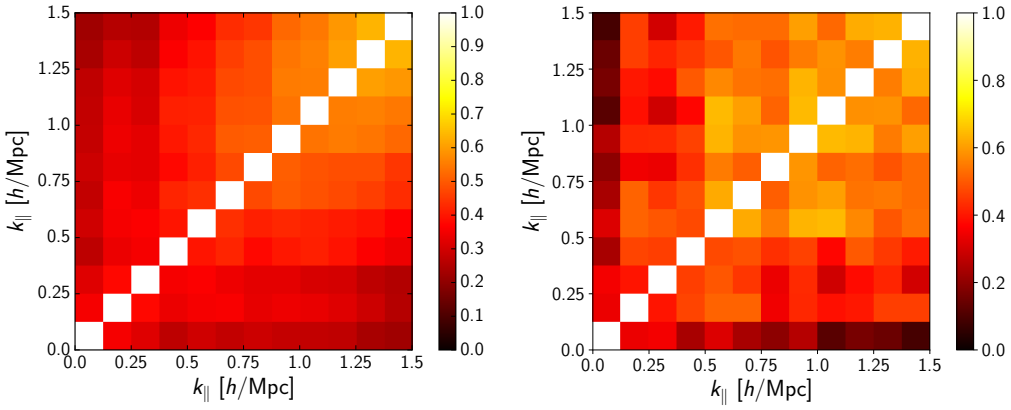

Figure 5.12 – Correlation matrix of the data-points between k-bins computed by (left) shuffling the indices of one of the variables or (right) using simulated reconstructions of CMB lensing. It shows significant correlation ranging from 20% up to almost 65% for the large k modes.

simulations makes the covariance matrix estimated with the second method noisier.

5.3.2.2 Comparison with theory

Finally, we aim at comparing our theoretical model and fitting a value of the effective non-linear bias $b_2^{\rm eff}$ defined in equation (5.24). We measure a single number, *i.e.* a scale and redshift averaged non-linear bias integrated over μ, characterizing the non-linear response in our sample. This parametrization is incomplete, but sufficient given the signal-to-noise ratio. For each line of sight, we evaluate the expected signal using section 5.2.3 given the redshift range $[z_{\rm min}, z_{\rm max}]$ of the forest, and the linear bias $b_\delta(z)$ from the power law best fit. We then weight the theoretical expected value by the weights in equation (5.35). The best fit value is $b_2^{\rm eff} = 1.16 \pm 0.53$. The theoretical curve (in orange in figure 5.11) is the sum of two contributions, one from the linear power spectrum (dashed line) and the other from the non-linear terms (dotted line).

Using the covariance matrix obtained by our shuffling method and the measured data points, we find a χ^2 value for the null hypothesis $\chi^2_{\rm null} = 30.1$ for 12 data points. The probability to exceed is 0.27% and the null hypothesis is therefore rejected at a significance of 3.0σ. For the best fit in b_2, we find $\chi^2_{\rm best-fit} = 5.37$, a small value that could be explained by over-estimated error bars, which would lead to a better detection. The signal-to-noise ratio for the detection is SNR $= \sqrt{\chi^2_{\rm null} - \chi^2_{\rm best-fit}} = 4.97$ (of order 4.5 for the second method of covariance estimation), hence this constitutes a 5σ detection of the non-linear response of the Lyman-α power spectrum.

5.3.3 Null tests

In order to assess the cosmological nature of this signal, we proceed to a number of null tests.

First, we make sure that the correlation estimator is consistent with zero in the case of no correlation. To do so, we compute the mean of the values of the signal measured with shuffled indices in κ_i^{WF} as we expect different lines to be uncorrelated. The result is consistent with zero, as shown on figure 5.11 by the thin red boxes. Using the simulated lensing maps results in the same conclusion. Moreover, the shuffling method has a caveat: if there are many quasars in a given patch on the sky where lensing is coherent, then shuffling their associated convergence value could result in too low error bars (as they still have the same convergence value). However, the lensing signal is noise-dominated, such that the variance of our estimator is dominated by noise as well, and we find very similar results with the method using simulations, thus eliminating the possibility of catastrophic underestimation of the error bars.

Second, we want to verify that the signal we measure does not originate in a possible correlation of the lensing convergence in the directions of quasars with their intrinsic properties. We split our sample in two equal parts according to the median values of various quasar parameters. For each of these parameters, we measure the signal in the two sub-samples using equation (5.36) and compute the difference (divided by two such that error bars are the same as that of the signal). The results are shown in figure 5.13 and the meaning of the tested parameters' names are detailed in table 5.1. We test for galactic latitude of the quasars and galactic HI column density in their directions to verify that the signal is not related to galactic foregrounds. We test for quasar redshift and find no statistically significant variation of the signal. We also test for various intrinsic properties of the quasars linked to their masses: colors (PSF magnitudes in the g and i bands), near and far UV fluxes (from GALEX, Robotham and Driver 2011)) and quasar spectral index. We also test for contamination by carbon lines using the rest equivalent width of the emissions of CIII and CIV. We find that all tests are consistent with zero at the $0.2 - 1.6\ \sigma$ level. Lack of data prevents us from testing the contamination from the SiIV line; however, it is at most a 5% effect according to Palanque-Delabrouille *et al.* 2013.

5.4 Discussion

We have presented the first detection of a cross-correlation between the Lyman-α forest of quasars and the gravitational lensing of the CMB. Our understanding of this correlation is based on the response of small-scale fluctuations in the matter density, measured by the one-dimensional power spectrum of the transmission in the Lyman-α forest, to large-scale overdensities probed by the convergence of CMB lensing. This signal corresponds to a bispectrum in the squeezed limit configuration where the two

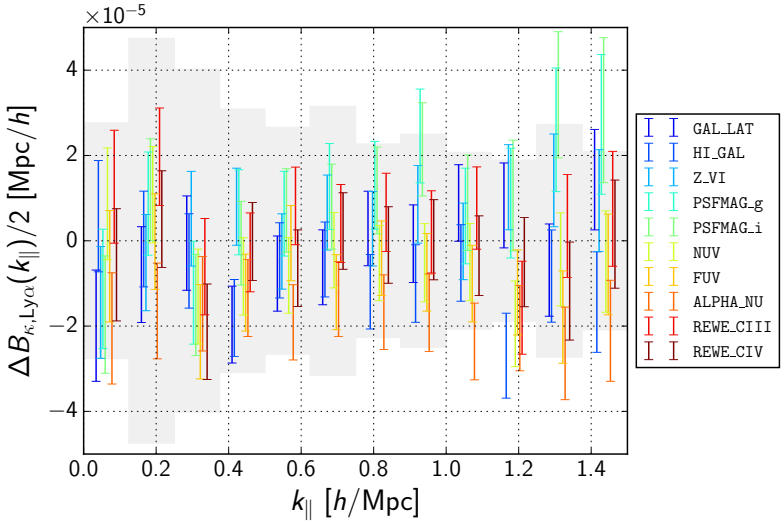

Figure 5.13 – Null tests for various quasar properties. For each parameter, the sample is split in two parts according to the median value. We then compute the CMB lensing – Lyα integrated bispectrum for these two sub-samples, using equation (5.36) and compute the difference (divided by 2 in order to have the same error bars as the signal itself). The greyed area is delimited by the absolute level of the measured bispectrum for the full sample (as in figure 5.11).

small-scale modes are of order $k \sim 0.1 - 1\,h\,\mathrm{Mpc}^{-1}$. This is the first measurement of the CMB lensing–Lyman-α integrated bispectrum, and it measures the non-linearity in the Lyman-α forest. Finally, this new observable tests our understanding of the relation between neutral hydrogen and dark matter.

We measured the one-dimensional power spectrum and the linear bias of the Lyman-α forest, finding values consistent with hydrodynamical simulations. Even though the power spectrum is sensitive to a number of systematic effects, these are much less important in a cross-correlation measurement like the integrated bispectrum that we computed. The theoretical bispectrum is the sum of two contributions: the response of the linear matter power spectrum, theoretically well-understood and involving no free parameters, and the response of the bias and non-linear terms, computed up to an effective non-linear bias b_2^{eff} which we have fitted. We believe this model provides a reasonable explanation of the observed signal.

However, we note that our interpretation of the measured bispectrum is limited by theoretical uncertainties, mainly related to baryonic physics. That is, the term $D(k, \mu)$, taken from Arinyo-i-Prats *et al.* 2015, encodes a number of effects that are significant at very small scales (of order $k \sim 60\,h\,\mathrm{Mpc}^{-1}$, see Cieplak and Slosar 2016), but the integral of the three-dimensional power spectrum gets contributions from k-modes greater than $10\,h\,\mathrm{Mpc}^{-1}$, and we cannot neglect these effects. Moreover, this term and the redshift-space distortion term β may also respond to large-scale overdensities. Therefore, the effective non-linear bias term b_2^{eff} encompasses several uncertain contributions: comparing it with simulations could provide both a valuable

Table 5.1 – Results of the null tests seeking for correlation between the lensing signal and intrinsic quasars properties.

Label	Description	Null test
GAL_LAT	Galactic latitude (absolute value)	1.6σ
HI_GAL	log of galactic HI column density	1.1σ
Z_VI	Quasar redshift from visual inspection	0.2σ
PSFMAG_g	PSF magnitude (flux in g band)	1.0σ
PSFMAG_i	PSF magnitude (flux in i band)	1.4σ
NUV	Near UV flux (from GALEX)	0.7σ
FUV	Far UV flux (from GALEX)	0.5σ
ALPHA_NU	Quasar spectral index	0.5σ
REWE_CIII	Rest equivalent width of CIII emission	1.1σ
REWE_CIV	Rest equivalent width of CIV emission	0.3σ

check for the simulation assumptions while shedding light on the relation between Lyman-α and dark matter.

Another uncertainty arises from the fact that the ionizing UV flux of the quasars reduces the amount of neutral hydrogen around them, a phenomenon known as the proximity effect (Pontzen 2014). Because overdense regions radiate more, the bias of neutral hydrogen $b_{\rm HI}(k)$ becomes negative at scales larger than $k \sim 0.01\,h\,\mathrm{Mpc}^{-1}$ (see figure 5.14). This impacts the HI power spectrum for scales $k \lesssim 0.1\,h\,\mathrm{Mpc}^{-1}$ and may also affect our measurement in the lowest k-bin (which is off by about 1σ).

5.5 Perspectives

Since the publication of the article, two articles (Chiang and Slosar n.d.; Chiang *et al.* 2017) presented predictions for the position-dependent power spectrum of the Lyman-α forest transmission based on simulations using the separate Universe approach. This technique enables predictions for the position-dependent power spectrum by mapping differences in the local mean density to simulations with different cosmological parameters. For instance, it is possible to map an overdense region of a given universe to an average region of another universe with a higher initial power spectrum (or σ_8). Their predictions are globally consistent with the results presented here.

However, Chiang and Slosar n.d. pointed out that a large-scale absorption mode in the forest cannot be distinguished from a lower quasar flux, which in turn is correlated to the environment of the quasar. Bright quasars are found in more massive haloes, which contribute more to CMB lensing. Therefore, this degeneracy impacts continuum fitting in a way that is correlated to the observed convergence of CMB lensing (though not directly). The signal that we measure could therefore imply

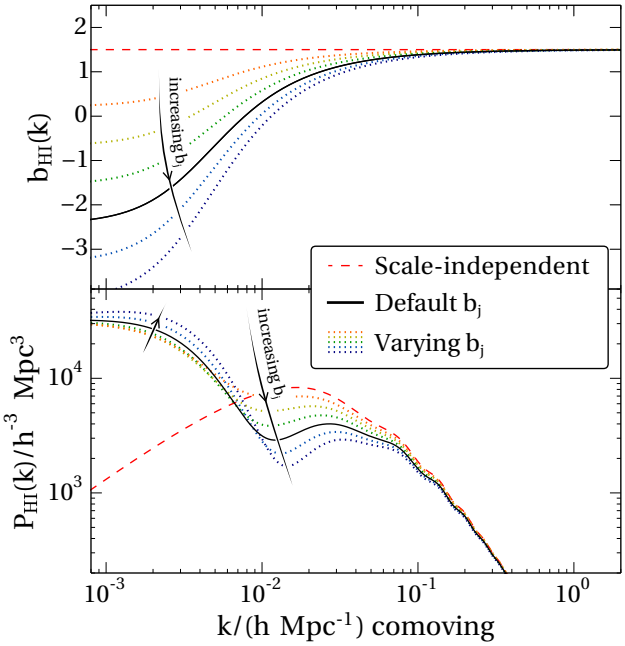

Figure 5.14 – The proximity effect causes the clustering bias of HI to become negative at large scale, and more so as the bias of UV sources b_j increases. Consequently, the shape of the power spectrum is affected at large scale. Figure from PONTZEN 2014.

a contribution from this effect that does not originate from non-linear gravitational or baryonic effects, but rather from systematic error in continuum effect. This, in turn, could explain that we find a positive b_2^{eff} while simulations predict a higher response of the matter power spectrum than that of the transmission power spectrum at all scales. This paper found that the effect has only a moderate impact for the redshift distribution of the sample of Lyman-α forests that we used, artificially increasing the signal by about 1σ, but that it could dominate the signal at large redshift. Overall, no statistically significant disagreement has been found yet.

Future data from upcoming spectroscopic surveys (in particular DESI) and CMB mapping experiments will definitely allow more precise measurements and better calibration of IGM simulations. Several extensions of this work could also be performed. In particular, the anisotropic linear bias of the Lyman-α forest, *i.e.* its dependence on angle μ, could be explored. Other avenues of exploration are to study the dependence of the signal on redshift and perpendicular separation $r_\perp$ (a first step in this direction was taken in CHIANG and SLOSAR n.d.). Because this bispectrum is sensitive to small scales observed in the Lyman-α forest, it could also provide additional constraints on the total mass of neutrinos and be used as a tool to study alternative models of dark matter predicting small-scale cut-offs. Finally, it would be interesting to explore measurements of the non-linear correlation between CMB lensing and the Lyman-α power spectrum, with techniques mentioned in section 4.2.3.2. This seems particularly fit as the power spectrum is constrained to

be positive.

CHAPTER 6

Joint analysis of Planck and SDSS-III/BOSS data

Contents

6.1 Introduction . . . 150
6.2 Theoretical background [reloaded] . . . 151
6.3 Data . . . 154
6.3.1 Planck data . . . 154
6.3.2 SDSS-III/BOSS data . . . 155
6.3.3 CMB lensing–large-scale structure correlations data . . . 158
6.4 Methodology . . . 160
6.4.1 Pseudo spectra . . . 160
6.4.2 Covariance matrix and likelihood . . . 163
6.4.3 Validation . . . 164
6.4.4 Null tests . . . 168
6.5 Analyses and results . . . 172
6.5.1 Cosmological model . . . 172
6.5.2 Statistical analysis . . . 173
6.5.3 Limits and perspectives . . . 188
6.6 Conclusion . . . 191
Appendices . . . 193
6.A X/Y matrices in the covariance . . . 193
6.B MCMC convergence tests . . . 194
6.B.1 Visual inspection . . . 194
6.B.2 Shrink factor . . . 195
6.B.3 Heidelberger-Welch test . . . 196

6.B.4 Effective sample size 197
6.C Profile likelihood 198

In this chapter, we present a joint analysis of Planck CMB temperature and lensing data with the spectroscopic tracers of SDSS-III/BOSS. The goal is to develop the methods to perform such an analysis, from the individual map or catalog level up to constraints on cosmological models, and to point out difficulties in doing so, in particular from the point of view of future experiments. This work led to a paper which is currently under review (Doux *et al.* 2017).

6.1 Introduction

Over the last few years, there has been a growing activity around this kind of analysis (see section 4.4.1) with multiple purposes: analysing available data sets, making forecasts for the next generation of surveys, or developing numerical tools. In particular, the corresponding working groups of LSST and Euclid are surveying and developing tools to perform joint analysis of multiple probes, and in combination with external data sets (including CMB data). The ultimate goal is to exhaust the cosmological information contained in multiple, disparate and complementary data sets, so as to be able, perhaps, to distinguish between various models of dark energy and dark matter.

To this end, we thus first construct the maps of projected galaxy density of the three spectroscopic samples of SDSS-III/BOSS, that is, LOWZ, CMASS and the uniform quasar sample (which we will simply call QSO). We then measure their auto-power spectra and cross-power spectra with the CMB lensing convergence map from Planck. Next, we build a joint likelihood for the pseudo-spectra and run Markov Chain Monte Carlo (MCMC) analyses, testing various configurations and demonstrating the constraining power of a joint analysis. Finally, we perform a joint analysis with CMB temperature to constrain the parameters of the ΛCDM model (H_0, ω_b, ω_c, A_s, n_s and z_re) and the galaxy/quasar biases. Finally, we extend the model and additionally constrain the sum of the masses of neutrinos, m_ν, and the dark energy equation of state, $w = p/\rho$.

The whole analysis was performed within the general-purpose framework of the `NumCosmo` library. I created, with the help of Sandro Vitenti and Mariana Penna-Lima, a module called `xcor` to compute and analyse the power spectra of an arbitrary number of probes. Details can be found appendix C.

The chapter is organised as follows. In section 6.2, we recall the theoretical formalism, considering the Limber formula, to compute the angular power spectra of CMB lensing and galaxy overdensities. In section 6.3, we describe the data used in this work and build the galaxy and quasar density maps. In section 6.4, we develop

the pseudo power spectrum estimators and construct the likelihood used in this work, and then we perform the validation and null tests. In section 6.5, we detail the results of the statistical analyses and present constraints on cosmological parameters (see figure 6.1 for a full pipeline diagram). Finally, we draw conclusions in section 6.6.

6.2 Theoretical background [reloaded]

In this section, we recall some of the theoretical tools already mentioned in chapters 2 and 4. The power spectrum of two projected variables is given, within the Limber approximation, by

$$C_\ell^{AB} = \int \mathrm{d}z \, \frac{H(z)}{c\chi(z)^2} W^A(z) W^B(z) P\left(k = \frac{\ell + 1/2}{\chi(z)}, z\right) + \mathcal{O}\left(\frac{1}{\ell^2}\right). \tag{6.1}$$

The kernels used here are:

CMB convergence The kernel for the convergence of CMB is given by the lensing efficiency, where the source redshift is that of the last scattering surface (denoted by an asterisk), such that

$$W_{\kappa_{\mathrm{CMB}}} = \frac{3}{2}\left(\frac{H_0}{c}\right)^2 \Omega_{\mathrm{m}}^0 \frac{(1+z)}{H(z)} \chi(z) \left(1 - \frac{\chi(z)}{\chi_*}\right). \tag{6.2}$$

Galaxy overdensity Including lensing effects (Bonvin and Durrer 2011; Peiris and Spergel 2000), the kernel $W^g(z)$ is given by

$$W^g(z) = b(z)\frac{\mathrm{d}n}{\mathrm{d}z} + \frac{3}{2}\left(\frac{H_0}{c}\right)^2 \Omega_{\mathrm{m}}^0 \frac{(1+z)}{H(z)} \chi(z)(5s-2)g(z), \tag{6.3}$$

where

$$g(z) = \int_z^{z_*} \mathrm{d}z' \left(1 - \frac{\chi(z)}{\chi(z')}\right) \frac{\mathrm{d}n}{\mathrm{d}z'}. \tag{6.4}$$

The function $b(z)$ is the linear bias relating the galaxy overdensity to the matter overdensity at large scales as $\delta_g(\chi\hat{\boldsymbol{n}}, z) = b(z)\delta(\chi\hat{\boldsymbol{n}}, z)$, and $\mathrm{d}n/\mathrm{d}z$ is the normalised redshift distribution of the tracers, which also contains the survey selection function. The second term in equation (6.3) is due to the effects of gravitational lensing, with two opposing contributions (see the $(5s-2)$ term): the dilation of the apparent surveyed volume and the magnification bias effect for flux-limited samples[1], where

$$s = \left.\frac{\mathrm{d}\log N(<m)}{\mathrm{d}m}\right|_{m=m_{\mathrm{max}}}. \tag{6.5}$$

$N(<m)$ denotes the cumulative count of objects with a magnitude smaller

[1] Lensed galaxies may appear brighter than they are and pass the luminosity threshold.

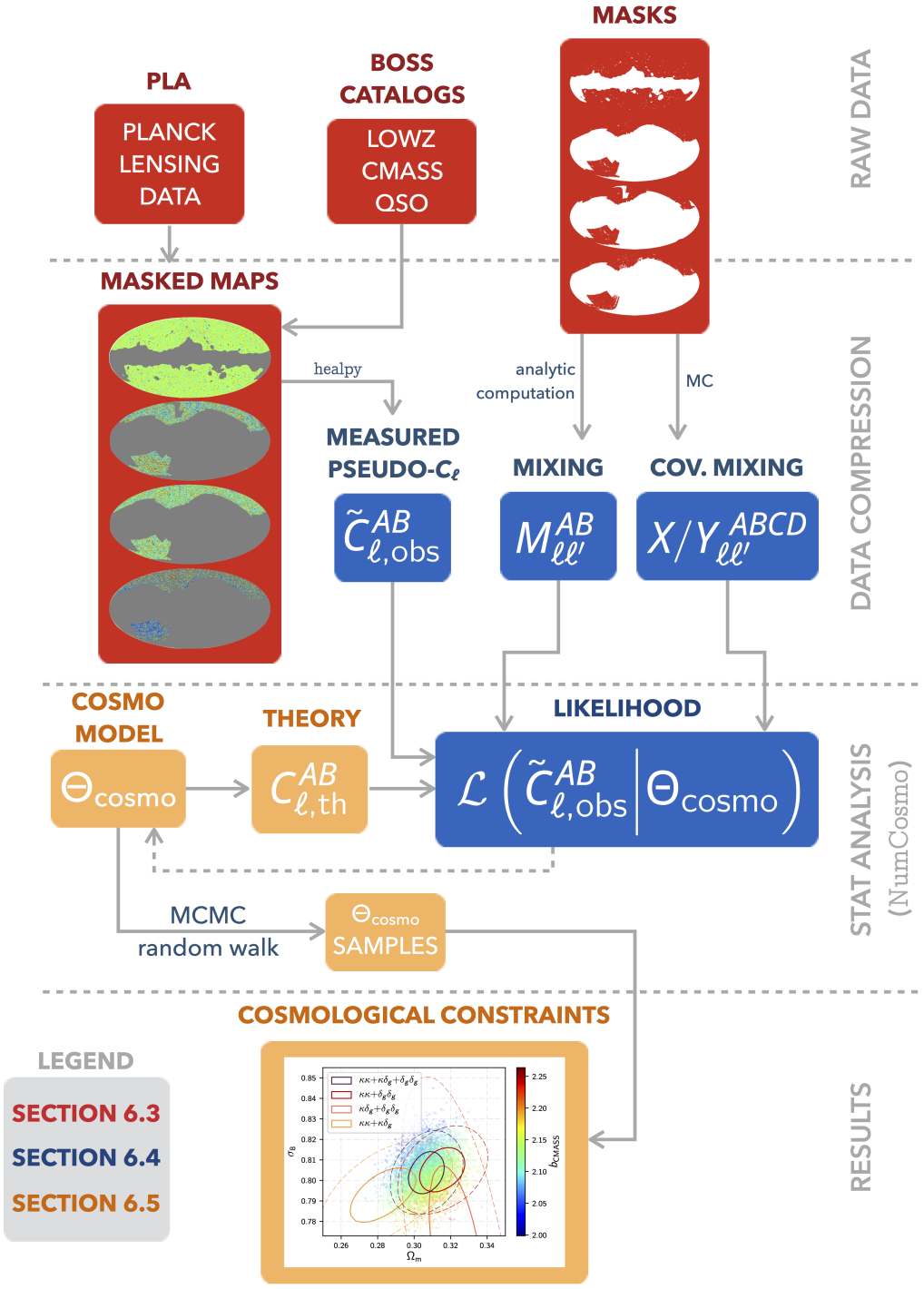

Figure 6.1 – Pipeline diagram. Sections 6.3 to 6.5 are color-coded.

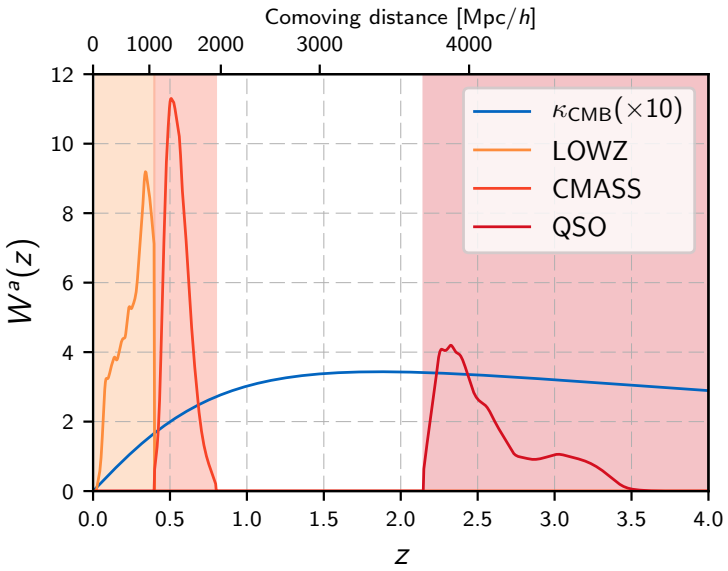

Figure 6.2 – Kernel functions $W^A(z)$ of the observables used for cross-correlation as defined in equations (6.2) and (6.3). For the LOWZ, CMASS and QSO samples, $W^g(z)$ reflects the redshift distribution (multiplied by the bias). The background colours correspond to the extent of the redshift distributions of the three samples. The CMB lensing kernel (multiplied by 10 on this plot for visibility) is very broad and peaks around $z \approx 2$.

than m and the derivative is estimated at the faint end of the catalog (Hui *et al.* 2007; Scranton *et al.* 2005). This term can be neglected when for the low-redshfit LOWZ and CMASS samples, but it is relevant (at the few percent level) for quasars (Chisari and Dvorkin 2013). Following Scranton *et al.* 2005, we use $s_{\mathsf{QSO}} = 0.2$ throughout this analysis.

Kernels of the observables used in this work are shown in figure 6.2.

As seen in section 4.2.2.2, the Limber approximation is valid when the kernel functions vary slowly on the scales that are being probed. In particular, the CMB lensing spectra are accurate for $\ell > 10$ (Lesgourgues and Tram 2014). Moreover, the selection functions of galaxies and quasars are wider than the largest scales probed for the spectroscopic tracers used here. Indeed, for a given sample, the largest scale probed is $\chi_{\max} \sim \pi/k_{\min}$ with $k_{\min} = (\ell_{\min} + 1/2)/\chi(z_{\mathrm{eff}})$, where $\chi(z_{\mathrm{eff}})$ is the comoving distance at the mean redshift of the sample and $\ell_{\min} = 20$ (see section 6.3). For LOWZ, CMASS and QSO, these scales are of order 110, 220 and 630 h^{-1} Mpc, while the selection functions have widths of order 1 080, 860 and 970 h^{-1} Mpc. Therefore, we can safely make use of this approximation to compute theoretical power spectra, which are integrals of the matter power spectrum weighted by the kernel functions corresponding to each observable.

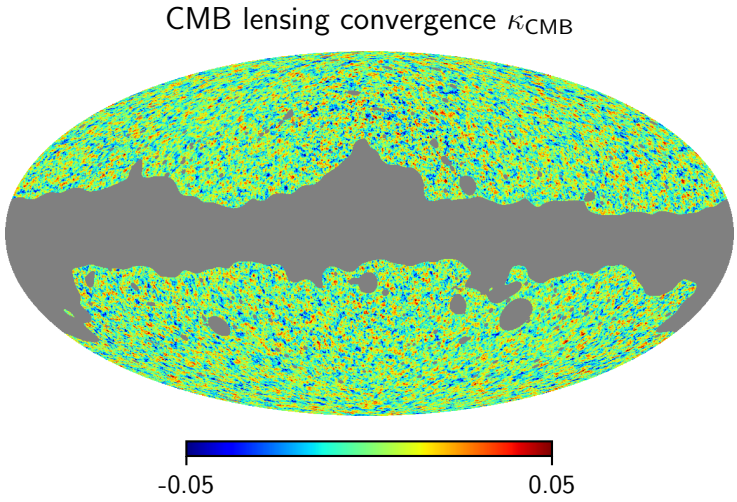

Figure 6.3 – Planck CMB lensing convergence map in galactic coordinates. Grey areas correspond to the masked areas near the galactic plane. The lensing map has been Wiener-filtered for visualisation purposes only.

6.3 Data

This section presents in grater detail the input data used in this work, the construction of the density maps and the pseudo-power spectra used in the cosmological analysis.

6.3.1 Planck data

In this work, we use Planck data for both the primordial CMB temperature anisotropies (Planck Collaboration *et al.* 2016a) and the CMB lensing (Planck Collaboration *et al.* 2016f). For temperature anisotropies, we use the two Planck likelihood codes: `Plik` for the high multipoles, $\ell \geq 30$, and `Commander` for low multipoles, $\ell < 30$ (see Planck Collaboration *et al.* 2016d, for detail and a summary in section 3.1.3.4).

We also use the CMB lensing convergence map from the Planck 2015 data release (Planck Collaboration *et al.* 2016f). The Planck Collaboration provides the convergence map[2] in the `Healpix`[3] (Górski *et al.* 2005) format, with resolution parameter $N_{\rm side} = 2048$, and the corresponding binary mask, with a sky fraction $f_{\rm sky} = 0.67$. Lensing potential maps were reconstructed from foreground-cleaned temperature and polarisation maps, obtained from the `SMICA` code (also briefly described in section 3.1.3.4). These were used to form five quadratic estimators $\hat{\phi}^{TT}$, $\hat{\phi}^{TE}$, $\hat{\phi}^{EE}$, $\hat{\phi}^{EB}$ and $\hat{\phi}^{TB}$, combined into a minimum-variance estimator (see section 2.3.2.2 for the general method and Planck Collaboration *et al.* 2016f, for specificities about the Planck reconstruction). The Wiener-filtered convergence

[2]The convergence map and mask files are publicly available at `http://pla.esac.esa.int/pla/`.
[3]`http://healpix.jpl.nasa.gov/`

map is shown in figure 6.3 with its mask. Throughout this analysis, we will assume that the dependence of the reconstructed lensing map on the fiducial cosmological model (see Planck Collaboration *et al.* 2016f, Appendix C) does not impact cosmological constraints and reserve this question for future work.

6.3.2 SDSS-III/BOSS data

The spectroscopic samples Baryon Oscillations Spectroscopic Survey (BOSS, Dawson *et al.* 2013) consists of two galaxy catalogs named LOWZ and CMASS and one quasar catalog, a subset of which has a uniform selection function. They are described in section 3.2.2.3 and we only recall relevant information in this section.

6.3.2.1 Luminous Red Galaxies: LOWZ & CMASS

LOWZ contains Luminous Red Galaxies (LRG) at low redshift ($z \lesssim 0.4$), and it aims at a constant number density of about $\bar{n} \sim 3 \times 10^{-4}\, h^3\,\mathrm{Mpc}^{-3}$ over the redshift range $[0.1, 0.4]$. This is done using a redshift dependent magnitude cut. In this work, we use the twelfth data release (DR12) and select galaxies in the range $[0.1, 0.4]$, which contains 383876 galaxies. The CMASS sample contains galaxies at higher redshifts $0.4 \lesssim z \lesssim 0.8$ with a constant stellar mass in this redshift range. The twelfth data release contains 849637 galaxies in the redshift range $[0.4, 0.8]$ used in this work. The normalised redshift distributions of the two samples are shown on figure 6.2 (multiplied by their respective biases).

BOSS's spectroscopic fibres are plugged into tiles of diameter 3° to observe predetermined targets. The combined footprints of all tiles can be decomposed into non-overlapping sky sectors. Because of the finite size of fibres, galaxies closer than $62''$ may not be observed even after multiple observations of the same field. The pipeline may also fail in determining the redshift of some galaxies (especially the faintest ones). Therefore, for each sector i, the completeness is defined as the ratio of observed galaxies with a measured redshift to the number of targets lying in that same sector

$$C_i = \frac{N_{\mathrm{obs,i}}}{N_{\mathrm{targ,i}}}. \tag{6.6}$$

The completeness maps are defined in the `Mangle` software[4] format and are converted to `Healpix` maps with resolution parameter $N_{\mathrm{side}} = 2048$. The mask functions of the galaxy samples are obtained by assigning 1 to pixels where the completeness is above 75% and then removing small areas that were vetoed for bad photometry, bright objects and stars and instrumental constraints, such as fibre centerposts and fibre collisions.

[4] See `http://space.mit.edu/~molly/mangle/`.

In order to correct for completeness, each galaxy is thus assigned a weight

$$w_{\rm tot} = w_{\rm star} w_{\rm seeing} (w_{\rm cp} + w_{\rm noz} - 1), \tag{6.7}$$

where $w_{\rm star}$ and $w_{\rm seeing}$ correct for non-cosmological fluctuation in the target selection due to stellar density (only for the CMASS sample) and atmospheric seeing, $w_{\rm cp}$ corrects for fibre collisions and $w_{\rm noz}$ corrects for redshift failures (in these cases, the closest successfully observed galaxy is up-weighted by 1).

6.3.2.2 Quasars

The selection function (over the sky) of the full quasar sample of BOSS is not uniform due to the observing strategy, hence we shall use the so-called CORE sample which contains QSOs with redshift $z \geq 2.15$ that were uniformly selected by the `XDQSO` algorithm (Bovy *et al.* 2011). There are 94971 quasars in the CORE sample of DR12 within this redshift range. The completeness is computed using the `BOSSQSSOMASK` software[5] from Eftekharzadeh *et al.* 2015 and is then combined with the veto mask to build the mask of the quasar density map.

6.3.2.3 Building the maps

We build `Healpix` maps with resolution parameter $N_{\rm side} = 2048$ for the projected overdensity of the three spectroscopic samples. For the LOWZ and CMASS samples, we proceed as follow. For each pixel p,

$$\delta_p = \frac{N_p}{\overline{N}} - 1, \tag{6.8}$$

where $N_p = \sum_{i \in p} w_i$ is the number of galaxies in pixel p counted with their weights and $\overline{N} = \frac{1}{N_{\rm pix}} \sum_{p=1}^{N_{\rm pix}} N_p$ is the mean pixel count (where the sum runs only on pixels in the observed area, *i.e.* where the mask function is equal to 1).

For the quasars, there is no weight provided in the BOSS DR12 catalog and the density map is computed as

$$\delta_p = \frac{N_p}{\overline{N}} - 1, \tag{6.9}$$

where this time $N_p = \sum_{i \in p} 1/C_{s(p)}$ denotes the number of QSOs lying in pixel p, up-weighted by the completeness $C_{s(p)}$ of the sector $s(p)$ where the pixel p lies, and $\overline{N}$ denotes the mean weighted pixel count in the observed area.

[5] See `http://faraday.uwyo.edu/~admyers/bossqsomask/`.

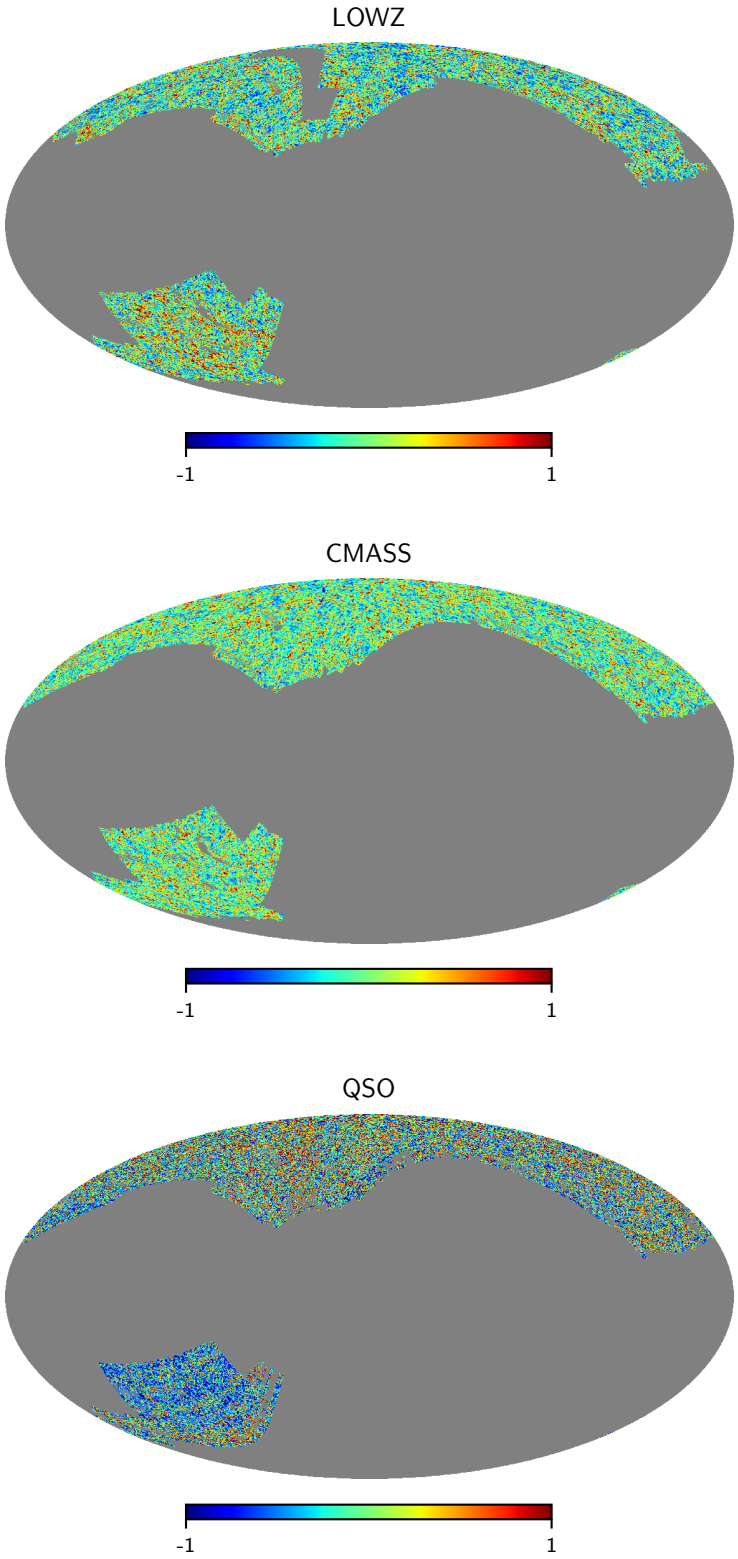

Figure 6.4 – BOSS galaxy and quasar overdensity maps in galactic coordinates. Grey areas correspond to the masked areas near the galactic plane. The overdensity maps have been smoothed on one degree scale for visualisation purposes only.

The angular densities of the samples are

$$\bar{n}_{\mathsf{LOWZ}} = 150 \times 10^3\,\mathrm{sr}^{-1}, \tag{6.10}$$
$$\bar{n}_{\mathsf{CMASS}} = 300 \times 10^3\,\mathrm{sr}^{-1}, \tag{6.11}$$
$$\bar{n}_{\mathsf{QSO}} = 36 \times 10^3\,\mathrm{sr}^{-1}. \tag{6.12}$$

The maps of the estimated overdensity for the three samples are shown in figure 6.4.

6.3.3 CMB lensing–large-scale structure correlations data

In this work, we will use, in addition to CMB temperature data, auto and cross spectra of CMB lensing from Planck and spectroscopic tracers from BOSS. More precisely, we will use the auto-pseudo spectra of the CMB lensing map κ_{CMB} and of the density contrast maps of the LOWZ and CMASS samples. We also use the pseudo-cross-spectra of the CMB lensing map with the three LSS tracers. The collection of these six spectra (shown in figure 6.5) will henceforth be referred to as "*CMB lensing-LSS correlations*", and denoted CMB lensing $\otimes$ LSS in the figures.

We do not use the auto spectrum of the QSO map because it is completely shot-noise-dominated in multipole space. We do not use the galaxy cross spectra because their redshift ranges do not overlap and the cross spectra should therefore be zero in the Limber approximation (which we check in the next section).

We use multipoles in the range $[\![20, 500[\![$ for all auto- and cross-pseudo spectra. The small-scale limit $\ell_{\mathrm{max}} = 500$ is determined by:

- the CMB lensing resolution: 90% of the lensing signal lies in the conservative multipole range $[\![40, 400]\!]$ used by the Planck collaboration;
- the shot-noise of the galaxy/quasar auto spectra: $\tilde{C}_\ell^{gg}$ becomes noise dominated for all samples at $\ell \geq \ell_{\mathrm{max}}$ (CMASS being the limiting one);
- validity of the galaxy clustering model: we will use the linear bias model and the `halofit` model for the non-linear power spectrum. The linear bias approximation is assumed to be valid for scales larger than $10\,h^{-1}\,\mathrm{Mpc}$, while the smallest scales probed are $\chi_{\mathrm{min}} \sim 2\pi/k_{\mathrm{max}}$ where $k_{\mathrm{max}} = (\ell_{\mathrm{max}} + 1/2)/\chi(z_{\mathrm{eff}})$, which correspond to scales of order 15.2, 26.8 and $71.4\,h^{-1}\,\mathrm{Mpc}$. We also assume that the `halofit` model is a correct description up to these scales. These assumptions are discussed in more detail in section 6.5.3, in the light of the results.

The large-scale limit is fixed at $\ell_{\mathrm{min}} = 20$ for of the following reasons:

- validity of the Limber approximation, which is known to fail at very low ℓ;
- partial sky coverage limits the number of large-scale modes accessible;

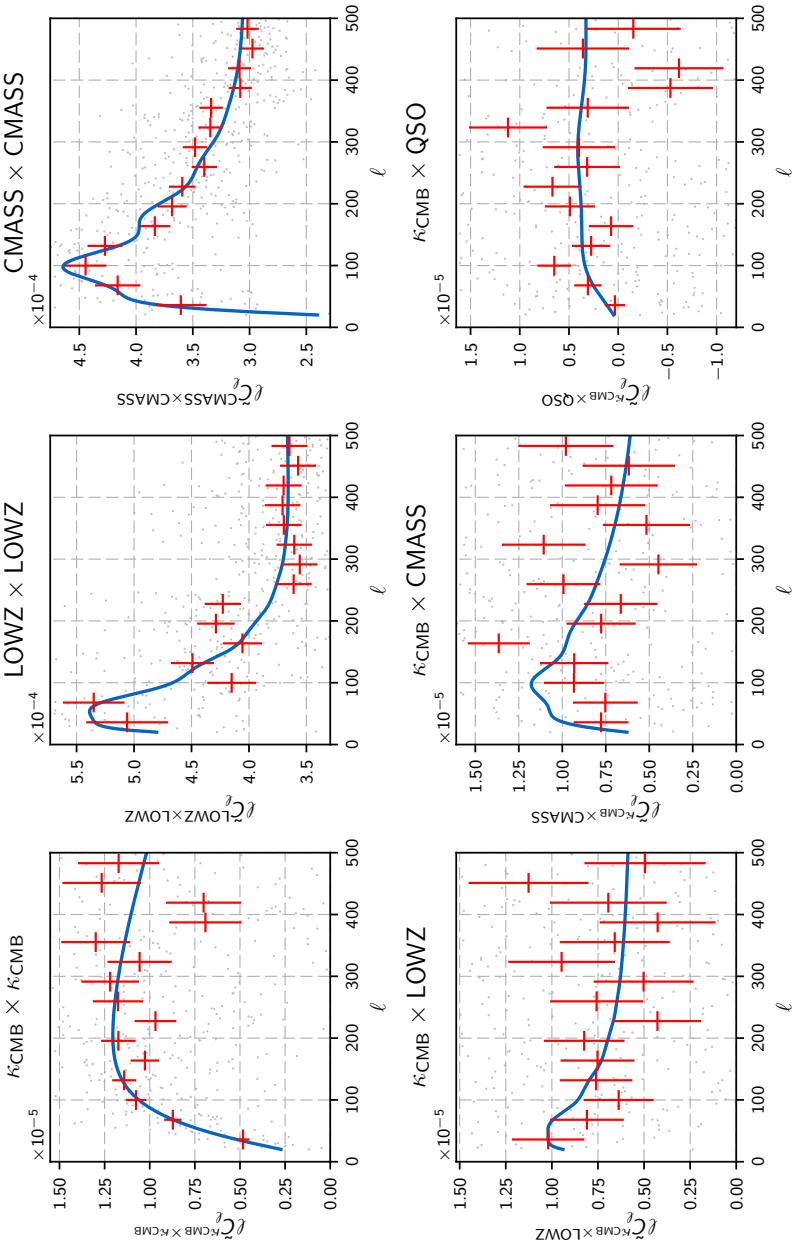

Figure 6.5 – Auto- and cross-pseudo spectra used in this work. Observed spectra are represented by the light grey points in the multipole range $20 - 500$, and binned as red error bars (only for visualisation). The theoretical curves, for best-fit biases and fixed Planck cosmology, are represented by the solid blue curves. Pseudo spectra are multiplied by ℓ to help visualise features of the theoretical power spectra, especially the wiggling related to baryon acoustic oscillations (and the covariance matrix is modified accordingly).

- CMB lensing is measured from $\ell_{\rm min} = 8$, as reconstruction is not stable below;
- field-dependent observing conditions during the SDSS photometric and spectroscopic surveys could contaminate the measurement of the overdensity fields on large-scales[6] (we check for such contamination in section 6.4.4 and find no evidence of it).

The six observed pseudo spectra are shown in figure 6.5 together with theoretical curves for our best-fit biases ($b_{\mathsf{LOWZ}} = 1.871 \pm 0.025$, $b_{\mathsf{CMASS}} = 2.095 \pm 0.022$ and $b_{\mathsf{QSO}} = 2.21 \pm 0.44$) and with fixed cosmology[7]. We report detections for the CMB lensing-galaxy density cross-correlations of 4.7σ, 13.9σ and 10.6σ for LOWZ, CMASS and QSO, respectively.

6.4 Methodology

This section describes the method to analyse the data. We choose to use the pseudo-power spectrum formalism, which takes into account partial sky coverage by appropriately scaling the theoretical full-sky power spectra and comparing them to the observed pseudo-spectra. This forward-modelling method has the advantage that it is simple to obtain an unbiased prediction, without the need to reverse the effects of the mask on the observation, an operation that can be difficult and unstable given the complexity of the masks. The drawback is that the covariance matrix is impossible to compute analytically: instead, we must either estimate it with Monte-Carlo simulations, or, as we do here, use a semi-analytical approximation. We perform several tests to validate this method and the statistical pipeline used in the next section. Finally, we also perform null tests searching for possible contamination of the power spectra by effects due to the masks or the SDSS photometry.

6.4.1 Pseudo spectra

6.4.1.1 Definition

Many galaxy and CMB surveys cover only a fraction of the sky due to, for example, the limited field of view or galactic contamination, among others. In order to properly account for the partial sky coverage in the calculation of the angular power spectra, we define the mask function $\mathcal{W}^A(\hat{\boldsymbol{n}})$ associated with the field $A(\hat{\boldsymbol{n}})$. It has value 1 if the direction $\hat{\boldsymbol{n}}$ lies in the observed region, and 0 otherwise.

The cross-pseudo spectrum of observables A and B is thus defined as the cross spectrum of the cut-sky fields $\tilde{A}(\hat{\boldsymbol{n}}) = \mathcal{W}^A(\hat{\boldsymbol{n}})A(\hat{\boldsymbol{n}})$ and $\tilde{B}(\hat{\boldsymbol{n}}) = \mathcal{W}^B(\hat{\boldsymbol{n}})B(\hat{\boldsymbol{n}})$, and

[6] The size of the BOSS plates (3°) correspond to a multipole of $\ell \sim \pi/\theta \approx 60$.

[7] Parameters' values are fixed at the best-fit cosmology for Planck "TT,TE,EE+lowP+lensing+ext" (Planck Collaboration *et al.* 2016e) for the flat ΛCDM model with a mass of neutrinos $m_\nu = 0.06\,\mathrm{eV}$.

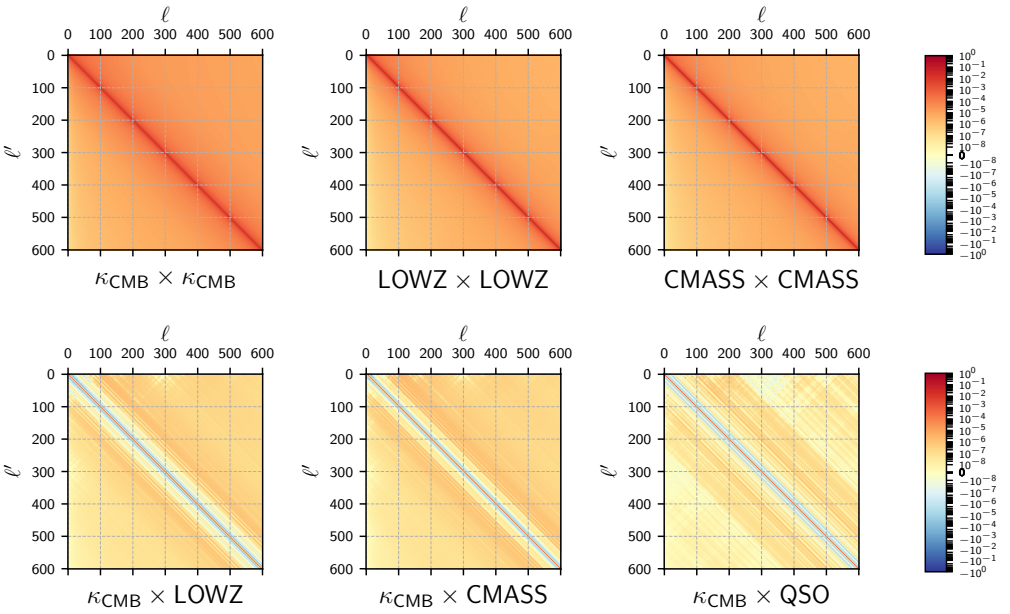

Figure 6.6 – Mixing matrices of the six power spectrum used in the analysis (see the masks in figures 6.3 and 6.4), relating the full-sky power spectrum C_ℓ to the pseudo spectrum $\tilde{C}_\ell$ as in equation (6.13). The matrices' elements are strongly dominated by the diagonal terms and the coupling between modes is given by off-diagonal elements.

its expected value can be related to the (true) full-sky cross power spectrum by (Brown *et al.* 2005)

$$\langle \tilde{C}_\ell^{AB} \rangle = \sum_{\ell'} M_{\ell\ell'}^{AB} C_{\ell'}^{AB}, \tag{6.13}$$

where $M_{\ell\ell'}^{AB}$ is the mixing matrix, which is given in terms of the Wigner-3j symbols

$$M_{\ell\ell'}^{AB} = \frac{2\ell+1}{4\pi} \sum_{\ell''} (2\ell''+1) \mathcal{W}_{\ell''}^{AB} \begin{pmatrix} \ell & \ell' & \ell'' \\ 0 & 0 & 0 \end{pmatrix}^2. \tag{6.14}$$

The cross spectra of the masks are

$$\mathcal{W}_\ell^{AB} = \frac{1}{2\ell+1} \sum_m w_{\ell m}^A (w_{\ell m}^B)^*, \tag{6.15}$$

where

$$w_{\ell m}^A = \int \mathrm{d}\hat{\boldsymbol{n}}\, \mathcal{W}^A(\hat{\boldsymbol{n}}) Y_{\ell m}^*(\hat{\boldsymbol{n}}). \tag{6.16}$$

The mixing matrix introduces a scaling factor equal to $\left(f_{\rm sky}^A f_{\rm sky}^B\right)^{1/2}$, i.e., the geometric mean of the observed sky fractions for the observables A and B (Hivon *et al.* 2002). It also couples the multipoles ℓ and ℓ', that would be otherwise uncorrelated,

especially at large scales. Mixing matrices are computed analytically[8] for each pair of observables and are shown on figure 6.6.

6.4.1.2 Pseudo spectra estimator

Pseudo spherical harmonic coefficients of the four maps are estimated with the `map2alm` function of `Healpix` and summed to give an estimator of the pseudo spectra as

$$\hat{\tilde{C}}_\ell^{AB} = \frac{1}{2\ell+1} \sum_{m=-\ell}^{m=+\ell} \tilde{A}_{\ell m} \tilde{B}^*_{\ell m}, \tag{6.17}$$

for $A, B \in \{\mathsf{LOWZ}, \mathsf{CMASS}, \mathsf{QSO}, \kappa_{\rm CMB}\}$. These pseudo spectra have a noise contribution and an expectation value given by

$$\langle \hat{\tilde{C}}_\ell^{AB} \rangle = \sum_{\ell'} M_{\ell\ell'}^{AB} C_{\ell'}^{AB} + \delta_{AB} \tilde{N}_\ell^A, \tag{6.18}$$

where $\tilde{N}_\ell^A$ is the noise pseudo-spectrum of the measured field $A(\hat{\boldsymbol{n}})$, which needs to be subtracted. It is assumed here that different observables have uncorrelated noise, *i.e.* that noise cross spectra are null (for both full-sky and pseudo).

In principle, noise pseudo spectra can be computed using the mixing matrix and equation (6.13),

$$\tilde{N}_\ell^A = \sum_{\ell'} M_{\ell\ell'}^{AA} N_{\ell'}^A. \tag{6.19}$$

However, the sum over ℓ' runs from 0 to infinity, so, in practice, it has to be cut at some maximum multipole $\ell_{\rm max}$. But convergence is not guaranteed, since noise spectra are increasing functions of ℓ (they are quasi-constant for galaxies and grow like $\sim \ell^2$ for CMB lensing). Therefore, we used instead simulated noise maps for both CMB lensing and galaxies.

For CMB lensing, we used the 100 simulated lensing reconstruction maps provided by the Planck Legacy Archive.[9] Given a known, full-sky, input convergence map (to be masked) and a masked, reconstructed convergence map, one can compute the difference of the pseudo spectra in order to obtain an estimate of the noise pseudo power spectrum $\tilde{N}_\ell^\kappa$, which is then averaged over realisations of the simulation.

For the galaxy catalogs, the full-sky shot noise spectrum is $N_\ell = 1/\bar{n}$, where $\bar{n}$ is the angular density of objects (weighted and expressed in steradian^{-1}). In order to estimate the pseudo spectra, random maps with a pure Poisson distribution of appropriate density are generated and then masked. The pseudo spectra of 100 maps are averaged to get an estimate of the pseudo noise spectra $\tilde{N}_\ell^g$. However, weights slightly increase the noise level, which is henceforth assumed to be of the form $\tilde{N}_\ell^g + a^g$

[8] The Wigner-3j symbols are computed using a Fortran routine provided by Jean-Christophe Hamilton.

[9] See `http://pla.esac.esa.int/pla/`.

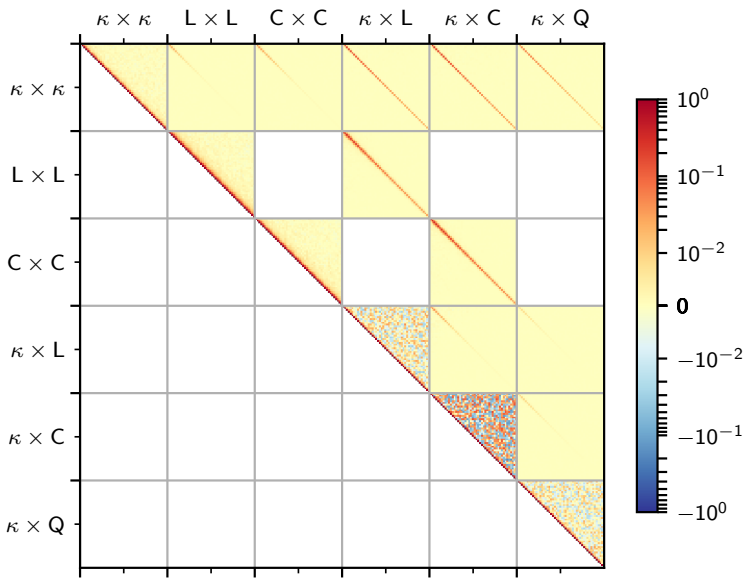

Figure 6.7 – Full covariance matrix (normalised to unit diagonal) of the CMB lensing-LSS correlations computed from equation (6.21) in symmetric logarithmic scale. It is divided in blocks corresponding to the six angular spectra: κ, L, C and Q correspond to respectively κ_{CMB}, LOWZ, CMASS and QSO. Note the (small) numerical noise in the variance blocks of the cross power spectra from the **X**/**Y** matrices. Only the upper part is displayed. The white blocks in the upper parts correspond to non-correlated spectra.

(like in Ho *et al.* 2012), where a^g is a small nuisance parameter to be marginalised over during the analysis, and that we found to be one order of magnitude smaller than $\tilde{N}^g_\ell$. As noted in Putter *et al.* 2012, this term may also absorb contributions of non-linear biasing, a possibility that we discuss in section 5.4.

Our estimator thus reads

$$\hat{\tilde{C}}^{AB}_\ell = \frac{1}{2\ell+1}\sum_{m=-\ell}^{m=+\ell} \tilde{A}_{\ell m}\tilde{B}^*_{\ell m} - \delta_{AB}\frac{1}{N_{\mathrm{sim}}}\sum_{i=1}^{N_{\mathrm{sim}}} \hat{\tilde{N}}^{A,i}_\ell, \tag{6.20}$$

where $\hat{\tilde{N}}^{A,i}_\ell$ is the estimated pseudo-noise spectrum of simulation number i. The pseudo spectra used in this work are shown in figure 6.5.

6.4.2 Covariance matrix and likelihood

The covariance matrix of the pseudo spectra is computed using an extension of Efstathiou's symmetrisation approximation (Efstathiou 2004) following Brown

et al. 2005 (the full computation is performed in appendix B.1.2) and is given by

$$\begin{aligned}\mathrm{Cov}\left(\tilde{C}_\ell^{AB}, \tilde{C}_{\ell'}^{CD}\right) =& \sqrt{D_\ell^{AD} D_{\ell'}^{AD} D_\ell^{BC} D_{\ell'}^{BC}} \mathbf{X}_{\ell\ell'}^{ABCD} \\ &+ \sqrt{D_\ell^{AC} D_{\ell'}^{AC} D_\ell^{BD} D_{\ell'}^{BD}} \mathbf{Y}_{\ell\ell'}^{ABCD}\end{aligned} \tag{6.21}$$

with

$$D_\ell^{AB} = \begin{cases} C_\ell^{AB} & \text{if } A \neq B \\ C_\ell^{AA} + N_\ell^A & \text{if } A = B \end{cases}, \tag{6.22}$$

where C_ℓ^{AB} and N_ℓ^A are the full-sky theoretical signal and noise spectra. $\mathbf{X}_{\ell\ell'}^{abcd}$ and $\mathbf{Y}_{\ell\ell'}^{abcd}$ are two matrices depending only on the masks of observables A, B, C, D, determined to arbitrary precision by a Monte-Carlo (MC) simulation (see section 6.A for more detail). The covariance matrix (estimated for a fiducial cosmology) is shown in figure 6.7.

A Gaussian likelihood is used for the stacked pseudo spectra vector

$$\mathcal{L}\left(\tilde{\boldsymbol{C}}_\ell^{\mathrm{obs}} | b_g, \Theta_{\mathrm{cosmo}}\right) = \frac{1}{(2\pi)^{n/2} |\mathbf{Cov}|^{1/2}} e^{-\chi^2/2}, \tag{6.23}$$

where

$$\chi^2 = \left(\tilde{\boldsymbol{C}}^{\mathrm{obs}} - \tilde{\boldsymbol{C}}^{\mathrm{th}}\right)^{\mathrm{T}} [\mathbf{Cov}]^{-1} \left(\tilde{\boldsymbol{C}}^{\mathrm{obs}} - \tilde{\boldsymbol{C}}^{\mathrm{th}}\right), \tag{6.24}$$

$\tilde{\boldsymbol{C}}^{\mathrm{obs}}$ is the stacked vector of observed pseudo spectra (see figure 6.5) and $\tilde{\boldsymbol{C}}^{\mathrm{th}}$ is the stacked vector of theoretical pseudo spectra computed from the Limber approximation (see equation (6.1)) and multiplied by the mixing matrices. The covariance matrix **Cov** is that of the stacked vector as defined in equation (6.21) and is shown in figure 6.7.

6.4.3 Validation

In this section, we perform validation tests for the pseudo spectrum estimator, the covariance matrix and the statistical pipeline.

6.4.3.1 Validation of the pseudo spectrum estimator

In order to validate the pseudo spectrum estimator and the semi-analytical expression of the covariance matrix given in equation (6.21), we generate 1000 sets of four correlated, full-sky maps with appropriate auto and cross spectra (for $\mathsf{LOWZ}, \mathsf{CMASS}, \mathsf{QSO}, \kappa_{\mathrm{CMB}}$) computed using equation (6.1). These maps are then added realistic noise and are masked as follows: for each lensing convergence map, we add an uncorrelated Gaussian noise with spectrum N_ℓ^κ given by the approximate spectrum delivered by the Planck Legacy Archive, which is precise enough for the covariance validation. For each galaxy density map, we also need to simulate Poisson sampling. To do so, we generate a map where the value in pixel p is a Poisson random

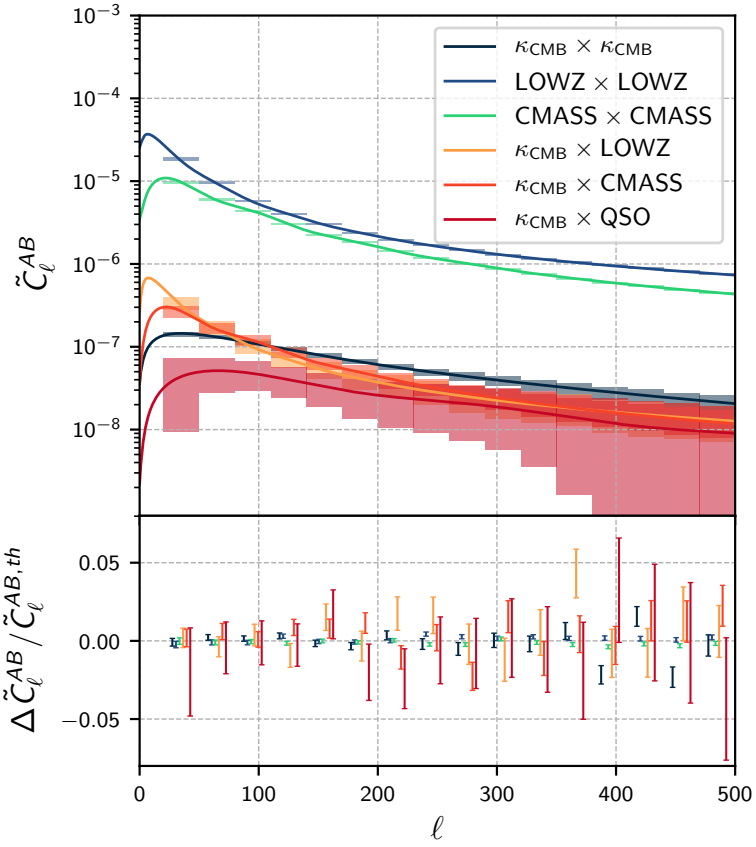

Figure 6.8 – Validation of the pseudo spectrum estimator: the upper plot shows in solid line the theoretical pseudo spectra, computed using full-sky spectra and mixing matrices as in equation (6.13). Boxes show the mean of the simulated pseudo spectra and its spread for 1000 realisations, binned for visualisation. The lower plots shows the relative error on the mean. All spectra are consistent with the theoretical expectations in the multipole range used for this work.

variable of mean λ_p, i.e.,

$$n_p \sim \text{Poisson}\left(\lambda_p\right) \quad \text{with} \quad \lambda_p = \overline{N}\left(1+\delta_p\right), \tag{6.25}$$

where δ_p is the simulated overdensity at pixel p and $\overline{N}$ is the mean number of galaxies per pixel (different for the three samples). A reconstructed density map is then built using equation (6.8), which now incorporates Poisson shot-noise. These full-sky maps are then masked and their pseudo spectra are evaluated. The mean of the estimated pseudo spectra is compared with that of the theoretical pseudo spectra computed using the mixing matrices on figure 6.8, proving strong agreement and validating the estimator.

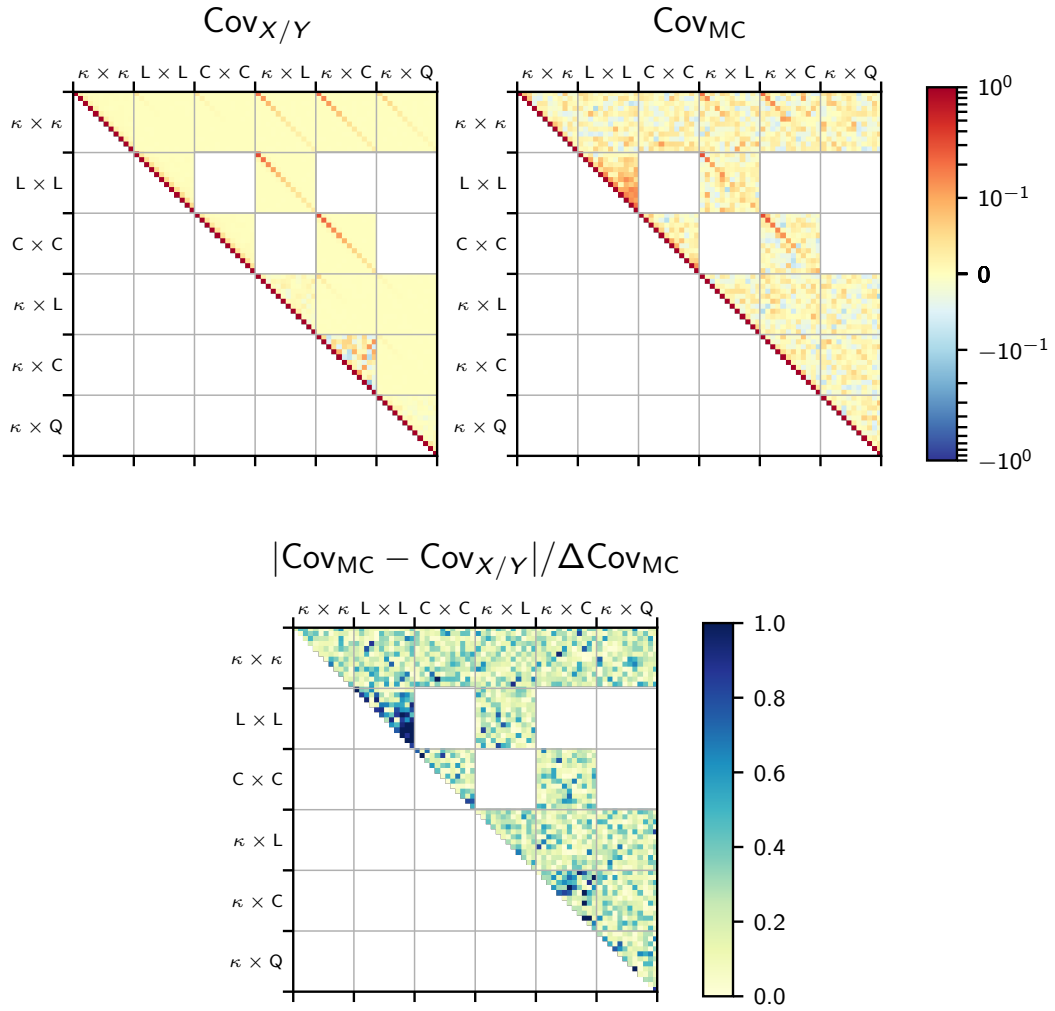

Figure 6.9 – Validation of the covariance matrix. On the left panel, the covariance matrix used in the analysis from equation (6.21), denoted $\mathrm{Cov}_{X/Y}$; on the middle panel, the empirical covariance matrix of 1000 simulated stacked pseudo spectra, denoted $\mathrm{Cov}_{\mathrm{MC}}$. Both have been normalised by the diagonal elements of $\mathrm{Cov}_{X/Y}$, therefore the diagonal is 1 by construction on the left panel, and the fact that it is very close to 1 on the middle panel proves the agreement between the two estimates. Off-diagonal elements are polluted on $\mathrm{Cov}_{\mathrm{MC}}$ by numerical noise (which is one order of magnitude smaller than the diagonal elements and would reduce with more simulations). On the right panel, the absolute difference between the two estimates of the covariance matrix (non-normalised) is shown, element-wise divided by the standard deviation of $\mathrm{Cov}_{\mathrm{MC}}$ (obtained from bootstrapping the simulated pseudo spectra). Note the different colour scale of the right panel: the deviation is at most of order 1 σ, showing good agreement between our two estimates and validating equation (6.21).

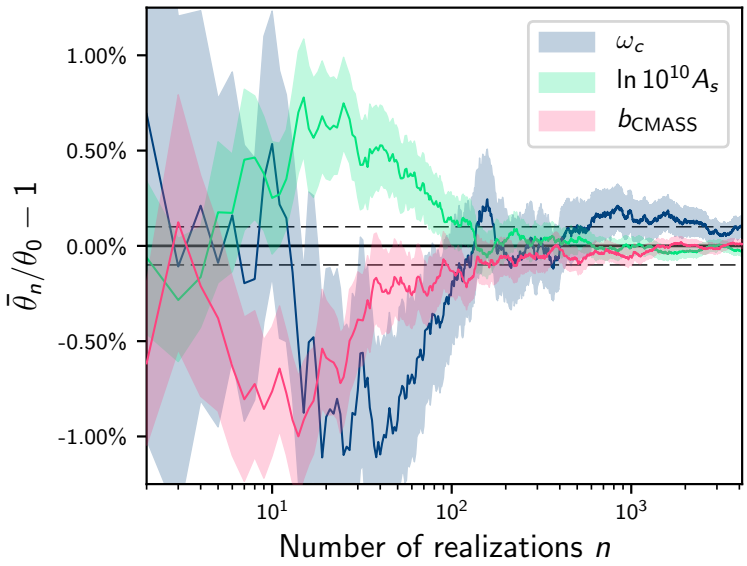

Figure 6.10 – Statistical pipeline validation with Monte-Carlo simulation: realisations of the pseudo spectra are drawn from the likelihood $\mathcal{L}$ and best-fit parameters $\boldsymbol{\theta} = (\omega_\mathrm{c}, \ln 10^{10} A_\mathrm{s}, b_{\mathsf{CMASS}})$ are computed. The relative error on the mean values of best-fit parameters $\overline{\boldsymbol{\theta}}_n$ as a function of the number of realisations n is shown here. The dotted lines show the 0.1% requirement for this test, reached after 4146 realisations. The variance (displayed by the coloured bands) decreases as $1/\sqrt{n}$ while the mean values converge towards their input values, demonstrating the internal consistency of the statistical pipeline. Note however the very small deviation on ω_c, within the error requirement, but in consistent with the fact that the maximum likelihood estimator is only asymptotically unbiased.

6.4.3.2 Validation of the covariance matrix

The empirical covariance of the sets of pseudo spectra is finally computed and compared to the semi-analytical covariance we use throughout this analysis. The result in figure 6.9 shows good agreement and validates the estimator and the simulation of the matrices **X** and **Y** (that were computed using generic spectra, see section 6.A).

6.4.3.3 Consistency of the statistical pipeline

The statistical pipeline is validated by performing a Monte Carlo analysis similar to the one performed in Penna-Lima *et al.* 2014. Specifically, we want to check if the estimated parameters are unbiased. For that purpose, given the adopted fiducial model, we use the likelihood as the probability distribution of the pseudo spectra $\tilde{C}_\ell^{AB}$ to generate random samples (*i.e.* sets of stacked vectors $\tilde{\boldsymbol{C}}^{\mathrm{obs}}$). For each sample, we fit all parameters to be tested, thus building a collection $\{\boldsymbol{\theta}_i\}$ of best-fit values for these parameters. At step n, the means $\overline{\boldsymbol{\theta}}_n = \sum_{i=1}^{n} \boldsymbol{\theta}_i / n$ and standard deviations of the collection of best-fit values are computed. The largest

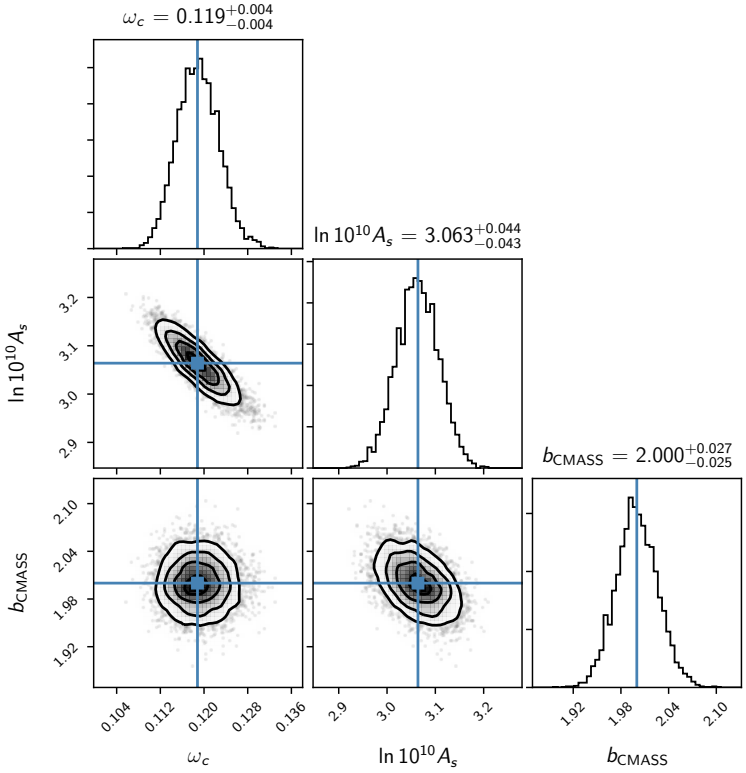

Figure 6.11 – Same test as figure 6.10, now showing the distribution of best-fit parameters for 4146 realisations. The ellipses show the 0.5, 1, 1.5 and 2σ contours and the blue lines show the input values of the parameters.

relative error (LRE) over parameter means is computed and we repeat the process, adding more samples, until the LRE has reached a level of 0.1% and check that the fiducial values are within the error bars. For this test, we only use one sample of galaxies with the redshift distribution of the CMASS sample and generate samples of $\tilde{\boldsymbol{C}}_\ell^{\kappa_{\mathrm{CMB}}\times\kappa_{\mathrm{CMB}}}$, $\tilde{\boldsymbol{C}}_\ell^{\kappa_{\mathrm{CMB}}\times\delta_{\mathrm{CMASS}}}$ and $\tilde{\boldsymbol{C}}_\ell^{\delta_{\mathrm{CMASS}}\times\delta_{\mathrm{CMASS}}}$. Results of this test are plotted in figures 6.10 and 6.11, showing respectively the evolution of the mean values of the best fit parameters $\overline{\boldsymbol{\theta}}_n$ as a function of the number of realisations n and the distribution of the best-fit parameters for those same realisations. They confirm that the parameters' estimators are unbiased at least at the 0.1% level.

6.4.4 Null tests

We present in this section null tests that were performed to exclude potential systematic errors related to the masks and selection of the spectroscopic tracers.

6.4.4.1 Mask-related contamination

In order to assess potential leakage of power in the cross spectra due to the masking, we cross-correlate the 100 simulated reconstructed lensing maps of the Planck Legacy

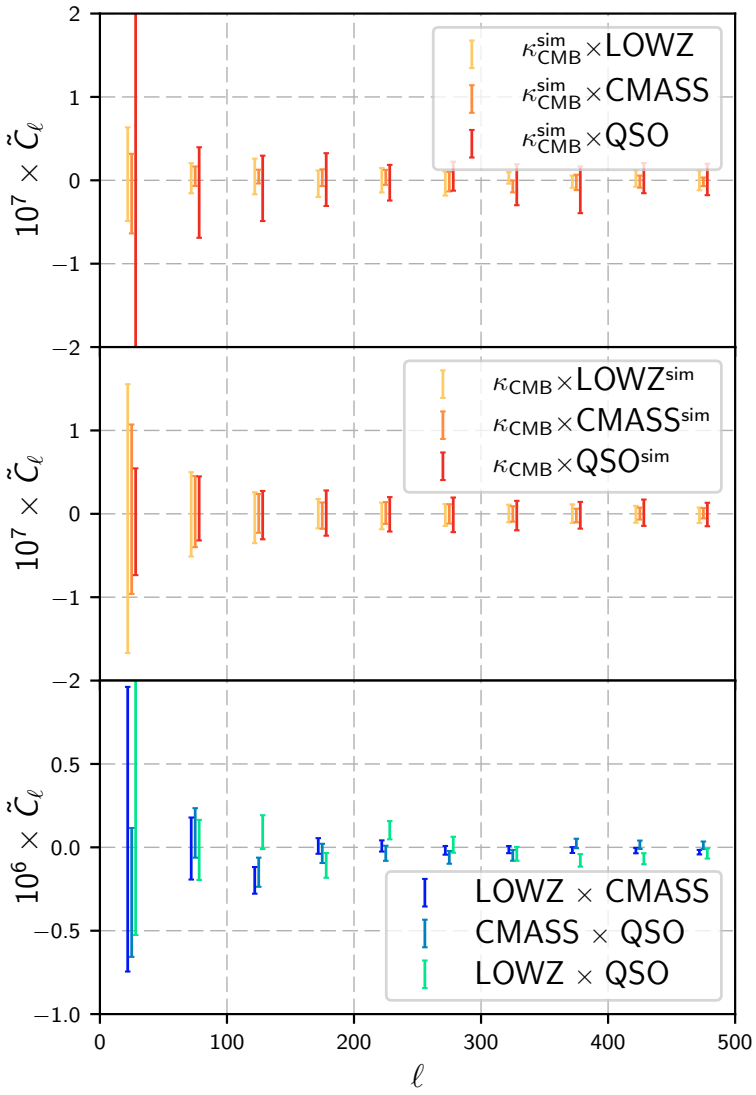

Figure 6.12 – Null test for residual correlation. The top panel shows the mean cross-pseudo spectrum between simulated lensing maps and the real galaxy/quasar density maps, the middle panel shows the mean cross-pseudo spectrum between the real lensing map and simulated galaxy/quasar density maps, and the bottom panel shows the cross-pseudo spectra between the tracers. The cross-correlations with simulated maps are consistent with zero, showing no leakage of power from the masks, while the cross-correlation of the tracers density show marginal correlation, at worst one order of magnitude lower than the autocorrelation signals.

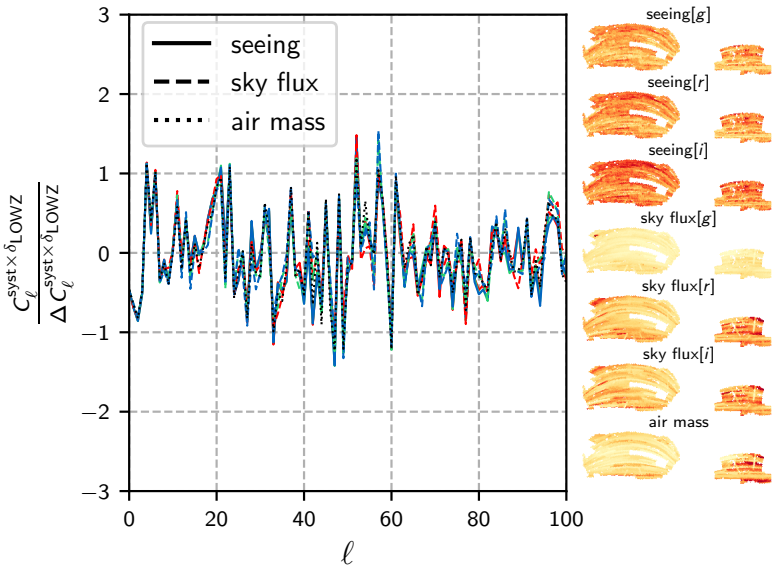

Figure 6.13 – Null test of photometric systematics contamination: normalised large-scale cross spectra of the seeing (solid lines), sky flux (dashed lines) and air mass (dotted line) during photometric observations with the density of LOWZ galaxies. They are consistent with zero, with no discernable trend across multipoles. The seeing and sky flux are shown in the three main colour bands (g, r and i) which are displayed in red, green and blue. The maps of these observables are shown on the right in equatorial coordinates where the north and south galactic caps of the SDSS survey can be seen. The χ^2 statistics for these cross spectra are respectively 32, 33, 33, 30, 32, 32 and 33 for the seven observables listed on the right, for 101 degrees of freedom, excluding a large contamination.

Archive with the observed density maps of the three galaxy samples, and then correlate the observed lensing map with 100 simulated galaxy maps. This procedure removes cosmological angular correlation, and what correlation remains will be linked to the masks themselves. We find that all results are consistent with no correlation, excluding strong contamination from masking. We also measure the cross spectra between the galaxy and quasars sample and find marginal correlations, well below the auto-correlation signals.

6.4.4.2 Photometry-related contamination

Variable observational conditions during the SDSS photometric survey could potentially result in non-uniform selection functions of the galaxy and quasar samples, and introduce artificial power in the auto spectra at large scales. In order to exclude dramatic power leakage, we constructed maps of resolution $N_{\mathrm{side}} = 64$ of the seeing, sky flux (for the g, r and i bands) and air mass of the photometric observations that were used to select galaxies and quasars in the spectroscopic catalogs,[10] and we

[10]To do so, we made use of the CasJob service of the SDSS SkyServer, at http://skyserver.sdss.org/casjobs/.

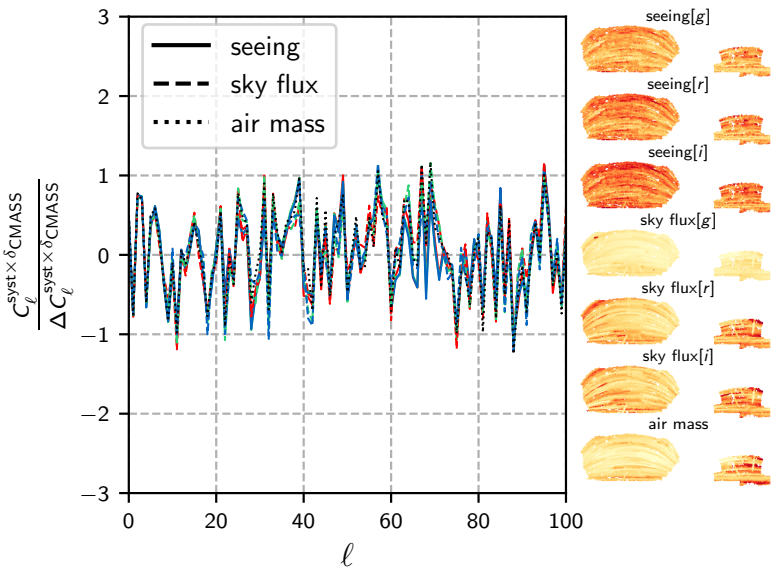

Figure 6.14 – Same as figure 6.13 for the CMASS galaxies. The χ^2 statistics are respectively 27, 27, 27, 28, 30, 28 and 31.

verify that the cross power spectra with the density maps (built in section 6.3.2.3) are consistent with a null value. To do so, we approximate the error bars on the cross spectra by

$$\Delta^2\left(\tilde{C}_\ell^{\mathrm{syst}\times\delta_g}\right) \approx \frac{\hat{\tilde{C}}_\ell^{\mathrm{syst}}\hat{\tilde{C}}_\ell^{\delta_g}}{f_{\mathrm{sky}}(2\ell+1)}, \tag{6.26}$$

where $\hat{\tilde{C}}_\ell^{\mathrm{syst}}$ and $\hat{\tilde{C}}_\ell^{\delta_g}$ are the measured pseudo auto spectra of the systematics and density maps, respectively. Figures 6.13 to 6.15 show the measured cross power spectra $\tilde{C}_\ell^{\mathrm{syst}\times\delta_g}$ for multipoles $0 \leq \ell \leq 100$: they are consistent with no correlation, with no discernable trend across multipoles. Assuming that our approximation of the error is correct, we construct a χ^2 statistics as the sum of squared errors,

$$\chi^2 = \sum_{\ell=0}^{100}\left(\frac{C_\ell^{\mathrm{syst}\times\delta_g}}{\Delta C_\ell^{\mathrm{syst}\times\delta_g}}\right)^2, \tag{6.27}$$

and find generally acceptable agreement with a null correlation (with a rejection significance at worst 2.4 σ for LOWZ with the seeing or airmass). However, this test can be misleading if we over- or underestimate the error. We partially relax the hypothesis on the error and suppose there is an unknown scale factor with respect to the true one. Considering the normalised spectra $x_\ell = C_\ell^{\mathrm{syst}\times\delta_g}/\Delta C_\ell^{\mathrm{syst}\times\delta_g}$ as independent, identically distributed random variables with the same mean and unknowns variance, we perform one-sample t-tests that reveal no significant departure from a null mean over the multipole range, with p-values always greater than 0.5. From these tests, we conclude that photometric systematics do not strongly correlate

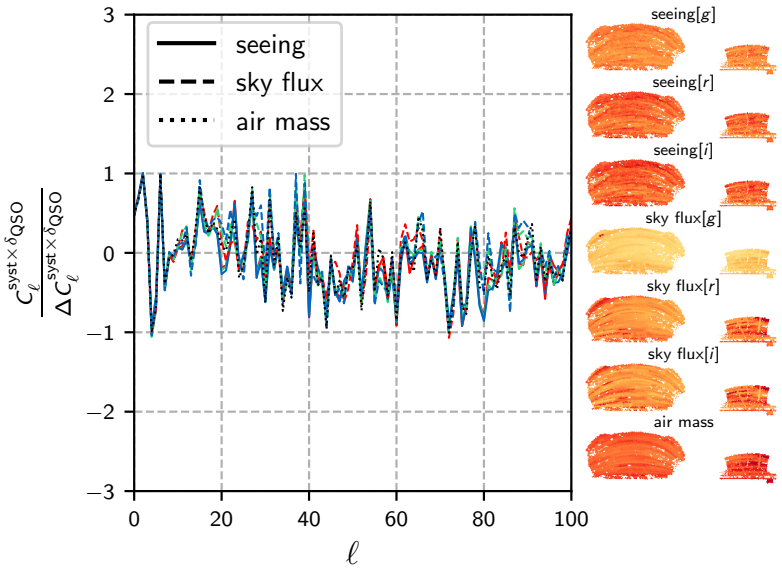

Figure 6.15 – Same as figure 6.13 for the quasar sample. The χ^2 statistics are respectively 20, 20, 20, 19, 21, 23 and 21.

with our overdensity maps.

6.5 Analyses and results

This section describes the statistical, joint analysis of the Planck and BOSS data. We first detail the cosmological model that is adopted throughout this work in section 6.5.1, and then describe the different analyses and their results in terms of cosmological contraints.

6.5.1 Cosmological model

Our base model is the standard ΛCDM model with flat spatial sections (hence $\Omega_k = 0$) and a dark energy component with equation of state $w = -1$. The base parameters are the present-day baryon and CDM densities, $\omega_\mathrm{b} \equiv \Omega_\mathrm{b} h^2$ and $\omega_\mathrm{c} \equiv \Omega_\mathrm{c} h^2$, respectively – where $\Omega_i = \rho_i/\rho_c$ is the ratio of the component's energy density to the critical energy density ρ_c –, the Hubble constant today $H_0 = 100\,h\,\mathrm{km\,s^{-1}\,Mpc^{-1}}$, the redshift of reionization z_re, the logarithm of the primordial curvature ζ dimensionless power spectrum $\ln 10^{10} A_\mathrm{s}$ and its tilt n_s such that

$$\mathcal{P}_\zeta(k) = A_\mathrm{s} \left(\frac{k}{k_0}\right)^{n_\mathrm{s}-1}, \tag{6.28}$$

with the pivot scale $k_0 = 0.05\,\mathrm{Mpc}^{-1}$. We include massive neutrinos, parametrised by the effective number of neutrinos in the relativistic limit $N_\mathrm{eff} = 3.046$ (taking into account non-instantaneous decoupling), an effective temperature $T_\nu/T_\gamma = 0.71611$,

where T_γ is the photon temperature (slightly departing from $(4/11)^{1/3}$ to take into account neutrino heating from electron/positron annihilation, see LESGOURGUES *et al.* 2009), and using one massive neutrino of mass $m_\nu = 0.06\,\mathrm{eV}$ and two massless neutrinos, consistent with the Planck base ΛCDM model. The linear matter power spectrum $P_\mathrm{m}(k,z)$ and the CMB temperature power spectrum C_ℓ^{TT} are computed using the Cosmic Linear Anisotropy Solving System (`CLASS`) as a backend to `NumCosmo`. The non-linear matter power spectrum is computed using a Halofit prescription (SMITH *et al.* 2003) implemented in `NumCosmo`, with parameters from TAKAHASHI *et al.* 2012, modified to take into account neutrinos as in `CLASS`. Reionization is modelled in a `CAMB`-like fashion (LEWIS *et al.* 2000) and parametrised by the mid-point z_re, fixed width $\Delta z_\mathrm{re} = 0.5$, and includes Helium reionization at a fixed redshift $z_\mathrm{re}^\mathrm{He} = 3.5$. Recombination is computed within `CLASS` and Big Bang nucleosynthesis is computed with `PArthENoPE`[11](PISANTI *et al.* 2008).

From the constraints that we will obtain in our analyses, we will also estimate the total matter density parameter[12] $\Omega_\mathrm{m} = \Omega_\mathrm{b} + \Omega_\mathrm{c} + \Omega_\nu$, the optical depth to the last scattering surface τ and the variance of the linear matter density fluctuations σ_8^2 in spheres of radius $R = 8\,h^{-1}\,\mathrm{Mpc}$ extrapolated to $z = 0$,

$$\sigma_8^2 = \int dk \frac{k^2}{2\pi^2} P_\mathrm{m}(k, z=0)\,|W(k,R)|^2\,, \tag{6.29}$$

where the top-hat window function is $W(k,R) = 3j_1(kR)/kR$ and the matter power spectrum is computed from linear theory.

6.5.2 Statistical analysis

In this section, we describe our Bayesian statistical analysis and present constraints on cosmological parameters of the ΛCDM model and the galaxy/quasar biases.

We first apply the Markov Chain Monte Carlo (MCMC) approach using only CMB lensing-LSS correlations data – the set of the six auto and cross spectra of CMB lensing and BOSS galaxy and quasar overdensities, as shown in figure 6.5 – and varying only a subset of cosmological parameters in order to assess the constraining power of these. In particular, we also consider different combinations of the auto and cross spectra to measure the effects on the parameter constraints provided by these probes. Then, we add CMB temperature information and obtain constraints on the ΛCDM model and extensions including the mass of neutrinos – that impacts small-scale structure formation – and the dark energy equation of state w – that impacts the expansion in the low redshift Universe.

We run the MCMC algorithm using an *ensemble sampler*[13] with many walkers,

[11] http://parthenope.na.infn.it/

[12] The dark energy density parameter today is $\Omega_\Lambda \approx 1 - \Omega_\mathrm{m}$ since we consider only flat space sections (neglecting radiation).

[13] Some authors refers to ensemble samplers as *population Monte Carlo*.

moving their positions in the parameter space as an ensemble *via* a *stretch move* scheme (Goodman and Weare 2010) implemented in `NumCosmo`. In particular, we found that an efficient protocole is to start the MCMC with a reasonably small number of walkers (we used 32) until approximate convergence is attained, and then to restart another chain with many walkers (we used 1000) which initial positions are distributed according to the converged part of the first chain. This protocole enables fast convergence as well as low correlation length in the second run.

We monitored the convergence of the chains using three numerical tools, namely the Multivariate Potential Scale Reduction Factor (MPSRF, Brooks and Gelman 2012; Gelman and Rubin 1992), the Heidelberger-Welch test (Heidelberger and Welch 1981, 1983) and the Effective Sample Size (ESS); see section 6.B for more details.

These diagnostics can fail in different situations. For this reason, we also performed three different visual inspections for each parameter:

1. the parameter trace plot, *i.e.* the value of the parameter for a given walker *vs* iteration time.

2. the ensemble distribution trace plot, that is, the empirical ensemble distribution given by the walkers' positions *vs* iteration time. This allows us to monitor the evolution of the ensemble mean and variance.

3. the total mean *vs* the cumulative sum of the ensemble means: if the chain has reached convergence, the difference (scaled by the spectral density at null frequency) is distributed as a brownian bridge, the L_2 norm of which is used in the Schruben test.

For all MCMCs, we ran them until all the relative errors of the means were smaller than 10^{-2}; at this point, we applied all the tests above, and if the chains failed some of them, we continued the run until all tests were satisfied.

6.5.2.1 Constraints from CMB lensing–LSS correlations

Data from CMB lensing and spectroscopic tracers of matter alone cannot efficiently constrain all cosmological parameters. However, we want to highlight the cosmological information carried by these probes. To do so, we perform several MCMC analyses considering a subset of free cosmological parameters. These are only illustrative in the sense that the posterior distribution of cosmological parameters will be shrunk from fixing some others.

The theoretical spectra have different dependences on the cosmological parameters and galaxy/quasar biases. The most explicit dependencies of the angular spectra $\tilde{C}_\ell$ are on the power spectrum amplitude (A_s or σ_8), the matter density parameter Ω_m

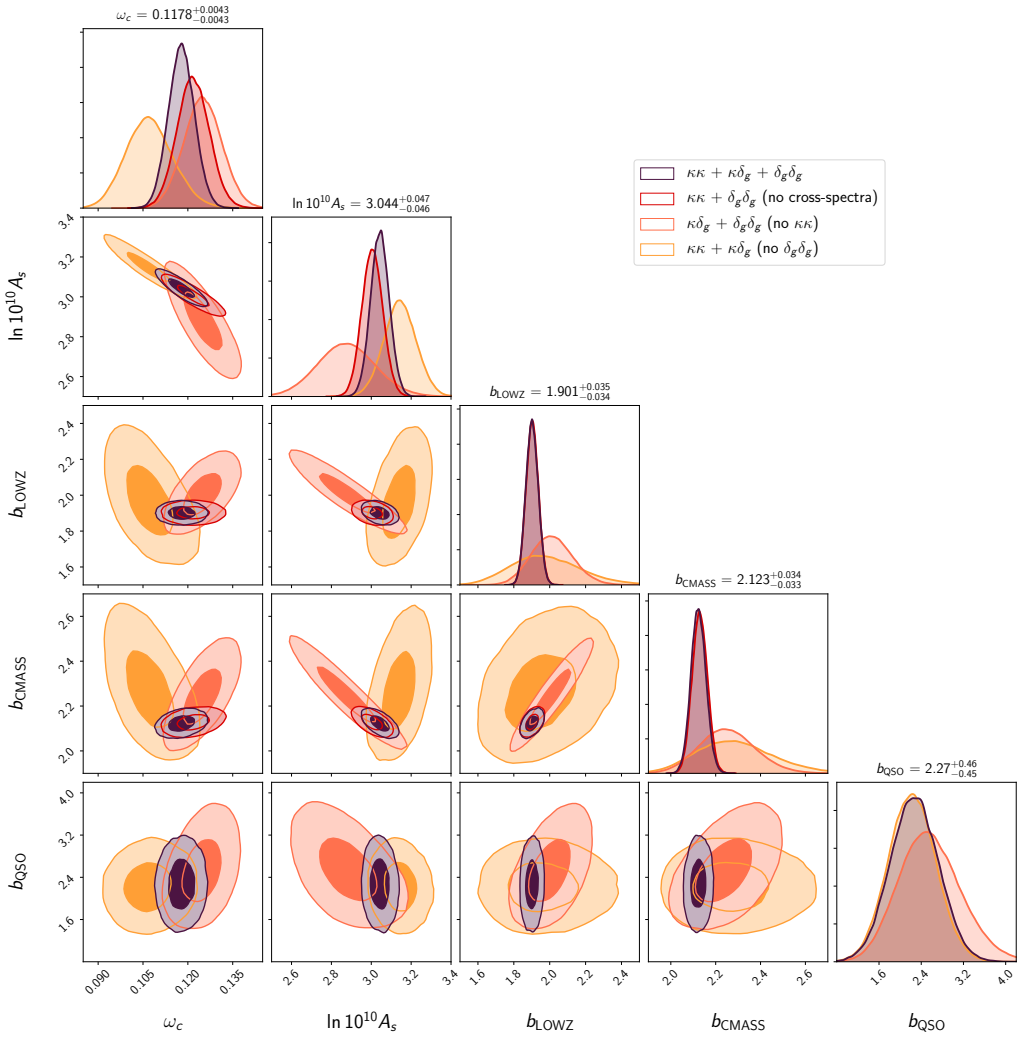

Figure 6.16 – One and two-dimensional projections of the posterior distribution sampled by the MCMC algorithm for the CMB lensing-LSS correlations. Biases, $\omega_{\rm c}$ and $A_{\rm s}$ are sampled, the other cosmological parameters being fixed at Planck 2015 "TT,TE,EE+lowP+lensing+ext" best fit values. The contours show the 1- and 2-σ confidence regions for subsets of our data. The values of the parameters above the histograms are the medians with asymmetrical errors (the $16^{\rm th}$ and $84^{\rm th}$ percentiles corresponding to $\pm\sigma$ for a Gaussian distribution). The $(\ln 10^{10} A_{\rm s}, \omega_{\rm c})$ plane illustrates the degeneracy breaking and the confidence region shrinkage due to the addition of the cross spectra (compare the dark purple and burgundy contours). The integral of the histograms are normalised to unity, therefore in the approximation of Gaussian distributions, the maxima of the histograms are inversely proportional to the standard deviation of the parameters, allowing to directly read the improvement of the constraints. Note that the quasar bias is not fitted for the subset including only auto spectra ("$\kappa\kappa + \delta_g\delta_g$").

and the galaxy/quasar biases (see the kernels in section 6.2):

$$C_\ell^{\kappa\kappa} \propto {\Omega_\mathrm{m}}^2 A_\mathrm{s}, \tag{6.30}$$

$$C_\ell^{\kappa\delta_g} \propto \Omega_\mathrm{m} b_g A_\mathrm{s}, \tag{6.31}$$

$$C_\ell^{\delta_g\delta_g} \propto b_g^2 A_\mathrm{s}. \tag{6.32}$$

This system is closed, *i.e.* in principle, comparing the various auto and cross spectra should allow for an non-degenerate estimation of the parameters.

Therefore, we run MCMCs freeing ω_c, $\ln 10^{10} A_\mathrm{s}$ and the galaxy/quasar biases, and fixing all other cosmological parameters. Their fiducial values are from Planck 2015 "TT,TE,EE+lowP+lensing+ext" best fits (Planck Collaboration *et al.* 2016e). We assume flat prior distributions over wide ranges (larger than the sampled ranges, see table 6.1). In order to distinguish and quantify the information contained in the various measured auto and cross spectra, we try different combinations. That is, we run an MCMC with the full dataset ("$\kappa\kappa$+$\kappa\delta_g$+$\delta_g\delta_g$"), and then repeat without the cross spectra ("$\kappa\kappa$+$\delta_g\delta_g$"), without the CMB lensing auto spectrum ("$\kappa\delta_g$+$\delta_g\delta_g$") and without the galaxy auto spectra ("$\kappa\kappa$+$\kappa\delta_g$"). We run these chains with 100 walkers to ensure a good mixing. Their MPSRFs are below 1.02 and the correlation lengths are of order 20-40, varying amongst parameters.

The sampled posterior distributions of these parameters are shown in figure 6.16 for the full dataset and the three subsets aforementioned. We note that the "$\kappa\delta_g$+$\delta_g\delta_g$" and "$\kappa\kappa$+$\kappa\delta_g$" subsets, dominated by respectively galaxy clustering and CMB lensing information, provide complementary information, since the correlations between the parameters, except those in the (b_LOWZ, b_CMASS) plane, present different alignments (see the orange and yellow confidence regions in figure 6.16). Therefore, the constraints on the parameters are greatly improved when combining both auto spectra, "$\kappa\kappa$+$\delta_g\delta_g$". Apart from the constraints on b_LOWZ, b_CMASS, which are already strongly determined by galaxy density auto spectra, the additional information contained in the cross spectra narrows the distribution, as can be observed in the ($\ln 10^{10} A_\mathrm{s}$,ω_c) plane by comparing the confidence regions for "$\kappa\kappa$+$\delta_g\delta_g$" (in burgundy) with "$\kappa\kappa$+$\kappa\delta_g$+$\delta_g\delta_g$" (in dark purple). The addition of the cross spectra decreases the statistical error by 10% for $\ln 10^{10} A_\mathrm{s}$ and 20% for ω_c, and slightly shifts the best fits (by less than 1 σ). This plane is translated into the (σ_8, Ω_m) plane in figure 6.17 where the degeneracy breaking expected from the joint analysis is highlighted.

6.5.2.2 Constraints from CMB temperature and CMB lensing–LSS correlations

In this section, we carry out the analysis combining CMB temperature and the correlations of CMB lensing and galaxy/quasar densities used in the previous section (that is all six power spectra of figure 6.5) to obtain constraints on the cosmological parameters of the ΛCDM model (ω_b, ω_c, H_0, z_re, $\ln 10^{10} A_\mathrm{s}$ and n_s) in paragraph 6.5.2.2.1.

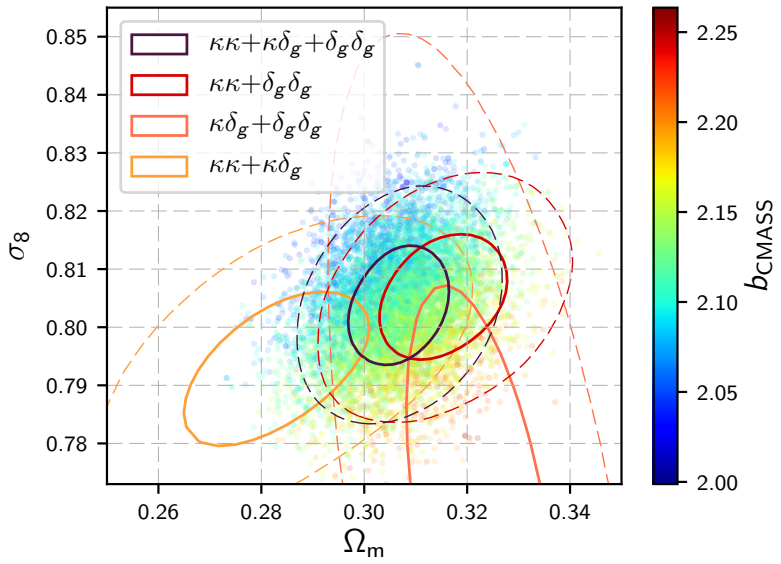

Figure 6.17 – Confidence regions for σ_8 and Ω_m corresponding to the distributions sampled by the ensemble sampler MCMC algorithm for the CMB lensing-LSS correlations dataset only, with the other cosmological parameters fixed at Planck 2015 "TT,TE,EE+lowP+lensing+ext", and various subsets of the dataset. 1σ contours (respectively 2σ contours) are represented by solid (dashed) lines. CMB lensing and galaxy densities show different degeneracies, that are partially broken by combining the observations. Coloured points are samples from the full dataset chains, that show how σ_8, Ω_m and galaxy biases are degenerated.

We then extend the model, constraining the sum of the mass of neutrinos, m_ν, and the dark energy equation of state, w, first separately in paragraph 6.5.2.2.2 and then together in paragraph 6.5.2.2.3. The results of this analysis will be denoted "CMB TT + CMB lensing $\otimes$ LSS" in the figures. In addition, we run, for comparison, the MCMC algorithm using only CMB temperature data ("CMB TT"), and CMB temperature and lensing ("CMB TT + CMB lensing"). The configurations of these analyses are summed up in table 6.1.

We neglect the correlation between CMB temperature and the matter density at later times (either baryonic matter in galaxies and quasars or dark matter weighted by CMB lensing), *i.e.*, we neglect the late ISW effect, as it is not yet detected with a strong significance (Nicola *et al.* 2016; Planck Collaboration *et al.* 2016g), and we discuss possible consequences in section 6.5.3. In practice, this means that we approximate the total likelihood by the product of the CMB temperature and CMB lensing-LSS correlations likelihood functions.

We use the Planck likelihood codes `Plik` and `Commander` (Planck Collaboration *et al.* 2016d) respectively for high and low multipoles of the temperature-only power spectrum C_ℓ^{TT}. The likelihood code introduces 15 additional nuisance parameters related to foreground and instrument models ($A_{217}^{\rm CIB}$, $\xi^{\rm tSZ\times CIB}$, $A^{\rm tSZ}$, $A_{100}^{\rm PS}$, $A_{143}^{\rm PS}$, $A_{143\times217}^{\rm PS}$, $A_{217}^{\rm PS}$, $A^{\rm kSZ}$, $A_{100}^{{\rm dust}TT}$, $A_{143}^{{\rm dust}TT}$, $A_{143\times217}^{{\rm dust}TT}$, $A_{217}^{{\rm dust}TT}$, c_{100}, c_{217} and $y_{\rm cal}$; see

Table 6.1 – Cosmological constraints obtained from "CMB TT + CMB lensing $\otimes$ LSS" for the ΛCDM model. Constraints on clustering biases and noise biases are also given in the second part of the table. A dash means that the parameter is not fitted. All MCMC include a subfitting procedure, as described in the text, of CMB TT nuisance parameters. Finally, the rightmost column indicates the interval of the flat priors used for all MCMC analyses.

Parameters [units]	ΛCDM	ΛCDM + m_ν	wCDM	wCDM + m_ν	Priors (flat)
H_0 [km s^{-1} Mpc^{-1}]	$68.73^{+0.87}_{-0.83}$	$67.76^{+1.20}_{-1.51}$	$68.03^{+5.10}_{-4.44}$	$65.78^{+5.43}_{-4.35}$	$[0, 50]$
ω_c	$0.1168^{+0.0018}_{-0.0019}$	$0.1170^{+0.0018}_{-0.0019}$	$0.1171^{+0.0015}_{-0.0015}$	$0.1168^{+0.0018}_{-0.0019}$	$[0.05, 0.2]$
ω_b	$0.02250^{+0.00019}_{-0.00018}$	$0.02246^{+0.00018}_{-0.00018}$	$0.02248^{+0.00017}_{-0.00017}$	$0.02248^{+0.00018}_{-0.00019}$	$[0.01, 0.03]$
$\ln 10^{10} A_s$	$3.092^{+0.035}_{-0.034}$	$3.108^{+0.038}_{-0.036}$	$3.088^{+0.027}_{-0.027}$	$3.121^{+0.043}_{-0.044}$	$[2.5, 3.5]$
n_s	$0.9760^{+0.0050}_{-0.0049}$	$0.9755^{+0.0050}_{-0.0050}$	$0.9753^{+0.0041}_{-0.0041}$	$0.9758^{+0.0052}_{-0.0050}$	$[0.8, 1.1]$
z_{re}	$10.20^{+1.58}_{-1.70}$	$10.96^{+1.68}_{-1.75}$	$10.03^{+1.27}_{-1.37}$	$11.56^{+1.85}_{-2.06}$	$[0, 30]$
w	–	–	$-0.98^{+0.14}_{-0.16}$	$-0.94^{+0.15}_{-0.18}$	$[-2, 0]$
m_ν [eV]	–	$0.159^{+0.121}_{-0.099}$	–	$0.168^{+0.125}_{-0.097}$	$[0, 1]$
b_{LOWZ}	$1.855^{+0.037}_{-0.035}$	$1.893^{+0.060}_{-0.047}$	$1.867^{+0.074}_{-0.073}$	$1.923^{+0.089}_{-0.084}$	$[0, 10]$
$10^7 a_{\mathsf{LOWZ}}$	$4.74^{+1.59}_{-1.59}$	$5.59^{+1.80}_{-1.80}$	$4.97^{+1.65}_{-1.65}$	$5.87^{+1.87}_{-1.87}$	$]-\infty, +\infty[$
b_{CMASS}	$2.077^{+0.036}_{-0.035}$	$2.114^{+0.056}_{-0.048}$	$2.086^{+0.055}_{-0.051}$	$2.134^{+0.070}_{-0.061}$	$[0, 10]$
$10^7 a_{\mathsf{CMASS}}$	$6.68^{+0.89}_{-0.89}$	$7.04^{+0.99}_{-0.99}$	$6.62^{+0.86}_{-0.86}$	$7.08^{+1.05}_{-1.05}$	$]-\infty, +\infty[$
b_{QSO}	$2.19^{+0.44}_{-0.43}$	$2.25^{+0.44}_{-0.44}$	$2.20^{+0.46}_{-0.45}$	$2.22^{+0.46}_{-0.44}$	$[0, 10]$

Planck Collaboration *et al.* 2016d). We use the profile likelihood to speed up our MCMC analyses, subfitting the nuisance parameters for each set of cosmological parameters. We describe this methodology in section 6.C, and also show that it does not affect the results on cosmological parameters.

6.5.2.2.1 Constraints on ΛCDM

figure 6.18 shows the constraints on the base ΛCDM model's parameters for the three aforementioned data combinations. When using CMB TT only, we find parameter constraints that are in perfect agreement with the Planck analysis.[14] The strong degeneracy observed between the power spectrum amplitude A_s and the reionization redshift z_{re} corresponds to the amplitude of the power spectrum of CMB temperature anisotropies, which is proportional to $A_s e^{-2\tau}$ where τ is the optical depth to the last scattering surface, strongly dependent on reionization history. Adding CMB lensing drives A_s and z_{re} towards lower values with a shift of about 1σ for each parameter as evinced by the one- and two-dimensional projection of the posterior distributions. Finally, adding information of LSS tracers (both the auto-correlations and cross-correlations with CMB lensing) provides slightly smaller contours and, therefore, they do not significantly help in breaking this degeneracy. We find no significant improvement for τ or σ_8, although it is consistent with the constraints

[14] The detailed results of the Planck MCMC analyses are available here: https://wiki.cosmos.esa.int/planckpla2015/images/f/f7/Baseline_params_table_2015_limit68.pdf

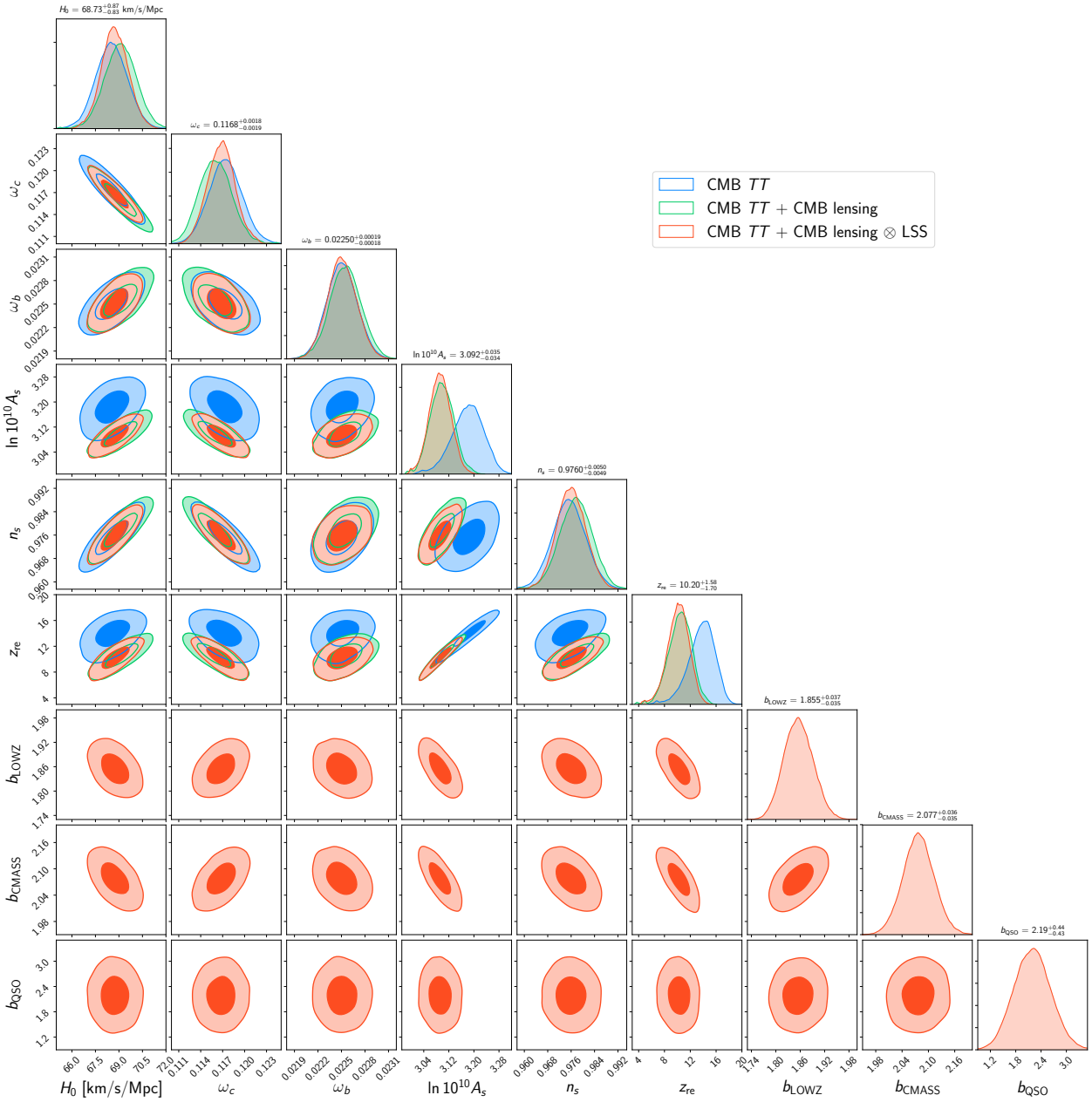

Figure 6.18 – Constraints on the parameters of the base 6-parameters ΛCDM model and galaxy biases. Confidence regions are shown respectively in blue, green and red for CMB temperature only, CMB temperature combined with CMB lensing, and the joint analysis of CMB temperature and the correlations of CMB lensing and LSS tracers. The constraints above the marginal posteriors are for this last data set.

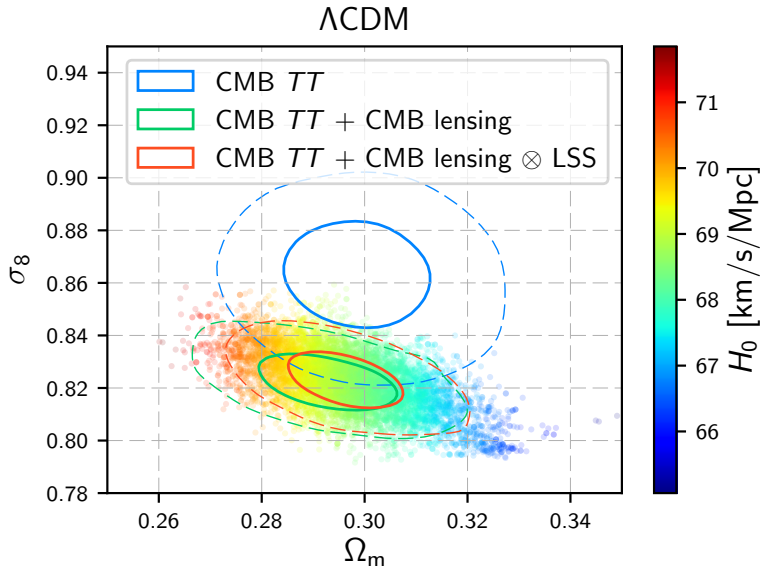

Figure 6.19 – Constraints on σ_8 and Ω_m for the 6-parameter base ΛCDM model from the combination of CMB temperature and the correlations of CMB lensing and spectroscopic tracers. The 1 and 2 σ contours are represented by the respectively solid and dashed lines. The coloured points show the degeneracy with H_0 (in $\mathrm{km\,s^{-1}\,Mpc^{-1}}$) and are samples from the "CMB TT + CMB lensing ⊗ LSS" chain.

from CMB lensing. In the (σ_8, Ω_m) plane (see figure 6.19), we observe that early Universe data favors bigger values of σ_8 than the late one, as reported repeatedly (Hildebrandt *et al.* 2017; Planck Collaboration *et al.* 2016j). Whether this is indication of new physics or a systematics artefact is beyond the scope of this work, but it might be an important issue in the future.

Nonetheless, there is an improvement of order 20% on the measurements of H_0 and ω_c. We find $H_0 = (68.7 \pm 0.9)\,\mathrm{km\,s^{-1}\,Mpc^{-1}}$, slightly higher than CMB temperature alone – albeit still lower than distance measurements from supernovæ (Riess *et al.* 2016) or time delays in strong lensing (Bonvin *et al.* 2017) – and $\omega_\mathrm{c} = 0.117 \pm 0.002$ as the degeneracy between A_s and ω_c is broken by the lensing–LSS correlations (see figure 6.16). This results in a constraint on the matter density parameter $\Omega_\mathrm{m} = 0.296 \pm 0.011$. Additionally, we obtain strong constraints on the biases of the galaxy samples, respectively

$$\begin{aligned} b_\mathsf{LOWZ} &= 1.855 \pm 0.037 \\ b_\mathsf{CMASS} &= 2.077 \pm 0.036. \end{aligned} \tag{6.33}$$

These 4% constraints are in general agreement with previous measurements (Ho *et al.* 2012). Our analysis has the advantage that our data is model-independent in the sense that estimating pseudo spectra $\tilde{C}_\ell$ does not require any assumption on cosmology since we don't measure distances. Moreover, all the cosmological parameters of the ΛCDM model are fitted jointly. Note, however, that our modelling assumes a

constant bias, that can be interpreted as a redshift- and scale-averaged bias, when other analyses used a scale-dependent bias (in the form of a Taylor expansion, *e.g.* in Gil-Marìn *et al.* 2016) or simply more redshift bins. Interestingly, the analysis also shows significant correlations between the biases and cosmological parameters, in particular with ω_c, H_0 and A_s. If one considers biases as effective parameters encoding structure formation and clustering of galaxies, these correlations can shed light on the astrophysical and cosmological processes governing the formation of such structures. Finally, we also obtain a broad constraint on the bias of the uniform sample of quasars from the cross-correlation with CMB lensing

$$b_{\mathsf{QSO}} = 2.19 \pm 0.44. \tag{6.34}$$

This value is in tension with other measurements (DiPompeo *et al.* 2015; Laurent *et al.* 2016, 2017; White *et al.* 2012) that found a bias of order 3 to 4 (although they did assume a cosmology). We found no difference when fitting for this bias when using data from only the northern or southern galactic caps, excluding a possible strong asymmetry and contamination of higher multipoles. We note a surprising trough in the $\tilde{C}_\ell^{\kappa_{\mathrm{CMB}}\times\mathrm{QSO}}$ cross spectrum (see figure 6.5) around $\ell \sim 400$ that we could not explain. However, this bias directly depends on the amplitude of lensing that may be underestimated (Planck Collaboration *et al.* 2014b).

6.5.2.2.2 Independent constraints on the mass of neutrinos m_ν and the dark energy equation of state w

In the next set of MCMCs, we additionally sample the mass of neutrinos m_ν (with one massive and two massless neutrinos) or the dark energy equation of state w (where w is constant over time) separately and compare the performance of the joint analysis in these extended models.

In the first case, we find that the joint analysis yields a constraint on the neutrino mass of $m_\nu < 0.29\,\mathrm{eV}$ [68%], dividing the higher bound by a factor of two with respect to the constraint from CMB TT alone (see figure 6.20). We do not detect a statistically significant neutrino mass, but the best fit we obtain around $m_\nu \sim 0.12\,\mathrm{eV}$ is in agreement with lower bounds around 0.05 eV derived from neutrino oscillations (Olive 2014), and in agreement with cosmological upper bounds around 0.12 eV, *e.g.* that derived from the combination of CMB, either with the Lyman-α forest power spectrum (Palanque-Delabrouille *et al.* 2015a) or with BAO measurement (Vagnozzi *et al.* 2017). As shown in figure 6.21, the galaxy auto power spectra are sensitive to the mass of neutrinos as they can probe small scales at low redshift, where massive neutrinos tend to smooth out density fluctuations. This means that the mass of neutrinos should be positively correlated with galaxy biases, which is indeed observed in the lower panels of figure 6.20. We also observe that adding LSS information significantly improves the constraints on the other cosmological parameters in this

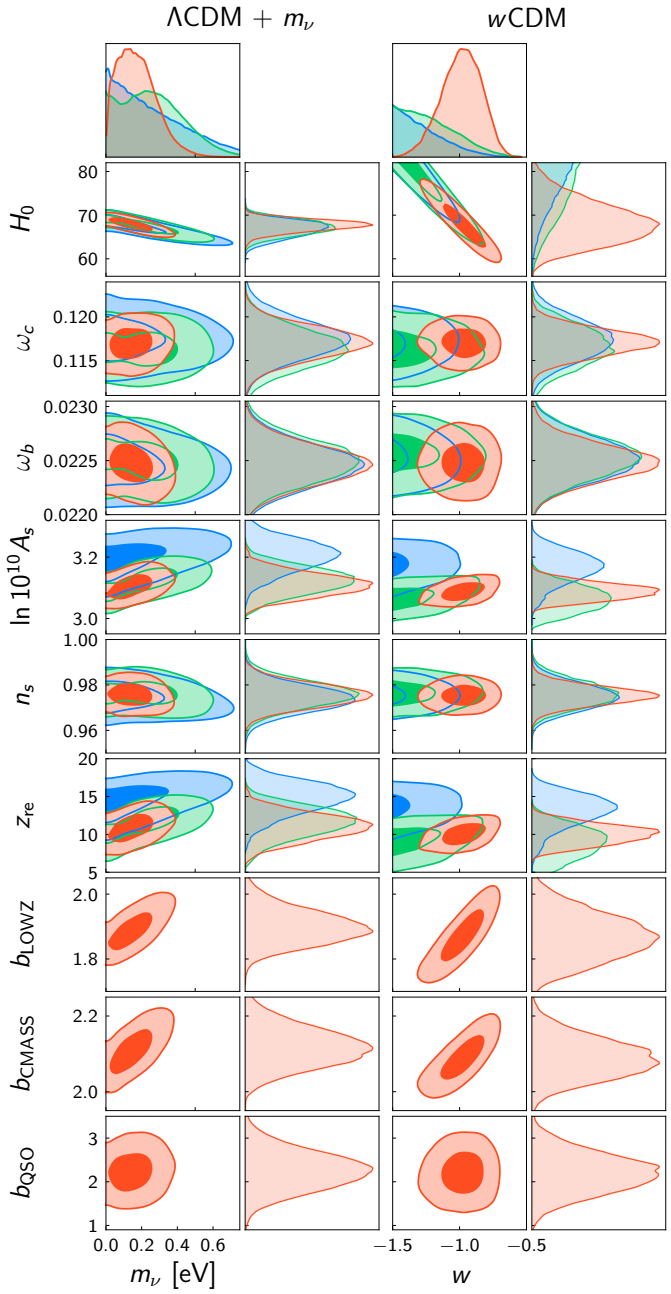

Figure 6.20 – Cosmological constraints on two one-parameter extensions of the base 6-parameters ΛCDM model used here. On the column labeled ΛCDM + m_ν, the mass of the neutrinos m_ν (expressed in eV) is set free and sampled in addition to the six cosmological parameters and the galaxy and quasar biases, w being fixed to -1. On the column labelled wCDM, w is set free and the mass of neutrinos is fixed at its fiducial value of 0.06 eV. Only the two-dimensional distributions involving m_ν or w are shown, together with marginal posteriors for the other cosmological parameters (rotated to match the leftmost vertical axes). The two upmost plots show the marginal distributions obtained for m_ν and w. The colours are the same as in figure 6.18: blue is for CMB temperature alone, green is for CMB temperature and lensing and red is for CMB temperature and the CMB lensing-LSS correlations.

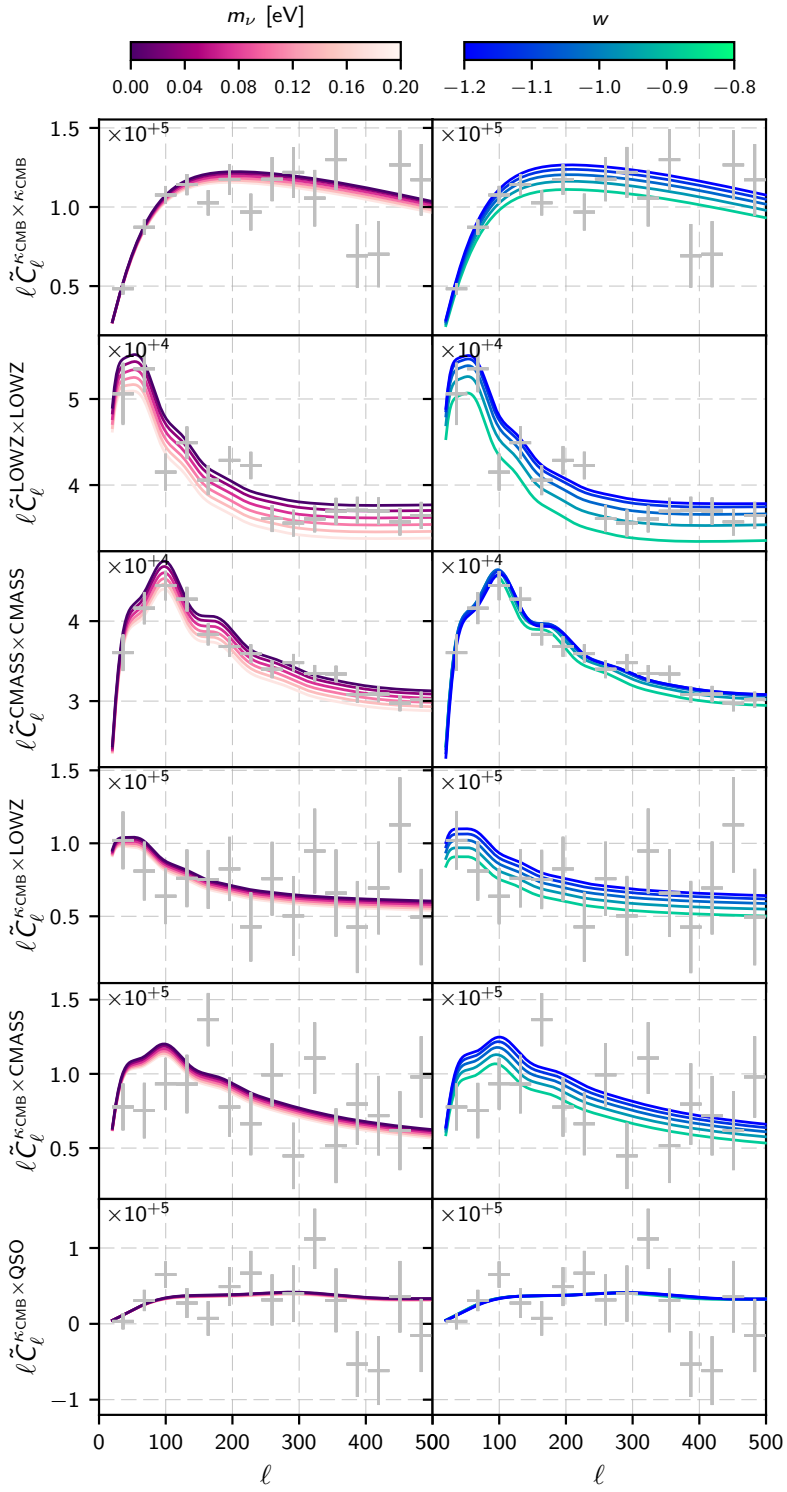

Figure 6.21 – Theoretical pseudo spectra for different values of the mass of neutrinos m_ν and w. On the left column, m_ν varies from 0 eV (dark purple) to 0.20 eV (light pink); on the right column, w varies from −1.2 (green) to −0.8 (blue). Data points from figure 6.5 are overlaid in light grey.

extended model. Because of the anti-correlation between H_0 and the mass of neutrinos, the joint analysis favours a higher expansion rate $H_0 = (67.76^{+1.20}_{-1.51})\mathrm{km\,s^{-1}\,Mpc^{-1}}$ than CMB data alone. It also noticeably shifts the posterior distributions for $z_{\rm re}$ and $A_{\rm s}$ towards lower values, resulting in a lower value of the reionization optical depth $\tau = 0.090 \pm 0.020$.

In the second case, we release w, the mass of neutrinos being fixed to $m_\nu = 0.06\,\mathrm{eV}$. CMB temperature anisotropies are only very weakly sensitive to dark energy and CMB lensing probes the Universe at redshift $z \sim 2$, where matter is still dominating; therefore these probes do not contain much information on w. Adding the correlations with LSS information becomes necessary and rewarding as it breaks the degeneracies of the constraints on H_0, $\ln 10^{10} A_s$, $z_{\rm re}$ and w. We observe a strong anti-correlation between w and the Hubble parameter H_0, meaning that observations can be matched by a more slowly expanding Universe with a more negative dark energy pressure. Constraints from the joint analysis ($w = -0.98^{+0.14}_{-0.16}$) are consistent with a cosmological constant ($w = -1$), while constraints from CMB favour a lower value of w. We also note a strong correlation between the biases and w of 81% and 89% for CMASS and LOWZ respectively.

In summary, in both cases, constraints from the joint analysis are substantially better for almost all parameters because of its ability to break degeneracies related to the chosen new parameters. This result constitutes a forceful encouragement to perform this type of analysis when data from the next generation of surveys becomes available.

6.5.2.2.3 Constraints on wCDM + m_ν

Finally, in the last set of MCMC analyses, we release both the mass of neutrinos m_ν and the dark energy equation of state w and demonstrate that a joint analysis of currently available data can set constraints on a 8-parameter cosmological model (wCDM + m_ν). Similarly to the previous cases, the results are presented on figure 6.24 for the full joint analysis and for CMB data, allowing for comparison. We find constraints that are in agreement with the current picture of the ΛCDM model as well as those obtained in the previous sections, with a value of $w = -0.93^{+0.14}_{-0.18}$ consistent with a cosmological constant. We obtain a higher bound on the mass of the neutrinos of $m_\nu < 0.29\,\mathrm{eV}$ [68%] and a low value of the Hubble constant of $H_0 = (65.78^{+5.43}_{-4.35})\mathrm{km\,s^{-1}\,Mpc^{-1}}$, albeit with larger error bars. As opposed to the 6-parameter ΛCDM case, the joint analysis does not really outperform constraints from CMB TT data alone regarding the base parameters, except for H_0 which strongly correlates with w. In particular, the constraints on $\omega_{\rm c}$ or $n_{\rm s}$ are not as strong. However, the additional information extracted by the joint analysis (partially) breaks the $w - H_0$ degeneracy, enabling for control of all eight cosmological parameters, plus the biases, *i.e.* eleven parameters in total. The correlation coefficient matrix reveals a strong correlation of galaxy biases with H_0, w and m_ν (see figure 6.22)

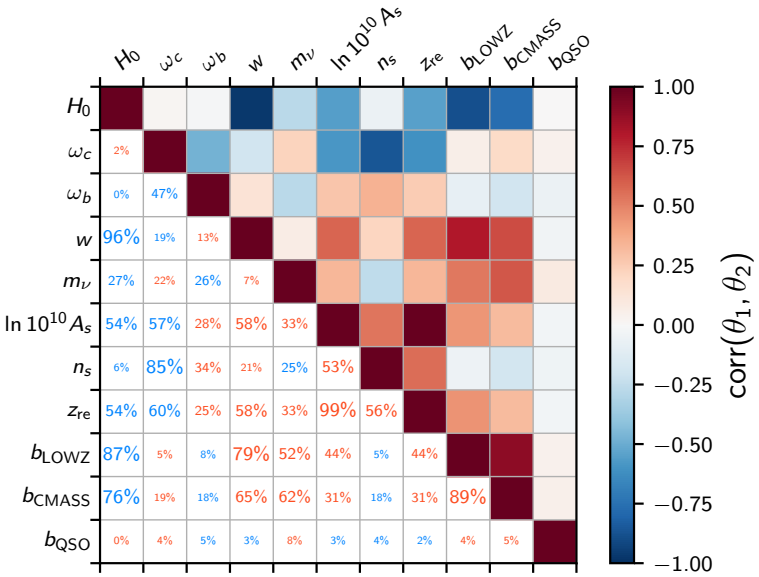

Figure 6.22 – Correlation coefficient matrix of the wCDM + m_ν model's parameters and biases from the joint analysis of CMB temperature and the correlations of CMB lensing and large-scale structure (see the constraints on figure 6.24). The upper triangle is colour encoded, red (respectively blue) meaning complete correlation (anti-correlation) between parameters. The lower triangle is given in percentage, written in red (blue) for positive (negative) correlation.

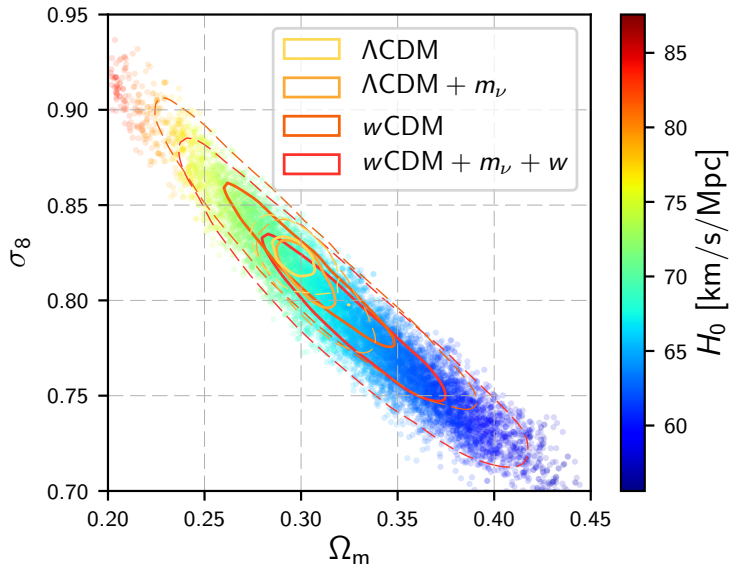

Figure 6.23 – Confidence regions for σ_8 and Ω_m from the combination of CMB temperature and the CMB lensing-LSS correlations for the ΛCDM model and extensions to the mass of neutrinos m_ν and the dark energy equation of state w. The coloured points are samples from the wCDM + m_ν chain.

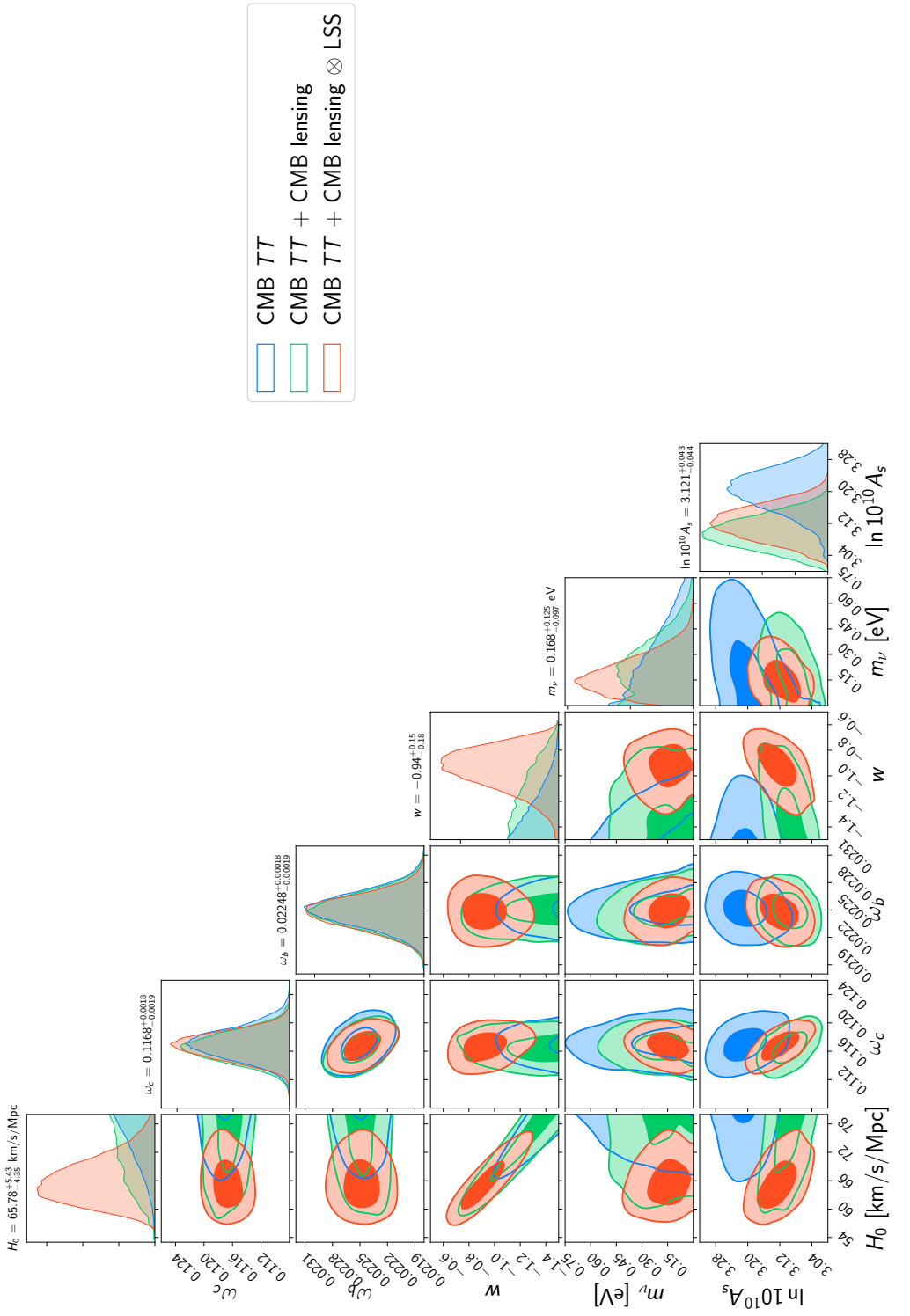
CMB TT
CMB TT + CMB lensing
CMB TT + CMB lensing ⊗ LSS
$H_0 = 65.78^{+5.43}_{-4.35}$ km/s/Mpc
$\omega_c = 0.1168^{+0.0018}_{-0.0019}$
$\omega_b = 0.02248^{+0.00018}_{-0.00019}$
$w = -0.94^{+0.15}_{-0.18}$
$m_\nu = 0.168^{+0.125}_{-0.097}$ eV
$\ln 10^{10} A_s = 3.121^{+0.043}_{-0.044}$
H_0 [km/s/Mpc]
ω_c
ω_b
w
m_ν [eV]
$\ln 10^{10} A_s$

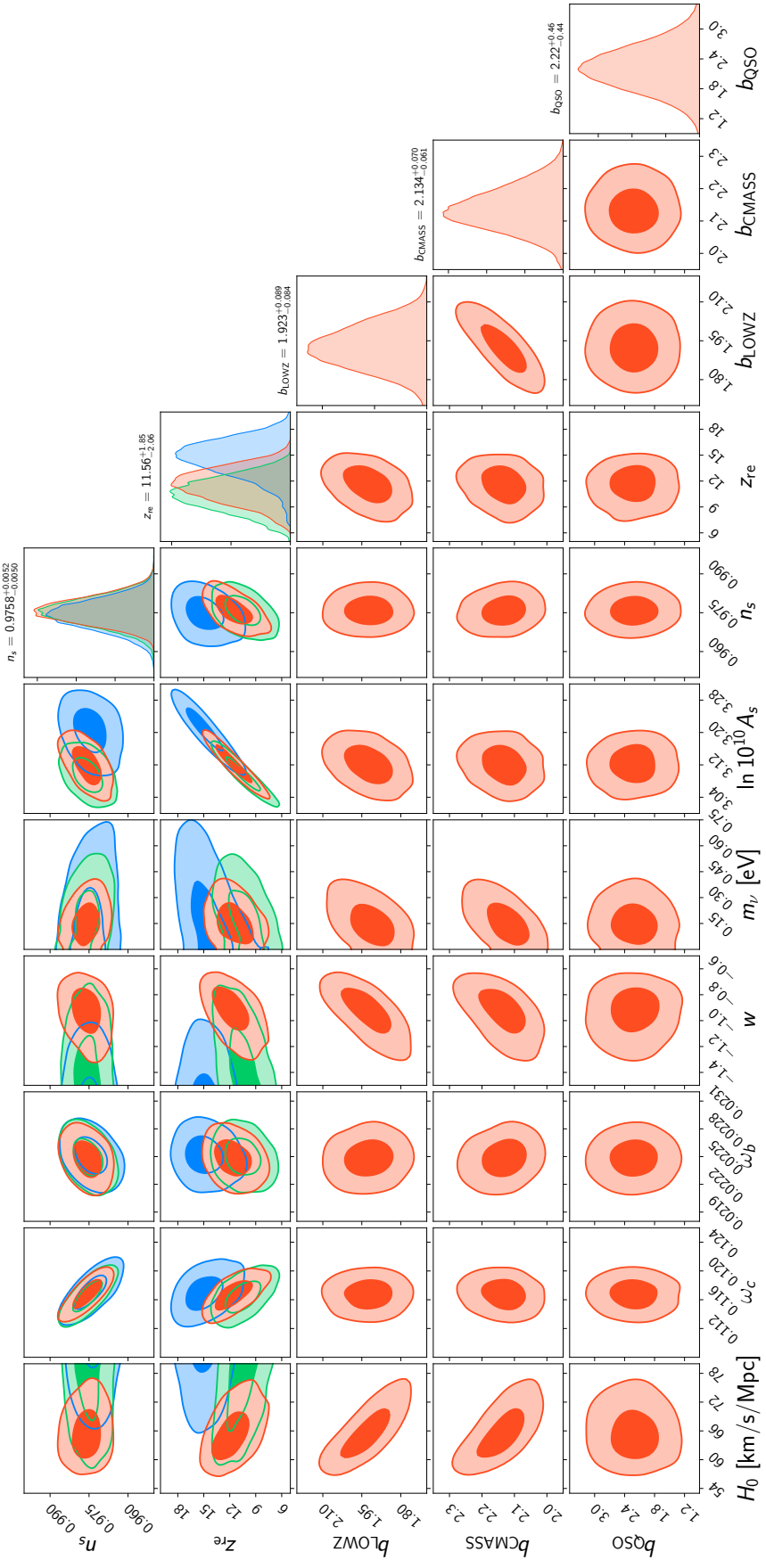

Figure 6.24 – Constraints on the parameters of the wCDM + m_ν model and biases from the combination of CMB temperature and the correlations of CMB lensing and large-scale structure.

Table 6.2 – Constraints on σ_8, τ and Ω_m from the joint analysis of CMB temperature and CMB lensing–large-scale structure correlations.

Model	σ_8	τ	Ω_m
ΛCDM	$0.823^{+0.010}_{-0.010}$	$0.082^{+0.019}_{-0.019}$	$0.296^{+0.011}_{-0.011}$
$\Lambda\mathrm{CDM} + m_\nu$	$0.806^{+0.018}_{-0.023}$	$0.090^{+0.021}_{-0.020}$	$0.307^{+0.019}_{-0.015}$
wCDM	$0.816^{+0.044}_{-0.039}$	$0.080^{+0.015}_{-0.015}$	$0.303^{+0.044}_{-0.041}$
$w\mathrm{CDM} + m_\nu$	$0.786^{+0.045}_{-0.038}$	$0.097^{+0.024}_{-0.023}$	$0.328^{+0.046}_{-0.046}$

indicating that upcoming surveys will require exquisite control of these biases to get tight constraints on w and its possible time evolution.

Because of the degeneracy between H_0, w and m_ν, precision is lost on Ω_m, even though the physical density $\omega_\mathrm{m} \equiv \Omega_\mathrm{m} h^2$ is well constrained by CMB TT and CMB lensing even in this model (we find $\omega_\mathrm{m} = 0.1413 \pm 0.0024$). In the ($\sigma_8$, Ω_m) plane (see figure 6.23), we obtain constraints that are consistent from the joint analysis over the models tested here, with increasing degeneracy. We measure ${\sigma_8 \Omega_\mathrm{m}}^{2.7} = 0.170 \pm 0.007$ from the joint analysis on the 8-parameter $w\mathrm{CDM} + m_\nu$ model.

6.5.3 Limits and perspectives

Forecasts predict strong improvements of the constraints on cosmological parameters from the combination of the next generation galaxy surveys and CMB experiments (Pearson and Zahn 2014; Schaan *et al.* 2017). One of the goals of this work was to identify the difficulties in running joint analyses on real data, while acting as a proof of concept. We discuss in this section assumptions that were made and technical difficulties that we were able to pinpoint.

ISW effect We neglected the correlation, generated by the ISW effect, between the CMB temperature map and the large-scale structure as traced by CMB lensing or spectroscopic tracers. This correlation originates in the net energy gain (loss) of photons crossing gravitational potentials wells (hills) evolving thanks to dark energy. In principle, this would lead to underestimation of error bars on cosmological parameters. However, this correlation is weak and affects only very large scales $\ell \lesssim 40$, and it has not been detected with a strong statistical significance on SDSS galaxies: the signal-to-noise ratios for the correlation with the LOWZ and CMASS samples reported by the Planck collaboration is of order 2.4, and that with the lensing map (corresponding to a temperature bispectrum) is of order 3.2 (Planck Collaboration *et al.* 2016g). Therefore, taking this cross-correlation term into account would not dramatically change our constraints.

SZ effect One possible source of systematics in the galaxy-lensing cross-correlations comes from the tSZ component separation that is required to produce the lensing

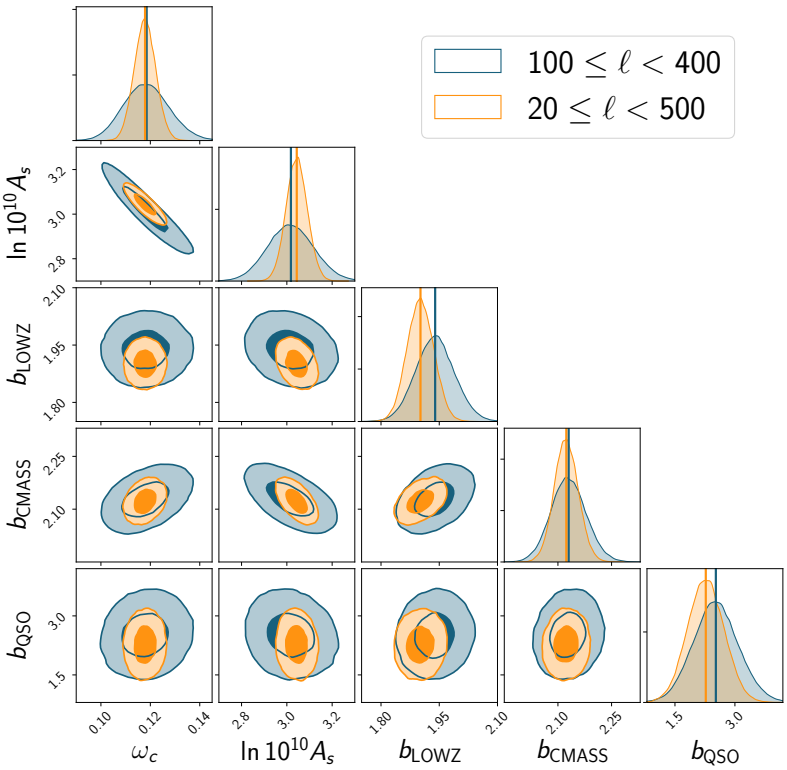

Figure 6.25 – Comparison between the posterior distributions sampled by MCMC analysis using the CMB lensing–LSS correlations dataset for different multipole ranges: in orange, the constraints resulting from the full multipole range ($20 \leq \ell < 500$) used in the rest of this work, and in blue those resulting from a smaller multipole range excluding small and large scales ($100 \leq \ell < 400$). The distribution are compatible, which means that if there is a modelling issue either at large scales (*e.g.* due to the RSD) or at small scales (*e.g.* due to uncertainties in the non-linear matter power spectrum), it does not dramatically affect the constraints on cosmological parameters.

map (Planck Collaboration *et al.* 2016a,c,h). Free electrons in hot galaxy clusters imprint a specific local spectral distortion on the CMB temperature map. These clusters must be identified and removed before measuring the spatial distortion due to gravitational lensing. If these clusters hold some of the galaxies in the samples we use, this might lead to a systematic underestimation of the lensing signal in the direction of these galaxies. However, the SZ decrement from SDSS LRGs is small, as can be seen in Table 2 of Hand *et al.* 2011. Moreover, the residual SZ signal primarily increases the noise in the lensing map and is unlikely to produce appreciable bias (see the systematics checks in Madhavacheril *et al.* 2015).

We know discuss theoretical uncertainties.

Limber approximation and RSD The first uncertainty comes from the Limber approximation (LoVerde and Afshordi 2008): it fails at very large scales, the

transition scale depending on the width of the redshift bin considered (Campagne *et al.* 2017). In this work, we used very broad redshift bins and discarded low multipoles $\ell < 20$, so as to be in the safe regime of the approximation. We also did not consider redshift space distortion (RSD) for the same reasons: RSD impact only large scales in the case of narrow redshift bins (since they can alter the redshift distribution, see Alonso *et al.* 2015; Padmanabhan *et al.* 2007; Saito 2016). To test that RSD or other large-scale effects were not driving parameter constraints inconsistently, we performed an MCMC analysis of CMB lensing-galaxy correlations on a smaller multipole range ($100 \leq \ell < 400$, see figure 6.25) and found no significant deviation, except for the bias of LOWZ, which is shifted by about 1σ. Future surveys, aiming at measuring extremely large-scales (Alonso and Ferreira 2015; Alonso *et al.* 2015), will require better modelling, especially for tomographic studies.

Non-gaussianity of the density field In this work, we used a Gaussian likelihood and a Gaussian covariance, *i.e.* we did not incorporate higher order statistics of the matter density field nor the so-called super-sample variance, which is due to the finite size of the surveyed volume and inaccessible modes therein (Krause and Eifler 2017; Schaan *et al.* 2014, 2017). At the current level of signal-to-noise ratio, these simplifications are probably safe but they should be lifted in future data analysis. One limitation of our method regarding the covariance matrix is that the computation of the $\mathbf{X}$ and $\mathbf{Y}$ matrices used in the covariance matrix is numerically expensive – they grow linearly with the multipole range but as $n^4/4$ with the number n of different masks – and remains noisy. However, this method has the advantage of naturally taking care of partial sky coverage, without the need of inverting the mixing matrix to recover full-sky spectra, necessarily introducing numerical noise in the data. Devising a method that takes care of partial sky coverage whilst incorporating all relevant non-Gaussian terms will be an important task for future surveys (Lacasa *et al.* 2016).

Non-linearities The non-linear power spectrum of the matter density field suffers from theoretical uncertainties (Baldauf *et al.* 2016b). Throughout this analysis, we used the `halofit` model, assuming it properly describes non-linear clustering. With our choice of multipole ranges, we explore scales smaller than the non-linear transition scale, around $k_{\rm nl} \sim 0.1\,h\,{\rm Mpc}^{-1}$. In particular, for LOWZ, we have $k_{\rm max} \sim \ell_{\rm max}/\chi(z_{\rm eff}) \sim 0.4\,{\rm Mpc}^{-1}$, which can explain the shift observed in the bias when removing high multipoles, or the consistently non-zero noise bias observed for both LOWZ and CMASS. Therefore, our constraints depend on the reliability of the model. Moreover, we assumed that the bias is scale-independent within our choice of scales. The impact of a more elaborate model, potentially marginalizing over a non-linear bias, remains to be studied. It could

be implemented by including higher-order term in the power spectrum from standard perturbation theory, as was recently done in Kwan *et al.* 2017. The scientific gain from near future surveys in terms of cosmological constraints will depend on our ability to model these non-linearities. In particular, the suppression of power due to massive neutrinos (Lesgourgues and Pastor 2006) and the contribution of baryonic and feedback processes (Leauthaud *et al.* 2017) at these scales will certainly be an important theoretical issue.

6.6 Conclusion

Cosmological experiments carried out in the last few decades have enabled the construction of the ΛCDM model. In this picture, CDM drives the formation of the large-scale structure of the Universe and dark energy fuels the recent accelerated expansion. The combination of independent observations, such as the map of the anisotropies of the cosmic microwave background, distances of type IA supernovæ and the measurement of the scale of the baryon acoustic oscillations, have set constraints on the content of the Universe. However, the analysis of currently available data cannot distinguish between various models of dark matter and dark energy. Going further and deciphering the nature of these components requires better constraints, and thus, more information. To this end, deep galaxy surveys – such as LSST, Euclid and WFIRST – and CMB imagers – such as CMB-S4 and the Simons Observatory – with wide sky coverage and high resolution are currently under development. In the coming decade, they will probe the matter density field with ground-breaking precision and significantly increase the amount of cosmological information. Independent cosmological analyses have a strong potential to reveal new science, but model comparison will rely on exhausting the cosmological information held in the measurements of different cosmic probes and all their cross-correlations. In other words, a joint analysis of these probes is required.

In this work, we have presented a detailed joint analysis of currently available data combining CMB measurements from the Planck satellite and LSS observations from the SDSS-III/BOSS spectroscopic survey. To this end, we developed a general framework in `NumCosmo` to compute and analyse the auto and cross correlations between an arbitrary number of cosmological probes. In particular, we applied our framework to analyse CMB lensing and galaxy clustering at once by measuring auto and cross angular power spectra. In section 6.5.2.1, we showed how including cross-correlation information – already present in the data sets – improves constraints on cosmological parameters and decreases the statistical errors, for example, by 10% for $\ln 10^{10} A_\mathrm{s}$ and 20% for ω_c (when other parameters are fixed). This highlights the fact that ignoring part of the cosmological information (in this case, the cross-correlations) could lead to inaccurate posterior distributions of the parameters.

Next, we included CMB temperature and carried out three different MCMC

analyses, the first using only CMB temperature anisotropies ("CMB TT"), then adding CMB lensing ("CMB TT + CMB lensing") and finally the joint analysis per se ("CMB TT + CMB lensing $\otimes$ LSS"). We compared the performance of these analyses for the base, 6-parameter, flat ΛCDM model, and then explored constraints on the mass of neutrinos and the dark energy equation of state, constraining four statistical models (see figures 6.18, 6.20 and 6.24). As expected, constraints from the joint analysis are stronger than those obtained from CMB data only, in all cases. Because of the sensitivity of galaxy clustering and the CMB lensing-galaxy cross-correlations to m_ν and w, we were able to study extended models and constrain up to eight cosmological parameters at once (that is, H_0, ω_b, ω_c, A_s, n_s, z_re, m_ν and w).

The joint analysis proves effective in doing so and yields the best constraints. This can be understood as the result of the strong correlations observed between galaxy clustering biases and some cosmological parameters, in particular H_0 and w. As a result, we observe the breaking of several degeneracies and significantly better constraints for various parameters, although this depends upon exactly which parameters are constrained and which are assumed to be fixed. A downside is that future surveys will have to measure these biases with great precision in order to be able to pin down the values of these parameters and to constrain a possible time dependence of dark energy. Interestingly, if we used a value of $H_0 = 72\,\mathrm{km\,s^{-1}\,Mpc^{-1}}$ consistent with distance measurements from type Ia supernovæ, then our constraints would favour a value of the dark energy equation of state of $w \sim -1.1$, *i.e.* a phantom dark energy, which is disfavoured by theoretical considerations. Finally, we also obtained upper limits on the total mass of neutrinos of 0.29 eV [68%] as a result of its impact on galaxy clustering at small scale. This is similar to limits obtained with other analyses.

In this work, we have used spectroscopic observations of galaxies and quasars, insulating us from uncertainties inherent to photometric redshifts. Similar work was done by Nicola *et al.* 2016, 2017 with photometric data from the SDSS and the Dark Energy Survey, combined with geometric probes, though using different methods and constraining fewer parameters. However, the trade-off between the precision of redshifts and the much larger number of galaxies observed by future deep surveys like LSST could potentially lead to even better results. Moreover, imaging surveys can detect cosmic shear, a powerful probe of dark energy, by measuring distortions in the shapes of galaxies. Combining CMB lensing, galaxy lensing and galaxy clustering in a joint analysis is a promising avenue for cosmological parameters estimation.

Finally, in this near-future scenario of large amounts of data and joint analyses (including cross-correlations), we will be able to study different cosmological models emerging from different theories of gravity, such as effective field theories of dark energy (Gleyzes *et al.* 2016) or non-local gravity (Dirian *et al.* 2016), and hopefully start to distinguish and rule out some models with strong statistical significance.

Appendices

6.A X/Y matrices in the covariance

The $\mathbf{X}$ and $\mathbf{Y}$ matrices appearing in equation (6.21) have the following analytical expressions (Brown *et al.* 2005),

$$\mathbf{X}^{ABCD}_{\ell_1\ell_2} = \frac{1}{(2\ell_1+1)(2\ell_2+1)} \times \sum_{m_1m_2}\sum_{\ell_3m_3}\sum_{\ell_4m_4} W^{A}_{\ell_1\ell_3m_1m_3}\overline{W}^{B}_{\ell_2\ell_3m_2m_3}W^{C}_{\ell_2\ell_4m_2m_4}\overline{W}^{D}_{\ell_1\ell_4m_1m_4} \quad (6.35)$$

and

$$\mathbf{Y}^{ABCD}_{\ell_1\ell_2} = \frac{1}{(2\ell_1+1)(2\ell_2+1)} \times \sum_{m_1m_2}\sum_{\ell_3m_3}\sum_{\ell_4m_4} W^{A}_{\ell_1\ell_3m_1m_3}\overline{W}^{C}_{\ell_2\ell_3m_2m_3}W^{B}_{\ell_2\ell_4m_2m_4}\overline{W}^{D}_{\ell_1\ell_4m_1m_4}, \quad (6.36)$$

where the $W^{A}_{\ell\ell'mm'}$ describe the convolution of the mask ($\overline{W}^{A}_{\ell\ell'mm'}$ is its complex conjugate), *i.e.* if the field $A(\hat{\boldsymbol{n}})$ has full-sky spherical harmonics coefficients $A_{\ell m}$ and pseudo-coefficients $\tilde{A}_{\ell m}$ then

$$\tilde{A}_{\ell m} = \sum_{\ell' m'} W^{A}_{\ell\ell'mm'}A_{\ell m}. \quad (6.37)$$

These cannot be analytically computed and MC simulations are therefore required. We take advantage of the fact that equation (6.21) is exact if initial full-sky spectra do not depend on ℓ and that they need not have physically relevant values. The algorithm then proceeds as follows. First, we generate sets of four correlated maps with generic constant input auto and cross spectra, which we mask by the four masks used in our analysis. We then compute the spectra of the masked maps, thus building a collection of estimated pseudo spectra $\{\tilde{C}^{AB,i}_{\ell}\}_i$ where i represents the simulation index. The empirical covariance of the set of pseudo spectra is finally computed. Knowing the input spectra, an estimate of $\mathbf{X}^{ABCD}_{\ell\ell'}$ and $\mathbf{Y}^{ABCD}_{\ell\ell'}$ can be obtained using equation (6.21). In the case where $A = B$ or $C = D$ and only in this case, the terms in the square roots in equation (6.21) are equal and $\mathbf{X}^{ABCD}_{\ell\ell'}$ and $\mathbf{Y}^{ABCD}_{\ell\ell'}$ cannot be distinguished, but for all the other cases, it requires two sets of simulations to disentangle them.

We estimate the error on the empirical covariance matrices by bootstrapping the pseudo spectra $\{\tilde{C}^{AB,i}_{\ell}\}_i$ and require that the ratio of the norms[15] of the error matrix

[15] Note that this choice is somewhat arbitrary and insures convergence of the diagonal elements, with degrading precision away from the diagonal. Uniform convergence, which could be measured by the norm of the matrix SC^{-1}, where S is the error and C the covariance, would require much

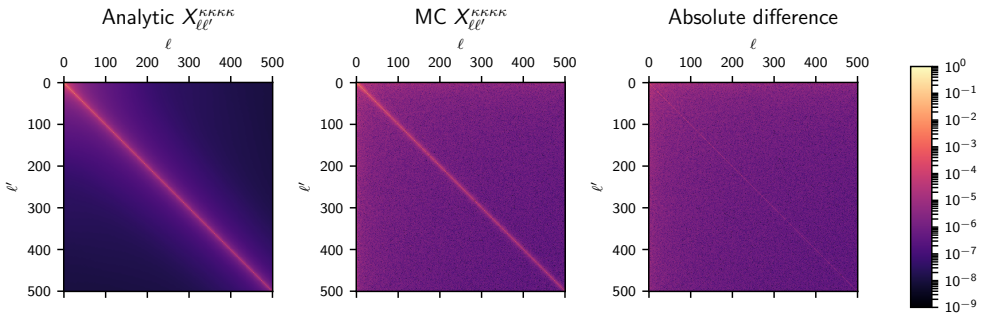

Figure 6.26 – Comparison between the analytically-estimated (left panel) and simulation-estimated (middle panel) $\mathbf{X}^{\kappa\kappa\kappa\kappa}_{\ell\ell'}$ matrices in logarithmic scale. The absolute difference is shown on the right panel. The important features are well captured: the precision is better than 2% on the diagonal and degrades when getting further away from the diagonal. The middle panel shows that the far off-diagonal terms are dominated by numerical noise from our MC simulations, but are four orders of magnitudes smaller than the diagonal terms which are the most important, making it safe to use in the covariance matrix. The right panel shows the absolute difference.

to that of the empirical covariance matrix is smaller than 1%, which in our analysis necessitated more than 200 000 simulations.

In the case where $A = B = C = D$, these matrices reduce to symmetrized mixing matrices

$$\mathbf{X}^{AAAA}_{\ell\ell'} = \mathbf{Y}^{AAAA}_{\ell\ell'} = \frac{1}{2\ell'+1}\mathbf{M}^{AA}_{\ell\ell'}, \tag{6.38}$$

which allows for comparison and validation of the MC simulations (see figure 6.26). We find percent-level agreement on the diagonal, with a decreasing precision when moving further away from the diagonal as numerical noise (at least four orders of magnitude smaller than the diagonal elements) starts dominating.

6.B MCMC convergence tests

In this work, we checked the convergence of the MCMC chains using visual inspection methods and three different diagnostics, which Sandro Vitenti implemented closely following the `R` package `CODA` (Plummer *et al.* 2006).

6.B.1 Visual inspection

figure 6.27 shows an example of a trace plot. When the chain is converged, each walker should oscillate around a common, mean value. The ensemble mean – that is, average over walkers – should also oscillate around that same mean. Additionally, we can define *forward* and *backward* means as the means of the sample, respectively up to

more simulations (and the inversion of the noisy matrix C). However, the covariance is strongly dominated by terms close to the diagonal, which makes our choice reasonable.

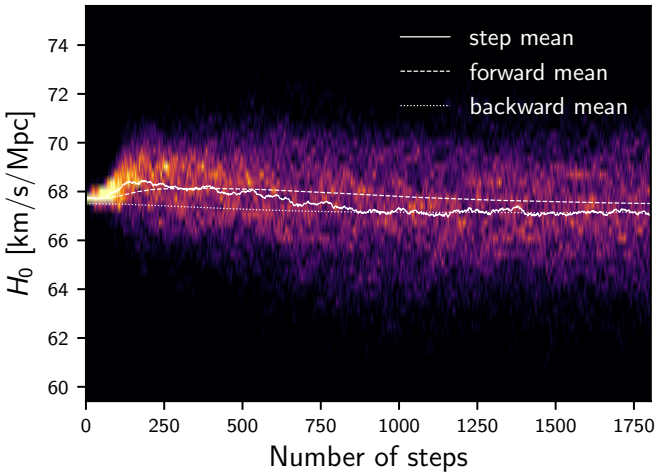

Figure 6.27 – Example of trace plot for H_0: at each step, the empirical distribution of walkers is shown in color (bright color indicating high probability). The solid white line indicates the mean over walkers at each step, while the dashed (respectively dotted) white line indicates the mean over all points up to that step (respectively, from that step up to the end). The mean values progressively stabilize around a common value.

some step, or from that step to the end of the chain. Deviations from that behaviour indicate that the chain is not converged yet, and allow for a visual estimation of the burning phase, which is confirmed by the following quantitative tests.

6.B.2 Shrink factor

The first diagnostic is the Multivariate Potential Scale Reduction Factor (MPSRF, also called the *shrink factor*, Brooks and Gelman 2012; Gelman and Rubin 1992). This method requires multiple chains, whose initial values must be over-dispersed in comparison with the posterior, and quantifies the mixing of the walkers by comparing the ensemble variance to the per-walker variance. In order to be more quantitative, let us consider samples of a p-dimensional parameter vectors, $\boldsymbol{\theta}_t^i$, where $1 \leq t \leq n$ indicates the time step and $1 \leq i \leq m$ refers to the walker index. The per-walker variance is a $p \times p$ matrix given by

$$\boldsymbol{W}^i = \frac{1}{n-1} \sum_{t=1}^{n} \left(\boldsymbol{\theta}_t^i - \overline{\boldsymbol{\theta}}^i\right) \left(\boldsymbol{\theta}_t^i - \overline{\boldsymbol{\theta}}^i\right)^\intercal, \tag{6.39}$$

where $\overline{\boldsymbol{\theta}}^i = \sum_{t=1}^{n} \boldsymbol{\theta}_t^i \Big/ n$ is the per-walker mean. We then take the average over walkers

$$\boldsymbol{W} = \frac{1}{m} \sum_{i=1}^{m} \boldsymbol{W}^i. \tag{6.40}$$

The variance of the per-walker means[16] is

$$\boldsymbol{B} = \frac{n}{m-1}\sum_{i=1}^{m}\left(\overline{\boldsymbol{\theta}}^{i} - \overline{\boldsymbol{\theta}}\right)\left(\overline{\boldsymbol{\theta}}^{i} - \overline{\boldsymbol{\theta}}\right)^{\intercal} \tag{6.41}$$

where $\overline{\boldsymbol{\theta}} = \sum_{i=1}^{m}\sum_{t=1}^{n}\boldsymbol{\theta}_t^i \Big/ n\,m$ is the overall mean. If λ_1 denotes the largest eigenvalue of the symmetric, positive-definite matrix $\boldsymbol{W}^{-1}\boldsymbol{B}\Big/n$, then

$$r = \frac{n-1}{n} + \frac{m+1}{m}\lambda_1 \xrightarrow[n\to\infty]{} 1. \tag{6.42}$$

Note that this factor can also be computed for each parameter individually, usually (note the square root here) as

$$r = \sqrt{\frac{n-1}{n} + \frac{1}{n}\frac{B}{W}}, \tag{6.43}$$

where W and B are per- and between-walker variances (given by the diagonal elements of $\boldsymbol{W}$ and $\boldsymbol{B}$). Nevertheless, we do not know *a priori* the posterior and, for this reason, we may only guess what an initial, over-dispersed distribution would be.

6.B.3 Heidelberger-Welch test

The second method is the Heidelberger-Welch diagnostic (Heidelberger and Welch 1981, 1983), which is based on the Schruben stationarity test (Schruben 1982). Consider a Markov chain X_i, and its cumulative sum and mean given by

$$Y_n = \sum_{i=1}^{n} X_i, \quad \overline{X} = \frac{Y_n}{n}. \tag{6.44}$$

If the chain is stationary, the forward mean should oscillate around the full-sample mean. The Schruben test thus defines the continuous process

$$B_n(t) = \frac{Y_{\lfloor nt\rfloor} - \lfloor nt\rfloor\overline{X}}{\sqrt{nS(0)}}, \tag{6.45}$$

where $S(0)$ is the spectral density of the chain evaluated at frequency 0 (see the next diagnostic). Under the assumption of stationarity, $B_n(t)$ approximates a standard Brownian bridge. Its L_2 norm, $T = \int_0^1 \mathrm{d}t\,|B_n(t)|^2$, called the Cramér-von Mises statistic, has a tabulated distribution (Tolmatz 2002) which can be used to test this hypothesis.

The Heidelberger-Welch diagnostic applies this test to subsets of a chain to obtain one that satisfies the test for a given p-value. In practice, we cut the chains in

[16] Note the rescaling factor n, due to the fact that $\mathrm{Var}\left(\overline{\boldsymbol{\theta}}^{i}\right) = \mathrm{Var}\left(\boldsymbol{\theta}_t^i\right)\Big/n$.

100 blocks, then compute the test for the sub-chain made of the n last blocks, for $1 \leq n \leq 100$. This test is performed for each parameter[17] and provides an estimation of the length of the burning phase. Since we are using an ensemble sampler, we can apply this test to each individual chain, or, more efficiently, to the ensemble mean of each parameter. We applied the individual approach only when the Markov chain presents convergence problems.

6.B.4 Effective sample size

In the third approach, we calculated the autocorrelation time as proposed by Goodman and Weare 2010. However, in `NumCosmo`, instead of estimating the autocorrelation time directly from the autocorrelations, we fit an Auto Regressive (AR) model of order p as in `CODA`, *i.e.* we fit for parameters ϕ_i, $0 \leq i \leq p$, such that the chain can be written

$$X_t = \phi_0 + \sum_{i=1}^{p} \phi_i X_{t-i} + \epsilon_t, \tag{6.46}$$

where ϵ_t is white noise. The spectral density is then given by

$$S(f) = \frac{\mathrm{Var}(X)}{\left|1 - \sum_{k=1}^{p} \phi_k e^{-2\pi i f k}\right|^2}, \tag{6.47}$$

and the autocorrelation function by

$$\rho(\tau) \equiv \frac{\langle (X_t - \langle X \rangle)(X_{t+\tau} - \langle X \rangle) \rangle}{\mathrm{Var}(X)} = \sum_{k=1}^{p} a_k |y_k|^{-\tau}, \tag{6.48}$$

where y_k are the roots of the polynomial $1 - \sum_{k=1}^{p} \phi_k X^k$. The autocorrelation time is then given by $\tau_0 = 1 + 2\sum_{k=1}^{p} \phi_k$. In the AR model fitting, we use the bias-corrected Akaike Information Criterion[18] (Hurvich and Tsai 1989) to choose the best AR order to use for a given parameter in a chosen chain. This provides a less noisy estimate of the autocorrelation time than the direct inference from the autocorrelations (see Goodman and Weare 2010). The Effective Sample Size (ESS) is computed using that estimated autocorrelation time as

$$\mathrm{ESS} = \frac{n_{\mathrm{samples}}}{\tau_0}, \tag{6.49}$$

and provides an equivalent measure of the effective number of independent points in each chain. Finally, the variance of the sample mean of the parameters is given by

[17] We additionally correct for the so-called "look elsewhere effect", *i.e.* the fact that if one performs many tests, some are likely to fail. Therefore, our p-value is the probability that one of the Cramér-von Mises statistics is larger than a given value.

[18] We select the model which yields the highest value of $2k - \ln \hat{\mathcal{L}}$ where k is the number of parameters in the model and $hat\mathcal{L}$ is the maximum likelihood of the model. This approximates the Kullback-Liebler divergence between the model and the "truth".

the empirical variance of the sampled values divided by the ESS.

6.C Profile likelihood

In order to accelerate our MCMC analyses, we choose to use the profile likelihood instead of the marginal likelihood for the nuisance parameters. The reason is that this procedure decreases the dimension of the parameter space and requires less calls to the Boltzmann code, resulting in an overall faster convergence of the posterior distribution of the cosmological parameters. In practice, it amounts to compute the maximum likelihood estimator value of the nuisance parameters $\hat{\boldsymbol{A}}(\boldsymbol{\theta})$ for each set of cosmological parameters $\boldsymbol{\theta}$ given the data (which is fast), and use this value in the likelihood. The posterior distribution is then given by

$$\mathcal{L}_{\text{profile}}\left(\boldsymbol{\theta}\middle|C_\ell^{TT}\right) \propto \mathcal{L}\left(C_\ell^{TT}\middle|\boldsymbol{\theta}, \hat{\boldsymbol{A}}(\boldsymbol{\theta})\right) \tag{6.50}$$

while the marginal likelihood is

$$\mathcal{L}_{\text{marginal}}\left(\boldsymbol{\theta}\middle|C_\ell^{TT}\right) \propto \int \mathcal{L}\left(C_\ell^{TT}\middle|\boldsymbol{\theta}, \boldsymbol{A}\right) \mathrm{d}\boldsymbol{A}\,. \tag{6.51}$$

We demonstrate that it doesn't affect the results on the cosmological parameters by running two MCMC using only the CMB temperature power spectrum C_ℓ^{TT}, one performing the nuisance parameters subfitting procedure and the other using the standard marginalisation procedure. figure 6.28 shows the posterior distribution in these two cases. The mean value of each parameter in both runs is shown in the one-dimensional plots on the diagonal. In all cases, the variation of the mean is much smaller than the statistical variance, and the standard deviation is at worst decreased by 15% in the profile likelihood (for n_s and ω_b, two parameters which are poorly constrained by the other observations), with almost no difference for the other parameters. This indicates that we can use either likelihoods indifferently. Since the profile likelihood method is faster overall, and that we don't have other nuisance parameters, we used it for all simulations in section 6.5.2.2.

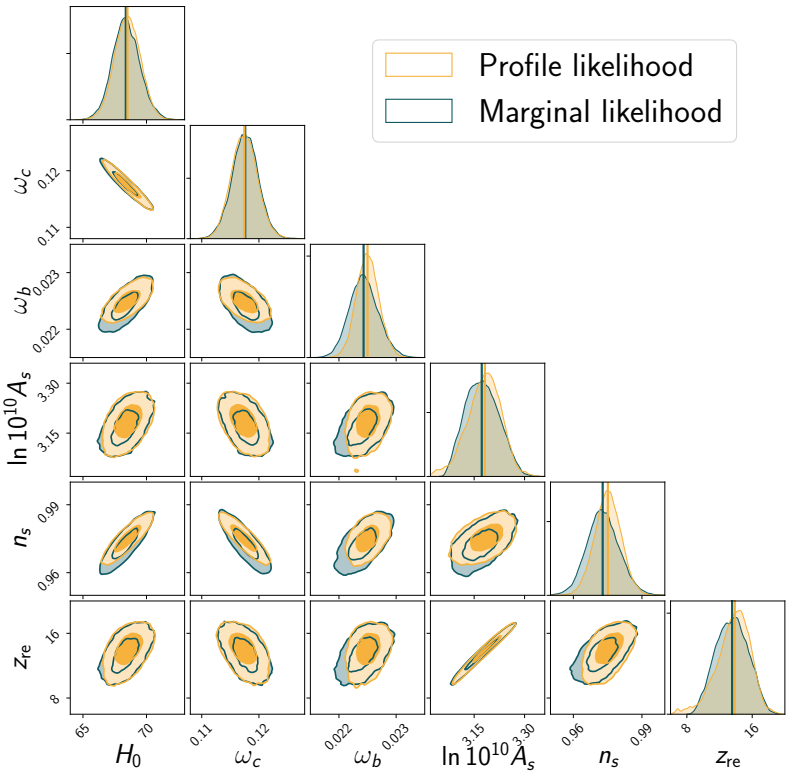

Figure 6.28 – Comparison between the marginal likelihood (dark blue) and the profile likelihood (yellow). On the diagonal, the one-dimensional projections of the posterior distribution for each parameter is shown, the vertical lines corresponding to the mean value. For all the parameters, the difference between the means of the two distribution is much smaller than the statistical error. The standard deviations are also very close, with at worst a 10% decrease for for n_s and ω_b.

Conclusion

Summary

This manuscript reports work that I carried out between September 2014 and September 2017. After introducing the standard cosmological model, we reviewed a selection of cosmological observables – the cosmic microwave background, tracers of large-scale structure and gravitational lensing – that probe the matter density field over different periods of time and scales. Then, we presented two experiments, Planck and SDSS-III/BOSS, that were combined in two different ways in chapters 5 and 6.

First, in chapter 5, we proposed a novel approach to the cross-correlation of the convergence of CMB lensing with the one-dimensional power spectrum of the Lyman-α forest. We successfully applied this method to Planck and SDSS-III/BOSS data, demonstrating a correlation between the data sets that originates in non-linear gravitational and baryonic processes. This is the first detection of this new signal, and its amplitude is in agreement with expectations from our theoretical approach – modulo an effective non-linear bias that we fit – and from hydrodynamical simulations, as reported by recent papers.

Then, in chapter 6, we presented a methodology to perform a joint cosmological analysis of CMB lensing and the projected density contrast of galaxies and quasars, using a pseudo-power spectrum approach that includes both auto- and cross-power spectra. After validating the method with various tests, we applied it to Planck and BOSS data, then complemented the analysis with CMB temperature data and finally obtained cosmological constraints on the ΛCDM model. The additional information included in the joint analysis enabled us to explore constraints on dark energy and neutrinos.

The near future

Happily, there is plenty of avenues for extending and improving work presented here in the near future.

Let us first consider the Lyman-α forest-CMB lensing cross-correlation. As mentioned in chapter 5, this signal is interesting because it provides a test for expectations of the position-dependent Lyman-α power spectrum, which involves

non-linear gravitational evolution, but also baryonic processes in the IGM that are difficult to model. As a cross-correlation signal, it provides an independent test against which simulations can be calibrated. Further extensions include measuring the radial dependence, not so much to get more information (it would simply probe the matter correlation function) but rather to disentangle a possible contribution from unresolved DLAs that have small transverse extensions (this was pointed out to me by Anže Slosar, BNL). It is likely that one will have to wait for data from the upcoming DESI survey to extract cosmological information from this signal, but in principle, it could constrain small-scale cosmology and therefore the neutrino masses.

I performed a similar cross-correlation analysis replacing the CMB lensing signal by the CIB observed in the direction of each quasar (traced by the 545 GHz map from Planck) and found similar results[19]. At the moment, this very preliminary work lacks a theoretical interpretation, although, intuitively, this measurement could shed light on the interplay between star-forming galaxies and neutral hydrogen in the IGM.

Then, the joint analysis presented here will be improved in several ways. In the near future, the model of the galaxy non-linear power spectrum could be replaced by one that is more elaborate on small scales. More generally, a meticulous study of the impact and validity of using small scales to derive cosmological constraints is still needed (it motivates ongoing, active research for future surveys). Another improvement could be to cut the samples in thinner redshift bins, thus imposing a less stringent model for galaxy biases, though RSDs would become more important. Finally, pseudo-C_ℓ estimators could be improved with mode projection techniques to correct for any possible bias due to astrophysical foregrounds and observational systematics (Elsner *et al.* 2017).

Perspectives

We hope, at this point, that it appears clearly that cross-correlations and joint analyses are useful *and* necessary, and we also hope that work presented here will be helpful. This kind of analyses, now blooming, needs further development in the perspective of future surveys, that we discuss here.

Indeed, summary statistics used to date —mostly angular correlation functions or power spectra— might not capture cosmological information held in the data set in an optimal way, and modelling the covariance matrix for partial sky observations is still challenging. Moreover, the precision of theoretical predictions, *e.g.* for the non-linear power spectrum, will have to meet the high requirements set by the steadily growing stream of data from future surveys.

Angular two-point statistics are a well-established way of quantifying clustering information because we know how to compute them efficiently, both theoretically and from observations. However, they cannot capture non-gaussian nor radial information.

[19] This is not very surprising since Planck found a strong correlation between CMB lensing and the CIB, both sourced at redshift z 2. In a way, that measurement is only closing the loop.

Data compression methods such as spherical Fourier-Bessel transforms could capture the redshift evolution more efficiently, but obtaining reliable and computationally competitive theoretical expectations is a challenging task. Moreover, codes that include relativistic corrections (mostly RSD and lensing), such as `CLASSgal` (Di Dio *et al.* 2013) and `AngPow` (Campagne *et al.* 2017) are still under active development.

Whichever means of data compression is used also requires the corresponding covariance matrices. Angular-power-spectra covariance receives non-gaussian contributions that shouldn't be neglected for the next generation of surveys. At small scales, extra covariance comes from non-linear gravitational evolution and involves integrals over the trispectrum (which can be estimated, for instance, with the halo-model). At large scales, the super-sample covariance characterizes the response of the measured observable to modes larger than the survey's extent (and thus unobserved) and involves integrals over the response of the power spectrum. The `cosmolike` code (Krause and Eifler 2017) computes these integrals from their analytical expressions, but not quickly enough to vary the covariance matrix when running MCMCs. Although it has been argued that this could actually either be preferable for gaussian likelihoods[20] or solved by some means of marginalization (Sellentin and Heavens 2016), the problem needs clarification. Additionally, covariance must take the finite size and non-trivial geometry of surveys into account. While efficient methods have been developed for CMB studies, more theoretical work is needed to include the intrinsic non-gaussian covariance mentioned above.

Finally, let us mention another important use of cross-correlation: systematics control. Inconsistencies between auto- and cross-spectra can judiciously be used as a warning sign, indicating that something somewhere is off. If forecasts show that combining data for next-generation surveys at the power-spectrum level will boost the outcome of joint statistical analyses, one can do even better by performing a fully joint analysis, starting from raw data. In particular, future weak lensing surveys (Euclid, LSST and WFIRST), because of their different instrumental designs, can greatly benefit from each other. Galaxies seen by two or more surveys can be more accurately de-blended and analyzed. Developing common analysis frameworks presents financial, organizational and technical challenges, but the opportunities for science become countless.

We have only just scratched the surface of cross-correlation techniques. They won't solve every issue in cosmology, but in the near future, they will offer many novel ways of combining experiments, probes and wavelengths and deliver great science.

[20] Carron 2013 showed that varying the covariance matrix within an approximate gaussian likelihood could pick up spurious, artificial information from the estimators, for the very reason that their true distributions are not gaussian (see also appendix B.2).

APPENDIX A

Statistical tools

A.1 Confidence regions: n-σ contours

Consider a multivariate gaussian distribution of mean $\boldsymbol{\mu} \in \mathbb{R}^k$ and covariance matrix $\boldsymbol{\Sigma} \in \mathbb{R}^{k\times k}$, denoted $\mathcal{N}(\boldsymbol{\mu}, \boldsymbol{\Sigma})$. Its density reads

$$p(\boldsymbol{x}) = \frac{1}{\sqrt{(2\pi)^k |\boldsymbol{\Sigma}|}} \exp\left(-\frac{1}{2}\chi^2\right) \quad \text{where} \quad \chi^2 = (\boldsymbol{x}-\boldsymbol{\mu})^\intercal (\Sigma)^{-1} (\boldsymbol{x}-\boldsymbol{\mu}) \,. \tag{A.1}$$

and its marginal distributions are also gaussian.

For a one-dimensional marginal distribution $\mathcal{N}(\mu, \sigma)$, the n-σ contours correspond to the intervals defined as $|x-\mu| \leq n\sigma$, which has a measure

$$\int_{|x-\mu|\leq n\sigma} p(x)\,\mathrm{d}x = \mathrm{erf}\left(\frac{n}{\sqrt{2}}\right). \tag{A.2}$$

For $n = 1, 2$ and 3, this corresponds to 68%, 95% and 99% probabilities. For a marginal distribution that is not gaussian, the n-σ contours is thus defined as limits of the region $\mathcal{R} = \{x \in \mathbb{R} \mid p(x) \geq s\}$ where s is such that

$$\int_{x\in\mathcal{R}} p(x)\,\mathrm{d}x = \mathrm{erf}\left(\frac{n}{\sqrt{2}}\right). \tag{A.3}$$

This interval may not be symmetric around μ and its limits give the upper and lower n-σ bounds.

Let us now turn to the two dimensional case, an interesting case for MCMC corner plots. In the gaussian case, the n-σ contours correspond to the elliptical region where

$\chi^2 \leq n^2$, which has a measure

$$\int_{\chi^2 \leq n^2} p(\boldsymbol{x})\, \mathrm{d}^2\boldsymbol{x} = \int_0^n r e^{-r^2/2}\, \mathrm{d}r = 1 - e^{-n^2/2}. \tag{A.4}$$

For $n = 1, 2$ and 3, this corresponds to 39%, 86% and 99% probabilities. The n-σ contours of other distribution is defined the same way as in the one-dimensional case: it is the inner region of an iso-density curve with a measure given by $1 - e^{-n^2/2}$.

A.2 Bayesian inference

This section is based on personal lecture notes from the courses at ENS of Zhan Shi and Josselin Garnier on integration, probability and random processes and Stéphane Boucheron on statistics.

A.2.1 Bayes theorem

Consider a random variable X in a probability space[1] $\mathcal{X}$, with a probability distribution $P_{\boldsymbol{\theta}}$ that depends on parameters $\boldsymbol{\theta} \in \Theta$. Now, assume that Θ can be given the structure of a probability space, such that $\boldsymbol{\theta}$ is a random variable too. Its probability measure $P(\boldsymbol{\theta})\, \mathrm{d}\boldsymbol{\theta}$ is called the *prior*. If the probability spaces $\mathcal{X}$ and Θ have the correct properties, then one can define the conditional probability of $\boldsymbol{\theta}$ given X, called the *posterior*. In the case of continuous spaces (for instance if $\mathcal{X}$ and $\boldsymbol{\theta}$ are open sets in $\mathbb{R}^d$), Bayes theorem then states that the probability densities are related by

$$P(\boldsymbol{\theta} \,|\, X) = \frac{\mathcal{L}(X \,|\, \boldsymbol{\theta}) P(\boldsymbol{\theta})}{P(X)}, \tag{A.5}$$

where $\mathcal{L}(X \,|\, \boldsymbol{\theta})$ is the *likelihood*, *i.e.* the probability density distribution associated with the law $P_{\boldsymbol{\theta}}$, and

$$P(X) = \int_\Theta \mathcal{L}(X \,|\, \boldsymbol{\theta}')\, \mathrm{d}\boldsymbol{\theta}', \tag{A.6}$$

which is the *bayesian evidence* (and may be difficult to compute). However, one can forget about this term, and simply use

$$P(\boldsymbol{\theta} \,|\, X) \propto \mathcal{L}(X \,|\, \boldsymbol{\theta}) P(\boldsymbol{\theta}). \tag{A.7}$$

Bayesian inference interprets the prior distribution as information on $\boldsymbol{\theta}$ that is available *before* new data or evidence X is used to update our knowledge of $\boldsymbol{\theta}$, as

[1] Technically, a probability space consists in a sample space Ω, a set $\mathcal{F}$ of subsets of Ω stable under coutable union and intersection (a σ-algebra) and a probability measure P that gives a weight to each event $F \in \mathcal{F}$. Here, we consider a set of such probability measures, indexed by a parameter vector $\boldsymbol{\theta}$.

represented by the posterior distribution. One can then estimate confidence regions on $\boldsymbol{\theta}$, as in the previous section, using the posterior distribution.

A.2.2 Markov chain Monte Carlo methods

In principle, if one can compute the likelihood $\mathcal{L}(X \,|\, \theta)$, then it is possible to obtain the marginal distributions of $\boldsymbol{\theta}$, *i.e.* the distribution of each of its components, by integrating out the other components. However, if the number of dimensions of $\boldsymbol{\theta}$ is higher than a few, it becomes computationally expensive to compute these integrals, and much CPU time is lost in low probability regions of the parameter space Θ.

Markov chain Monte Carlo (MCMC) methods solve this problem by sampling the likelihood where it is non-negligible. More precisely, they consist in drawing a sample of parameter values, $\boldsymbol{\theta}_n$, by creating a random walk (a Markov chain[2]) in the parameter space. Given that ergodicity is ensured, the empirical distribution of the sample $\boldsymbol{\theta}_n$ can then be used to approximate marginal distributions. In other words, integrals are replaced by simple histograms.

A.2.2.1 The Metropolis-Hastings algorithm

Once a random initial point has been chosen, the Metropolis-Hastings algorithm (see, for instance, Lebeau 2009), when applied to the case of sampling the posterior distribution, proceeds, at time n, as follows:

1. Pick a random point $\boldsymbol{\theta}$ from a proposal distribution $g(\cdot \,|\, \boldsymbol{\theta}_n)$ that depends on $\boldsymbol{\theta}_n$ only;

2. Compute the acceptance ratio

$$\frac{P(X \,|\, \boldsymbol{\theta})}{P(X \,|\, \boldsymbol{\theta}_n)} \frac{g(\boldsymbol{\theta}_n \,|\, \boldsymbol{\theta})}{g(\boldsymbol{\theta} \,|\, \boldsymbol{\theta}_n)}; \tag{A.8}$$

   - if it is larger than 1, then the transition is accepted and $\boldsymbol{\theta}_{n+1} = \boldsymbol{\theta}$;
   - otherwise, $\boldsymbol{\theta}$ is accepted with probability given by this ratio; if rejected, then $\boldsymbol{\theta}_{n+1} = \boldsymbol{\theta}_n$.

Convergence of the empirical distribution of the sample towards the posterior distribution is ensured in the case of *detailed balance*, *i.e.* the probability of the transition from $\boldsymbol{\theta}$ to $\boldsymbol{\theta}'$ is equal to that from $\boldsymbol{\theta}'$ to $\boldsymbol{\theta}$. However, the choice of the proposal distribution, and particularly the scale of the "jumps", is not dictated by the algorithm, and must be adjusted by hand.

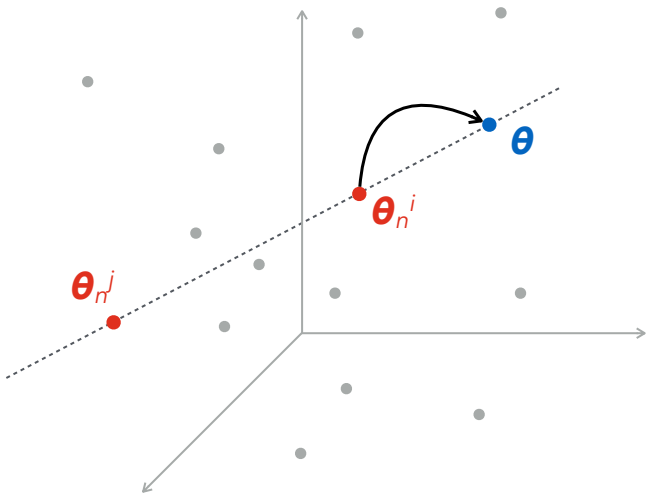

Figure A.1 – MCMC ensemble sampler stretch move implemented in `NumCosmo` as suggested in Goodman and Weare 2010.

A.2.2.2 Ensemble sampler

For the work presented in Chapter 6, we used an *ensemble sampler* MCMC, with a specific transition scheme called a *stretch move* as in Goodman and Weare 2010. It collectively moves an ensemble of *walkers* in the parameter space, creating a sample $\boldsymbol{\theta}_n^i$, indexed by time n and walker index i. It proceeds, at step n and for walker i, as follows:

1. Pick another walker, j, at random;
2. Draw a line between $\boldsymbol{\theta}_n^i$ and $\boldsymbol{\theta}_n^j$, and pick a point on this line

$$\boldsymbol{\theta} = \boldsymbol{\theta}_n^i + Z(\boldsymbol{\theta}_n^i - \boldsymbol{\theta}_n^j), \tag{A.9}$$

   where Z has a probability density function given by

$$p(Z) \propto \begin{cases} \frac{1}{\sqrt{z}} & \text{if } z \in \left[\frac{1}{\alpha}, \alpha\right] \\ 0 & \text{otherwise} \end{cases}, \tag{A.10}$$

   where the scale α is a hyperparameter to be adjusted (this will impact the average fraction of steps that are accepted).
3. Compute the acceptance ratio

$$Z^{d-1} \frac{P(X \mid \boldsymbol{\theta})}{P(X \mid \boldsymbol{\theta}_n^i)}, \tag{A.11}$$

[2] A Markov chain is a discrete random process X_n, where $n \in \mathbb{N}$, such that X_{n+1} is independent of X_k for $k < n$.

where d is the dimension of $\boldsymbol{\theta}$ and decide whether or not to move the walker, as in the Metropolis-Hastings algorithm.

In order to maintain the detailed balance, it is actually necessary to split the sample of walkers in half, updating the first half by choosing walkers from the second half, and then the opposite.

This type of MCMC sampler has several advantages. First, as an ensemble sampler, it provides a better mixing than a single walker. Then, the stretch move means that the speed of sampling is independent of the scale and absolute value of the parameters, a property called *affine invariance*. Moreover, intuitively, it means that when a walker reaches a high probability region, it will "attract" other walkers.

APPENDIX B

On angular power spectra

B.1 Pseudo power spectra

B.1.1 Expectation value

The mask or window function $W^A(\hat{\boldsymbol{n}})$ relates the full-sky multipoles $a_{\ell m}$ to the pseudo-multipoles via the relationship

$$\tilde{a}_{\ell m} = \sum_{\ell' m'} A^{m m'}_{\ell\ \ell'} a_{\ell' m'} \tag{B.1}$$

where

$$A^{m m'}_{\ell\ \ell'} = \int \mathrm{d}\hat{\boldsymbol{n}}\, Y^*_{\ell m}(\hat{\boldsymbol{n}}) Y_{\ell' m'}(\hat{\boldsymbol{n}}) W^A(\hat{\boldsymbol{n}}). \tag{B.2}$$

Therefore, the pseudo-power spectrum estimator reads

$$\tilde{C}^{AB}_\ell = \frac{1}{2\ell+1} \sum_m \tilde{a}_{\ell m} \tilde{b}^*_{\ell m} \tag{B.3}$$

$$= \frac{1}{2\ell+1} \sum_m \sum_{\ell' m'} \sum_{\ell'' m''} A^{m m'}_{\ell\ \ell'} B^{* m m''}_{\ell\ \ell''} a_{\ell' m'} . b^*_{\ell'' m''} \tag{B.4}$$

The expectation value of the estimator is

$$\left\langle \tilde{C}^{AB}_\ell \right\rangle = \frac{1}{2\ell+1} \sum_m \sum_{\ell' m'} A^{m m'}_{\ell\ \ell'} B^{* m m'}_{\ell\ \ell'} C^{AB}_{\ell'} \tag{B.5}$$

$$= \sum_{\ell'} M_{\ell\ell'} C^{AB}_{\ell'}. \tag{B.6}$$

where the *mixing matrix* is given by

$$\mathbf{M}_{\ell\ell'} = \frac{1}{2\ell+1}\sum_{mm'} A^{mm'}_{\ell\ \ell'} B^{*mm'}_{\ell\ \ell'}. \tag{B.7}$$

B.1.2 Covariance of pseudo spectra

In order to obtain the covariance of these estimators, let us first compute the expectation value of the product for four observables (A, B, C and D) and two multipoles (ℓ_1 and ℓ_2). It is

$$\left\langle \tilde{C}^{AB}_{\ell_1}\tilde{C}^{CD}_{\ell_2}\right\rangle = \frac{1}{2\ell_1+1}\frac{1}{2\ell_2+1}\sum_{m_1}\sum_{\ell_1'm_1'}\sum_{\ell_1''m_1''}\sum_{m_2}\sum_{\ell_2'm_2'}\sum_{\ell_2''m_2''} A^{m_1m_1'}_{\ell_1\ \ell_1'} B^{*m_1m_1''}_{\ell_1\ \ell_1''} C^{m_2m_2'}_{\ell_2\ \ell_2'} D^{*m_2m_2''}_{\ell_2\ \ell_2''} \underbrace{\left\langle a_{\ell_1'm_1'} b^*_{\ell_1''m_1''} c_{\ell_2'm_2'} d^*_{\ell_2''m_2''}\right\rangle}_{\langle\rangle} \tag{B.8}$$

where the expectation value of the product of four multipoles is decomposed, thanks to Wick's theorem, as

$$\langle\rangle = \underbrace{\left\langle a_{\ell_1'm_1'} b^*_{\ell_1''m_1''}\right\rangle\left\langle c_{\ell_2'm_2'} d^*_{\ell_2''m_2''}\right\rangle}_{①} + \underbrace{\left\langle a_{\ell_1'm_1'} c_{\ell_2'm_2'}\right\rangle\left\langle b^*_{\ell_1''m_1''} d^*_{\ell_2''m_2''}\right\rangle}_{②} + \underbrace{\left\langle a_{\ell_1'm_1'} d^*_{\ell_2''m_2''}\right\rangle\left\langle b^*_{\ell_1''m_1''} c_{\ell_2'm_2'}\right\rangle}_{③}. \tag{B.9}$$

The first term, when the sums in Equation (B.8), becomes

$$① \to \left\langle \tilde{C}^{AB}_{\ell_1}\right\rangle\left\langle \tilde{C}^{CD}_{\ell_2}\right\rangle \tag{B.10}$$

and will cancel when computing the covariance of $\tilde{C}^{AB}_{\ell_1}$ and $\tilde{C}^{CD}_{\ell_2}$.

Using the reality condition,

$$a^*_{\ell m} = (-1)^m a_{\ell,-m}, \tag{B.11}$$

the third term, when summed, becomes

$$③ \to \frac{1}{2\ell_1+1}\frac{1}{2\ell_2+1}\sum_{m_1}\sum_{\ell_1'm_1'}\sum_{m_2}\sum_{\ell_2'm_2'} A^{m_1m_1'}_{\ell_1\ \ell_1'} B^{*m_1m_2'}_{\ell_1\ \ell_2'} C^{m_2m_2'}_{\ell_2\ \ell_2'} D^{*m_2m_1'}_{\ell_2\ \ell_1'} C^{AD}_{\ell_1'} C^{BC}_{\ell_2'}. \tag{B.12}$$

Using, again, the reality condition, the expectation value of the second term is

$$② = (-1)^{m_1'+m_1''}\,\delta_{\ell_1',\ell_2'}\delta_{m_1',-m_2'}\delta_{\ell_1'',\ell_2''}\delta_{m_1'',-m_2''} C^{AC}_{\ell_1'} C^{BD}_{\ell_1''}. \tag{B.13}$$

Using properties of the spherical harmonics, we also have that

$$A^{mm'}_{\ell\ \ell'} = (-1)^{m+m'} A^{*-m-m'}_{\ell\quad\ell'} \tag{B.14}$$

such that, when the sums are perform and indices renamed, the second term becomes

$$\textcircled{2} \xrightarrow[m_2\to -m_2]{m_1''\to m_2', \ell_1''\to \ell_2'} \frac{1}{2\ell_1+1}\frac{1}{2\ell_2+1}\sum_{m_1}\sum_{\ell_1' m_1'}\sum_{m_2}\sum_{\ell_2' m_2'} A^{m_1 m_1'}_{\ell_1\ \ell_1'} B^{*m_1 m_2'}_{\ell_1\ \ell_2'} C^{*m_2 m_1'}_{\ell_2\ \ell_1'} D^{m_2 m_2'}_{\ell_2\ \ell_2'} C^{AC}_{\ell_1'} C^{BD}_{\ell_2'}. \tag{B.15}$$

Finally, using Eisenstein symmetrization (valid if the spectra vary smoothly and that the mixing does not strongly couple very different multipole indices),

$$C^{AD}_{\ell_1'} C^{BC}_{\ell_2'} \to \sqrt{C^{AD}_{\ell_1} C^{AD}_{\ell_2} C^{BC}_{\ell_1} C^{BC}_{\ell_2}}, \tag{B.16}$$

as in Brown *et al.* 2005, the final result is

$$\boxed{\begin{aligned}\mathrm{Cov}\left(\tilde{C}^{AB}_{\ell_1}, \tilde{C}^{CD}_{\ell_2}\right) \approx &\sqrt{D^{AD}_{\ell_1} D^{AD}_{\ell_2} D^{BC}_{\ell_1} D^{BC}_{\ell_2}}\mathbf{X}^{ABCD}_{\ell_1\ell_2} \\ &+ \sqrt{D^{AC}_{\ell_1} D^{AC}_{\ell_2} D^{BD}_{\ell_1} D^{BD}_{\ell_2}}\mathbf{Y}^{ABCD}_{\ell_1\ell_2}\end{aligned}} \tag{B.17}$$

with

$$D^{AB}_{\ell} = \begin{cases} C^{AB}_{\ell} & \text{if } A \neq B \\ C^{AA}_{\ell} + N^{A}_{\ell} & \text{if } A = B \end{cases}, \tag{B.18}$$

where C^{AB}_{ℓ} and N^{A}_{ℓ} are the full-sky theoretical and noise spectra. The two matrices involved are

$$\mathbf{X}^{ABCD}_{\ell_1\ell_2} = \frac{1}{2\ell_1+1}\frac{1}{2\ell_2+1}\sum_{m_1}\sum_{\ell_1' m_1'}\sum_{m_2}\sum_{\ell_2' m_2'} A^{m_1 m_1'}_{\ell_1\ \ell_1'} B^{*m_1 m_2'}_{\ell_1\ \ell_2'} C^{m_2 m_2'}_{\ell_2\ \ell_2'} D^{*m_2 m_1'}_{\ell_2\ \ell_1'} \tag{B.19}$$

and

$$\mathbf{Y}^{ABCD}_{\ell_1\ell_2} = \frac{1}{2\ell_1+1}\frac{1}{2\ell_2+1}\sum_{m_1}\sum_{\ell_1' m_1'}\sum_{m_2}\sum_{\ell_2' m_2'} A^{m_1 m_1'}_{\ell_1\ \ell_1'} B^{*m_1 m_2'}_{\ell_1\ \ell_2'} C^{*m_2 m_1'}_{\ell_2\ \ell_1'} D^{m_2 m_2'}_{\ell_2\ \ell_2'}. \tag{B.20}$$

In the case where $A = B = C = D$ (by which we mean that the four observables have the same mask), and only in that case, they reduce to symmetrized versions of the mixing matrix,

$$\mathbf{X}^{AAAA}_{\ell\ell'} = \mathbf{Y}^{AAAA}_{\ell\ell'} = \frac{1}{2\ell'+1}\mathbf{M}^{AA}_{\ell\ell'}. \tag{B.21}$$

As a by-product, we also obtain the variance of the full-sky spectrum, given by

$$\mathrm{Var}\Big(\hat{C}_\ell^{AB}\Big) = \frac{\Big(C_\ell^{AB}\Big)^2 + C_\ell^{AA} C_\ell^{BB}}{2\ell+1}. \tag{B.22}$$

B.2 On the distribution of the cross-power spectrum estimator

Let us consider the cross-power spectrum estimator

$$\hat{C}_\ell^{AB} = \frac{1}{2\ell+1} \sum_{m=-\ell}^{\ell} a_{\ell m} b_{\ell m}^* \tag{B.23}$$

where the multipoles are assumed to be normally distributed with zero mean and covariances

$$\big\langle a_{\ell m} a_{\ell' m'}^* \big\rangle = \delta_{\ell\ell'}\delta_{mm'} C_\ell^{AA}, \tag{B.24}$$
$$\big\langle a_{\ell m} b_{\ell' m'}^* \big\rangle = \delta_{\ell\ell'}\delta_{mm'} C_\ell^{AB}, \tag{B.25}$$
$$\big\langle b_{\ell m} b_{\ell' m'}^* \big\rangle = \delta_{\ell\ell'}\delta_{mm'} C_\ell^{BB}. \tag{B.26}$$

These are complex numbers (except for $m = 0$), so this means that their real and imaginary parts are independent and gaussian distributed with zero mean and variances divided by 2, such that, for $m \neq 0$,

$$\Big\langle \mathrm{Re}(a_{\ell m})^2 \Big\rangle = \Big\langle \mathrm{Im}(a_{\ell m})^2 \Big\rangle = \frac{C_\ell^{AA}}{2} \tag{B.27}$$
$$\Big\langle \mathrm{Re}(b_{\ell m})^2 \Big\rangle = \Big\langle \mathrm{Im}(b_{\ell m})^2 \Big\rangle = \frac{C_\ell^{BB}}{2} \tag{B.28}$$

and

$$\Big\langle \mathrm{Re}(a_{\ell m})\,\mathrm{Re}(b_{\ell m}) \Big\rangle = \Big\langle \mathrm{Im}(a_{\ell m})\,\mathrm{Im}(b_{\ell m}) \Big\rangle = \frac{C_\ell^{AB}}{2} \tag{B.29}$$
$$\Big\langle \mathrm{Re}(a_{\ell m})\,\mathrm{Im}(a_{\ell m}) \Big\rangle = \Big\langle \mathrm{Re}(b_{\ell m})\,\mathrm{Im}(b_{\ell m}) \Big\rangle = 0 \tag{B.30}$$
$$\Big\langle \mathrm{Re}(a_{\ell m})\,\mathrm{Im}(b_{\ell m}) \Big\rangle = \Big\langle \mathrm{Re}(b_{\ell m})\,\mathrm{Im}(a_{\ell m}) \Big\rangle = 0. \tag{B.31}$$

Therefore, the auto-power spectrum reads

$$\hat{C}_\ell^{AA} = \frac{1}{2\ell+1}\left[a_{\ell 0}^2 + \sum_{m=1}^{\ell}\Big(x_{\ell m}^2 + y_{\ell m}^2\Big)\right], \tag{B.32}$$

where $x_{\ell m} = \sqrt{2}\,\mathrm{Re}(a_{\ell m})$ and $y_{\ell m} = \sqrt{2}\,\mathrm{Im}(a_{\ell m})$, which is the sum of $2\ell+1$ indepen-

dent normal variables with mean 0 and variance C_ℓ^{AA}. Therefore,

$$V_\ell \equiv (2\ell+1)\frac{\hat{C}_\ell^{AA}}{C_\ell^{AA}} \tag{B.33}$$

follows a χ^2 distribution with $2\ell+1$ degrees of freedom, such that

$$p\left(\hat{C}_\ell^{AA}\right) = \frac{V_\ell^{\ell-1/2}e^{-V_\ell/2}}{2^{\ell+1/2}\Gamma\left(\ell+\frac{1}{2}\right)}. \tag{B.34}$$

Now, the situation is slightly different for cross-spectra (which may be negative). The estimator may be rewritten as

$$\hat{C}_\ell^{AB} = \frac{1}{2\ell+1}\left[a_{\ell 0}b_{\ell 0} + 2\sum_{m=1}^{\ell}\Big(\mathrm{Re}(a_{\ell m})\,\mathrm{Re}(b_{\ell m}) + \mathrm{Im}(a_{\ell m})\,\mathrm{Im}(b_{\ell m})\Big)\right] \tag{B.35}$$

$$= \frac{\sqrt{C_\ell^{AA}C_\ell^{BB}}}{2\ell+1}\sum_{m=-\ell}^{\ell} X_m Y_m \tag{B.36}$$

where

$$X_m = \frac{1}{\sqrt{C_\ell^{AA}}}\begin{cases} a_{\ell 0} & m=0, \\ \sqrt{2}\,\mathrm{Re}\{a_{\ell m}\} & m>0, \\ \sqrt{2}\,\mathrm{Im}\{a_{\ell -m}\} & m<0, \end{cases} \tag{B.37}$$

and similarly for Y_m with b's instead. This is the sum of the products of correlated, gaussian random variables with zero means and correlation coefficient

$$\rho \equiv C_\ell^{AB}\Big/\sqrt{C_\ell^{AA}C_\ell^{BB}}\,, \tag{B.38}$$

but independent for different values of m. The product $Z_m \equiv X_m Y_m$ has a probability density distribution given by (Nadarajah and Pogány 2016)

$$p(z) = \frac{1}{\pi\sqrt{1-\rho^2}}\exp\left[\frac{\rho z}{1-\rho^2}\right]K_0\left(\frac{|z|}{1-\rho^2}\right) \tag{B.39}$$

where $K_0(\cdot)$ denotes the modified Bessel function of second kind of order zero[1]. The distribution of the sum can be obtained by convolving this distribution $2\ell+1$ times with itself[2], and we conclude that the probability density function of the estimator $\hat{C}_\ell^{AB}$ is given by (see Nadarajah and Pogány 2016, as well)

$$p\left(\hat{C}_\ell^{AB}\right) = \frac{\rho}{C_\ell^{AB}}\frac{(2\ell+1)^{\ell+1}\left(|z|/2\right)^\ell}{\sqrt{\pi\left(1-\rho^2\right)}\Gamma\left(\ell+\frac{1}{2}\right)}\exp\left[\frac{\beta-\gamma}{2}z\right]K_{-\ell}\left(\frac{\beta+\gamma}{2}|z|\right) \tag{B.40}$$

[1] The proof uses the characteristic function, *i.e.* the Fourier transform of the density $\left\langle e^{itZ_m}\right\rangle$.

[2] Which, in Fourier space, is equivalent to taking the characteristic function to the power $2\ell+1$.

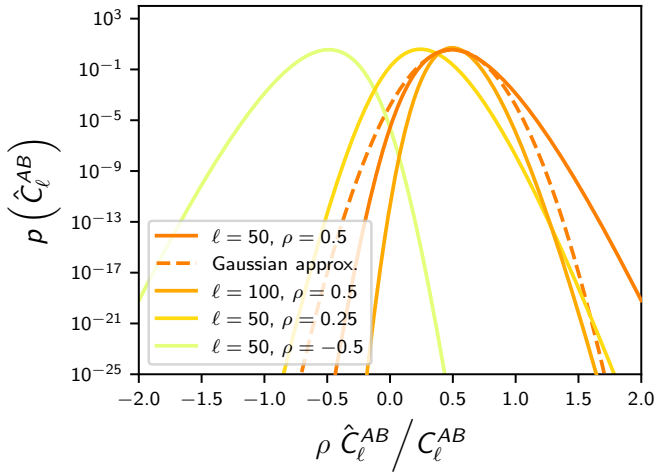

Figure B.1 – Probability density function of the cross-power spectrum estimator $\hat{C}_\ell^{AB}$ for a few values of ρ and ℓ. The Gaussian approximates the distribution for $\rho = 0.5$ and $\ell = 50$.

where $\beta = (2\ell+1)/(1-\rho)$, $\gamma = (2\ell+1)/(1+\rho)$ and $z = \rho\,\hat{C}_\ell^{AB} \Big/ C_\ell^{AB}$. It is plotted in figure B.1, has mean C_ℓ^{AB} and variance given by Equation (B.22).

APPENDIX C

The NumCosmo library

NumCosmo[1] contains a comprehensive set of tools to compute cosmological observables and to perform statistical analyses. The library is written in C, but since it uses the GObject framework[2], it is developed in a object-oriented fashion. Additionally, it has automatic bindings with every language that supports GObject introspection (*e.g.* Python, Ruby or Perl). Unless stated otherwise, all the plots in this manuscript were computed with NumCosmo in Python, using CLASS as a backend for perturbed quantities, when needed.

After a brief description of the library, I will detail the main modules and improvements that I coded during my PhD work, with help from Sandro Vitenti and Mariana Penna-Lima, the main developpers of NumCosmo. Additionally, I took part in many minor improvements, such as the creation of a Docker[3] image of NumCosmo to enable easy deployment in cloud computing infrastructures, which was used to run MCMCs at CC-IN2P3.

Philosophy The different modules of the library heavily rely on fast algorithms with controlled precision, implemented in well-tested libraries such as GSL[4], NLOpt[5], Sundials[6], FFTW[7], BLAS[8] and Lapack[9]. With the flexibility of object-oriented programming, the library allows the user to perform computations with end-to-end controlled precision.

[1] https://numcosmo.github.io/
[2] https://developer.gnome.org/gobject/stable/
[3] https://www.docker.com/
[4] https://www.gnu.org/software/gsl/
[5] http://ab-initio.mit.edu/nlopt
[6] https://computation.llnl.gov/projects/sundials
[7] http://www.fftw.org/
[8] Any implementation works, *e.g.* ATLAS (http://math-atlas.sourceforge.net/) or OpenBLAS (http://www.openblas.net/).
[9] http://www.netlib.org/lapack/

Structure The library contains two namespaces, `Ncm` and `Nc`, for, respectively, general-purpose mathematical functions and cosmology-specific objects. Physical models are implemented via the abstract class `NcmModel`. In particular, the ΛCDM and wCDM models, and all respective relevant functions are implemented in `NcHICosmoDE` and child classes (such as `NcHICosmoDEXcdm`), the primordial power spectrum is implemented in `NcHIPrim`, the reionization model in `NcHIReion`. Data objects deriving from the abstract class `NcmData` encapsulate observations and implement likelihood functions. A general object for statistical analysis `NcmFit` is then built from the data and the model.

Cosmological observables The library implements several cosmological probes. For each of those, it implements the computations of the cosmological quantities and a likelihood in separate objects. At the moment, it can be used to analyze distance observations from BAO and supernovæ and direct H_0 measurements. It also implements cluster-related observables (mass and redshift distributions), CMB temperature and polarization observations (via an interface with Planck likelihood codes, `Plik` and `Commander`), and, for the purpose of the work presented here, auto- and cross-correlations of projected observables, such as CMB lensing, galaxy density and galaxy lensing.

Statistical tools Besides standard mathematical tools, the library implement a number of statistical analysis facilities, which includes best-fit finders, Fisher matrix estimation (with adaptive numerical differentiation), Monte-Carlo analysis (which we used in section 6.4.3.3), Monte-Carlo bootstrap analysis, (ensemble) Markov chain Monte-Carlo analysis (described in appendix A.2.2.2), profile likelihood in 1 and 2D, and approximate bayesian computation.

The next sections describe two modules that I coded for the work presented in this thesis.

C.1 The `xcor` module

The `xcor` module addresses the computation of the theoretical angular power spectrum, C_ℓ^{AB}. At the moment, it implements the Limber approximation for any set of two probes, which is given by

$$C_\ell^{AB} = \int \mathrm{d}z \, \frac{H(z)}{c\chi(z)^2} W^A(z) W^B(z) P\left(k = \frac{\ell + 1/2}{\chi(z)}, z\right) + \mathcal{O}\left(\frac{1}{\ell^2}\right). \tag{C.1}$$

It is divided in several objects:

1. `NcXCor`: abstract class that comprises the methods to compute the auto and cross power spectra. It takes as input a distance object `NcDistance`, a power

spectrum object of the class `NcmPowSpec` and a cosmological model of the class `NcHICosmo`, all of which are easily interchangeable.

2. `NcXCorLimberKernel`: abstract class of the type `NcmModel`[10] which implements the kernel functions of the following probes:

   - `NcXCorLimberKernelCMBLensing` implements the CMB lensing kernel $W^{\kappa_{\rm CMB}}(z)$ from Equation (6.2);
   - `NcXCorLimberKernelGal` implements the galaxy density kernel, $W^{g}(z)$ from Equation (6.2), with a bias that can be constant or redshift dependent (modelled by a spline);
   - `NcXCorLimberKernelWeakLensing` implements the galaxy weak lensing kernel, $W^{\kappa_{\rm gal}}(z)$ from Equation (4.21).

   These objects also store the noise power spectrum of each probe.

3. `NcDataXCor`: this object builds the likelihood given by Equation (6.23) for an arbitrary number of probes, with arbitrary multipole ranges. It derives from `NcmDataGaussCov`, *i.e.*, the object that describes Gaussian-distributed data with non-diagonal covariance matrix. It performs the multiplications of the power spectra by the mixing matrices and takes care of the combinatorics amongst probes to form the covariance matrix.

All these objects are written so that they can be serialized (saved to hard disk), which enables easy and fast transfer of input data for MCMC runs.

There are two implemented methods to compute the angular power spectra with the Limber approximation. The first uses independent numerical integration for each multipole ℓ, which is performed by adaptative quadrature integration using the GSL function `gsl_integration_qag` with 61 Gauss-Kronrod rule[11]. However, this requires many calls to the functions evaluating the power spectrum and the kernels. The second methods makes use of the ordinary differential equation (ODE) solver `CVode` of the Sundials library. Since it can numerically integrate vector-valued ODE, we can integrate all the multipoles of the spectrum at once by defining the vector of

[10] Being a `NcmModel`, each implementation of `NcXCorLimberKernel` can define a respective set of parameters. For instance, the linear bias, $b(z)$, in Equation (6.3).

[11] Gaussian quadrature approximates integrals by a sum as

$$\int_a^b w(x) f(x)\,\mathrm{d}x \approx \sum_{i=1}^{n} w_i f(x_i),$$

where x_i are the roots of a polynomial of rank n, belonging to a class of polynomials that are orthogonal with respect to the inner product defined by the weight function $w(x)$, and w_i are the associated weights. This expression is exact if the function f is a polynomial of rank less than $2n-1$. The Gauss-Kronrod quadrature adds evaluation points, such that the scheme of evaluation points is self-nested (*i.e.* higher order quadratures use all evaluation points of lower order quadratures).

stacked spectra,

$$\boldsymbol{y} = \begin{pmatrix} C^{AB}_{\ell_{\min}} \\ \vdots \\ C^{AB}_{\ell_{\max}} \end{pmatrix}, \tag{C.2}$$

and integrating the system given by

$$\boldsymbol{y}'(z) = \begin{pmatrix} \dfrac{\mathrm{d}C^{AB}_{\ell_{\min}}}{\mathrm{d}z} \\ \vdots \\ \dfrac{\mathrm{d}C^{AB}_{\ell_{\max}}}{\mathrm{d}z} \end{pmatrix} = \frac{H(z)}{c\chi(z)^2} W^A(z) W^B(z) \begin{pmatrix} P\left(k = \dfrac{\ell_{\min}+1/2}{\chi(z)}, z\right) \\ \vdots \\ P\left(k = \dfrac{\ell_{\max}+1/2}{\chi(z)}, z\right) \end{pmatrix}. \tag{C.3}$$

This considerably reduces the number of evaluations of the `halofit` power spectrum at different redshifts (which is the slowest step). Profiling tests revealed that this increased speed of the integration by a factor of 10 (and up to 100 more after optimization of the evaluation of the power spectrum).

C.2 The `halofit` power spectrum

The `halofit` model was initially proposed by Smith *et al.* 2003, later corrected to include massive neutrinos (Bird *et al.* 2012) and updated on high-resolution N-body simulations (Takahashi *et al.* 2012). I implemented it in `NumCosmo` as an implementation of the abstract class of non-linear matter power spectrum `NcPowSpecMNL`.

The dimensionless power spectrum is given by the sum of a one-halo and a two-halo terms:

$$\Delta^2(k,z) \equiv \frac{k^3 P(k,z)}{2\pi^2} = \Delta^2_{\mathrm{Q}}(k,z) + \Delta^2_{\mathrm{H}}(k,z). \tag{C.4}$$

Here, we will drop the redshift dependence is the notation for readability, but all coefficients are redshift-dependent. The first step consists in computing the non-linear distance scale R_σ such that the variance of density fluctuations, $\sigma^2(R)$ (see section 1.4.3.2), is unity. The window function is gaussian, such that

$$\sigma^2(R) = \int \frac{k^2\,\mathrm{d}k}{2\pi^2} P(k) e^{-k^2R^2}. \tag{C.5}$$

We define the non-linear scale by $k_\sigma^{-1} = R_\sigma$. Additionally, we define the effective spectral index n_{eff} and the curvature C by

$$n_{\mathrm{eff}} = -3 - \left.\frac{\mathrm{d}\ln\sigma^2(R)}{\mathrm{d}\ln R}\right|_{R=R_\sigma} \quad \text{and} \quad C = -\left.\frac{\mathrm{d}^2\ln\sigma^2(R)}{\mathrm{d}\ln R^2}\right|_{R=R_\sigma}. \tag{C.6}$$

The variance $\sigma^2(R)$ and its derivatives can be computed by direct numerical integra-

tion, or more efficiently using FFTLog (Hamilton 2000), which is implemented in `NcmFFTLog`. The non-linear scale is the root of the function $f(\ln R) = \sigma^2(R) - 1$ and is determined by a root-finding algorithm using GSL's `gsl_root_fdfsolver`, which takes advantage of the easily computed derivatives of $\sigma^2(R)$ with respect to $\ln R$ to accelerate convergence towards the root. This method is more precise than the current implementations of `halofit` in `CLASS` or `CAMB`.

Instead of computing R_σ at each call of the evaluation function, a spline $R_\sigma(z)$ is prepared. `NumCosmo` implements an algorithm to automatically fill a spline given a required precision, which we use to automatically compute $R_\sigma(z)$ between $z = 0$ and some maximum redshift, usually $z = 10$, beyond which non-linear corrections are negligible.

The two-halo term is given by

$$\Delta^2_{\rm Q}(k) = \Delta^2_{\rm lin}(k) \left[\frac{\left(1 + \Delta^2_{{\rm lin},\nu}(k)\right)^\beta}{1 + \alpha \Delta^2_{{\rm lin},\nu}(k)} \right] e^{-f(y)}, \tag{C.7}$$

where $\Delta^2_{\rm lin}(k)$ is the dimensionless linear matter power spectrum, $y = k/k_\sigma$ and $f(y) = y/4 + y^2/8$. The linear matter power spectrum within the bracket term includes a correction related to massive neutrinos, written as

$$\Delta^2_{{\rm lin},\nu}(k) = \Delta^2_{\rm lin}(k) \left(1 + 47.48 f_{m_\nu} \frac{k_h^2}{1 + 1.5 k_h^2} \right), \tag{C.8}$$

where k_h^2 is k^2 expressed in $\left(h\,{\rm Mpc}^{-1}\right)^2$ and

$$f_{m_\nu} = \frac{\Omega_{m_\nu}(z)}{\Omega_{\rm m}(z)} \tag{C.9}$$

is the neutrino mass fraction.

The one-halo term is given by[12]

$$\Delta^2_{\rm H}(k) = \frac{\Delta'^2_{\rm H}(k)}{1 + \nu y^{-2}} \Big(1 + f_{m_\nu} \Big(0.977 - 18.015 (\Omega^0_{\rm m} - 0.3) \Big) \Big), \tag{C.10}$$

with

$$\Delta'^2_{\rm H}(k) = \frac{a y^{3 f_1}}{1 + b y^{f_2} + (c f_3 y)^{3-\gamma}} \tag{C.11}$$

[12]Note that we use the same parameters as in `CLASS`, which were updated by Simeon Bird, combining corrections for massive neutrinos and high-resolution simulations.

The parameters are given by

$$\begin{aligned}\log_{10} a = {} & 1.5222 + 2.8553 n_{\rm eff} + 2.3706 n_{\rm eff}^2 + 0.9903 n_{\rm eff}^3 + 0.2250 n_{\rm eff}^4 \\ & - 0.6038 C + 0.1749 \Omega_\Lambda (1 + w)\end{aligned} \tag{C.12}$$

$$\log_{10} b = -0.5642 + 0.5864 n_{\rm eff} + 0.5716 n_{\rm eff}^2 - 1.5474 C + 0.2279 \Omega_\Lambda (1 + w) \tag{C.13}$$

$$\log_{10} c = 0.3698 + 2.0404 n_{\rm eff} + 0.8161 n_{\rm eff}^2 + 0.5869 C \tag{C.14}$$

$$\gamma = 0.1971 - 0.0843 n_{\rm eff} + 0.8460 C \tag{C.15}$$

$$\alpha = \left| 6.0835 + 1.3373 n_{\rm eff} - 0.1959 n_{\rm eff}^2 - 5.5274 C \right| \tag{C.16}$$

$$\begin{aligned}\beta = {} & 2.0379 - 0.7354 n_{\rm eff} + 0.3157 n_{\rm eff}^2 + 1.2490 n_{\rm eff}^3 + 0.3980 n_{\rm eff}^4 \\ & - 0.1682 C + f_{m_\nu} (1.081 + 0.395 n_{\rm eff}^2)\end{aligned} \tag{C.17}$$

$$\log_{10} \nu = 5.2105 + 3.6902 n_{\rm eff} \tag{C.18}$$

$$\tag{C.19}$$

and

$$f_1 = f_\Lambda {\Omega_{\rm m}}^{-0.0307} + (1 - f_\Lambda) {\Omega_{\rm m}}^{-0.0732} \tag{C.20}$$

$$f_2 = f_\Lambda {\Omega_{\rm m}}^{-0.0585} + (1 - f_\Lambda) {\Omega_{\rm m}}^{-0.1423} \tag{C.21}$$

$$f_3 = f_\Lambda {\Omega_{\rm m}}^{0.0743} + (1 - f_\Lambda) {\Omega_{\rm m}}^{0.0725}. \tag{C.22}$$

where

$$f_\Lambda = \frac{\Omega_\Lambda(z)}{1 - \Omega_{\rm m}(z)} \tag{C.23}$$

is the fraction of the non-matter energy content which is dark energy.

APPENDIX D

Other numerical tools

This appendix describes two libraries heavily used for the work presented in this thesis. The `HEALPix` library offers facilities to visualize and analyze full-sky maps (all the maps shown in this manuscript use `HEALPix`) and the `CLASS` library implements a Boltzmann equations solver and provides estimations of CMB power spectrum C_ℓ^{TT} and the linear matter power spectrum.

D.1 `HEALPix`: spherical pixelization

`HEALPix`[1] is a C library that performs equal-area pixelization on the sphere, thus enabling the projection and visualization of digitized sky maps (Górski *et al.* 2005). The pixelization scheme has the following properties:

- pixels are curvilinear quadrilaterals with equal areas;
- the center of pixels are distributed along isolatitude rings;
- the pixelization is hierarchical, *i.e.* each pixel is divided into four smaller pixels when increasing the resolution parameter N_{side}.

Additionally, `HEALPix`, and its python wrapper `healpy`[2], implement fast spherical harmonics transform (FSHT), similar to the fast Fourier transform (FFT) in euclidian space, based on Muciaccia *et al.* 1997. The FFT accelerates the computation of the complex sum

$$X_k = \sum_{n=0}^{N_1} x_n e^{-\frac{2\pi i k n}{N}} \tag{D.1}$$

by using the decomposition in prime integers of N to decrease the number of evaluations of powers of $e^{-\frac{2\pi i}{N}}$. Similarly, FSHT is based on writing the function to be

[1] `http://healpix.sourceforge.net/`
[2] `https://healpy.readthedocs.io`

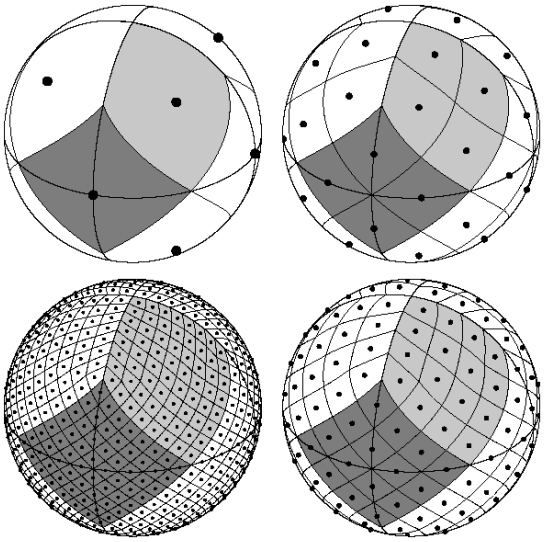

Figure D.1 – Pixelization of the sphere within `HEALPix` for resolution parameter $N_{\rm side} = 1, 2, 4$ and 8, corresponding to $N_{\rm pix} = 12, 48, 192$ and 768 pixels (in clockwise order, starting from top left). Figure from Górski *et al.* 2005.

evaluated as

$$A(\theta,\phi) = \sum_{\ell=0}^{\ell_{\rm max}} \sum_{m=-\ell}^{+\ell} a_{\ell m} Y_{\ell m}(\theta,\phi) = \sum_{m=-\ell_{\rm max}}^{+\ell_{\rm max}} b_m(\theta) e^{im\phi}, \tag{D.2}$$

where

$$b_m(\theta) = \sum_{\ell=|m|}^{\ell_{\rm max}} a_{\ell m} \lambda_\ell^m \tag{D.3}$$

is a function of latitude only. Therefore, at fixed latitude, the computation of the last sum in Equation (D.2) can be performed by means of an FFT. The λ_ℓ^m coefficients are given by

$$\lambda_\ell^m = \sqrt{\frac{2\ell+1}{4\pi}\frac{(l-m)!}{(l+m)!}} P_\ell^m(\cos\theta), \tag{D.4}$$

where P_ℓ^m are the associated Legendre polynomials, and can be evaluated analytically through a recurrence relation. The inverse transform, to obtain the multipole coefficients $a_{\ell m}$ from the map, is performed by noting that

$$b_m(\theta) = \int_0^{2\pi} A(\theta,\phi) e^{-im\phi}\,{\rm d}\phi\,, \tag{D.5}$$

which is the inverse Fourier transform of Equation (D.3), and then

$$a_{\ell m} = \int \lambda_\ell^m(\theta) b_m(\theta) \sin\theta\,{\rm d}\theta\,, \tag{D.6}$$

which, again, is computed by a recurrence relation.

These facilities can be used to evaluate multipole coefficients $a_{\ell m}$ and power spectra C_ℓ, to apply spatial filtering and to simulate full-sky maps (as done in section 6.4.3).

D.2 CLASS

The Cosmic Linear Anisotropy Solving System[3] (Blas *et al.* 2011) is a Boltzmann equations solver written in C. Perturbations of the densities and velocities of cosmic fluids (baryons, dark matter, neutrinos and photons) and perturbations of the space-time metric (parametrized by gravitational potentials) obey a set of linear, coupled equations, overviewed in Sections 1.4.2.3 and 2.1.6, and derived in Ma and Bertschinger 1995. `CLASS` derives from `CAMB` (Lewis *et al.* 2000), itself inspired from CMBFast (Seljak and Zaldarriaga 1996). All of these codes evolve the Boltzmann equations for an appropriate sample of Fourier modes k and compute the CMB power spectrum by line-of-sight integration of the temperature modes $\Theta_\ell^{(m)}(k,\eta)$ (see Equation (2.11)). These modes can be generically written as

$$\Theta_\ell^{(m)}(k,\eta_{\rm now}) = \int_0^{\eta_{\rm now}} S^{(m)}(k,\eta)\, j_\ell(k(\eta_{\rm now}-\eta))\,\mathrm{d}\eta\,, \tag{D.7}$$

where $S^{(m)}(k,\eta)$ is a source term depending on perturbed quantities and $j_\ell(x)$ are the spherical Bessel function. The source term is a slowly varying function of k depending on the cosmological model, while the Bessel function are independent of cosmology. Thus, numerical techniques can be applied to quickly compute this integral.

[3] `http://class-code.net/`

Bibliography

Abazajian, K. N. *et al.* (2016). CMB-S4 Science Book, First Edition. *arXiv.org*, arXiv:1610.02743. arXiv: 1610.02743 [1610].

Abdo, A. A. *et al.* (2010). Spectrum of the Isotropic Diffuse Gamma-Ray Emission Derived from First-Year Fermi Large Area Telescope Data. *Physical Review Letters*, 104.1, p. 101101. doi: 10.1103/PhysRevLett.104.101101.

Abramo, L. R., Secco, L. F. and Loureiro, A. (2016). Fourier analysis of multitracer cosmological surveys. *Monthly Notices of the Royal Astronomical Society*, 455.4, pp. 3871–3889. doi: 10.1093/mnras/stv2588.

Ade, P. A. R. *et al.* (2014). Evidence for Gravitational Lensing of the Cosmic Microwave Background Polarization from Cross-Correlation with the Cosmic Infrared Background. *Physical Review Letters*, 112.1, p. 131302. doi: 10.1103/PhysRevLett.112.131302.

Afshordi, N., McDonald, P. and Spergel, D. N. (2003). Primordial Black Holes as Dark Matter: The Power Spectrum and Evaporation of Early Structures. *The Astrophysical Journal Letters*, 594.2, pp. L71–L74. doi: 10.1086/378763.

Afshordi, N., Loh, Y.-S. and Strauss, M. A. (2004). Cross-correlation of the cosmic microwave background with the 2MASS galaxy survey: Signatures of dark energy, hot gas, and point sources. *Physical Review D*, 69.8, p. 083524. doi: 10.1103/PhysRevD.69.083524.

Ajello, M. *et al.* (2015). The Origin of the Extragalactic Gamma-Ray Background and Implications for Dark Matter Annihilation. *The Astrophysical Journal Letters*, 800.2, p. L27. doi: 10.1088/2041-8205/800/2/L27.

Alam, S. *et al.* (2017). The clustering of galaxies in the completed SDSS-III Baryon Oscillation Spectroscopic Survey: cosmological analysis of the DR12 galaxy sample. *Monthly Notices of the Royal Astronomical Society*, 470.3, pp. 2617–2652. doi: 10.1093/mnras/stx721.

Alcock, C. and Paczynski, B. (1979). An evolution free test for non-zero cosmological constant. *Nature*, 281, pp. 358–. doi: 10.1038/281358a0.

Allison, R. *et al.* (2015). The Atacama Cosmology Telescope: measuring radio galaxy bias through cross-correlation with lensing. *Monthly Notices of the Royal Astronomical Society*, 451.1, pp. 849–858. doi: 10.1093/mnras/stv991.

Alonso, D. and Ferreira, P. G. (2015). Constraining ultralarge-scale cosmology with multiple tracers in optical and radio surveys. *Physical Review D*, 92.6, p. 063525. doi: 10.1103/PhysRevD.92.063525.

Alonso, D. *et al.* (2015). Ultra-large-scale Cosmology in Next-generation Experiments with Single Tracers. *The Astrophysical Journal*, 814.2, p. 145. doi: 10.1088/0004-637X/814/2/145.

Alpher, R. A., Bethe, H. and Gamow, G. (1948). The Origin of Chemical Elements. *Physical Review*, 73.7, pp. 803–804. doi: 10.1103/PhysRev.73.803.

Andersen, R. (2015). *Will we ever understand the beginning of the universe?*

Anderson, L. *et al.* (2012). The clustering of galaxies in the SDSS-III Baryon Oscillation Spectroscopic Survey: baryon acoustic oscillations in the Data Release 9 spectroscopic galaxy sample. *Monthly Notices of the Royal Astronomical Society*, 427.4, pp. 3435–3467. doi: 10.1111/j.1365-2966.2012.22066.x.

Anderson, L. *et al.* (2014). The clustering of galaxies in the SDSS-III Baryon Oscillation Spectroscopic Survey: baryon acoustic oscillations in the Data Releases 10 and 11 Galaxy samples. *Monthly Notices of the Royal Astronomical Society*, 441.1, pp. 24–62. doi: 10.1093/mnras/stu523.

Arinyo-i-Prats, A. *et al.* (2015). The non-linear power spectrum of the Lyman alpha forest. *Journal of Cosmology and Astroparticle Physics*, 12.1, pp. 017–017. doi: 10.1088/1475-7516/2015/12/017.

Arnold, K. *et al.* (2014). "The Simons Array: expanding POLARBEAR to three multi-chroic telescopes". In: *Proceedings of the SPIE*. Univ. of California, San Diego (United States), 91531F. doi: 10.1117/12.2057332.

Ashby, M. L. N. *et al.* (2009). The Spitzer Deep, Wide-field Survey. *The Astrophysical Journal*, 701.1, pp. 428–453. doi: 10.1088/0004-637X/701/1/428.

Aubourg, E. *et al.* (2015). Cosmological implications of baryon acoustic oscillation measurements. *Physical Review D*, 92.1, p. 123516. doi: 10.1103/PhysRevD.92.123516.

Baldauf, T. *et al.* (2016a). Linear response to long wavelength fluctuations using curvature simulations. *Journal of Cosmology and Astroparticle Physics*, 09.0, pp. 007–007. doi: 10.1088/1475-7516/2016/09/007.

Baldauf, T. *et al.* (2016b). LSS constraints with controlled theoretical uncertainties. arXiv: 1602.00674.

Bartelmann, M. and Schneider, P. (2001). Weak gravitational lensing. *Physics Reports*, 340.4, pp. 291–472. doi: 10.1016/S0370-1573(00)00082-X.

Bassett, B. A. and Hlozek, R. (2009). Baryon Acoustic Oscillations. *arXiv.org*, arXiv:0910.5224. arXiv: 0910.5224 [0910].

Baumann, D. (2015). *Cosmology*. Part III Mathematical Tripos.

Bautista, J. E. *et al.* (2017). Measurement of baryon acoustic oscillation correlations at z = 2.3 with SDSS DR12 Lyα-Forests. *Astronomy & Astrophysics*, 603, A12. doi: 10.1051/0004-6361/201730533.

Baxter, E. *et al.* (2016). Joint measurement of lensing-galaxy correlations using SPT and DES SV data. *Monthly Notices of the Royal Astronomical Society*, 461.4, pp. 4099–4114. doi: 10.1093/mnras/stw1584.

Becker, G. D., Rauch, M. and Sargent, W. L. W. (2007). The Evolution of Optical Depth in the Lyα Forest: Evidence Against Reionization at z 6. *The Astrophysical Journal*, 662.1, pp. 72–93. doi: 10.1086/517866.

Becker, G. D. *et al.* (2015). Evidence of patchy hydrogen reionization from an extreme Lyα trough below redshift six. *Monthly Notices of the Royal Astronomical Society*, 447.4, pp. 3402–3419. doi: 10.1093/mnras/stu2646.

Becker, R. H., White, R. L. and Helfand, D. J. (1995). The FIRST Survey: Faint Images of the Radio Sky at Twenty Centimeters. *Astrophysical Journal v.450*, 450, pp. 559–. doi: 10.1086/176166.

Bennett, C. L. *et al.* (2003). First-Year Wilkinson Microwave Anisotropy Probe (WMAP) Observations: Preliminary Maps and Basic Results. *The Astrophysical Journal Supplement Series*, 148.1, pp. 1–27. doi: 10.1086/377253.

Bernardeau, F. *et al.* (2002). Large-scale structure of the Universe and cosmological perturbation theory. *Physics Reports*, 367.1, pp. 1–248. doi: 10.1016/S0370-1573(02)00135-7.

Bersanelli, M. *et al.* (2010). Planck pre-launch status: Design and description of the Low Frequency Instrument. *Astronomy & Astrophysics*, 520, A4. doi: 10.1051/0004-6361/200912853.

Beutler, F. *et al.* (2017). The clustering of galaxies in the completed SDSS-III Baryon Oscillation Spectroscopic Survey: baryon acoustic oscillations in the Fourier space. *Monthly Notices of the Royal Astronomical Society*, 464.3, pp. 3409–3430. doi: 10.1093/mnras/stw2373.

Bianchini, F. *et al.* (2015). Cross-correlation between the CMB Lensing Potential Measured by Planck and High-z Submillimeter Galaxies Detected by the Herschel-Atlas Survey. *The Astrophysical Journal*, 802.1, p. 64. doi: 10.1088/0004-637X/802/1/64.

Bianchini, F. *et al.* (2016). Toward a Tomographic Analysis of the Cross-Correlation between Planck CMB Lensing and H-ATLAS Galaxies. *The Astrophysical Journal*, 825.1, p. 24. doi: 10.3847/0004-637X/825/1/24.

Bird, S., Viel, M. and Haehnelt, M. G. (2012). Massive neutrinos and the non-linear matter power spectrum. *Monthly Notices of the Royal Astronomical Society*, 420.3, pp. 2551–2561. doi: 10.1111/j.1365-2966.2011.20222.x.

Birkinshaw, M. (1999). The Sunyaev-Zel'dovich effect. *Physics Reports*, 310.2, pp. 97–195. doi: 10.1016/S0370-1573(98)00080-5.

Blake, C. *et al.* (2016). RCSLenS: testing gravitational physics through the cross-correlation of weak lensing and large-scale structure. *Monthly Notices of the Royal Astronomical Society*, 456.3, pp. 2806–2828. doi: 10.1093/mnras/stv2875.

Blanton, M. R. *et al.* (2003). An Efficient Targeting Strategy for Multiobject Spectrograph Surveys: the Sloan Digital Sky Survey "Tiling" Algorithm. *The Astronomical Journal*, 125.4, pp. 2276–2286. doi: 10.1086/344761.

Blanton, M. R. *et al.* (2017). Sloan Digital Sky Survey IV: Mapping the Milky Way, Nearby Galaxies, and the Distant Universe. *The Astronomical Journal*, 154.1, p. 28. doi: 10.3847/1538-3881/aa7567.

Blas, D., Lesgourgues, J. and Tram, T. (2011). The Cosmic Linear Anisotropy Solving System (CLASS). Part II: Approximation schemes. *Journal of Cosmology and Astroparticle Physics*, 07.0, p. 034. doi: 10.1088/1475-7516/2011/07/034.

Blaustein, R. (0015). *Craft astrophysics*.

Bleem, L. E. *et al.* (2012). A Measurement of the Correlation of Galaxy Surveys with CMB Lensing Convergence Maps from the South Pole Telescope. *The Astrophysical Journal Letters*, 753.1, p. L9. doi: 10.1088/2041-8205/753/1/L9.

Blomqvist, M. *et al.* (2015). Broadband distortion modeling in Lyman-α forest BAO fitting. *Journal of Cosmology and Astroparticle Physics*, 11.1, pp. 034–034. doi: 10.1088/1475-7516/2015/11/034.

Bolton, A. S. *et al.* (2012). Spectral Classification and Redshift Measurement for the SDSS-III Baryon Oscillation Spectroscopic Survey. *The Astronomical Journal*, 144.5, p. 144. doi: 10.1088/0004-6256/144/5/144.

Bonvin, C. and Durrer, R. (2011). What galaxy surveys really measure. *Physical Review D*, 84.6, p. 063505. doi: 10.1103/PhysRevD.84.063505.

Bonvin, V. *et al.* (2017). H0LiCOW - V. New COSMOGRAIL time delays of HE 0435-1223: H0 to 3.8 per cent precision from strong lensing in a flat ΛCDM model. *Monthly Notices of the Royal Astronomical Society*, 465.4, pp. 4914–4930. doi: 10.1093/mnras/stw3006.

Borde, A. *et al.* (2014). New approach for precise computation of Lyman-α forest power spectrum with hydrodynamical simulations. *Journal of Cosmology and Astroparticle Physics*, 07.0, pp. 005–005. doi: 10.1088/1475-7516/2014/07/005.

Boughn, S. P. and Crittenden, R. G. (2001). Cross Correlation of the Cosmic Microwave Background with Radio Sources: Constraints on an Accelerating Universe. *Physical Review Letters*, 88.2, p. 021302. doi: 10.1103/PhysRevLett.88.021302.

Boulade, O. *et al.* (2002). "MegaCam: the new Canada-France-Hawaii Telescope wide-field imaging camera". In: *Astronomical Telescopes and Instrumentation*. Ed. by M. Iye and A. F. M. Moorwood. SPIE, p. 72. doi: 10.1117/12.459890.

Bovy, J. *et al.* (2011). Think Outside the Color Box: Probabilistic Target Selection and the SDSS-XDQSO Quasar Targeting Catalog. *The Astrophysical Journal*, 729.2, p. 141. doi: 10.1088/0004-637X/729/2/141.

Bridle, S. *et al.* (2009). Handbook for the GREAT08 Challenge: An image analysis competition for cosmological lensing. *Annals of Applied Statistics*, 3, pp. 6–37. doi: 10.1214/08-AOAS222.

Brooks, S. P. and Gelman, A. (2012). General Methods for Monitoring Convergence of Iterative Simulations. *Journal of Computational and Graphical Statistics*, 7.4, pp. 434–455. doi: 10.1080/10618600.1998.10474787.

Brown, M. L., Castro, P. G. and Taylor, A. N. (2005). Cosmic microwave background temperature and polarization pseudo-Cl estimators and covariances. *Monthly Notices of the Royal Astronomical Society*, 360.4, pp. 1262–1280. doi: 10.1111/j.1365-2966.2005.09111.x.

Busca, N. G. *et al.* (2013). Baryon acoustic oscillations in the Lyα forest of BOSS quasars. *Astronomy & Astrophysics*, 552, A96. doi: 10.1051/0004-6361/201220724.

Cabré, A. *et al.* (2006). Cross-correlation of Wilkinson Microwave Anisotropy Probe third-year data and the Sloan Digital Sky Survey DR4 galaxy survey: new evidence for dark energy. *Monthly Notices of the Royal Astronomical Society: Letters*, 372.1, pp. L23–L27. doi: 10.1111/j.1745-3933.2006.00218.x.

Cai, Y.-C. and Bernstein, G. (2012). Combining weak-lensing tomography and spectroscopic redshift surveys. *Monthly Notices of the Royal Astronomical Society*, 422.2, pp. 1045–1056. doi: 10.1111/j.1365-2966.2012.20676.x.

Calabrese, M. *et al.* (2015). Multiple lensing of the cosmic microwave background anisotropies. *Journal of Cosmology and Astroparticle Physics*, 03.0, p. 049. doi: 10.1088/1475-7516/2015/03/049.

Campagne, J. E., Neveu, J. and Plaszczynski, S. (2017). Angpow: a software for the fast computation of accurate tomographic power spectra. *Astronomy & Astrophysics*, 602, A72. doi: 10.1051/0004-6361/201730399.

Carlstrom, J. E. *et al.* (2011). The 10 Meter South Pole Telescope. *Publications of the Astronomical Society of Pacific*, 123.9, pp. 568–. doi: 10.1086/659879.

Carron, J. (2013). On the assumption of Gaussianity for cosmological two-point statistics and parameter dependent covariance matrices. *Astronomy & Astrophysics*, 551, A88. doi: 10.1051/0004-6361/201220538.

Casas, S. *et al.* (2017). Linear and non-linear Modified Gravity forecasts with future surveys. arXiv: 1703.01271.

Challinor, A. and Lewis, A. (2011). Linear power spectrum of observed source number counts. *Physical Review D*, 84.4, p. 043516. doi: 10.1103/PhysRevD.84.043516.

Chang, C. *et al.* (2016). Galaxy bias from the Dark Energy Survey Science Verification data: combining galaxy density maps and weak lensing maps. *Monthly Notices of the Royal Astronomical Society*, 459.3, pp. 3203–3216. doi: 10.1093/mnras/stw861.

Chiang, C.-T. and Slosar, A. (n.d.). "The Lyman-α power spectrum - CMB lensing convergence cross-correlation ".

Chiang, C.-T. *et al.* (2014). Position-dependent power spectrum of the large-scale structure: a novel method to measure the squeezed-limit bispectrum. *Journal of Cosmology and Astroparticle Physics*, 05.0, p. 048. doi: 10.1088/1475-7516/2014/05/048.

Chiang, C.-T. *et al.* (2015). Position-dependent correlation function from the SDSS-III Baryon Oscillation Spectroscopic Survey Data Release 10 CMASS sample. *Journal of Cosmology and Astroparticle Physics*, 09.0, pp. 028–028. doi: 10.1088/1475-7516/2015/09/028.

Chiang, C.-T. *et al.* (2017). Response approach to the squeezed-limit bispectrum: application to the correlation of quasar and Lyman-α forest power spectrum. *Journal of Cosmology and Astroparticle Physics*, 06.0, pp. 022–022. doi: 10.1088/1475-7516/2017/06/022.

Chisari, N. E. and Dvorkin, C. (2013). Cosmological information in the intrinsic alignments of luminous red galaxies. *Journal of Cosmology and Astroparticle Physics*, 12.1, p. 029. doi: 10.1088/1475-7516/2013/12/029.

Cieplak, A. M. and Slosar, A. (2016). Towards physics responsible for large-scale Lyman-α forest bias parameters. *Journal of Cosmology and Astroparticle Physics*, 03.0, pp. 016–016. doi: 10.1088/1475-7516/2016/03/016.

Cohn, J. D. *et al.* (2016). Combining galaxy and 21-cm surveys. *Monthly Notices of the Royal Astronomical Society*, 457.2, pp. 2068–2077. doi: 10.1093/mnras/stw108.

Condon, J. J. *et al.* (1998). The NRAO VLA Sky Survey. *The Astronomical Journal*, 115.5, pp. 1693–1716. doi: 10.1086/300337.

Conley, A. *et al.* (2011). Supernova Constraints and Systematic Uncertainties from the First Three Years of the Supernova Legacy Survey. *The Astrophysical Journal Supplement*, 192.1, p. 1. doi: 10.1088/0067-0049/192/1/1.

Cooray, A. and Sheth, R. (2002). Halo models of large scale structure. *Physics Reports*, 372.1, pp. 1–129. doi: 10.1016/S0370-1573(02)00276-4.

Crittenden, R. G. and Turok, N. (1996). Looking for a Cosmological Constant with the Rees-Sciama Effect. *Physical Review Letters*, 76.4, pp. 575–578. doi: 10.1103/PhysRevLett.76.575.

Crocce, M. and Scoccimarro, R. (2006). Renormalized cosmological perturbation theory. *Physical Review D*, 73.6, p. 063519. doi: 10.1103/PhysRevD.73.063519.

Croft, R. A. C., Banday, A. J. and Hernquist, L. (2006). Lyman α forest-CMB cross-correlation and the search for the ionized baryons at high redshift. *Monthly Notices of the Royal Astronomical Society*, 369.3, pp. 1090–1102. doi: 10.1111/j.1365-2966.2006.10292.x.

Croft, R. A. C. *et al.* (1998). Recovery of the Power Spectrum of Mass Fluctuations from Observations of the Lyα Forest. *The Astrophysical Journal*, 495.1, pp. 44–62. DOI: 10.1086/305289.

Cuesta, A. J. *et al.* (2016). The clustering of galaxies in the SDSS-III Baryon Oscillation Spectroscopic Survey: baryon acoustic oscillations in the correlation function of LOWZ and CMASS galaxies in Data Release 12. *Monthly Notices of the Royal Astronomical Society*, 457.2, pp. 1770–1785. DOI: 10.1093/mnras/stw066.

Cuoco, A. *et al.* (2015). Dark Matter Searches in the Gamma-ray Extragalactic Background via Cross-correlations with Galaxy Catalogs. *The Astrophysical Journal Supplement Series*, 221.2, p. 29. DOI: 10.1088/0067-0049/221/2/29.

Cyr-Racine, F.-Y. *et al.* (2016). Dark census: Statistically detecting the satellite populations of distant galaxies. *Physical Review D*, 94.4, p. 043505. DOI: 10.1103/PhysRevD.94.043505.

Dark Energy Survey Collaboration *et al.* (2016). The Dark Energy Survey: more than dark energy - an overview. *Monthly Notices of the Royal Astronomical Society*, 460.2, pp. 1270–1299. DOI: 10.1093/mnras/stw641.

Dawson, K. S. *et al.* (2013). The Baryon Oscillation Spectroscopic Survey of SDSS-III. *The Astronomical Journal*, 145.1, p. 10. DOI: 10.1088/0004-6256/145/1/10.

Delubac, T. *et al.* (2015). Baryon acoustic oscillations in the Lyα forest of BOSS DR11 quasars. *Astronomy & Astrophysics*, 574, A59. DOI: 10.1051/0004-6361/201423969.

Demetroullas, C. and Brown, M. L. (2016). Cross-correlation cosmic shear with the SDSS and VLA FIRST surveys. *Monthly Notices of the Royal Astronomical Society*, 456.3, pp. 3100–3118. DOI: 10.1093/mnras/stv2876.

DES Collaboration *et al.* (2017). Dark Energy Survey Year 1 Results: Cosmological Constraints from Galaxy Clustering and Weak Lensing. arXiv: 1708.01530.

Desjacques, V., Jeong, D. and Schmidt, F. (2016). Large-Scale Galaxy Bias. *arXiv.org*, arXiv:1611.09787. arXiv: 1611.09787 [1611].

Di Dio, E. *et al.* (2013). The CLASSgal code for relativistic cosmological large scale structure. *Journal of Cosmology and Astroparticle Physics*, 11.1, pp. 044–044. DOI: 10.1088/1475-7516/2013/11/044.

Dicke, R. H. *et al.* (1965). Cosmic Black-Body Radiation. *The Astrophysical Journal*, 142, pp. 414–419. DOI: 10.1086/148306.

Diego, J. M., Silk, J. and Sliwa, W. (2003). The Sunyaev-Zel'dovich effect contribution to WMAP: a cross-correlation between WMAP and ROSAT. *Monthly Notices of the Royal Astronomical Society*, 346.3, pp. 940–948. DOI: 10.1111/j.1365-2966.2003.07150.x.

DiPompeo, M. A. *et al.* (2015). Weighing obscured and unobscured quasar hosts with the cosmic microwave background. *Monthly Notices of the Royal Astronomical Society*, 446.4, pp. 3492–3501. DOI: 10.1093/mnras/stu2341.

Dirian, Y. *et al.* (2016). Non-local gravity and comparison with observational datasets. II. Updated results and Bayesian model comparison with ΛCDM. *Journal of Cosmology and Astroparticle Physics*, 05.0, pp. 068–068. DOI: 10.1088/1475-7516/2016/05/068.

Dodelson, S. (2003). *Modern Cosmology*. Academic Press.

Doux, C. *et al.* (2016). First detection of cosmic microwave background lensing and Lyman-α forest bispectrum. *Physical Review D*, 94.1, p. 103506. DOI: 10.1103/PhysRevD.94.103506.

Doux, C. *et al.* (2017). Cosmological constraints from a joint analysis of cosmic microwave background and large-scale structure. *arXiv.org*, arXiv:1706.04583. arXiv: 1706.04583 [1706].

Driver, S. P. *et al.* (2009). GAMA: towards a physical understanding of galaxy formation. *Astronomy & Geophysics*, 50.5, pp. 5.12–5.19. doi: 10.1111/j.1468-4004.2009.50512.x.

Eales, S. *et al.* (2010). The Herschel ATLAS. *Publications of the Astronomical Society of Pacific*, 122.8, pp. 499–. doi: 10.1086/653086.

Efstathiou, G. (2004). Myths and truths concerning estimation of power spectra: the case for a hybrid estimator. *Monthly Notices of the Royal Astronomical Society*, 349.2, pp. 603–626. doi: 10.1111/j.1365-2966.2004.07530.x.

Eftekharzadeh, S. *et al.* (2015). Clustering of intermediate redshift quasars using the final SDSS III-BOSS sample. *Monthly Notices of the Royal Astronomical Society*, 453.3, pp. 2779–2798. doi: 10.1093/mnras/stv1763.

Einstein, A. (1916). Die Grundlage der allgemeinen Relativitätstheorie. *Annalen der Physik*, 354.7, pp. 769–822. doi: 10.1002/andp.19163540702.

Eisenstein, D. J., Seo, H.-J. and White, M. (2007). On the Robustness of the Acoustic Scale in the Low-Redshift Clustering of Matter. *The Astrophysical Journal*, 664.2, pp. 660–674. doi: 10.1086/518755.

Eisenstein, D. J. *et al.* (2005). Detection of the Baryon Acoustic Peak in the Large-Scale Correlation Function of SDSS Luminous Red Galaxies. *The Astrophysical Journal*, 633.2, pp. 560–574. doi: 10.1086/466512.

Eisenstein, D. J. *et al.* (2011). SDSS-III: Massive Spectroscopic Surveys of the Distant Universe, the Milky Way, and Extra-Solar Planetary Systems. *The Astronomical Journal*, 142.3, p. 72. doi: 10.1088/0004-6256/142/3/72.

Ellis, G. F. R., Maartens, R. and MacCallum, M. A. H. (2012). *Relativistic Cosmology*. Cambridge University Press.

Elsner, F., Leistedt, B. and Peiris, H. V. (2017). Unbiased pseudo-Cℓ power spectrum estimation with mode projection. *Monthly Notices of the Royal Astronomical Society*, 465.2, pp. 1847–1855. doi: 10.1093/mnras/stw2752.

Fabbian, G., Calabrese, M. and Carbone, C. (2017). CMB weak-lensing beyond the Born approximation: a numerical approach. *arXiv.org*, arXiv:1702.03317. arXiv: 1702.03317 [1702].

Feldman, H. A., Kaiser, N. and Peacock, J. A. (1994). Power-spectrum analysis of three-dimensional redshift surveys. *The Astrophysical Journal*, 426, pp. 23–37. doi: 10.1086/174036.

Ferraro, S. *et al.* (2016). Kinematic Sunyaev-Zel'dovich effect with projected fields. II. Prospects, challenges, and comparison with simulations. *Physical Review D*, 94.1, p. 123526. doi: 10.1103/PhysRevD.94.123526.

Feynman, R. P. (1942). *Feynman's Thesis*. Ed. by L. M. Brown. A New Approach to Quantum Theory. World Scientific. doi: 10.1142/5852.

Fixsen, D. J. *et al.* (1996). The Cosmic Microwave Background Spectrum from the Full COBE FIRAS Data Set. *Astrophysical Journal v.473*, 473.2, pp. 576–. doi: 10.1086/178173.

Font-Ribera, A. *et al.* (2013). The large-scale quasar-Lyman α forest cross-correlation from BOSS. *Journal of Cosmology and Astroparticle Physics*, 05.0, pp. 018–018. doi: 10.1088/1475-7516/2013/05/018.

Font-Ribera, A. *et al.* (2014). Quasar-Lyman α forest cross-correlation from BOSS DR11: Baryon Acoustic Oscillations. *Journal of Cosmology and Astroparticle Physics*, 05.0, pp. 027–027. doi: 10.1088/1475-7516/2014/05/027.

Fornengo, N. *et al.* (2015). Evidence of Cross-correlation between the CMB Lensing and the γ-Ray Sky. *The Astrophysical Journal Letters*, 802.1, p. L1. doi: 10.1088/2041-8205/802/1/L1.

Fosalba, P., Gaztañaga, E. and Castander, F. J. (2003). Detection of the Integrated Sachs-Wolfe and Sunyaev-Zeldovich Effects from the Cosmic Microwave Background-Galaxy Correlation. *The Astrophysical Journal*, 597.2, pp. L89–L92. doi: 10.1086/379848.

Furlanetto, S. R., Oh, S. P. and Briggs, F. H. (2006). Cosmology at low frequencies: The 21 cm transition and the high-redshift Universe. *Physics Reports*, 433.4, pp. 181–301. doi: 10.1016/j.physrep.2006.08.002.

Gaztañaga, E. *et al.* (2012). Cross-correlation of spectroscopic and photometric galaxy surveys: cosmology from lensing and redshift distortions. *Monthly Notices of the Royal Astronomical Society*, 422.4, pp. 2904–2930. doi: 10.1111/j.1365-2966.2012.20613.x.

Geach, J. E. *et al.* (2013). A Direct Measurement of the Linear Bias of Mid-infrared-selected Quasars at z $\approx$ 1 Using Cosmic Microwave Background Lensing. *The Astrophysical Journal Letters*, 776.2, p. L41. doi: 10.1088/2041-8205/776/2/L41.

Gelman, A. and Rubin, D. B. (1992). Inference from Iterative Simulation Using Multiple Sequences. *Statistical Science*, 7.4, pp. 457–472. doi: 10.2307/2246093?ref=search-gateway:fed5b504da1f4fd0e68819a098155134.

Giannantonio, T. and Percival, W. J. (2014). Using correlations between cosmic microwave background lensing and large-scale structure to measure primordial non-Gaussianity. *Monthly Notices of the Royal Astronomical Society: Letters*, 441.1, pp. L16–L20. doi: 10.1093/mnrasl/slu036.

Giannantonio, T. *et al.* (2016). CMB lensing tomography with the DES Science Verification galaxies. *Monthly Notices of the Royal Astronomical Society*, 456.3, pp. 3213–3244. doi: 10.1093/mnras/stv2678.

Gilbank, D. G. *et al.* (2011). The Red-sequence Cluster Survey-2 (RCS-2): Survey Details and Photometric Catalog Construction. *The Astronomical Journal*, 141.3, p. 94. doi: 10.1088/0004-6256/141/3/94.

Gil-Marìn, H. *et al.* (2015a). The power spectrum and bispectrum of SDSS DR11 BOSS galaxies - I. Bias and gravity. *Monthly Notices of the Royal Astronomical Society*, 451.1, pp. 539–580. doi: 10.1093/mnras/stv961.

Gil-Marìn, H. *et al.* (2015b). The power spectrum and bispectrum of SDSS DR11 BOSS galaxies - II. Cosmological interpretation. *Monthly Notices of the Royal Astronomical Society*, 452.2, pp. 1914–1921. doi: 10.1093/mnras/stv1359.

Gil-Marìn, H. *et al.* (2016). The clustering of galaxies in the SDSS-III Baryon Oscillation Spectroscopic Survey: RSD measurement from the LOS-dependent power spectrum of DR12 BOSS galaxies. *Monthly Notices of the Royal Astronomical Society*, 460.4, pp. 4188–4209. doi: 10.1093/mnras/stw1096.

Gil-Marìn, H. *et al.* (2017). The clustering of galaxies in the SDSS-III Baryon Oscillation Spectroscopic Survey: RSD measurement from the power spectrum and bispectrum of the DR12 BOSS galaxies. *Monthly Notices of the Royal Astronomical Society*, 465.2, pp. 1757–1788. doi: 10.1093/mnras/stw2679.

Gleyzes, J. *et al.* (2016). Effective theory of dark energy at redshift survey scales. *Journal of Cosmology and Astroparticle Physics*, 02.0, p. 056. doi: 10.1088/1475-7516/2016/02/056.

Goodman, J. and Weare, J. (2010). Ensemble samplers with affine invariance. *Communications in Applied Mathematics and Computational Science*, 5.1, pp. 65–80. doi: 10.2140/camcos.2010.5.65.

Górski, K. M. *et al.* (2005). HEALPix: A Framework for High-Resolution Discretization and Fast Analysis of Data Distributed on the Sphere. *The Astrophysical Journal*, 622.2, pp. 759–771. doi: 10.1086/427976.

Gourgoulhon, E. (2013). *Relativité générale*. luth.obspm.fr.

Griffin, M. J. *et al.* (2010). The Herschel-SPIRE instrument and its in-flight performance. *Astronomy & Astrophysics*, 518, p. L3. doi: 10.1051/0004-6361/201014519.

Gross, D. J. and Wilczek, F. (1973). Ultraviolet Behavior of Non-Abelian Gauge Theories. *Physical Review Letters*, 30.2, pp. 1343–1346. doi: 10.1103/PhysRevLett.30.1343.

Gunn, J. E. and Knapp, G. R. (1993). "The Sloan Digital Sky Survey". In: *Sky Surveys. Protostars to Protogalaxies. Proceedings of a Conference in Honor of Gerry Neugebauer*, pp. 267–.

Gunn, J. E. *et al.* (1998). The Sloan Digital Sky Survey Photometric Camera. *The Astronomical Journal*, 116.6, pp. 3040–3081. doi: 10.1086/300645.

Gunn, J. E. and Peterson, B. A. (1965). On the Density of Neutral Hydrogen in Intergalactic Space. *Astrophysical Journal*, 142, pp. 1633–1641. doi: 10.1086/148444.

Gunn, J. E. *et al.* (2006). The 2.5 m Telescope of the Sloan Digital Sky Survey. *The Astronomical Journal*, 131.4, pp. 2332–2359. doi: 10.1086/500975.

Hall, A. and Taylor, A. (2014). Intrinsic alignments in the cross-correlation of cosmic shear and cosmic microwave background weak lensing. *Monthly Notices of the Royal Astronomical Society: Letters*, 443.1, pp. L119–L123. doi: 10.1093/mnrasl/slu094.

Hamilton, A. J. S. (2000). Uncorrelated modes of the non-linear power spectrum. *Monthly Notices of the Royal Astronomical Society*, 312.2, pp. 257–284. doi: 10.1046/j.1365-8711.2000.03071.x.

Hand, N. *et al.* (2011). The Atacama Cosmology Telescope: Detection of Sunyaev-Zel'Dovich Decrement in Groups and Clusters Associated with Luminous Red Galaxies. *The Astrophysical Journal*, 736.1, p. 39. doi: 10.1088/0004-637X/736/1/39.

Hand, N. *et al.* (2012). Evidence of Galaxy Cluster Motions with the Kinematic Sunyaev-Zel'dovich Effect. *Physical Review Letters*, 109.4, p. 041101. doi: 10.1103/PhysRevLett.109.041101.

Hand, N. *et al.* (2015). First measurement of the cross-correlation of CMB lensing and galaxy lensing. *Physical Review D*, 91.6, p. 062001. doi: 10.1103/PhysRevD.91.062001.

Hanson, D. *et al.* (2011). CMB temperature lensing power reconstruction. *Physical Review D*, 83.4, p. 043005. doi: 10.1103/PhysRevD.83.043005.

Hanson, D. *et al.* (2013). Detection of B-Mode Polarization in the Cosmic Microwave Background with Data from the South Pole Telescope. *Physical Review Letters*, 111.1, p. 141301. doi: 10.1103/PhysRevLett.111.141301.

Harnois-Déraps, J. *et al.* (2016). CFHTLenS and RCSLenS cross-correlation with Planck lensing detected in fourier and configuration space. *Monthly Notices of the Royal Astronomical Society*, 460.1, pp. 434–457. doi: 10.1093/mnras/stw947.

Hastie, T., Tibshirani, R. and Friedman, J. (2013). *The Elements of Statistical Learning*. Data Mining, Inference, and Prediction. Springer Science & Business Media.

Heidelberger, P. and Welch, P. D. (1981). A spectral method for confidence interval generation and run length control in simulations. *Communications of the ACM*, 24.4, pp. 233–245. doi: 10.1145/358598.358630.

— (1983). Simulation Run Length Control in the Presence of an Initial Transient. *Operations Research*, 31.6, pp. 1109–1144. doi: 10.1287/opre.31.6.1109.

Hilbert, S. *et al.* (2009). Ray-tracing through the Millennium Simulation: Born corrections and lens-lens coupling in cosmic shear and galaxy-galaxy lensing. *Astronomy & Astrophysics*, 499.1, pp. 31–43. doi: 10.1051/0004-6361/200811054.

Hildebrandt, H. *et al.* (2017). KiDS-450: cosmological parameter constraints from tomographic weak gravitational lensing. *Monthly Notices of the Royal Astronomical Society*, 465.2, pp. 1454–1498. doi: 10.1093/mnras/stw2805.

Hill, J. C. and Spergel, D. N. (2014). Detection of thermal SZ-CMB lensing cross-correlation in Planck nominal mission data. *Journal of Cosmology and Astroparticle Physics*, 02.0, pp. 030–030. doi: 10.1088/1475-7516/2014/02/030.

Hill, J. C. *et al.* (2016). Kinematic Sunyaev-Zel'dovich Effect with Projected Fields: A Novel Probe of the Baryon Distribution with Planck, WMAP, and WISE Data. *Physical Review Letters*, 117.5, p. 051301. doi: 10.1103/PhysRevLett.117.051301.

Hinshaw, G. *et al.* (2003). First-Year Wilkinson Microwave Anisotropy Probe (WMAP) Observations: The Angular Power Spectrum. *The Astrophysical Journal Supplement Series*, 148.1, pp. 135–159. doi: 10.1086/377225.

Hirata, C. M. *et al.* (2004). Cross-correlation of CMB with large-scale structure: Weak gravitational lensing. *Physical Review D*, 70.1, p. 103501. doi: 10.1103/PhysRevD.70.103501.

Hivon, E. *et al.* (2002). MASTER of the Cosmic Microwave Background Anisotropy Power Spectrum: A Fast Method for Statistical Analysis of Large and Complex Cosmic Microwave Background Data Sets. *The Astrophysical Journal*, 567.1, pp. 2–17. doi: 10.1086/338126.

Ho, S. *et al.* (2012). Clustering of Sloan Digital Sky Survey III Photometric Luminous Galaxies: The Measurement, Systematics, and Cosmological Implications. *The Astrophysical Journal*, 761.1, p. 14. doi: 10.1088/0004-637X/761/1/14.

Hoekstra, H. and Jain, B. (2008). Weak Gravitational Lensing and Its Cosmological Applications. *Annual Review of Nuclear and Particle Science*, 58.1, pp. 99–123. doi: 10.1146/annurev.nucl.58.110707.171151.

Holder, G. P. *et al.* (2013). A Cosmic Microwave Background Lensing Mass Map and Its Correlation with the Cosmic Infrared Background. *The Astrophysical Journal Letters*, 771.1, p. L16. doi: 10.1088/2041-8205/771/1/L16.

Hu, W. and Okamoto, T. (2002). Mass Reconstruction with Cosmic Microwave Background Polarization. *The Astrophysical Journal*, 574.2, pp. 566–574. doi: 10.1086/341110.

Hubble, E. (1929). "A Relation between Distance and Radial Velocity among Extra-Galactic Nebulae". In: *Proceedings of the National Academy of Sciences of the United States of America*. Mount Wilson Observatory, Carnegie Institution of Washington. National Acad Sciences, pp. 168–173. doi: 10.1073/pnas.15.3.168.

Hui, L., Gaztañaga, E. and LoVerde, M. (2007). Anisotropic magnification distortion of the 3D galaxy correlation. I. Real space. *Physical Review D*, 76.10, p. 103502. DOI: 10.1103/PhysRevD.76.103502.

HURVICH, C. M. and TSAI, C.-L. (1989). Regression and time series model selection in small samples. *Biometrika*, 76.2, pp. 297–307. DOI: 10.1093/biomet/76.2.297.

Jain, B. *et al.* (2015). The Whole is Greater than the Sum of the Parts: Optimizing the Joint Science Return from LSST, Euclid and WFIRST. *arXiv.org*, arXiv:1501.07897. arXiv: 1501.07897 [1501].

Jarrett, T. H. *et al.* (2000). 2MASS Extended Source Catalog: Overview and Algorithms. *The Astronomical Journal*, 119.5, pp. 2498–2531. DOI: 10.1086/301330.

Jelic, V. *et al.* (2015). "SKA - EoR correlations and cross-correlations: kSZ, radio galaxies, and NIR background". In: *Proceedings of Advancing Astrophysics with the Square Kilometre Array (AASKA14). 9 -13 June*, p. 8.

Jeong, D. (2010). *Cosmology with high (z > 1) redshift galaxy surveys*. PhD thesis.

Joachimi, B. and Bridle, S. L. (2010). Simultaneous measurement of cosmology and intrinsic alignments using joint cosmic shear and galaxy number density correlations. *Astronomy & Astrophysics*, 523, A1. DOI: 10.1051/0004-6361/200913657.

Jong, J. T. A. de *et al.* (2013). The Kilo-Degree Survey. *Experimental Astronomy*, 35.1, pp. 25–44. DOI: 10.1007/s10686-012-9306-1.

Joudaki, S. *et al.* (2017). KiDS-450 + 2dFLenS: Cosmological parameter constraints from weak gravitational lensing tomography and overlapping redshift-space galaxy clustering. arXiv: 1707.06627.

Kaiser, N. (1987). Clustering in real space and in redshift space. *Monthly Notices of the Royal Astronomical Society (ISSN 0035-8711)*, 227, pp. 1–21.

— (1992). Weak gravitational lensing of distant galaxies. *Astrophysical Journal*, 388, pp. 272–286. DOI: 10.1086/171151.

Keiner, J., Kunis, S. and Potts, D. (2009). Using NFFT 3—A Software Library for Various Nonequispaced Fast Fourier Transforms. *ACM Transactions on Mathematical Software*, 36.4, pp. 1–30. DOI: 10.1145/1555386.1555388.

Kermish, Z. D. *et al.* (2012). "The POLARBEAR experiment". In: *SPIE Astronomical Telescopes + Instrumentation*. Ed. by W. S. Holland. SPIE, p. 84521C. DOI: 10.1117/12.926354.

Kirk, D. *et al.* (2016). Cross-correlation of gravitational lensing from DES Science Verification data with SPT and Planck lensing. *Monthly Notices of the Royal Astronomical Society*, 459.1, pp. 21–34. DOI: 10.1093/mnras/stw570.

Kitching, T. D. and Heavens, A. F. (2017). Unequal-time correlators for cosmology. *Physical Review D*, 95.6, p. 063522. DOI: 10.1103/PhysRevD.95.063522.

Kitching, T. D. *et al.* (2017). The limits of cosmic shear. *Monthly Notices of the Royal Astronomical Society*, 469.3, pp. 2737–2749. DOI: 10.1093/mnras/stx1039.

Kowalski, M. *et al.* (2008). Improved Cosmological Constraints from New, Old, and Combined Supernova Data Sets. *The Astrophysical Journal*, 686.2, pp. 749–778. DOI: 10.1086/589937.

Krause, E. and Eifler, T. (2017). cosmolike – cosmological likelihood analyses for photometric galaxy surveys. *Monthly Notices of the Royal Astronomical Society*, 470.2, pp. 2100–2112. DOI: 10.1093/mnras/stx1261.

Krause, E., Eifler, T. and Blazek, J. (2016). The impact of intrinsic alignment on current and future cosmic shear surveys. *Monthly Notices of the Royal Astronomical Society*, 456.1, pp. 207–222. doi: 10.1093/mnras/stv2615.

Krause, E. *et al.* (2017). Dark Energy Survey Year 1 Results: Multi-Probe Methodology and Simulated Likelihood Analyses. arXiv: 1706.09359.

Kullback, S. and Leibler, R. A. (1951). On Information and Sufficiency. *The Annals of Mathematical Statistics*, 22.1, pp. 79–86. doi: 10.2307/2236703?ref=search-gateway:45196e549b1a05a7c2be508eb22f4abf.

Kwan, J. *et al.* (2017). Cosmology from large-scale galaxy clustering and galaxy-galaxy lensing with Dark Energy Survey Science Verification data. *Monthly Notices of the Royal Astronomical Society*, 464.4, pp. 4045–4062. doi: 10.1093/mnras/stw2464.

Lacasa, F., Lima, M. and Aguena, M. (2016). Super-sample covariance approximations and partial sky coverage. *arXiv.org*, arXiv:1612.05958. arXiv: 1612.05958v1 [1612].

Lamarre, J. M. *et al.* (2010). Planck pre-launch status: The HFI instrument, from specification to actual performance. *Astronomy & Astrophysics*, 520, A9. doi: 10.1051/0004-6361/200912975.

Larsen, P. and Challinor, A. (2016). Intrinsic alignment contamination to CMB lensing-galaxy weak lensing correlations from tidal torquing. *Monthly Notices of the Royal Astronomical Society*, 461.4, pp. 4343–4352. doi: 10.1093/mnras/stw1645.

Laureijs, R. *et al.* (2011). Euclid Definition Study Report. *arXiv.org*, arXiv:1110.3193. arXiv: 1110.3193 [1110].

Laurent, P. *et al.* (2016). A 14 h-3 Gpc3 study of cosmic homogeneity using BOSS DR12 quasar sample. *Journal of Cosmology and Astroparticle Physics*, 11.1, pp. 060–060. doi: 10.1088/1475-7516/2016/11/060.

Laurent, P. *et al.* (2017). Clustering of quasars in SDSS-IV eBOSS: study of potential systematics and bias determination. *Journal of Cosmology and Astroparticle Physics*, 07.0, pp. 017–017. doi: 10.1088/1475-7516/2017/07/017.

Lawrence, E. *et al.* (2017). The Mira-Titan Universe II: Matter Power Spectrum Emulation. arXiv: 1705.03388.

Le Gall, J.-F. (2006). *Intégration, Probabilités et Processus Aléatoires*. math.u-psud.fr.

Leauthaud, A. *et al.* (2017). Lensing is low: cosmology, galaxy formation or new physics? *Monthly Notices of the Royal Astronomical Society*, 467.3, pp. 3024–3047. doi: 10.1093/mnras/stx258.

Lebeau, G. (2009). Introduction à l'analyse de l'algorithme de Metropolis, pp. 1–47.

Lee, K.-G., Suzuki, N. and Spergel, D. N. (2012). Mean-flux-regulated Principal Component Analysis Continuum Fitting of Sloan Digital Sky Survey Lyα Forest Spectra. *The Astronomical Journal*, 143.2, p. 51. doi: 10.1088/0004-6256/143/2/51.

Lee, K.-G. *et al.* (2013). The BOSS Lyα Forest Sample from SDSS Data Release 9. *The Astronomical Journal*, 145.3, p. 69. doi: 10.1088/0004-6256/145/3/69.

Lee, K.-G. *et al.* (2014a). Lyα Forest Tomography from Background Galaxies: The First Megaparsec-resolution Large-scale Structure Map at z $>$ 2. *The Astrophysical Journal Letters*, 795.1, p. L12. doi: 10.1088/2041-8205/795/1/L12.

Lee, K.-G. *et al.* (2014b). Observational Requirements for Lyα Forest Tomographic Mapping of Large-scale Structure at z 2. *The Astrophysical Journal*, 788.1, p. 49. doi: 10.1088/0004-637X/788/1/49.

Lee, K.-G. *et al.* (2016). Shadow of a Colossus: A z = 2.44 Galaxy Protocluster Detected in 3D Lyα Forest Tomographic Mapping of the COSMOS Field. *The Astrophysical Journal*, 817.2, p. 160. DOI: 10.3847/0004-637X/817/2/160.

Lemos, P., Challinor, A. and Efstathiou, G. (2017). The effect of Limber and flat-sky approximations on galaxy weak lensing. *Journal of Cosmology and Astroparticle Physics*, 05.0, p. 014. DOI: 10.1088/1475-7516/2017/05/014.

Lesgourgues, J. and Pastor, S. (2006). Massive neutrinos and cosmology. *Physics Reports*, 429.6, pp. 307–379. DOI: 10.1016/j.physrep.2006.04.001.

Lesgourgues, J. and Tram, T. (2011). The Cosmic Linear Anisotropy Solving System (CLASS) IV: efficient implementation of non-cold relics. *Journal of Cosmology and Astroparticle Physics*, 09.0, pp. 032–032. DOI: 10.1088/1475-7516/2011/09/032.

— (2014). Fast and accurate CMB computations in non-flat FLRW universes. *Journal of Cosmology and Astroparticle Physics*, 09.0, p. 032. DOI: 10.1088/1475-7516/2014/09/032.

Lesgourgues, J. *et al.* (2009). *Neutrino Cosmology*. Cambridge: Cambridge University Press. DOI: 10.1017/CBO9781139012874.

Levi, M. *et al.* (2013). The DESI Experiment, a whitepaper for Snowmass 2013. arXiv: 1308.0847.

Lewis, A., Challinor, A. and Lasenby, A. (2000). Efficient Computation of Cosmic Microwave Background Anisotropies in Closed Friedmann-Robertson-Walker Models. *The Astrophysical Journal*, 538.2, pp. 473–476. DOI: 10.1086/309179.

Li, Y., Hu, W. and Takada, M. (2014). Super-sample signal. *Physical Review D*, 90.1, p. 103530. DOI: 10.1103/PhysRevD.90.103530.

Limber, D. N. (1953). The Analysis of Counts of the Extragalactic Nebulae in Terms of a Fluctuating Density Field. *Astrophysical Journal*, 117, pp. 134–. DOI: 10.1086/145672.

— (1954). The Analysis of Counts of the Extragalactic Nebulae in Terms of a Fluctuating Density Field. II. *Astrophysical Journal*, 119, pp. 655–. DOI: 10.1086/145870.

Liu, A. *et al.* (2016a). Eliminating the optical depth nuisance from the CMB with 21 cm cosmology. *Physical Review D*, 93.4, p. 043013. DOI: 10.1103/PhysRevD.93.043013.

Liu, J. and Hill, J. C. (2015). Cross-correlation of Planck CMB lensing and CFHTLenS galaxy weak lensing maps. *Physical Review D*, 92.6, p. 063517. DOI: 10.1103/PhysRevD.92.063517.

Liu, J., Ortiz-Vazquez, A. and Hill, J. C. (2016b). Constraining multiplicative bias in CFHTLenS weak lensing shear data. *Physical Review D*, 93.1, p. 103508. DOI: 10.1103/PhysRevD.93.103508.

LoVerde, M. and Afshordi, N. (2008). Extended Limber approximation. *Physical Review D*, 78.1, p. 123506. DOI: 10.1103/PhysRevD.78.123506.

LSST Science Collaborations and LSST Project *et al.* (2009). LSST Science Book, Version 2.0. *arXiv.org*, arXiv:0912.0201. arXiv: 0912.0201v1 [0912].

Ma, C.-P. and Bertschinger, E. (1995). Cosmological Perturbation Theory in the Synchronous and Conformal Newtonian Gauges. *The Astrophysical Journal*, 455, p. 7. DOI: 10.1086/176550.

Madhavacheril, M. *et al.* (2015). Evidence of Lensing of the Cosmic Microwave Background by Dark Matter Halos. *Physical Review Letters*, 114.1, p. 151302. DOI: 10.1103/PhysRevLett.114.151302.

Maraston, C. *et al.* (2013). Stellar masses of SDSS-III/BOSS galaxies at z ˜ 0.5 and constraints to galaxy formation models. *Monthly Notices of the Royal Astronomical Society*, 435.4, pp. 2764–2792. doi: 10.1093/mnras/stt1424.

McDonald, P. *et al.* (2000). The Observed Probability Distribution Function, Power Spectrum, and Correlation Function of the Transmitted Flux in the Lyα Forest. *The Astrophysical Journal*, 543.1, pp. 1–23. doi: 10.1086/317079.

McDonald, P. *et al.* (2006). The Lyα Forest Power Spectrum from the Sloan Digital Sky Survey. *The Astrophysical Journal Supplement Series*, 163.1, pp. 80–109. doi: 10.1086/444361.

McQuinn, M. (2016). The Evolution of the Intergalactic Medium. *Annual Review of Astronomy and Astrophysics*, 54.1, pp. 313–362. doi: 10.1146/annurev-astro-082214-122355.

McQuinn, M. and White, M. (2011). On estimating Lyα forest correlations between multiple sightlines. *Monthly Notices of the Royal Astronomical Society*, 415.3, pp. 2257–2269. doi: 10.1111/j.1365-2966.2011.18855.x.

Melin, J.-B. and Bartlett, J. G. (2015). Measuring cluster masses with CMB lensing: a statistical approach. *Astronomy & Astrophysics*, 578, A21. doi: 10.1051/0004-6361/201424720.

Miralda-Escudé, J. *et al.* (1996). The Lyα Forest from Gravitational Collapse in the Cold Dark Matter + Λ Model. *The Astrophysical Journal*, 471.2, pp. 582–616. doi: 10.1086/177992.

Miyatake, H. *et al.* (2015). The Weak Lensing Signal and the Clustering of BOSS Galaxies. I. Measurements. *The Astrophysical Journal*, 806.1, p. 1. doi: 10.1088/0004-637X/806/1/1.

Miyatake, H. *et al.* (2017). Measurement of a Cosmographic Distance Ratio with Galaxy and Cosmic Microwave Background Lensing. *Physical Review Letters*, 118.1, p. 161301. doi: 10.1103/PhysRevLett.118.161301.

Moradinezhad Dizgah, A. and Durrer, R. (2016). Lensing corrections to the Eg(z) statistics from large scale structure. *Journal of Cosmology and Astroparticle Physics*, 09.0, pp. 035–035. doi: 10.1088/1475-7516/2016/09/035.

More, S. *et al.* (2015). The Weak Lensing Signal and the Clustering of BOSS Galaxies. II. Astrophysical and Cosmological Constraints. *The Astrophysical Journal*, 806.1, p. 2. doi: 10.1088/0004-637X/806/1/2.

Muciaccia, P. F., Natoli, P. and Vittorio, N. (1997). Fast Spherical Harmonic Analysis: A Quick Algorithm for Generating and/or Inverting Full-Sky, High-Resolution Cosmic Microwave Background Anisotropy Maps. *The Astrophysical Journal*, 488.2, pp. L63–L66. doi: 10.1086/310921.

Nadarajah, S. and Pogány, T. K. (2016). On the distribution of the product of correlated normal random variables. *Comptes Rendus Mathematique*, 354.2, pp. 201–204. doi: 10.1016/j.crma.2015.10.019.

Navarro, J. F., Frenk, C. S. and White, S. D. M. (1996). The Structure of Cold Dark Matter Halos. *Astrophysical Journal v.462*, 462, pp. 563–. doi: 10.1086/177173.

Nicola, A., Refregier, A. and Amara, A. (2016). Integrated approach to cosmology: Combining CMB, large-scale structure, and weak lensing. *Physical Review D*, 94.8, p. 083517. doi: 10.1103/PhysRevD.94.083517.

— (2017). Integrated cosmological probes: Extended analysis. *Physical Review D*, 95.8, p. 083523. DOI: 10.1103/PhysRevD.95.083523.

Noterdaeme, P. *et al.* (2012). Column density distribution and cosmological mass density of neutral gas: Sloan Digital Sky Survey-III Data Release 9. *Astronomy & Astrophysics*, 547, p. L1. DOI: 10.1051/0004-6361/201220259.

Ogburn, R. W. I. *et al.* (2010). "The BICEP2 CMB polarization experiment". In: *Proceedings of the SPIE*. Stanford Univ., United States; Kavli Institute for Particle Astrophysics and Cosmology, United States, 77411G. DOI: 10.1117/12.857864.

Okamoto, T. and Hu, W. (2003). Cosmic microwave background lensing reconstruction on the full sky. *Physical Review D*, 67.8, p. 083002. DOI: 10.1103/PhysRevD.67.083002.

Olive, K. A. (2014). Review of Particle Physics. *Chinese Physics C*, 38.9, p. 090001. DOI: 10.1088/1674-1137/38/9/090001.

Osmer, P. (2001). "Quasistellar Objects: Overview". In: *The Encyclopedia of Astronomy and Astrophysics*. IOP Publishing Ltd. DOI: 10.1888/0333750888/1585.

Padmanabhan, N. *et al.* (2007). The clustering of luminous red galaxies in the Sloan Digital Sky Survey imaging data. *Monthly Notices of the Royal Astronomical Society*, 378.3, pp. 852–872. DOI: 10.1111/j.1365-2966.2007.11593.x.

Palanque-Delabrouille, N. *et al.* (2013). The one-dimensional Lyα forest power spectrum from BOSS. *Astronomy & Astrophysics*, 559, A85. DOI: 10.1051/0004-6361/201322130.

Palanque-Delabrouille, N. *et al.* (2015a). Constraint on neutrino masses from SDSS-III/BOSS Lyα forest and other cosmological probes. *Journal of Cosmology and Astroparticle Physics*, 02.0, pp. 045–045. DOI: 10.1088/1475-7516/2015/02/045.

Palanque-Delabrouille, N. *et al.* (2015b). Neutrino masses and cosmology with Lyman-alpha forest power spectrum. *Journal of Cosmology and Astroparticle Physics*, 11.1, pp. 011–011. DOI: 10.1088/1475-7516/2015/11/011.

Pâris, I. *et al.* (2017). The Sloan Digital Sky Survey Quasar Catalog: Twelfth data release. *Astronomy & Astrophysics*, 597, A79. DOI: 10.1051/0004-6361/201527999.

Park, Y. *et al.* (2016). Joint analysis of galaxy-galaxy lensing and galaxy clustering: Methodology and forecasts for Dark Energy Survey. *Physical Review D*, 94.6, p. 063533. DOI: 10.1103/PhysRevD.94.063533.

Passaglia, S., Manzotti, A. and Dodelson, S. (2017). Cross-correlating 2D and 3D galaxy surveys. *Physical Review D*, 95.1, p. 123508. DOI: 10.1103/PhysRevD.95.123508.

Pearson, R. and Zahn, O. (2014). Cosmology from cross correlation of CMB lensing and galaxy surveys. *Physical Review D*, 89.4, p. 043516. DOI: 10.1103/PhysRevD.89.043516.

Peebles, P. J. E. (1993). *Principles of Physical Cosmology*. Princeton University Press.

Peiris, H. V. and Spergel, D. N. (2000). Cross-Correlating the Sloan Digital Sky Survey with the Microwave Sky. *The Astrophysical Journal*, 540.2, pp. 605–613. DOI: 10.1086/309373.

Penna-Lima, M., Makler, M. and Wuensche, C. A. (2014). Biases on cosmological parameter estimators from galaxy cluster number counts. *Journal of Cosmology and Astroparticle Physics*, 05.0, pp. 039–039. DOI: 10.1088/1475-7516/2014/05/039.

Penna-Lima, M. *et al.* (2017). Calibrating the Planck cluster mass scale with CLASH. *Astronomy & Astrophysics*, DOI: 10.1051/0004-6361/201629971.

Penzias, A. A. and Wilson, R. W. (1965). A Measurement of Excess Antenna Temperature at 4080 Mc/s. *The Astrophysical Journal*, 142, pp. 419–421. DOI: 10.1086/148307.

Percival, W. J. (2013). "Large-scale structure observations". In: *Post-Planck Cosmology*. Oxford University Press, pp. 317–351. DOI: 10.1093/acprof:oso/9780198728856.003.0007.

Perlmutter, S. *et al.* (1999). Measurements of Ω and Λ from 42 High-Redshift Supernovae. *The Astrophysical Journal*, 517.2, pp. 565–586. DOI: 10.1086/307221.

Peter, P. and Uzan, J.-P. (2013). *Primordial Cosmology*. Oxford University Press.

Pilbratt, G. L. *et al.* (2010). Herschel Space Observatory. An ESA facility for far-infrared and submillimetre astronomy. *Astronomy & Astrophysics*, 518, p. L1. DOI: 10.1051/0004-6361/201014759.

Pisanti, O. *et al.* (2008). PArthENoPE: Public algorithm evaluating the nucleosynthesis of primordial elements. *Computer Physics Communications*, 178.1, pp. 956–971. DOI: 10.1016/j.cpc.2008.02.015.

Planck Collaboration (2006). The Scientific Programme of Planck. *arXiv.org*, arXiv:astro–ph–0604069. arXiv: astro-ph/0604069.

Planck Collaboration *et al.* (2011). Planck early results. I. The Planck mission. *Astronomy & Astrophysics*, 536, A1. DOI: 10.1051/0004-6361/201116464.

Planck Collaboration *et al.* (2014a). Planck 2013 results. XVI. Cosmological parameters. *Astronomy & Astrophysics*, 571, A16. DOI: 10.1051/0004-6361/201321591.

Planck Collaboration *et al.* (2014b). Planck 2013 results. XVII. Gravitational lensing by large-scale structure. *Astronomy & Astrophysics*, 571, A17. DOI: 10.1051/0004-6361/201321543.

Planck Collaboration *et al.* (2014c). Planck 2013 results. XVIII. The gravitational lensing-infrared background correlation. *Astronomy & Astrophysics*, 571, A18. DOI: 10.1051/0004-6361/201321540.

Planck Collaboration *et al.* (2014d). Planck 2013 results. XX. Cosmology from Sunyaev–Zeldovich cluster counts. *Astronomy & Astrophysics*, 571, A20. DOI: 10.1051/0004-6361/201321521.

Planck Collaboration *et al.* (2014e). Planck 2013 results. XXI. Power spectrum and high-order statistics of the Planck all-sky Compton parameter map. *Astronomy & Astrophysics*, 571, A21. DOI: 10.1051/0004-6361/201321522.

Planck Collaboration *et al.* (2014f). Planck 2013 results. XXX. Cosmic infrared background measurements and implications for star formation. *Astronomy & Astrophysics*, 571, A30. DOI: 10.1051/0004-6361/201322093.

Planck Collaboration *et al.* (2016a). Planck 2015 results. IX. Diffuse component separation: CMB maps. *Astronomy & Astrophysics*, 594, A9. DOI: 10.1051/0004-6361/201525936.

Planck Collaboration *et al.* (2016b). Planck 2015 results. VIII. High Frequency Instrument data processing: Calibration and maps. *Astronomy & Astrophysics*, 594, A8. DOI: 10.1051/0004-6361/201525820.

Planck Collaboration *et al.* (2016c). Planck 2015 results. X. Diffuse component separation: Foreground maps. *Astronomy & Astrophysics*, 594, A10. DOI: 10.1051/0004-6361/201525967.

Planck Collaboration *et al.* (2016d). Planck 2015 results. XI. CMB power spectra, likelihoods, and robustness of parameters. *Astronomy & Astrophysics*, 594, A11. DOI: 10.1051/0004-6361/201526926.

Planck Collaboration *et al.* (2016e). Planck 2015 results. XIII. Cosmological parameters. *Astronomy & Astrophysics*, 594, A13. doi: 10.1051/0004-6361/201525830.

Planck Collaboration *et al.* (2016f). Planck 2015 results. XV. Gravitational lensing. *Astronomy & Astrophysics*, 594, A15. doi: 10.1051/0004-6361/201525941.

Planck Collaboration *et al.* (2016g). Planck 2015 results. XXI. The integrated Sachs-Wolfe effect. *Astronomy & Astrophysics*, 594, A21. doi: 10.1051/0004-6361/201525831.

Planck Collaboration *et al.* (2016h). Planck 2015 results. XXII. A map of the thermal Sunyaev-Zeldovich effect. *Astronomy & Astrophysics*, 594, A22. doi: 10.1051/0004-6361/201525826.

Planck Collaboration *et al.* (2016i). Planck 2015 results. XXIII. The thermal Sunyaev-Zeldovich effect-cosmic infrared background correlation. *Astronomy & Astrophysics*, 594, A23. doi: 10.1051/0004-6361/201527418.

Planck Collaboration *et al.* (2016j). Planck 2015 results. XXIV. Cosmology from Sunyaev-Zeldovich cluster counts. *Astronomy & Astrophysics*, 594, A24. doi: 10.1051/0004-6361/201525833.

Planck Collaboration *et al.* (2016k). Planck intermediate results. XXX. The angular power spectrum of polarized dust emission at intermediate and high Galactic latitudes. *Astronomy & Astrophysics*, 586, A133. doi: 10.1051/0004-6361/201425034.

Planck Collaboration *et al.* (2016l). Planck intermediate results. XXXVII. Evidence of unbound gas from the kinetic Sunyaev-Zeldovich effect. *Astronomy & Astrophysics*, 586, A140. doi: 10.1051/0004-6361/201526328.

Plummer, M. *et al.* (2006). CODA: convergence diagnosis and output analysis for MCMC. *R news*,

Politzer, H. D. (1973). Reliable Perturbative Results for Strong Interactions? *Physical Review Letters*, 30.26, pp. 1346–1349. doi: 10.1103/PhysRevLett.30.1346.

Pontzen, A. (2014). Scale-dependent bias in the baryonic-acoustic-oscillation-scale intergalactic neutral hydrogen. *Physical Review D*, 89.8, p. 083010. doi: 10.1103/PhysRevD.89.083010.

Pullen, A. R. *et al.* (2016). Constraining gravity at the largest scales through CMB lensing and galaxy velocities. *Monthly Notices of the Royal Astronomical Society*, 460.4, pp. 4098–4108. doi: 10.1093/mnras/stw1249.

Putter, R. de *et al.* (2012). New Neutrino Mass Bounds from SDSS-III Data Release 8 Photometric Luminous Galaxies. *The Astrophysical Journal*, 761.1, p. 12. doi: 10.1088/0004-637X/761/1/12.

Rauch, M. (1998). The Lyman Alpha Forest in the Spectra of QSOs. *Annual Review of Astronomy and Astrophysics*, 36, pp. 267–316. doi: 10.1146/annurev.astro.36.1.267.

— (2001). "Lyman Alpha Forest". In: *The Encyclopedia of Astronomy and Astrophysics*. IOP Publishing Ltd. doi: 10.1888/0333750888/2140.

Refregier, A. *et al.* (2010). Euclid Imaging Consortium Science Book. *arXiv.org*, arXiv:1001.0061. arXiv: 1001.0061 [1001].

Reid, B. A. *et al.* (2012). The clustering of galaxies in the SDSS-III Baryon Oscillation Spectroscopic Survey: measurements of the growth of structure and expansion rate at z = 0.57 from anisotropic clustering. *Monthly Notices of the Royal Astronomical Society*, 426.4, pp. 2719–2737. doi: 10.1111/j.1365-2966.2012.21779.x.

Reid, B. *et al.* (2016). SDSS-III Baryon Oscillation Spectroscopic Survey Data Release 12: galaxy target selection and large-scale structure catalogues. *Monthly Notices of the Royal Astronomical Society*, 455.2, pp. 1553–1573. DOI: 10.1093/mnras/stv2382.

Rhodes, J. *et al.* (2015). Exploiting cross correlations and joint analyses. *Astroparticle Physics*, 63, pp. 42–54. DOI: 10.1016/j.astropartphys.2014.02.009.

Riess, A. G. *et al.* (1998). Observational Evidence from Supernovae for an Accelerating Universe and a Cosmological Constant. *The Astronomical Journal*, 116.3, pp. 1009–1038. DOI: 10.1086/300499.

Riess, A. G. *et al.* (2016). A 2.4% Determination of the Local Value of the Hubble Constant. *The Astrophysical Journal*, 826.1, p. 56. DOI: 10.3847/0004-637X/826/1/56.

Rini, M. (2016). *Synopsis: Seeing Dark Matter Through the Clouds*.

Robotham, A. S. G. and Driver, S. P. (2011). The GALEX-SDSS NUV and FUV flux density and local star formation rate. *Monthly Notices of the Royal Astronomical Society*, 413.4, pp. 2570–2582. DOI: 10.1111/j.1365-2966.2011.18327.x.

Ross, N. P. *et al.* (2012). The SDSS-III Baryon Oscillation Spectroscopic Survey: Quasar Target Selection for Data Release Nine. *The Astrophysical Journal Supplement*, 199.1, p. 3. DOI: 10.1088/0067-0049/199/1/3.

Rossi, G. *et al.* (2014). Suite of hydrodynamical simulations for the Lyman-α forest with massive neutrinos. *Astronomy & Astrophysics*, 567, A79. DOI: 10.1051/0004-6361/201423507.

Roston, M. (2015). Albert Einstein and Relativity in the Pages of The Times. *The New York Times*,

Rubin, V. C., Thonnard, N. and Ford, W. K. J. (1978). Extended rotation curves of high-luminosity spiral galaxies. IV - Systematic dynamical properties, SA through SC. *Astrophysical Journal*, 225, pp. L107–L111. DOI: 10.1086/182804.

Sachs, R. K. and Wolfe, A. M. (1967). Perturbations of a Cosmological Model and Angular Variations of the Microwave Background. *Astrophysical Journal*, 147, pp. 73–. DOI: 10.1086/148982.

Saito, S. (2016). "Galaxy Clustering in Redshift Space ". In: *Lecture Series on Cosmology at MPA*.

Schaan, E., Takada, M. and Spergel, D. N. (2014). Joint likelihood function of cluster counts and n -point correlation functions: Improving their power through including halo sample variance. *Physical Review D*, 90.1, p. 123523. DOI: 10.1103/PhysRevD.90.123523.

Schaan, E. *et al.* (2016). Evidence for the kinematic Sunyaev-Zel'dovich effect with the Atacama Cosmology Telescope and velocity reconstruction from the Baryon Oscillation Spectroscopic Survey. *Physical Review D*, 93.8, p. 082002. DOI: 10.1103/PhysRevD.93.082002.

Schaan, E. *et al.* (2017). Looking through the same lens: Shear calibration for LSST, Euclid, and WFIRST with stage 4 CMB lensing. *Physical Review D*, 95.1, p. 123512. DOI: 10.1103/PhysRevD.95.123512.

Schlegel, D. J. *et al.* (2009). BigBOSS: The Ground-Based Stage IV Dark Energy Experiment. *arXiv.org*, arXiv:0904.0468. arXiv: 0904.0468 [0904].

Schneider, P., Ehlers, J. and Falco, E. E. (1992). *Gravitational Lenses*. Astronomy and Astrophysics Library. Berlin, Heidelberg: Springer Berlin Heidelberg. DOI: 10.1007/978-3-662-03758-4.

Schneider, P., Kochanek, C. S. and Wambsganss, J. (2006). *Gravitational Lensing: Strong, Weak and Micro*. Saas-Fee Advanced Courses, Swiss Society for Astrophysics and Astronomy. Berlin, Heidelberg: Springer. doi: 10.1007/978-3-540-30310-7.

Schruben, L. W. (1982). Detecting Initialization Bias in Simulation Output. *Operations Research*, 30.3, pp. 569–590. doi: 10.1287/opre.30.3.569.

Scranton, R. *et al.* (2005). Detection of Cosmic Magnification with the Sloan Digital Sky Survey. *The Astrophysical Journal*, 633.2, pp. 589–602. doi: 10.1086/431358.

Seager, S., Sasselov, D. D. and Scott, D. (1999). A New Calculation of the Recombination Epoch. *The Astrophysical Journal*, 523.1, pp. L1–L5. doi: 10.1086/312250.

Seljak, U. (2009). Extracting Primordial Non-Gaussianity without Cosmic Variance. *Physical Review Letters*, 102.2, p. 021302. doi: 10.1103/PhysRevLett.102.021302.

Seljak, U. and Zaldarriaga, M. (1996). A Line-of-Sight Integration Approach to Cosmic Microwave Background Anisotropies. *Astrophysical Journal v.469*, 469, pp. 437–. doi: 10.1086/177793.

Seljak, U. *et al.* (2006). Can Sterile Neutrinos Be the Dark Matter? *Physical Review Letters*, 97.1, p. 191303. doi: 10.1103/PhysRevLett.97.191303.

Sellentin, E. and Heavens, A. F. (2016). Parameter inference with estimated covariance matrices. *Monthly Notices of the Royal Astronomical Society: Letters*, 456.1, pp. L132–L136. doi: 10.1093/mnrasl/slv190.

Seo, H.-J. and Eisenstein, D. J. (2007). Improved Forecasts for the Baryon Acoustic Oscillations and Cosmological Distance Scale. *The Astrophysical Journal*, 665.1, pp. 14–24. doi: 10.1086/519549.

Sherwin, B. D. *et al.* (2012). The Atacama Cosmology Telescope: Cross-correlation of cosmic microwave background lensing and quasars. *Physical Review D*, 86.8, p. 083006. doi: 10.1103/PhysRevD.86.083006.

Simon, P. (2007). How accurate is Limber's equation? *Astronomy & Astrophysics*, 473.3, pp. 711–714. doi: 10.1051/0004-6361:20066352.

Singh, S., Mandelbaum, R. and Brownstein, J. R. (2017). Cross-correlating Planck CMB lensing with SDSS: lensing-lensing and galaxy-lensing cross-correlations. *Monthly Notices of the Royal Astronomical Society*, 464.2, pp. 2120–2138. doi: 10.1093/mnras/stw2482.

Slosar, A. *et al.* (2011). The Lyman-α forest in three dimensions: measurements of large scale flux correlations from BOSS 1st-year data. *Journal of Cosmology and Astroparticle Physics*, 09.0, pp. 001–001. doi: 10.1088/1475-7516/2011/09/001.

Slosar, A. *et al.* (2013). Measurement of baryon acoustic oscillations in the Lyman-α forest fluctuations in BOSS data release 9. *Journal of Cosmology and Astroparticle Physics*, 04.0, pp. 026–026. doi: 10.1088/1475-7516/2013/04/026.

Smee, S. A. *et al.* (2013). The Multi-object, Fiber-fed Spectrographs for the Sloan Digital Sky Survey and the Baryon Oscillation Spectroscopic Survey. *The Astronomical Journal*, 146.2, p. 32. doi: 10.1088/0004-6256/146/2/32.

Smith, K. M. and Ferraro, S. (2017). Detecting Patchy Reionization in the Cosmic Microwave Background. *Physical Review Letters*, 119.2, p. 021301. doi: 10.1103/PhysRevLett.119.021301.

Smith, K. M., Zahn, O. and Dore, O. (2007). Detection of gravitational lensing in the cosmic microwave background. *Physical Review D*, 76.4, p. 043510. doi: 10.1103/PhysRevD.76.043510.

Smith, R. E. *et al.* (2003). Stable clustering, the halo model and non-linear cosmological power spectra. *Monthly Notice of the Royal Astronomical Society*, 341.4, pp. 1311–1332. doi: 10.1046/j.1365-8711.2003.06503.x.

Smoot, G. *et al.* (1990). COBE Differential Microwave Radiometers - Instrument design and implementation. *Astrophysical Journal*, 360, pp. 685–695. doi: 10.1086/169154.

Snowden, S. L. *et al.* (1997). ROSAT Survey Diffuse X-Ray Background Maps. II. *The Astrophysical Journal*, 485.1, pp. 125–135. doi: 10.1086/304399.

Sobacchi, E., Mesinger, A. and Greig, B. (2016). Cross-correlation of the cosmic 21-cm signal and Lyman α emitters during reionization. *Monthly Notices of the Royal Astronomical Society*, 459.3, pp. 2741–2750. doi: 10.1093/mnras/stw811.

Soergel, B. *et al.* (2015). Constraining dark sector perturbations II: ISW and CMB lensing tomography. *Journal of Cosmology and Astroparticle Physics*, 02.0, p. 037. doi: 10.1088/1475-7516/2015/02/037.

Spergel, D. *et al.* (2013). Wide-Field InfraRed Survey Telescope-Astrophysics Focused Telescope Assets WFIRST-AFTA Final Report. arXiv: 1305.5422.

Steinhardt, P. J. and Turok, N. (2007). *Endless Universe*. Beyond the Big Bang. Broadway Books.

Sunyaev, R. A. and Zeldovich, Y. B. (1970). Small-Scale Fluctuations of Relic Radiation. *Astrophysics and Space Science*, 7.1, pp. 3–19. doi: 10.1007/BF00653471.

Suzuki, A. *et al.* (2016). The Polarbear-2 and the Simons Array Experiments. *Journal of Low Temperature Physics*, 184.3-4, pp. 805–810. doi: 10.1007/s10909-015-1425-4.

Swetz, D. S. *et al.* (2011). Overview of the Atacama Cosmology Telescope: Receiver, Instrumentation, and Telescope Systems. *The Astrophysical Journal Supplement*, 194.2, p. 41. doi: 10.1088/0067-0049/194/2/41.

Takada, M. and Spergel, D. N. (2014). Joint analysis of cluster number counts and weak lensing power spectrum to correct for the super-sample covariance. *Monthly Notices of the Royal Astronomical Society*, 441.3, pp. 2456–2475. doi: 10.1093/mnras/stu759.

Takahashi, R. *et al.* (2012). Revising the Halofit Model for the Nonlinear Matter Power Spectrum. *The Astrophysical Journal*, 761.2, p. 152. doi: 10.1088/0004-637X/761/2/152.

Takeuchi, Y., Ichiki, K. and Matsubara, T. (2012). Application of cross correlations between CMB and large-scale structure to constraints on the primordial non-Gaussianity. *Physical Review D*, 85.4, p. 043518. doi: 10.1103/PhysRevD.85.043518.

Tauber, J. A. *et al.* (2010a). Planck pre-launch status: The optical system. *Astronomy & Astrophysics*, 520, A2. doi: 10.1051/0004-6361/200912911.

Tauber, J. A. *et al.* (2010b). Planck pre-launch status: The Planck mission. *Astronomy & Astrophysics*, 520, A1. doi: 10.1051/0004-6361/200912983.

Taylor, M. S. *et al.* (2013). On the Source of Astrometric Anomalous Refraction. *The Astronomical Journal*, 145.3, p. 82. doi: 10.1088/0004-6256/145/3/82.

Tegmark, M. and Zaldarriaga, M. (2002). Separating the early universe from the late universe: Cosmological parameter estimation beyond the black box. *Physical Review D*, 66.1, p. 103508. doi: 10.1103/PhysRevD.66.103508.

Tegmark, M., Zaldarriaga, M. and Hamilton, A. J. (2001). Towards a refined cosmic concordance model: Joint 11-parameter constraints from the cosmic microwave background and large-scale structure. *Physical Review D*, 63.4, p. 043007. doi: 10.1103/PhysRevD.63.043007.

Tolmatz, L. (2002). On the Distribution of the Square Integral of the Brownian Bridge. *The Annals of Probability*, 30.1, pp. 253–269. doi: 10.1214/aop/1020107767.

Tröster, T. *et al.* (2017). Cross-correlation of weak lensing and gamma rays: implications for the nature of dark matter. *Monthly Notices of the Royal Astronomical Society*, 467.3, pp. 2706–2722. doi: 10.1093/mnras/stx365.

Troxel, M. A. and Ishak, M. (2014). Cross-correlation between cosmic microwave background lensing and galaxy intrinsic alignment as a contaminant to gravitational lensing cross-correlated probes of the Universe. *Physical Review D*, 89.6, p. 063528. doi: 10.1103/PhysRevD.89.063528.

Uitert, E. van *et al.* (2017). KiDS+GAMA: Cosmology constraints from a joint analysis of cosmic shear, galaxy-galaxy lensing and angular clustering. arXiv: 1706.05004.

Vagnozzi, S. *et al.* (2017). Unveiling ν secrets with cosmological data: neutrino masses and mass hierarchy. arXiv: 1701.08172.

Vallinotto, A. (2012). Using Cosmic Microwave Background Lensing to Constrain the Multiplicative Bias of Cosmic Shear. *The Astrophysical Journal*, 759.1, p. 32. doi: 10.1088/0004-637X/759/1/32.

Vallinotto, A. *et al.* (2009). Lenses in the Forest: Cross Correlation of the Lyman-α Flux with Cosmic Microwave Background Lensing. *Physical Review Letters*, 103.9, p. 091304. doi: 10.1103/PhysRevLett.103.091304.

Vallinotto, A. *et al.* (2011). Cross-correlations of the Lyα Forest with Weak-lensing Convergence. Analytical Estimates of Signal-to-noise Ratio and Implications for Neutrino Mass and Dark Energy. *The Astrophysical Journal*, 735.1, p. 38. doi: 10.1088/0004-637X/735/1/38.

Viel, M. *et al.* (2013). Warm dark matter as a solution to the small scale crisis: New constraints from high redshift Lyman-α forest data. *Physical Review D*, 88.4, p. 043502. doi: 10.1103/PhysRevD.88.043502.

Vielva, P., Martinez-González, E. and Tucci, M. (2006). Cross-correlation of the cosmic microwave background and radio galaxies in real, harmonic and wavelet spaces: detection of the integrated Sachs-Wolfe effect and dark energy constraints. *Monthly Notices of the Royal Astronomical Society*, 365.3, pp. 891–901. doi: 10.1111/j.1365-2966.2005.09764.x.

Vitenti, S. D. P., Penna-Lima, M. and Doux, C. (n.d.). NumCosmo: Numerical Cosmology library.

Vogelsberger, M. *et al.* (2014). Introducing the Illustris Project: simulating the coevolution of dark and visible matter in the Universe. *Monthly Notices of the Royal Astronomical Society*, 444.2, pp. 1518–1547. doi: 10.1093/mnras/stu1536.

Vrbanec, D. *et al.* (2016). Predictions for the 21 cm-galaxy cross-power spectrum observable with LOFAR and Subaru. *Monthly Notices of the Royal Astronomical Society*, 457.1, pp. 666–675. doi: 10.1093/mnras/stv2993.

Wang, Y., Spergel, D. N. and Strauss, M. A. (1999). Cosmology in the Next Millennium: Combining Microwave Anisotropy Probe and Sloan Digital Sky Survey Data to Constrain Inflationary Models. *The Astrophysical Journal*, 510.1, pp. 20–31. doi: 10.1086/306558.

Weinberg, S. (1989). The cosmological constant problem. *Reviews of Modern Physics*, 61.1, pp. 1–23. doi: 10.1103/RevModPhys.61.1.

— (2005). *The Quantum Theory of Fields: Volume 1, Foundations*. Cambridge University Press.

White, M. (2015). Reconstruction within the Zeldovich approximation. *Monthly Notices of the Royal Astronomical Society*, 450.4, pp. 3822–3828. DOI: 10.1093/mnras/stv842.

White, M. *et al.* (2012). The clustering of intermediate-redshift quasars as measured by the Baryon Oscillation Spectroscopic Survey. *Monthly Notices of the Royal Astronomical Society*, 424.2, pp. 933–950. DOI: 10.1111/j.1365-2966.2012.21251.x.

Woithe, J., Wiener, G. J. and Van der Veken, F. F. (2017). Let's have a coffee with the Standard Model of particle physics! *Physics Education*, 52.3, pp. 034001–. DOI: 10.1088/1361-6552/aa5b25.

Wright, E. L. *et al.* (2010). The Wide-field Infrared Survey Explorer (WISE): Mission Description and Initial On-orbit Performance. *The Astronomical Journal*, 140.6, pp. 1868–1881. DOI: 10.1088/0004-6256/140/6/1868.

Xia, J.-Q. *et al.* (2015). Tomography of the Fermi-LAT γ-Ray Diffuse Extragalactic Signal via Cross Correlations with Galaxy Catalogs. *The Astrophysical Journal Supplement Series*, 217.1, p. 15. DOI: 10.1088/0067-0049/217/1/15.

Yoo, J. and Seljak, U. (2012). Joint analysis of gravitational lensing, clustering, and abundance: Toward the unification of large-scale structure analysis. *Physical Review D*, 86.8, p. 083504. DOI: 10.1103/PhysRevD.86.083504.

York, D. G. *et al.* (2000). The Sloan Digital Sky Survey: Technical Summary. *The Astronomical Journal*, 120.3, pp. 1579–1587. DOI: 10.1086/301513.

Zaldarriaga, M., Seljak, U. and Hui, L. (2001). Correlations in the Lyα Forest: Testing the Gravitational Instability Paradigm. *The Astrophysical Journal*, 551.1, pp. 48–56. DOI: 10.1086/320066.

Zegers, P. (2015). Fisher Information Properties. *Entropy*, 17, pp. 4918–4939. DOI: 10.3390/e17074918.

Ziour, R. and Hui, L. (2008). Magnification bias corrections to galaxy-lensing cross-correlations. *Physical Review D*, 78.1, p. 123517. DOI: 10.1103/PhysRevD.78.123517.

Zuber, J.-B. (2013). *Invariances en physique et théorie des groupes*. lpthe.jussieu.fr.